

---

# **Spectroscopy of high- $Z$ ions as a way to understanding the nature of Cas A knots and intergalactic shocks**

Dmitrijs Docenko

---



München 2008



---

# **Spectroscopy of high- $Z$ ions as a way to understanding the nature of Cas A knots and intergalactic shocks**

**Dmitrijs Docenko**

---

Dissertation  
an der Fakultät für Physik  
der Ludwig-Maximilians-Universität  
München

vorgelegt von  
Dmitrijs Docenko  
aus Riga

München, den 09 Mai 2008

Erstgutachter: Prof. Dr. Rashid Sunyaev

Zweitgutachter: Prof. Dr. Ralf Bender

Tag der mündlichen Prüfung: 02 Juli 2008

# Contents

<b>Zusammenfassung</b>	<b>xiii</b>
<b>Summary</b>	<b>xv</b>
<b>1 Introduction</b>	<b>1</b>
1.1 Astrophysical objects under consideration . . . . .	2
1.1.1 Hot intracluster medium . . . . .	2
1.1.2 Hot interstellar medium in and around elliptical galaxies . . . . .	3
1.1.3 Hot interstellar medium in our Galaxy and spiral galaxies . . . . .	3
1.1.4 Warm-hot intergalactic medium . . . . .	4
1.1.5 Young supernova remnants . . . . .	5
1.1.6 Older supernova remnants . . . . .	5
1.2 Elementary processes and atomic level populations . . . . .	6
1.2.1 Elementary processes influencing the line emission . . . . .	6
1.2.2 Level populations and line emissivities . . . . .	7
1.2.3 Formulae used in the main part of the thesis . . . . .	8
1.3 Spectral line types under discussion . . . . .	10
1.3.1 Level classification . . . . .	10
1.3.2 Fine-structure lines . . . . .	11
1.3.3 Hyperfine structure lines . . . . .	11
1.3.4 Metal recombination lines . . . . .	13
1.4 The Cassiopeia A supernova remnant . . . . .	15
1.5 Structure of the thesis . . . . .	19
<b>2 The <math>^{14}\text{N VII HFS}</math> line from hot ISM and WHIM</b>	<b>21</b>
2.1 Introduction . . . . .	23
2.2 Hyperfine structure transitions . . . . .	25
2.2.1 Optical depth and emissivity corrections . . . . .	28
2.3 Emission lines from hot ISM and supernova remnants . . . . .	31
2.3.1 Overview of the brightest objects . . . . .	31
2.3.2 Emission line intensity estimates . . . . .	34
2.3.3 Resonant scattering in the surroundings of quasar . . . . .	36
2.3.4 Disentangling Local Bubble and heliospheric emission . . . . .	37

2.4	Absorption lines in WHIM and hot ISM . . . . .	38
2.4.1	Warm-hot intergalactic medium . . . . .	38
2.4.2	Hot interstellar medium . . . . .	39
2.4.3	Gamma-ray burst afterglows . . . . .	39
2.4.4	Estimates of HFS line detectability . . . . .	39
2.5	Conclusions . . . . .	40
<b>3</b>	<b>Optical and NIR recombination lines from Cas A knots</b>	<b>43</b>
3.1	Introduction . . . . .	45
3.2	Computation of recombination line fluxes . . . . .	47
3.2.1	Elementary processes . . . . .	48
3.2.2	Cascade and $l$ -redistribution equations . . . . .	49
3.2.3	Recombination line emissivities . . . . .	49
3.2.4	Resulting line fluxes . . . . .	50
3.3	Astrophysical application: FMKs in Cassiopeia A . . . . .	52
3.3.1	Cooling region after the shock front . . . . .	54
3.3.2	Cold photoionized region . . . . .	56
3.3.3	Separating pre- and post-shock spectral lines . . . . .	59
3.3.4	Existing observational limits . . . . .	60
3.4	Individual line substructure . . . . .	62
3.5	Plasma diagnostics using recombination lines . . . . .	64
3.5.1	Temperature diagnostics . . . . .	64
3.5.2	Recombination lines as density diagnostics . . . . .	68
3.5.3	Recombination lines of other elements . . . . .	68
3.5.4	Recombination line flux ratios to collisionally-excited lines . . . . .	70
3.6	Conclusions . . . . .	72
<b>4</b>	<b>Fine-structure infrared lines from the Cassiopeia A knots</b>	<b>75</b>
4.1	Introduction . . . . .	77
4.2	Theoretical models of the fast-moving knots . . . . .	78
4.2.1	Infrared lines from the SD-200 model . . . . .	81
4.2.2	Line flux computation . . . . .	82
4.3	Archival observations of the FIR lines . . . . .	84
4.3.1	ISO observations . . . . .	85
4.3.2	<i>Spitzer</i> Space Telescope observations . . . . .	89
4.4	Physical conditions and abundances in the FMKs . . . . .	95
4.4.1	Information from the same ion line flux ratios . . . . .	96
4.4.2	Abundances from the flux ratios to the 5007 Å line . . . . .	99
4.5	Discussion . . . . .	103
4.5.1	On too high pre-shock intensities of some lines . . . . .	103
4.5.2	Post-shock photoionized region . . . . .	105
4.5.3	Effects of the dust on the post-shock PIR structure . . . . .	107
4.5.4	Comparison of the model predictions with observations . . . . .	107

4.5.5	Recombination lines in the infrared range . . . . .	108
4.6	Conclusions . . . . .	109
<b>5</b>	<b>Conclusions</b>	<b>113</b>
<b>A</b>	<b>Atomic physics for level population computations</b>	<b>115</b>
A.1	Determination of the upper cutoff $n_{\max}$ . . . . .	115
A.2	Radiative recombination . . . . .	116
A.3	Dielectronic recombination . . . . .	118
A.4	Highly-excited level energies . . . . .	121
A.5	Computation of the level shifts for high- $l$ states . . . . .	123
A.6	Computation of the line substructure . . . . .	125
A.7	Line emission without recombination . . . . .	125
A.8	Estimates of the resulting uncertainties . . . . .	126
<b>B</b>	<b><i>Spitzer</i> data cube PSF size estimate</b>	<b>129</b>
<b>C</b>	<b>Derivation of the equation (4.4)</b>	<b>131</b>
	<b>Acknowledgements</b>	<b>149</b>





# List of Figures

1.1	Cosmic abundances of isotopes with non-zero nuclear spin . . . . .	12
1.2	Cassiopeia A supernova remnant maps from radiowaves to X-rays . . . . .	16
2.1	Ionic abundances of isotopes having HFS splitting . . . . .	26
2.2	Low-density emissivities $\varepsilon(T_e)$ of the HFS transitions at $z = 0$ . . . . .	29
2.3	HFS sublevel populations as functions of electron density . . . . .	32
2.4	Correction coefficient $D(T_{R0}, n_e)$ as a function of electron density . . . . .	33
2.5	Correction coefficient $D(T_{R0}, n_e)$ as a function of redshift . . . . .	34
3.1	The O v $8\alpha$ recombination line low-density emissivity . . . . .	50
3.2	The plane-parallel SD95 model schematic structure . . . . .	53
3.3	Recombination and ionization timescales and plasma cooling time . . . . .	55
3.4	Emission measure and O <sup>5+</sup> abundances in the post-shock region . . . . .	56
3.5	Line luminosity distribution over temperature in the SD95 model . . . . .	58
3.6	Recombination line fluxes from the post-shock cooling region . . . . .	59
3.7	Recombination line fluxes from the pre-shock photoionized region . . . . .	61
3.8	Fine structure of recombination lines . . . . .	63
3.9	Model spectra near 0.8 and 2.1 $\mu\text{m}$ . . . . .	65
3.10	Variation of the O III $7\alpha$ line fine structure with temperature and density .	66
3.11	Low-density $l$ -summed emissivities of oxygen ion recombination lines. . . .	67
3.12	O v recombination line emissivity ratios as functions of temperature. . . .	67
3.13	Dependence of O v $7\alpha$ line emissivity on density . . . . .	69
3.14	Increase of O v $\alpha$ -line emissivities with density at $T_e = 3 \times 10^4$ K . . . .	69
3.15	Low-density $l$ -summed emissivities of Si and S ion recombination lines . . .	71
3.16	Low-density emissivity ratios of recombination lines to optical forbidden lines	72
3.17	Emissivity ratios of recombination lines to far-infrared forbidden lines . . .	73
4.1	Schematic representation of the FMK shock temperature structure. . . . .	80
4.2	Comparison of oxygen ion abundances in CIE and SD-200 model . . . . .	82
4.3	Line luminosity distribution over temperature in the SD-200 model . . . .	84
4.4	ISO LWS apertures overlaid on the HST ACS image of Cas A . . . . .	86
4.5	ISO LWS spectral cuts containing oxygen far-infrared lines . . . . .	87
4.6	Comparison of <i>Spitzer</i> and HST line maps of the Cas A northern region . .	91

---

4.7	Pixel-by-pixel comparison of the 5007 Å and the 25.91 μm lines . . . . .	92
4.8	The constraints on the pre-shock region from the [O III] lines . . . . .	98
4.9	Energy level and transition diagram of the lowest levels of Fe <sup>+</sup> ion . . . . .	104
A.1	Departure coefficients of recombining O <sup>5+</sup> in different approximations . . .	116
A.2	<i>n</i> -resolved recombination rates of O <sup>5+</sup> . . . . .	117
A.3	Comparison of O <sup>5+</sup> dielectronic recombination rates . . . . .	120
A.4	Comparison of scaled autoionization rates of O <sup>4+</sup> ion . . . . .	121
A.5	Elementary process rates of the recombining O <sup>5+</sup> ion . . . . .	122

# List of Tables

2.1	Hyperfine structure transition data . . . . .	27
2.2	HFS transition radiative corrections and critical densities . . . . .	31
2.3	Objects expected to be bright in the HFS lines and their parameters . . . .	32
2.4	Predicted brightness temperature in HFS lines . . . . .	36
2.5	HFS absorption line optical depth $\tau$ estimate from Cygnus X-3 . . . . .	39
3.1	Wavelengths $\lambda$ and emissivities $\varepsilon$ of some of O V recombination lines . . . .	51
3.2	Hydrogenic wavelengths of some of recombination $\alpha$ -lines . . . . .	51
3.3	Post-shock cooling region recombination line fluxes . . . . .	57
3.4	Pre-shock photoionized region recombination line fluxes . . . . .	60
4.1	Far-infrared line ratios to the 5007 Å line in models and observations . . . .	79
4.2	Summary of the ISO LWS archival observations of the Cassiopeia A . . . .	86
4.3	Far-infrared line fluxes from the ISO LWS observations of Cas A. . . . .	88
4.4	Far-infrared line flux ratios to the 5007 Å line from ISO data . . . . .	89
4.5	Infrared line fluxes and their ratios $I/I(5007 \text{ Å})$ from the <i>Spitzer</i> data . . .	94
4.6	Information from the same ion line flux ratios measured in the FMKs . . . .	97
4.7	Estimated FMK post-shock ionic abundances $n_{\text{ion}}/n_{\text{O}}$ . . . . .	100
4.8	Estimated FMK pre-shock ionic abundances $n_{\text{ion}}/n_{\text{O}}$ . . . . .	101
A.1	Atomic parameters used for computations of the line substructure . . . . .	124



# Zusammenfassung

Das Ziel der Studien dieser Doktorarbeit ist eine Analyse möglicher spektroskopischer Methoden im Bereich hoch-geladener Ionen Beobachtungen von heißem astrophysikalischen Plasma, die bisher noch nicht gründlich untersucht wurden.

Die erste Aufgabe, die hierzu durchgeführt werden muss ist eine Durchsicht verschiedene Spektrallinientypen und passende Typen astrophysikalischer Objekte. Danach werden eine theoretische Beschreibung und Bestimmung der besten Beobachtungsparameter in der viel versprechenden Richtung und Anwendung der Methode auf bestimmte Objekte vorgestellt. Zwei Ergebnisse solcher Studien (Kombinationen von Spektral- und Objekttyp) werden in dieser Arbeit näher betrachtet.

Es wird gezeigt, dass die Hyperfein-Struktur-Linien hoch-ionisierter Metall-Atome (primär die Linie von  $[^{14}\text{N VII}]$  bei 5.65  $\mu\text{m}$ ) mit modernen Radioteleskopen beobachtbar sind. Die astrophysikalischen Objekte, die für das Auftreten dieser Linien verantwortlich sind, entweder in Emission oder Absorption, das heiße interstellare Medium in der Galaxis und anderen Galaxien, das heiße Gas von Galaxienhaufen, Supernova-Überreste, Gas um Quasare und das warme intergalaktische Medium, als interessantestes Objekt für die Anwendung der vorgeschlagenen Methode.

Die hoch-ionisierten Metall-Rekombinations-Linien im optischen und nahen Infrarot-Bereich stellen ein weiteres viel versprechendes Resultat unserer Studien dar. Wir haben gezeigt dass die Linien dieses bisher nicht untersuchten Typs stark genug sein sollten, um auch in moderater Zeit mit modernen erdgebundenen optischen Teleskopen von dichten Knoten des Auswurfmaterials des jungen galaktischen Supernova-Überrestes Cassiopeia A beobachtet werden zu können. Solch viel versprechende Beobachtungen ermöglichen die Identifikation aller häufigen Ionen, die im Auswurf vorhanden sind, und von der umgekehrten Schockwelle der Supernova-Explosion getroffen werden. Eine derartige Studie erweitert unser Verständnis sowohl von der Zusammensetzung des Auswurfmaterials als auch über die Schockwelle-Interaktion mit den Metall-dominierten dichten Wolken.

Im Laufe dieser Arbeit wurde festgestellt, dass die physikalischen Bedingungen in den emittierenden Bereichen dieser dichten Auswurf-Wolken (so genannte schnell-bewegende Knoten) von Cassiopeia A und anderen jungen Sauerstoff-dominierten Supernova-Überresten recht unbeschränkt sind und die Vorhersagen verschiedener Modelle sich um Größenordnungen unterscheiden. Um bessere Abschätzungen dieser Bedingungen basierend auf existierenden Daten zu erhalten, haben wir archivierte ISO und Spitzer Beobachtungen herangezogen, um die relevanten, diagnostischen Feinstruktur-Linienverhältnisse zu be-

stimmen. Die Analyse dieser Beobachtungsdaten führte zu einem Verständnis der Wichtigkeit bestimmter Prozesse, die in verschiedenen Modellen vorgeschlagen wurden und in einer Bestimmung von physikalischen Parametern in einigen zuvor beobachtungstechnisch nicht untersuchten Bereichen von schnell-bewegenden Knoten. Diese Studie ist ebenfalls in dieser Arbeit enthalten.

# Summary

The *goal* of the studies comprising this thesis is a survey of prospective spectroscopical methods of highly-charged ion observations from hot astrophysical plasmas that have not been widely studied before.

The first main task that one needs to carry out in this case is a review of different types of spectral lines and matching types of astrophysical objects. This review is then followed by the development of the theoretical description and determination of the best observable parameters in the promising direction and application of the method to the specific objects. Two results of such study (combinations of spectral line type and object type) are presented in the thesis.

The *hyperfine structure lines* of highly-ionized metal atoms (primarily the line of  $^{14}\text{N VII}$  at 5.652 mm) are shown to be observable with modern radio telescopes. The astrophysical objects responsible for appearance of these lines either in emission or in absorption are hot interstellar medium in the Galaxy and other galaxies, hot intracluster medium in clusters of galaxies, supernova remnants, gas around quasars and the warm-hot intergalactic medium, being the most interesting object for the application of the proposed method.

The highly-ionized *metal recombination lines* in the optical and near-infrared ranges constitute another promising result of our studies. We have shown that the lines of this previously unstudied type should be strong enough to be observable even in moderate time on the modern ground-based optical telescopes from the dense knots of ejecta of the young Galactic supernova remnant Cassiopeia A. Such prospective observations will allow to identify all abundant ions present in the ejecta being crossed by the reverse shock wave of the supernova explosion, thus increasing our knowledge both on the ejecta composition and details of the shock wave interaction with the metal-dominated dense clouds.

In the course of the work, it was realized that the physical conditions in the emitting regions of these dense ejecta clouds (so-called fast-moving knots) of Cassiopeia A and other young oxygen-dominated supernova remnants are rather unconstrained with predictions of different models for the line intensities varying by orders of magnitude. To make better estimates of these conditions from the existing data, we have utilized the archival observations of ISO and *Spitzer* space observatories to determine the diagnostic fine-structure line ratios. Analysis of this observational data set has resulted in understanding of relative importances of various processes proposed in different theoretical models, as well as in determination of physical parameters in some of previously observationally unexplored regions of the fast-moving knots. This study is also included in the thesis.





# Chapter 1

## Introduction

Astrophysics is currently a science in the rapid development stage. This refers especially to the observational techniques. Sensitivities of modern astronomical instruments in most of the wavelength ranges have increased by an order of magnitude during the last 20-30 years. Further significant improvements are expected as the planned radio, sub-millimeter, far-infrared and X-ray observatories start their operation.

In contrast to this rapid observational development, most of the methods widely used to determine physical properties of the astronomical objects have not changed in the course of several decades. This fact also implies that the underlying physical theories were mostly worked out for observational limits of that time. Since then, these limits have noticeably shifted and modern increased capabilities of the astronomical instruments allow one to extract much more information from respectively planned observations, if only one knows what effects to look for.

According to these considerations, the general idea behind this thesis was to study if there exist previously neglected physical effects having observational manifestations that may be detected with the current or near-future instruments and that may be useful for better understanding of the physics of the astronomical objects.

To make this project feasible, we have limited ourselves to the studies of the highly-charged astrophysical plasmas and only to survey of the spectral lines, as a type of information that is most informative about the physical properties of the studied medium.

The following *goal* was then set up: to develop new spectroscopic methods for studies of the highly-charged astrophysical plasmas and to check theoretically their feasibility.

An additional requirement was also to ensure a possibility to observe the spectral line from the ground. This property allows for easier manufacture, service and modernization of the instruments, but limits the observed spectral line wavelength range to two regions: from 370 nm to approximately 5-10  $\mu\text{m}$ , and from 1-3 mm to tens of meters.

To reach this goal, the following *tasks* had to be fulfilled:

- To survey relevant spectral lines types and theoretically develop methods for extracting physical information from the observations;
- To look for objects that are the most promising for a given spectral line type detection;

- To estimate method feasibility for astrophysics, including predicting observability of the expected signal.

## 1.1 Astrophysical objects under consideration

Most of the baryonic mass of the Universe is hot and ionized, thus complying to our requirement of highly-ionized plasma. Four main modes of heating are responsible for this property:

- the shock waves (this is relevant to rarefied plasmas having long cooling times such as intergalactic medium and transient objects such as nova and supernova explosions),
- the liberation of gravitational energy (relevant for accretion disks and black hole jets),
- the energy produced in nuclear reactions (relevant for stars, their corona),
- and the energy transfer by photons (photoionization and heating in the hot star and accreting black hole environments).

We have not considered all classes of objects produced by all these types of heating, neglecting stellar atmospheres, their coronae, nova explosions and photoionized warm interstellar medium. The following subsections briefly present basic information on physical properties of the studied object types. Where appropriate, we also mention some of currently observationally unconstrained parameters of the described objects and indicate where spectral line observations could help in understanding these objects.

### 1.1.1 Hot intracluster medium

The hot intracluster medium (ICM) occupies the space between the galaxies within clusters of galaxies. Its typical temperature is of the order of virial temperature of a cluster of galaxies, i.e.,  $3 \times 10^7 - 1 \times 10^8$  K.

Emission of this medium is directly observed only in X-rays, where it is emitting an optically-thin thermal braking continuum radiation with metal spectral lines superimposed on it.

Observations in X-ray and other wavebands allow to extract the following typical ICM physical parameters: total masses of  $10^{12} - 10^{14} M_{\odot}$  ( $10^{42} - 10^{44}$  kg), sizes of about  $0.3 - 3$  Mpc ( $10^{24} - 10^{25}$  cm), electron densities of  $10^{-3} - 10^{-1} \text{ cm}^{-3}$  and temperatures, as already mentioned, of  $3 \times 10^7 - 1 \times 10^8$  K. At such high temperatures the heavy elements (e.g., silicon, sulfur, iron, etc.) are highly ionized up to H- or He-like ions and they emit in bright lines with energies from 0.7 to 8 keV.

Whereas a lot is known about the ICM, there are still many unknowns. For example, the details of the turbulence in the ICM are yet observationally unconstrained. The presence of the turbulence follows from the observations of the Faraday rotation maps (Vogt & Enßlin,

2005), ICM abundance gradients (Rebusco et al., 2005), absence of resonance scattering in 6.7 keV lines (Churazov et al., 2004) and small-scale ICM pressure fluctuations (Schuecker et al., 2004). The ICM turbulence is also observed in the numerical simulations of the galaxy cluster formation (Norman & Bryan, 1999; Ricker & Sarazin, 2001; Sunyaev et al., 2003). Unfortunately, none of the mentioned observational methods allows for the systematic studies of the ICM turbulence, and the existing cosmological simulations are not expected to produce quantitatively correct results (e.g., Schekochihin & Cowley, 2006).

In this respect the metal lines would be a very useful probe, as their smaller thermal velocity dispersions result in narrower line profiles, allowing one to follow subsonic bulk motions and turbulence in the intergalactic gas (Inogamov & Sunyaev, 2003). In X-rays, such studies will become possible only with the future observations using microcalorimeters.

In optical and ultraviolet ranges, the metal fine-structure line wavelengths are in the bands of the existing instruments, and could be observed provided that the lines are bright enough. This type of lines is further discussed in Section 1.3.2.

In radio range, the metal hyperfine structure lines could provide the necessary information. This type of lines is discussed in Section 1.3.3.

### 1.1.2 Hot interstellar medium in and around elliptical galaxies

In elliptical galaxies the general properties of the gas between stars and around the galaxy are similar to the case of the ICM. The interstellar medium (ISM) temperature is lower (typically about  $10^7$  K) because of lower system masses, resulting in higher proportion of lower-ionized atoms and higher spectral line emissivities. The electron densities are of the same order of  $n_e \approx 0.1 \text{ cm}^{-3}$ , but the typical sizes of the emitting regions  $l$  are much smaller (3–10 kpc), resulting in lower emission measures  $E_e = n_e^2 l$  and lower line intensities in case of the same emissivities. Coronae around elliptical galaxies, including ones embedded in hot ICM of clusters of galaxies, have approximately the same physical conditions (Sun et al., 2007).

### 1.1.3 Hot interstellar medium in our Galaxy and spiral galaxies

The classical model of the Galactic interstellar medium (McKee & Ostriker, 1977) assumes coexistence of three separated phases being mostly in pressure equilibrium: cold neutral medium, warm ionized medium and hot ionized medium. The hot ISM is in this model one of these components having typical temperature of about  $10^6$  K and electron density of  $0.1 \text{ cm}^{-3}$ .

However, the numerical simulations of the ISM (e.g., de Avillez & Breitschwerdt, 2004) show that this classical picture of the ISM is too simplified and there is no pressure equilibrium and phase separation. Instead, the interstellar gas in simulations is found to be turbulent on many scales, with the turbulence affecting the structure and motions of most of the phases of the ISM. This picture is also gaining wide observational confirmation, as discussed by Elmegreen & Scalo (2004).

The properties of the hot ISM are primarily probed by the far ultraviolet lines of O VI at 1032 and 1038 Å and by the soft X-ray background measurements. However, photons in these wavelength bands are rapidly absorbed in the ISM and therefore cannot probe high column densities of the interstellar gas. The hyperfine structure radio lines of highly-ionized metals could be therefore very helpful for studies of the hot ISM due to absence of interstellar absorption.

### 1.1.4 Warm-hot intergalactic medium

Existence of the warm-hot intergalactic medium (WHIM) was predicted about ten years ago by Hellsten et al. (1998) and Cen & Ostriker (1999) based on the results of the cosmological simulations. According to these results, almost one half of all baryonic mass in the Universe currently exists in the form of very dilute hot gas. This gas either did not collapse to galaxies and clusters of galaxies, or was ejected from them and forms the network of large-scale filaments between clusters of galaxies.

By definition, the WHIM temperature lies in the range from  $10^5$  to  $10^7$  K. These temperatures are reached by the shock heating during formation of the filaments and in the interaction of the surrounding gas with the galactic ejecta. Typical WHIM electron densities are very low – about  $10^{-6} - 10^{-4} \text{ cm}^{-3}$ , metallicities are of the order of 0.01-0.5 solar having strong correlation with the density (Hellsten et al., 1998), as the denser regions have higher probability of interaction with nearby galaxies. Typical thickness of a WHIM filament is several hundreds kpc, filament length is of the order of 10 Mpc.

Despite this large extent, the emission measure of the WHIM is very low because of the low electron density and its emission is much weaker than of other discussed astrophysical objects. However, the electron column densities  $N_e = n_e l$  are considerable, and in some cases even comparable to the ones of the ICM, showing that searching for absorption lines from this medium is more promising.

Very little is known about the WHIM from the observations. Its existence was proven by the observations of the O VI ultraviolet resonance lines at 1032 and 1038 Å in absorption. At low redshifts ( $z < 0.15$ ) such observations have been performed by the *FUSE* satellite (Danforth & Shull, 2005), at redshifts of up to  $z = 0.5$  the lines are observed by the Hubble Space Telescope (Thom & Chen, 2008), and at redshift of  $z \approx 2.5$  the lines are shifted to the range observable by the ground-based telescopes and have been observed by Simcoe et al. (2002, 2004). Results of these observations are generally consistent with the simulation predictions (Cen & Fang, 2006).

However, the O VI lines probe gas at the lowest temperature range of the WHIM, that corresponds to the lowest overdensities and metallicities. It was shown that the O VI-emitting gas contains about 7% of the total WHIM mass (Bregman, 2007), and that the major part of the warm-hot intergalactic medium could not be probed by this technique. To understand if the simulations are adequately representing also higher temperature WHIM fraction, other probes are necessary.

The soft X-ray lines of the higher ionization oxygen ions O VII and O VIII near 600 eV have been proposed as such a probe by Hellsten et al. (1998). There have been claims that

these absorption lines were detected at nonzero redshift in the spectra of the active galaxy Mrk 421 (Nicastro et al., 2005), although statistical significance of this detection is still disputed (Rasmussen et al., 2007; Kaastra et al., 2006). In any case, it will be possible to obtain most of the information on the WHIM from the soft X-ray lines only using observations to be performed by the future X-ray missions planned to be launched in the end of the next decade.

Concerning our study, as we show in Chapter 2, the  $[^{14}\text{N VII}]$  hyperfine structure line can be used as a feasible  $T \approx 10^6$  K WHIM probe already with the existing radio telescopes.

### 1.1.5 Young supernova remnants

Supernova is a stellar explosion. The supernova event is triggered by inability of the internal pressure of the matter in the core of the star to balance the gravitational attraction forces. After a short period of core implosion when the gravitational forces are winning over the pressure forces, a shock wave is formed in the core of the star that further drives the supernova explosion. This shock wave carries away energy of about  $10^{44}$  J that is later transferred into kinetic and thermal energy of the surrounding circumstellar material (i.e., stellar wind) and the interstellar medium.

When this blast wave exits the star and enters the circumstellar medium (CSM) having much lower density, the reverse shock wave is formed on this density discontinuity. This reverse shock wave then propagates back into the central regions of the exploded star and reaches its central regions in several thousand years. It is the reverse shock wave that gives us almost a unique possibility to probe directly the details of the inner structure of the exploded star, crossing the medium consisting of essentially pure heavy elements.

There are still a lot of observationally unknown details concerning the supernova explosions and its remnants: pre-supernova star structure, element mixing during the explosion, explosive nucleosynthesis yields, the shock wave interactions with the dense clouds (both blast wave interaction with ISM clouds and reverse shock interaction with ejecta and CSM clumps), dust formation and evolution, etc.

Even in one of the most studied cases of young supernova remnants (SNR) – Cassiopeia A – the existing observations are far from being fully interpreted. This remnant is discussed in more details in Section 1.4.

Obviously, new observational methods would be very helpful in disentangling effects caused by many physical processes taking place simultaneously in young supernova remnants. In our study, we have proposed to use metal optical recombination lines to extract information on the supernova ejecta (see Section 1.3.4 and Chapter 3).

### 1.1.6 Older supernova remnants

Older supernova remnants are observed in optical range and in soft X-rays as shells with the emitting gas located behind the blast wave. During  $10^4$  years after the supernova explosion the blast wave has weakened and slowed down considerably. heating the diffuse

interstellar medium to temperatures of about  $(1-5) \times 10^6$  K (in young SNRs the post-shock plasma temperature reaches up to  $10^8$  K).

This heated gas is emitting only in soft X-rays due to its lower temperatures. Its physical parameters are determined from the observed X-ray spectra. However, as already mentioned in Section 1.1.3, the soft X-rays are rapidly absorbed in the interstellar medium and other probes may be necessary for studies of supernova remnants located behind absorbing clouds, such as the hyperfine structure lines.

## 1.2 Elementary processes and atomic level populations

### 1.2.1 Elementary processes influencing the line emission

It is clear that emissivities, i.e., quantities proportional to the amount of photons emitted by an atom or ion in the unit of time, are proportional to the fraction of atoms or ions<sup>1</sup> in the upper level of the relevant transition. Therefore the level populations should be computed first, but they, in turn, in a general case are determined by the rates of atomic elementary processes, such as

- Spontaneous level decay,
- Induced radiative excitation and deexcitation,
- Photoionization and radiative recombination,
- Collisional excitation and deexcitation,
- Collisional ionization and three-body recombination,
- Dielectronic recombination and autoionization.

There is a variety of sources describing how to compute or estimate the rates of these elementary processes (e.g., Sobelman, 1979; Sobelman et al., 1981; Janev et al., 1985; Shevelko & Vainshtein, 1993). Generally, for the process rates in hydrogen atom and hydrogenic ions there exist expressions ensuring precision of better than 1%, but for the majority of other atoms and ions approximate expressions have to be used, even in the best cases having limited precision of 10-20%.

Details of our approach to calculate some of the relevant elementary process parameters are given in Appendix A.

---

<sup>1</sup>Further in the text we will use the word “atom” also for ions, i.e. ionized atoms.

### 1.2.2 Level populations and line emissivities

Number densities  $n_i$  of atoms in any level  $i$  are in a general case determined by the processes populating and depopulating all levels, including collisional transitions, induced radiative transitions and spontaneous decay. Based on relative importance of different processes, one may separate three different cases.

At high densities, when the timescales of the spontaneous decay are much longer than of collisions or induced radiative transitions, the level populations are determined by the parameters of external medium, rather than the atom. In this case, the levels are populated according to the Boltzmann distribution, i.e., number density  $n_i$  of atoms in state  $i$  is

$$n_i \propto n_{\text{at}} g_i \exp\left(-\frac{E_i - E_g}{kT}\right), \quad (1.1)$$

where  $n_{\text{at}}$  is the total number density of atoms of given type,  $g_i$  is the level  $i$  statistical weight (number of microstates within this energy level),  $E_i$  and  $E_g$  are the potential energies of a given state  $i$  and the atomic ground state  $g$ , and  $T$  is the electron, proton or radiation temperature, corresponding to the mechanism responsible for the atomic electron redistribution over levels (see, e.g., Field (1958) for expressions in case of several external temperatures together determining the level populations). Clearly, in this so-called thermodynamic limit the level populations do not depend on the electron density.

In the opposite low-density (so-called coronal) limit the spontaneous decay processes ensure that almost all atoms are in their ground states. Atoms are excited only rarely, and excitation is followed by the radiative cascade to the ground state. Therefore in calculations one may neglect collisional and induced radiative transitions from any state except the ground state. Then the number density of atoms in excited state  $i$  is proportional to the exciting particle (typically, electron) density, that gives a reason of defining the spectral line emissivity as

$$\varepsilon_{ul} = \frac{n_u A_{ul}}{n_e n_{\text{at}}}, \quad (1.2)$$

such that this quantity characterizes photon emission efficiency of a given  $u \rightarrow l$  transition and does not depend on electron density  $n_e$ . Here  $A_{ul}$  is the spontaneous decay rate (Einstein  $A$ -coefficient) and index  $ul$  denote that the atom is changing the state from  $u$  to  $l$ .

The intermediate case is the most complicated from the computational point of view. To compute the level populations, one has to account explicitly for all possible transitions between all possible states. The computations are made easier if the electrons have low temperature and only lowest states are excited by thermal particles, as it is in the case of photoionized or otherwise overionized plasmas.

There exist several large program packages able to compute line emissivities and intensities from astrophysical plasmas, such as Chianti (Dere et al., 1997; Landi et al., 2006), ATOMDB (Smith et al., 2001) and Cloudy (Ferland et al., 1998). However, Chianti and ATOMDB are mostly suited to X-ray emitting plasmas and do not cover low temperatures, whereas Cloudy is focused on the stationary photoionized plasmas.

Therefore in some cases of non-stationary low-temperature ionized plasmas discussed in Chapters 3 and 4, we computed the line emissivities and intensities ourselves. We have done also our own calculations for the lines not included in these databases, as it is the case for most of the line types we have considered.

For given elementary process rates, the relative populations  $n_l$  and  $n_u$  of a two-level system (denoting lower and upper levels by  $l$  and  $u$ ) are determined from the following balance equation:

$$n_l (B_{lu}\bar{J} + q_{lu,e}n_e + q_{lu,p}n_p + \dots) = n_u (A_{ul} + B_{ul}\bar{J} + q_{ul,e}n_e + q_{ul,p}n_p + \dots), \quad (1.3)$$

where  $B_{ul}$  and  $B_{lu}$  are Einstein coefficients for induced radiative transitions,  $\bar{J}$  is a mean intensity averaged over the line profile,  $q_{ul}$  and  $q_{lu}$  denote collisional deexcitation and excitation rates and subscripts e and p relate to electrons and protons. Normally, proton and other particle collisional transitions may be neglected, thus simplifying the balance equation.

Balance equation for more realistic case of large number of levels and including recombination and ionization processes is given, for example, in Section 3.2.2. This question is discussed in some more details, e.g., by Osterbrock & Ferland (2006).

Using the example of the two level system one can easily understand qualitative dependence of the spectral line emissivity on electron density if the surrounding radiation field is low. While the electron density is low, the upper level population is approximately equal to  $n_u \approx (n_u + n_l)n_e q_{lu}/A_{ul}$  and the line emissivity is just  $\varepsilon_{ul} \approx q_{lu}$ . With increasing density, the upper level population tends to a constant and the line emissivity starts steadily decreasing like  $1/n_e$ . The density at which the line emissivity starts decreasing is often called critical density and is found from relation  $n_{cr} = A_{ul}/q_{ul}$ .

There is a direct implication of this qualitative dependence of the line emissivity on the observed line intensities. One can easily deduce that the strongest emission lines are to be expected from the objects having highest emission measure  $n_e^2 l$  unless the electron density  $n_e$  is higher than its critical value  $n_{cr}$ . If this is the case, the electron column density  $n_e l$  becomes an important characteristic quantity.

Correspondingly, the strongest absorption lines are expected from objects having highest column density  $n_e l$  unless  $n_e > n_{cr}$ . If it is the case, the optical depth will be just proportional to the absorbing object extent  $l$  along the line of sight.

Of course, the ionic abundance  $X_{ion}$  should also be as large as possible. In collisional plasmas this is normally determined by the proper plasma temperature.

### 1.2.3 Formulae used in the main part of the thesis

There are certain general relations between several often used quantities that are useful to list or derive for further reference. These expressions are taken from Rybicki & Lightman (1979); Sobelman et al. (1981) with some modifications for easier comparison with the main part of the thesis.



The  $A$  and  $B$  Einstein coefficients are connected by relations

$$g_l B_{lu} = g_u B_{ul}, \quad (1.4)$$

$$A_{ul} = \frac{2h\nu^3}{c^2} B_{ul} = \frac{2h\nu^3}{c^2} \frac{g_l}{g_u} B_{lu}. \quad (1.5)$$

The cross section of a resonance photon absorption for an atom in the lower transition state is

$$\sigma^R(\nu) = \frac{h\nu}{4\pi} \phi(\nu) B_{lu}, \quad (1.6)$$

where  $\phi(\nu)$  is the line profile function,

$$\phi(\nu) = \frac{1}{\sqrt{2\pi}\Delta\nu} \exp\left(-\frac{(\nu - \nu_0)^2}{2\Delta\nu}\right) \quad (1.7)$$

if the line profile has a Gaussian shape with a dispersion  $\Delta\nu$ . In the line center then we have  $\phi(\nu_0) = (\sqrt{2\pi}\Delta\nu)^{-1}$ . In case of the Doppler effect dominating the line width the dispersion is equal to

$$\Delta\nu = \frac{\nu_0}{c} \sqrt{\frac{kT}{m}} = \frac{\Delta v}{\lambda_0}, \quad (1.8)$$

with  $m$  being the atomic mass,  $\lambda_0 = c/\nu_0$  the line wavelength and  $\Delta v = \sqrt{kT/m}$  is a root-mean-square radial velocity of an atom. Then, taking into account Eq. (1.5), we finally obtain

$$\sigma^R(\nu_0) = \frac{\lambda_0^3}{8\sqrt{2}\pi^{3/2}\Delta v} \frac{g_u}{g_l} A_{ul}. \quad (1.9)$$

The cross sections for the collisional excitation and deexcitation are often expressed via the so-called collision strengths  $\Omega$  (Seaton, 1955) as

$$\sigma_{lu}^C(v_i) = \frac{\pi\hbar^2}{(m_i v_i)^2} \frac{\Omega_{lu}(v_i)}{g_l}, \quad (1.10)$$

where  $m_i$  and  $v_i$  are mass and initial velocity of the colliding particle. The collision strengths are dimensionless quantities of order unity and are additive with respect to the atomic level substructure. From the detailed balance relation (Klein-Rosseland formula)

$$g_l v_l^2 \sigma_{lu}^C(v_l) = g_u v_u^2 \sigma_{ul}^C(v_u) \quad (1.11)$$

it follows that  $\Omega_{lu}(v_l) = \Omega_{ul}(v_u)$ . Here  $v_l$  and  $v_u$  are the colliding particle velocities, when the atom is in the states  $l$  and  $u$ , respectively (i.e.,  $v_l > v_u$ ).

As the collision strength as a function of incident electron energy has sometimes a complex behaviour with many narrow resonances, it is convenient to use a quantity averaged over Maxwellian distribution of incident particle velocities, the so-called effective collision strength

$$\Upsilon_{lu}(T) = \int_0^\infty \Omega_{lu}(v_f) \exp\left(-\frac{m_i v_f^2}{2kT}\right) d\left(\frac{m_i v_f^2}{2kT}\right), \quad (1.12)$$

where  $T$  is the temperature of colliding particles and  $v_f$  is the final velocity of the colliding particle. If the variation of  $\Omega$  with the colliding particle velocity may be neglected, then  $\Upsilon_{ul} = \Omega_{ul}$ . Using the definition of  $\Upsilon$ , one can express the collisional electronic deexcitation rates as

$$q_{ul}(T) \equiv \int_0^\infty \sigma_{ul}^C(v_i) v_i f(v_i, T) dv_i = \frac{8.629 \times 10^{-6}}{g_u \sqrt{T, \text{K}}} \Upsilon_{lu}(T) \text{ cm}^3/\text{s}, \quad (1.13)$$

where  $f(v_i, T)$  is the normalized Maxwell distribution function of incident particles

$$f(v, T) dv = \sqrt{\frac{2}{\pi}} \left( \frac{m}{kT} \right)^{3/2} v^2 \exp \left( -\frac{mv^2}{2kT} \right) dv, \quad (1.14)$$

and the numerical factor in Eq. (1.13) is equal to  $\sqrt{2\pi}\hbar^2/(m_e\sqrt{k})$  and therefore limits applicability of the rightmost expression of this equation to the electronic collisions.

Finally, the rate of collisional excitation is expressed via the deexcitation rate as

$$q_{lu} = \frac{g_u}{g_l} q_{ul} \exp \left( -\frac{E_u - E_l}{kT} \right). \quad (1.15)$$

## 1.3 Spectral line types under discussion

### 1.3.1 Level classification

Each energy level in the atom may be characterized by a set of quantum numbers<sup>2</sup>. In one-electron approximation these are principal quantum number  $n$ , orbital momentum quantum number  $l$ , spin quantum number  $s$  and angular momentum quantum number  $j$ . The level is then traditionally denoted as  $nl^{2s+1}L_j$ , where the values of  $l = 0, 1, 2, 3, 4, \dots$  are represented by letters  $s, p, d, f, g, \dots$ . For example,  $2p^3P_0$  denotes level having  $n = 2$ ,  $l = 1$ ,  $s = 1$ ,  $j = 0$ .

In the case of atom with several electrons, the level is often characterized by the electron configuration, i.e., the set of  $ns$  and  $ls$  of these electrons (e.g.,  $1s^22s2p^5$  denotes that atom contains 8 electrons, two with  $n = 1$ ,  $l = 0$ , one with  $n = 2$ ,  $l = 0$  and five with  $n = 2$ ,  $l = 1$ ) and the total electronic quantum numbers  $L$ ,  $S$  and  $J$ , that are written as  $^{2S+1}L_J$ .

Thanks to similar energy level structure of different ions with the same number of electrons it is convenient to characterize the ion with its isoelectronic sequence. For example, doubly ionized oxygen atom  $\text{O}^{2+}$  is said to be carbon-like (C-like) oxygen.

Traditionally, a spectrum produced by an atom is described by the so-called spectroscopic symbol, that is equal to electronic charge increased by one and written in Roman numerals. For example, the set of spectral lines produced by transitions within  $\text{O}^{+2}$  ion is described as O III.

Similarly, the spectroscopic symbol written in square brackets (e.g., [O III]) denotes the lines produced by the so-called forbidden transitions, corresponding to a change in quantum

---

<sup>2</sup>Only  $LS$  quantum numbers are introduced, as only they are used in the thesis.

numbers violating the so-called LS coupling electric dipole selection rules of  $|l - l'| = 1$ ,  $|L - L'| \leq 1$ ,  $|J - J'| \leq 1$ ,  $J + J' \geq 1$  (unprimed and primed quantities denote initial and final quantum numbers). Spontaneous transition rates of the forbidden transitions are several orders of magnitude smaller than of the allowed ones.

### 1.3.2 Fine-structure lines

The fine-structure lines correspond to transitions within one electronic configuration with upper and lower levels differing only in  $S$  and  $J$ . In astrophysical applications most often these are transitions within the lowest electronic configuration of an atom.

As the fine-structure (FS) transitions do not change the  $l$  of any electron, they are forbidden and the corresponding transition rates are very small. For example, the [O III] 5007 Å line discussed in Chapters 3 and 4 have transition rate of  $0.018 \text{ s}^{-1}$ , whereas allowed transitions of similar wavelength have rates up to  $10^7 - 10^8 \text{ s}^{-1}$ .

We have studied a wide range of fine-structure lines from the [O I] 145  $\mu\text{m}$  line to the [Fe XXIII] 1079 Å. Most of these lines are undetectable from the ground from an object at zero redshift  $z$ . However, observing high- $z$  objects, some of the lines may shift into the wavelength range observable by the ground-based telescopes.

For example, we have studied if the ultraviolet fine-structure lines of the highly-charged metal ions may be observed with the existing instrumentation from the clusters of galaxies at high redshift. It turned out that even the best existing telescopes would need about a hundred hours to achieve the convincing detection of these lines.

The weaker-charged ion lines are located in optical and infrared ranges. They are nowadays widely used for studies of various astrophysical plasmas (e.g., Osterbrock & Ferland, 2006). In our studies, we have used the observations of the fine-structure lines of O, Ne, Mg, Si, S, Ar and Fe ions to study the young Cassiopeia A supernova remnant, as described in detail in Section 1.4 and Chapter 4.

### 1.3.3 Hyperfine structure lines

Constructing the level classification, we have neglected several effects that affect the level energies. One of them is an interaction of the total electronic angular momentum with the nuclear spin resulting in the splitting of all previously discussed levels into several components, if the nuclear spin is non-zero.

To include this so-called hyperfine interaction into the level classification, it is usual to introduce the nuclear spin quantum number  $I$  and total atomic angular momentum quantum number  $F$ . If  $I > 0$ , each level is split into  $\min(2I + 1, 2J + 1)$  components having different values of  $F$  from  $|J - I|$  to  $J + I$ . The level energy changes induced by this interaction are very small, therefore the additional level structure was named hyperfine structure (HFS).

The transitions between hyperfine sublevels are forbidden, as they do not involve any

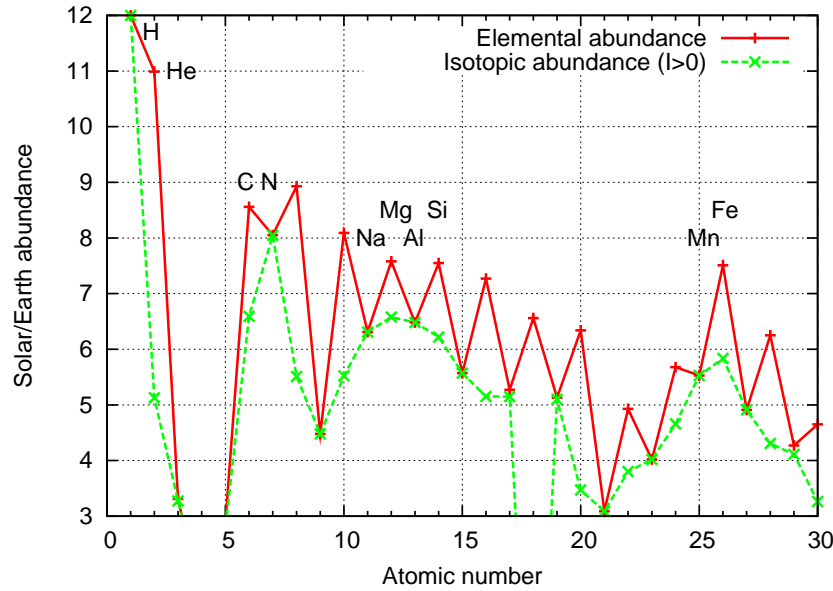


Figure 1.1: Cosmic abundances of isotopes with non-zero nuclear spin computed from solar elemental abundances and Earth isotopic mole fractions. To construct the plot, the data from Grevesse & Sauval (1998); Coursey et al. (2005) were used.

electron  $l$  change. This also means that the transition rates are very low, therefore in astrophysical plasma only the transitions within the ground state have practical importance.

The well-known example of the hyperfine structure line is the 21-cm line of neutral hydrogen, arising in transitions between hyperfine sublevels of its ground  $1s\ ^2S_{1/2}$  state. The proton spin quantum number is  $I = 1/2$ , therefore the ground state is split into two components with  $F = 0$  and  $F = 1$ .

One should note that the HFS lines are specific not to an atom, but to an isotope (i.e., 21-cm line is produced only by  $^1\text{H}$ , but not by  $^2\text{H}$ ) and that the most astrophysically abundant isotopes (except hydrogen) have zero nuclear spin. On Figure 1.1 the solar elemental abundances are compared with the abundances of the isotopes having non-zero nuclear spin.

It is seen that the most astrophysically abundant isotope after hydrogen having non-zero nuclear spin and, therefore, hyperfine splitting in their ions, is  $^{14}\text{N}$ . The hydrogen 21-cm line was first discussed by van de Hulst (1945), but the potential importance of  $^{14}\text{N}$  HFS lines for astrophysics was realized quite soon afterwards, already by Townes & Schawlow (1955).

Later, Sunyaev & Churazov (1984) have performed a systematic study of all H-like and Li-like ions of isotopes having non-zero nuclear spin up to  $^{59}\text{Co}$  and have shown that the most promising in astrophysical applications are the lines of  $[^{14}\text{N VII}]$  and  $[^{57}\text{Fe XXIV}]$ .

Despite much lower ionic abundances than hydrogen, the metal HFS lines are never-

theless promising because of high ionic charges, resulting in larger hyperfine splittings and consequently higher transition rates (the transition rate is proportional to  $\mu^3 Z^9$ , where  $\mu$  is the nuclear magnetic moment and  $Z$  is the ion spectroscopic symbol). Resulting line emissivities become therefore much larger and partially cancel the effect of low abundances.

In our study, we have extended the survey of Sunyaev & Churazov (1984), including the H- and Li-like ions of isotopes up to  $^{67}\text{Zn}$  and extending the studied ion range to include the B-like ions. The most promising of these is the  $^{57}\text{Fe XXII}$  line with wavelength 1.0518(3) cm (Oreshkina et al., 2008), that is nevertheless too weak to be detected by current instruments in a reasonable time.

We have concluded that the HFS lines from astrophysical hot diffuse gases are all too weak to be detected by the existing instruments except for the  $^{14}\text{N VII}$  line (Sunyaev & Docenko, 2007; Docenko & Sunyaev, 2007), which is detectable from several types of objects including the WHIM in the redshift range from 0.15 to 0.6 or so (Chapter 2). The planned radio interferometer SKA (Square Kilometer Array) will be able to detect also other weaker lines from different types of the hot astrophysical gases, and the  $^{14}\text{N VII}$  line detection will become possible in the redshift range from 1.1 to 2.5 or so (Docenko & Sunyaev, 2008, accepted).

Results of our investigations have been used for the interpretation of the results of the recent search for the  $^{14}\text{N VII}$  line from active galaxies and intergalactic medium by Bregman & Irwin (2007).

### 1.3.4 Metal recombination lines

Two previously discussed types of lines that arise in transitions between fine and hyperfine structure levels are mostly produced in astrophysical plasmas by the collisional excitation of respective transition upper levels from the atomic ground states.

However, as mentioned in Section 1.2.1, also recombination processes may influence the level populations. This is especially relevant to the highly-excited states having low probabilities of excitation from the ground state. The electrons populating these states are almost exclusively provided by the recombination processes, that is the reason why corresponding lines are called recombination lines (RLs).

The recombination lines of hydrogen and helium are well-studied (e.g., Seaton, 1964; Osterbrock & Ferland, 2006), but ones of the metals are not often discussed. The optical recombination lines arising in the excited electronic configurations of several C, N and O ions are used for measurements of the abundances of these elements in the planetary nebulae (e.g., Liu et al., 2001; Peimbert et al., 2004).

There have also been observations of Mg I, Al I and Si I recombination lines near 7 and 12  $\mu\text{m}$  from the Sun and some other stars, corresponding to the transitions  $n \rightarrow n'$  of  $6 \rightarrow 5$  and  $7 \rightarrow 6$ , respectively (Murcray et al., 1981; Ryde & Richter, 2004) which were interpreted by Brault & Noyes (1983); Chang & Noyes (1983) and a thorough theory was worked out by Carlsson et al. (1992).

We will further focus on similar lines produced by the transitions between highly-excited electron states (roughly only with  $n \geq 5$ ) because, as we will see below, these lines

of the highly-charged ions that we are primarily interested in are located in the optical or near-infrared bands directly observable from the ground.

Describing the RLs produced by the highly-excited electron transitions, it is usual to separate the quantum numbers of the atomic core (i.e., ion prior to recombination) and of the excited electron, denoting total core quantum numbers by  $L_c$ ,  $S_c$  and  $J_c$  and excited electrons quantum numbers by  $n$ ,  $l$ ,  $s$  and  $j$ .

In the first approximation, the core is acting on the highly-excited electron as a point charge, simplifying the atomic level structure (this approximation is applicable only for the so-called non-penetrating states having  $l \geq 3$ , and only for  $n \gg 1$ ). The level energies, like in the hydrogen atom, become dependent only on the principal quantum number  $n$  and the ion charge, and the line wavelength produced by the electronic transitions between neighbouring  $ns$  is approximately expressed as

$$\lambda((n+1) \rightarrow n) \approx \frac{0.091127}{Z^2} \frac{(n+1/2)^3}{2} \mu\text{m}, \quad (1.16)$$

where  $Z$  is the ion charge before recombination (equal to the recombined atom spectroscopic symbol), and  $n+1$  and  $n$  denote principal quantum numbers before and after the transition.

From this expression it is seen that the recombination lines appear in all wavelength ranges from optical (or even vacuum ultraviolet for  $Z \approx 20$ ) to radio. For larger ionic charges the line wavelength decreases and there are more lines per wavelength unit, increasing the total signal.

We have studied two types of recombination lines – radio recombination lines and optical recombination lines. The radio RLs arising in neutral hydrogen and carbon atoms have been widely observed and studied before (e.g., Gordon & Sorochenko, 2002). The metal radio recombination lines from the Sun were proposed for observations in the late 1960s by Dupree (1968), but the observations have not been successful (Dravskikh & Dravskikh, 1969; Berger & Simon, 1972; Shimabukuro & Wilson, 1973) due to too optimistic theoretical predictions (Berger & Simon, 1972). According to our investigations, the metal recombination lines both from the Sun and some other astrophysical objects are detectable with the existing instrumentation (Docenko & Sunyaev, to be submitted).

The metal optical recombination lines arising in transitions between highly-excited states been studied before in detail only in relation to the Mg I 12- $\mu\text{m}$  line (Carlsson et al., 1992). However, the optical RLs may provide much more information on the line-emitting region than the radio RLs. For example, due to interactions of the highly-excited electron with the atomic core, described in details in Appendix A, the optical RLs are shifted and split into several components, thus allowing to identify the parent ion, not only its ionic charge, like in the case of radio RLs (from Eq. (1.16) it is seen that the wavelength is independent on the atomic species).

We have developed a method allowing us to compute the optical recombination line emissivity accounting for the radiative and dielectronic recombination, radiative cascade and collisional  $l$ -redistribution processes. The search for the objects bright in these lines have resulted in finding that the metal-dominated ejecta of the young supernova remnant

Cassiopeia A (see Section 1.4) are very promising in this respect. The Chapter 3 is devoted to this application and other potential uses of the optical recombination lines.

## 1.4 The Cassiopeia A supernova remnant

The supernova remnant (SNR) Cassiopeia A is the youngest known SNR in the Galaxy and is rapidly evolving both dynamically and radiatively. Its high brightness at multiple wavebands, young age and proximity provide an excellent opportunity to study the pre-supernova star composition and shock wave interaction with the circumstellar medium and supernova ejecta.

Cassiopeia A (Cas A, also known as 3C 461 and G111.7-2.1) is situated at a distance of 3.4 kpc (Reed et al., 1995) and is currently about 330 years old, as deduced from the measurements of its fragment proper motions (Kamper & van den Bergh, 1976; Fesen et al., 2006). It is one of the brightest objects of the sky across the electromagnetic spectrum (except in the optical where its emission is highly absorbed). Cas A was first detected as a radio source by Ryle & Smith (1948) that provided its name (“A” denotes the brightest radio source of a constellation it is in). Several years later, it was identified with a diffuse optical feature by Baade & Minkowski (1954). Due to its brightness, Cas A is one of the primary targets for many new instruments. Detailed measurements of its flux, spectrum and morphology exist from 5 MHz to  $\gamma$ -rays at several TeV.

More specifically, Vinyaikin et al. (1987); Oya & Iizima (2003); Megn et al. (1993) report on the flux measurements, mapping and visibility function measurements at 5 – 25 MHz; Kassim et al. (1995) provides precise flux and spectral index maps between 75 and 330 MHz proving existence of ionized plasma inside the reverse shock; Baars et al. (1977) presents an accurate compilation of the Cas A radio spectrum from 300 to 3000 MHz; Wright et al. (1999); Liszt & Lucas (1999) report on measurements of the Cas A at millimeter wavelengths; the infrared observations are presented and reviewed by Hines et al. (2004); Ennis et al. (2006); Rho et al. (2008); latest optical and near-infrared photometry and spectroscopy are presented by Hurford & Fesen (1996); Gerardy & Fesen (2001); Fesen et al. (2006); the recent results of the X-ray observations are described by Willingale et al. (2002); Hwang et al. (2004); Lazendic et al. (2006); and, finally, the 0.3-5 TeV  $\gamma$ -ray detections from the Cas A are described by Aharonian et al. (2001); Albert et al. (2007).

It is surprising, however, that the supernova explosion itself has probably remained unnoticed. The possible identification with the star 3 Cas in the 17th century Flamsteed catalogue (Ashworth, 1980) is far from being certain (e.g., Kamper, 1980; Stephenson & Green, 2002). It is thought that the supernova explosion was either very weak intrinsically, or hidden by one of the dense molecular clouds mapped by Bieging & Crutcher (1986), as suggested by van den Bergh & Dodd (1970).

Figure 1.2 shows appearance of the Cas A in radio, mid-infrared, optical and X-ray bands. From this information we may derive the general structure of this supernova remnant.

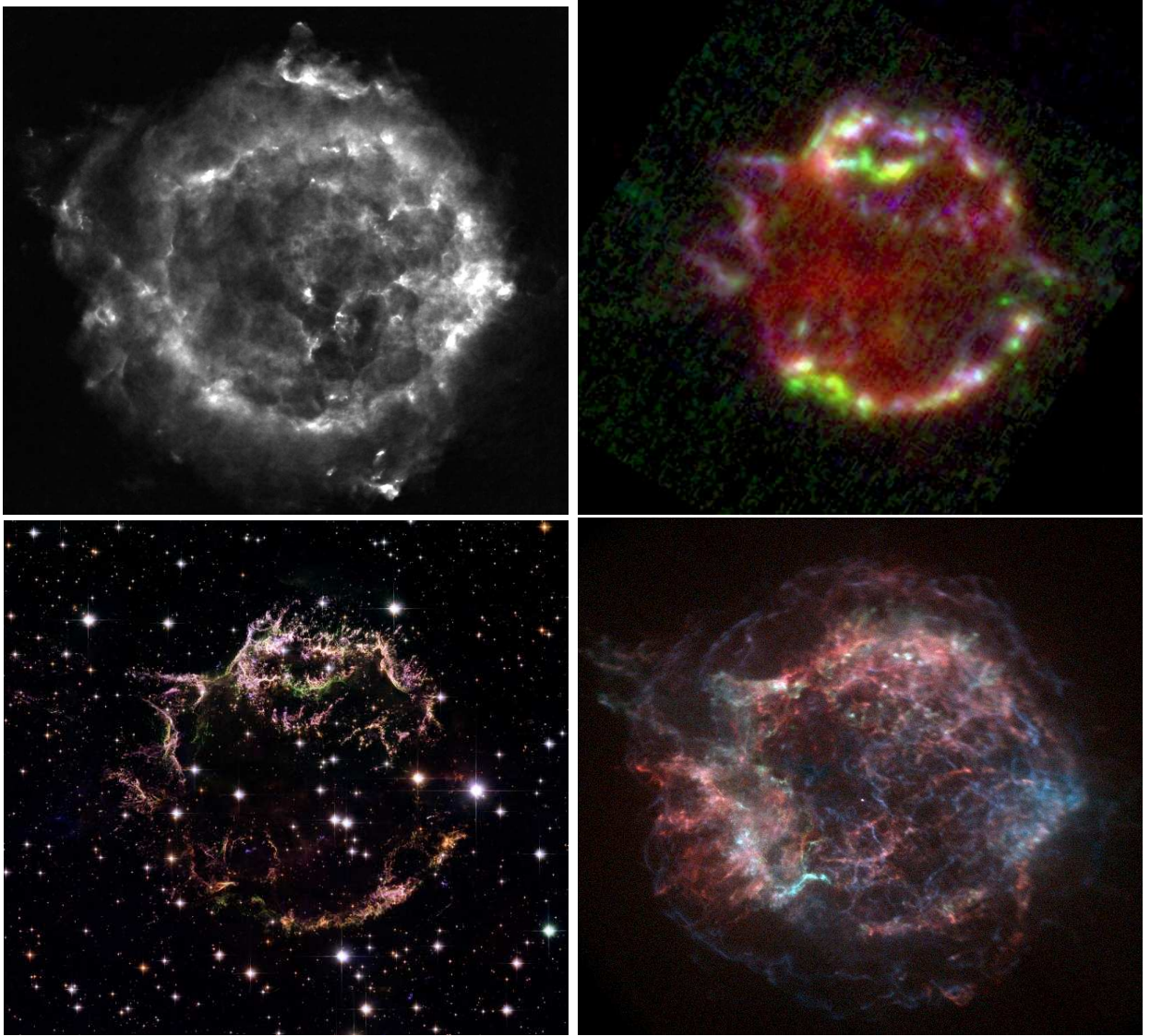


Figure 1.2: Maps of the Cassiopeia A SNR in different wavebands constructed by the author. All images correspond to the same area on the sky and are  $6.7 \times 6.2$  arcminutes in size. (*top left*) Radio image at 4.72 MHz taken by Very Large Array in April 2000 – April 2001. (*top right*) Infrared image in spectral lines (red – [O IV] 25.91  $\mu\text{m}$ , green – [Ne II] 12.81  $\mu\text{m}$ , blue – [Ar II] 6.985  $\mu\text{m}$  line emission) obtained by *Spitzer Space Telescope* in January 2005. (*bottom left*) Optical *Hubble Space Telescope* image obtained in December 2004. (*bottom right*) X-ray image collected by *Chandra X-ray Observatory* in January 2000. The colors denote the photon energies (red – 0.5-1.6 keV, green – 1.6-2.2 keV, blue – 2.2-5.0 keV).



The supernova forward shock (the blast wave) is currently propagating through the interstellar medium and is visible in radio and X-ray maps as thin outermost tangential filaments and extended diffuse outer emission. The reverse shock is visible in all four maps. Its interaction with dense ejecta clouds (so-called fast-moving knots, FMKs) and still denser pre-supernova wind clouds (so-called quasi-stationary flocculae, QSF) produces most of the emission in optical and infrared bands. Some bright FMKs are seen also in X-ray or in radio maps, but there is no direct correspondence for all of the small-scale features (Delaney, 2004).

The X-ray emitting plasma has two distinct components. One, heated by the forward shock, has temperature of about 7 keV (1 keV energy corresponds to temperature of  $1.16 \times 10^7$  K) and roughly solar abundances. Another component has temperature about 1 keV and is dominated by oxygen instead of hydrogen. This plasma have been identified with the explosion ejecta heated by the passage of the reverse shock (Willingale et al., 2002; Laming & Hwang, 2003; Hwang & Laming, 2003). Its electron number density is of the order of several tens  $\text{cm}^{-3}$  (Lazendic et al., 2006), i.e., this plasma is much more dilute than the optically-emitting plasma (see below). Surprisingly, the X-ray observations imply that at least some of the X-ray-bright knots do not represent denser material, in contrast to the optical knots (Laming & Hwang, 2003).

Based on the relative intensities of the He-like Si XIII  $\text{He}\alpha$  lines, the high-resolution X-ray observations have confidently showed that the metal-dominated X-ray-bright knots are out of the ionization equilibrium, i.e. they were recently crossed by the reverse shock wave (Lazendic et al., 2006).

The X-ray observations also provided an estimate of the absorbing ISM column density of  $N_{\text{H}} \approx 1.5 \times 10^{22} \text{ cm}^{-2}$ . As shown by Keohane et al. (1996), this is about a factor of 3 – 5 higher than the column density in the neutral hydrogen inferred from the 21-cm line observations (Bieging et al., 1991), with the additional column density probably provided by the hotter interstellar gas or colder molecular gas (Reynoso & Goss, 2002).

The optical emission is comprised of narrow forbidden lines of O, S and Ar ions highly absorbed in the intervening interstellar medium of the Perseus and Orion arms of the Galaxy (the least absorbed northern part of the Cas A has measured extinction of  $A_V \approx 5.0^{\text{m}}$  (Hurford & Fesen, 1996), while some of other parts have  $A_V$  reaching up to  $10^{\text{m}} - 15^{\text{m}}$  (Bieging & Crutcher, 1986)).

Analysis of these optical forbidden lines allowed Peimbert & van den Bergh (1971) and Chevalier & Kirshner (1978, 1979) to make the first analysis of the FMK composition and determine their highly unusual nature. The line-emitting region temperatures and electron densities were estimated to be around  $(1 - 5) \times 10^4$  K and  $(1 - 50) \times 10^3 \text{ cm}^{-3}$ .

Since then, there have been published several theoretical models that describe the optical line emission originating near the reverse shock front in the pure oxyge or oxygen-dominated plasmas (Itoh, 1981a,b; Borkowski & Shull, 1990; Sutherland & Dopita, 1995b). Some of these models are rather successful in describing the optical spectra of Cas A and other oxygen-rich supernova remnants, but they are obviously not accounting for all relevant physical effects.

The effects of elements other than oxygen are accounted in just one of the models

(Sutherland & Dopita, 1995b), the effects of the thermal electron conductivity - just in one other model (Borkowski & Shull, 1990). No models account for the potentially important effect of the shock structure modification due to particle acceleration on the shock front (Berezhko & Völk, 2004), no models account for the energy losses via the infrared emission of the dust particles (Chapter 4), all models are one-dimensional and therefore cannot treat the hydrodynamic flows and instabilities affecting the post-shock region (Itoh, 1986), etc. As a result of scarce model coverage of relevant parameter space the model predictions for the infrared line fluxes differ by orders of magnitude.

Most of the infrared emission is coming from the dust. This continuum emission was recently decomposed into multiple components by Rho et al. (2008). The dust continuum comprises about 90% of all energy emitted by the FMKs in the wavelength range of the *Spitzer Space Telescope* (between 6 and 40  $\mu\text{m}$ ). Derived dust temperatures are around 100 K (in the range from 60 to 150 K for most of the components) and estimated dust-to-gas mass ratio is of the order of unity (see Section 4.5.3). The fact that the dust emission morphology near 20  $\mu\text{m}$  is very similar to the optical morphology shows that at this wavelength we see only the dust that is currently heated by the ultraviolet and X-ray emission coming from the reverse shock front.

The observational maps of Cas A still contain a lot of not fully understood details:

- the origin of its complicated morphology with “jets”, “holes”, “filaments” (however, several models have been proposed to solve this problem by, e.g., Markert et al. (1983); Willingale et al. (2003a); Wheeler et al. (2008)),
- details of the pre-supernova star structure and element mixing in the explosion (Hughes et al., 2000; Ennis et al., 2006),
- element production yields and ejecta composition (Kifonidis et al., 2003; Fröhlich et al., 2006),
- dust production in the explosion and its evolution (Dunne et al., 2004),
- full interpretation of the complex X-ray spectra (Hwang & Laming, 2003), including prediction of the fluxes from the FMK theoretical model, etc.

In Chapter 3 of the thesis we propose a rich new diagnostic technique – optical recombination lines – allowing to detect *all* dominant ions of *all* elements from the optically-bright ejecta knot spectra. It is shown there that these lines may be confidently detected with the existing ground-based optical telescopes.

The Chapter 4 contains results of another work that was started as we have realized that there is enough information for a more detailed analysis of the ejecta chemical composition and physical conditions available from the existing near-, mid- and far-infrared spectra of the SNR.

## 1.5 Structure of the thesis

The main part of the thesis is laid out as follows.

In Chapter 2 we present our study of astrophysical applications of the metal HFS lines and predict the expected signal in these lines from variety of objects, such as old supernova remnants, hot interstellar medium and the warm-hot intergalactic medium. We show that only the  $[^{14}\text{Ne VII}]$  line at 5.652 mm is observable using existing instruments and that it may provide information on the WHIM in the temperature range about  $10^6$  K, that is currently impossible to obtain by any other means. The HFS lines of other ions from these objects will become observable as the planned radio interferometers start their operation.

In Chapter 3 we develop a new method allowing to compute theoretically the emissivities of the optical recombination lines of metal ions, focusing on their application for studies of the Cas A fast-moving knots. We show that the lines of oxygen as well as other metals should be observable with the existing optical telescopes. We also compute the line shifts and splittings that allow one to identify the ion producing the lines. Extensive tables containing the line positions and emissivities resulting from our computations are available as an online supplement at the CDS<sup>3</sup>.

In Chapter 4 we use the archival observations of ISO and *Spitzer* space observatories together with the published results of near-infrared observations of the Cas A fast-moving knots to infer the details of their structure. The results qualitatively confirm existing theoretical FMK models, but also show some quantitative differences. We were also able to make model-independent estimates of the physical parameters in the post-shock photoionized region of the FMKs that show significant deviations from the model-predicted values.

Finally, in Chapter 5 we summarize the major results.

The results presented in the Chapters 2 and 3 have been or are being published. The Chapter 4 results are submitted for publication and at the time of writing we are awaiting the referee report.

The Appendices contain supplementary information that appeared in the appendices of the papers. The readers unfamiliar with the elementary processes determining the recombination line emissivities are referred to Appendix A containing detailed information on this topic.

---

<sup>3</sup> Centre de Données astronomiques de Strasbourg, [cdsarc.u-strasbg.fr](http://cdsarc.u-strasbg.fr)



## Chapter 2

# Hydrogen-like nitrogen radio line from hot interstellar and warm-hot intergalactic gas

*Astronomy Letters*, Volume 33, Issue 2, pp. 67-79, February 2007  
R.A. Sunyaev and D. Docenko

## Abstract

Hyperfine structure lines of highly-charged ions may open a new window in observations of hot rarefied astrophysical plasmas. In this paper we discuss spectral lines of isotopes and ions abundant at temperatures  $10^5 - 10^7$  K, characteristic for warm-hot intergalactic medium, hot interstellar medium, starburst galaxies, their superwinds and young supernova remnants. Observations of these lines will allow to study bulk and turbulent motions of the observed target and will broaden the information about the gas ionization state, chemical and isotopic composition.

The most prospective is the line of the major nitrogen isotope having wavelength  $\lambda = 5.65$  mm (Sunyaev & Churazov, 1984). Wavelength of this line is well-suited for observation of objects at  $z \approx 0.15 - 0.6$  when it is redshifted to  $6.5 - 9$  mm spectral band widely-used in ground-based radio observations, and, for example, for  $z \geq 1.3$ , when the line can be observed in  $1.3$  cm band and at lower frequencies. Modern and future radio telescopes and interferometers are able to observe the absorption by  $^{14}\text{N}$  VII in the warm-hot intergalactic medium at redshifts above  $z \approx 0.15$  in spectra of brightest mm-band sources. Sub-millimeter emission lines of several most abundant isotopes having hyperfine splitting might also be detected in spectra of young supernova remnants.

PACS: 32.10.Fn, 98.62.Ra, 98.38.-j, 98.58.-w, 32.30.Bv

**Keywords:** hyperfine structure, intergalactic gas, supernova remnants, radio lines

## 2.1 Introduction

In the temperature range  $10^5 - 10^7$  K the most abundant ion having hyperfine splitting of the ground state is the H-like ion of the major nitrogen isotope  $^{14}\text{N}$  VII with line in radio range at around 5.64 mm (Sunyaev & Churazov, 1984). This wavelength of transition between its hyperfine structure (HFS) components has been estimated with high precision to be  $\lambda = 5.6519(11)$  mm (Shabaev et al., 1995). Wavelength of this line is well suited for observation of objects at  $z \approx 0.15 - 0.6$  when it is redshifted to 6.5 – 9 mm spectral band widely-used in ground-based radio observations, and, for example, for  $z \geq 1.3$ , when the line can be observed in 1.3 cm band and at lower frequencies. Unfortunately, for our Galaxy and its vicinity with  $z < 0.1$  it is difficult to observe this line due to atmospheric absorption. Possibly, this is the main reason why there have been no attempts to observe it from the ground after this line was reported by Sunyaev & Churazov (1984) as a promising candidate for detection of hot rarefied plasmas. Till now astrophysical plasma at such temperatures has been studied only by rocket-based instruments and space ultraviolet and soft X-ray missions such as *ROSAT*, *FUSE*, *Suzaku*, *Chandra* and *XMM-Newton*.

One of important and interesting predictions of large-scale structure simulations using hydrodynamical approach is the existence of rarefied intergalactic gas heated to temperatures  $T \approx 10^5 - 10^7$  K. This warm-hot intergalactic medium (WHIM, e.g., Cen & Ostriker (1999) and Croft et al. (2001); Davé et al. (2001)) contains dominant fraction of barions in the present Universe (according to the cosmic census of barions made by Fukugita & Peebles (2004)), but is practically unobserved till now. Computations by Hellsten et al. (1998); Cen & Ostriker (1999) show that heavy element abundances in it rise sharply in regions of higher temperature and density reaching values close to the solar ones.

There were many attempts to observe the WHIM at  $z > 0$ , but till now only far-ultraviolet absorption lines of lithium-like oxygen ( $\lambda\lambda = 1032, 1038$  Å) have been detected by *Hubble Space Telescope* for  $z > 0.12$  and by *FUSE* spacecraft for  $z < 0.15$  (e.g., Danforth & Shull (2005)). Despite many attempts using orbital telescopes *Chandra* and *Suzaku* (Takei et al., 2007), O VII and O VIII soft X-ray lines for  $z > 0$  are evading detection till now (for example, reported case of detection in Nicastro et al. (2005) was recently criticized by Rasmussen et al. (2007) and Kaastra et al. (2006)). Realization of planned proposals considering the micro-calorimeter X-ray sky surveys (e.g., Sanders et al. (2003)) will certainly highly increase the probability to detect soft X-ray emission and absorption lines from the WHIM.

It is obvious that existence of ground-based methods of detection of this gas will bring a lot of additional strength in such efforts. We are proposing radio observations of hyperfine structure lines of highly-charged ions in sub-millimeter to centimeter bands as a way to get additional information about the velocity field, mass, temperature and chemical abundance distribution of the warm-hot intergalactic medium.

It is important to mention that spectral resolution of radio detectors is better than even that of micro-calorimeters. Therefore these lines might permit to look for turbulence and bulk motions in the objects of interest (Inogamov & Sunyaev, 2003). In addition, radio methods do not only probe the absorption lines in spectra of brightest radio sources in

millimeter spectral band, but also the corresponding emission of the gas.

None of the lines we are discussing was detected so far neither in astrophysical objects, nor in physical laboratory conditions. Simplest estimates using well-known relativistic corrections and approximations (Sobelman, 1979) give precision of the HFS line wavelength on the order of few percents. The list of hyperfine structure lines of interest for study of hot plasmas, published by Sunyaev & Churazov (1984), attracted attention of atomic physicists. Zhang & Sampson (1997, 2000) made computations of electronic excitation of HFS levels in plasmas using relativistic distorted-wave method, accounting for resonance effects. Shabaev et al. (1995, 1997) calculated more precise transition wavelengths using a combination of configuration interaction Hartree-Fock method and the  $\frac{1}{Z}$  perturbation theory.

Observations of supernova remnants brightest in soft X-ray band (according to *ROSAT* All-Sky Survey (Voges et al., 1999) and recent *XMM-Newton* studies) indicate the most prospective objects to search for HFS line emission. Knowledge of the studied object radial velocity from optical observations will allow to measure wavelengths of the lines with precision of at least 10 km/s (corresponding to wavelength uncertainty of 30 ppm) that is better than the theoretical estimate precision (200 ppm or more). Knowledge of exact wavelengths will also be very important for study and identification of absorption lines from WHIM filaments. Additionally, one must not forget that such theoretical computations should always be confirmed by experimental measurements.

Among such brightest targets we made estimates of brightness of particular HFS lines arising in Cygnus Loop, North Polar Spur, Vela XYZ, N157B and Cas A supernova remnants (SNR). Our estimates show that in all these objects (except for too hot Cas A) the line of  $^{14}\text{N}$  VII is the brightest. Unfortunately, it is subject to atmospheric obscuration.

At Chajnantor plain height ( $h \approx 5100$  m, where *APEX* telescope is operating and *Atacama Cosmology Telescope* and *ALMA* interferometer are being built) the air specific attenuation is already significantly less than on the sea level (0.2 vs. 1.1 dB/km at 53 GHz, Liebe et al. (1992)) and atmospheric transmission of  $^{14}\text{N}$  VII line may be as high as 30–50% (Schwab & Hogg, 1989). This opens a possibility of direct detection of nitrogen radio line from bright supernova remnants of the southern skies and the Cygnus Loop. High-altitude radio telescopes, naturally, are able to observe this line also at much lower redshifts than the instruments at the sea level.

There are many well-studied star-forming galaxies at redshifts  $z = 0.2 - 0.5$  which should have a lot of relatively young supernova remnants with gas in interesting range of temperatures. Such SNRs and galaxies as a whole would be extremely interesting objects to study by means of hyperfine structure lines using existing (such as *Green Bank Telescope* and *VLA*) and future (such as *Square Kilometer Array* and *ALMA*) radio telescopes and interferometers. Hyperfine lines might be bright also in strong outflows of the hot gas from star-forming galaxies (e.g., Martin (1999)). It is commonly believed that such galactic winds is one of the ways of the intergalactic medium heavy element enrichment.

Hyperfine line observations in principle permit to separate contributions of heliospheric charge-exchange emission and of the Local Hot Bubble, that is now constituting a hardly



solvable problem for soft X-ray measurements (e.g., Smith et al. (2005)). This becomes possible due to HFS line emissivity dependence on the plasma density (see below), and the fact that the solar wind is much denser than the gas of the Local Bubble.

The Galaxy is essentially transparent in millimeter band. Therefore the HFS lines allow studying objects that are strongly obscured in visible and soft X-ray bands. Line emission will mostly probe young supernova remnants, but the total absorption column in HFS lines is a measure of hot ( $T \approx 10^6$  K) interstellar gas in the Galaxy, thus being complimentary to H I 21 cm line probing neutral interstellar medium (ISM).

In case of observations of young supernova remnants where the bulk of emission is coming from the enriched material, it becomes possible to measure the isotopic composition by comparing the HFS line intensity (sensitive to just one isotope) with X-ray lines of the same element (produced by all isotopes).

The structure of the paper is the following. In the first part we are presenting wavelengths and other data on the most abundant isotopes in the temperature range  $10^5 - 10^7$  K having hyperfine structure lines in sub-millimeter, millimeter and centimeter bands. We are discussing sub-millimeter lines in connection with *ALMA* array being able to observe in this spectral band. We are also computing the HFS level population as a function of electron density and radiation temperature for different transitions. In the second part we are presenting the results of the emission line differential brightness temperature computations from some of the brightest objects in our Galaxy and its surroundings. In the last Section we are presenting our estimates of HFS absorption line optical depth arising in WHIM and hot ISM.

## 2.2 Hyperfine structure transitions

Isotopic abundances  $X_{iso}$  (a product of solar elemental abundances from Grevesse & Sauval (1998) and Earth-measured isotopic mole fractions by Coursey et al. (2005)) clearly show (see Table 2.1) that among isotopes having non-zero nuclear spin the  $^{14}\text{N}$  is the most abundant after hydrogen. Its hydrogen-like and lithium-like ions have a hyperfine splitting of the ground state and produce hyperfine structure (HFS) line in spectra of objects with temperatures appropriate for existence of such ions. We include these ions in our analysis, as well as several less abundant H-like and Li-like ions of  $^{13}\text{C}$ ,  $^{17}\text{O}$ ,  $^{25}\text{Mg}$ ,  $^{27}\text{Al}$ ,  $^{29}\text{Si}$  and  $^{33}\text{S}$  (see Figure 2.1).

Non-relativistic formula of hyperfine splitting energy (Sobelman, 1979) of one-electron ion in  $ns\ ^2S_{1/2}$  state is (in Rydbergs)

$$\Delta E_{HFS} = \frac{8\mu}{3I} \cdot \frac{\alpha^2 Z^3 m_e}{n^3 m_p} \cdot (I + 1/2) Ry,$$

where  $\mu$  is the nuclear magnetic moment,  $I$  is the nuclear spin,  $\alpha$  is the fine structure splitting constant,  $Z$  is the nuclear charge,  $m_e$  and  $m_p$  are electron and proton mass and  $n$  is the principal quantum number of the level. Sharp (cubic) dependence on the

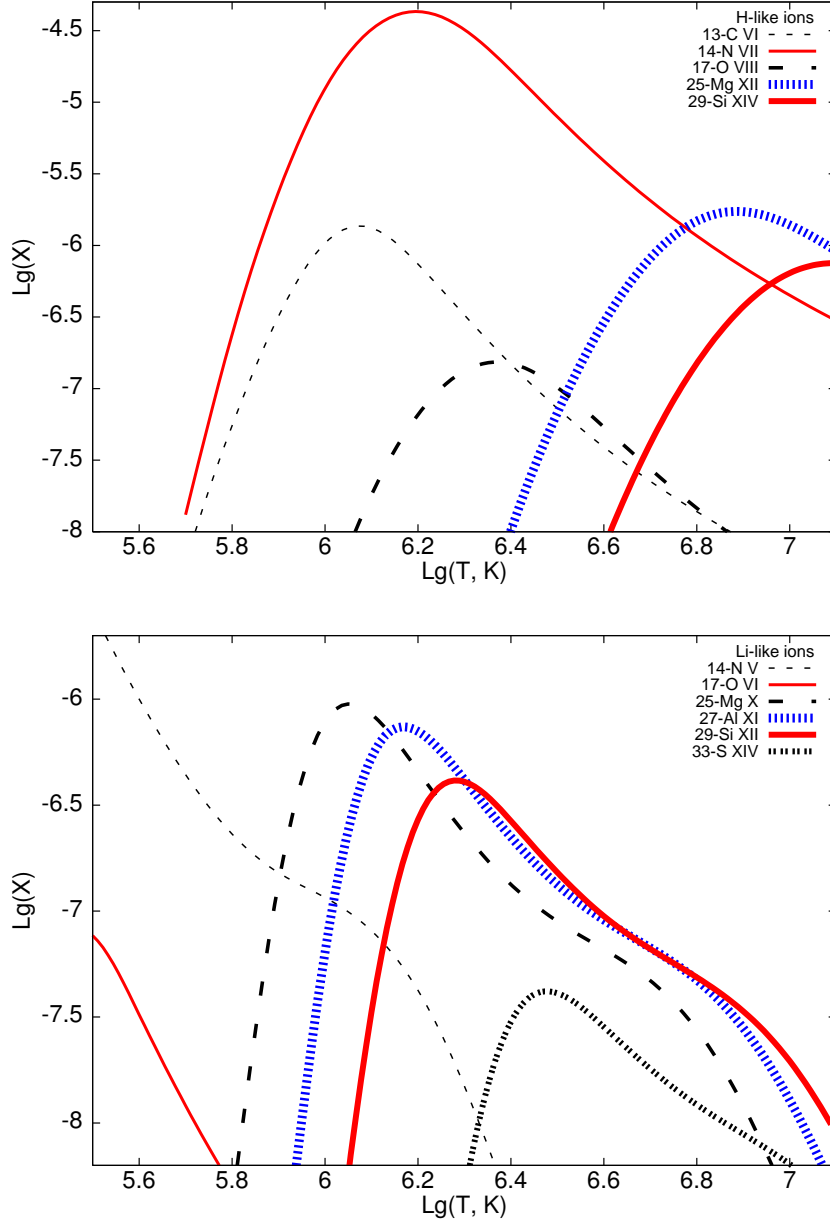


Figure 2.1: Abundance  $X = X_{ion}(T) \cdot X_{iso}$  of discussed ions of isotopes at WHIM, SNR and hot ISM temperatures. Collisional ionization equilibrium ionic fractions  $X_{ion}(T)$ , solar elemental abundances and Earth isotopic mole fractions are assumed. Left and right panels present data on H-like ions and Li-like ions respectively. Note the difference in the vertical scale.

Table 2.1: Parameters of transitions between the ground state hyperfine sublevels: wavelengths  $\lambda$ , transition rates  $A_{ul}$  and absorption cross-sections  $\sigma$  for velocity dispersion of 30 km/s.  $X_{iso}$  denotes isotopic fraction relative to hydrogen. Table also includes nuclear spin  $I$  and nuclear magnetic moment  $\mu$  expressed in nuclear magnetons (nm).

Isotope, ion	$X_{iso}$	$I$	$\mu$ , nm	$\lambda$ , mm	$A_{ul}$ , s <sup>-1</sup>	$\sigma$ , cm <sup>2</sup>
<sup>13</sup> C VI	$3.5 \cdot 10^{-6}$	1/2	+0.7024118(14)	3.8740(8)	$4.639(3) \cdot 10^{-10}$	$6.05 \cdot 10^{-19}$
<sup>14</sup> N V	$8.3 \cdot 10^{-5}$	1	+0.40376100(6)	70.72(4)	$1.018(2) \cdot 10^{-13}$	$5.39 \cdot 10^{-19}$
<sup>14</sup> N VII	$8.3 \cdot 10^{-5}$	1	+0.40376100(6)	5.6519(11)	$1.9920(12) \cdot 10^{-10}$	$5.39 \cdot 10^{-19}$
<sup>17</sup> O VI	$3.2 \cdot 10^{-7}$	5/2	-1.89379(9)	11.813(7)	$3.818(7) \cdot 10^{-11}$	$3.37 \cdot 10^{-19}$
<sup>17</sup> O VIII	$3.2 \cdot 10^{-7}$	5/2	-1.89379(9)	1.0085(2)	$6.136(4) \cdot 10^{-8}$	$3.37 \cdot 10^{-19}$
<sup>25</sup> Mg X	$3.8 \cdot 10^{-6}$	5/2	-0.85545(8)	6.680(4)	$2.111(4) \cdot 10^{-10}$	$3.37 \cdot 10^{-19}$
<sup>25</sup> Mg XII	$3.8 \cdot 10^{-6}$	5/2	-0.85545(8)	0.65809(13)	$2.2083(13) \cdot 10^{-7}$	$3.37 \cdot 10^{-19}$
<sup>27</sup> Al XI	$2.9 \cdot 10^{-6}$	5/2	+3.6415069(7)	1.2060(7)	$2.563(5) \cdot 10^{-8}$	$4.71 \cdot 10^{-19}$
<sup>29</sup> Si XII	$1.7 \cdot 10^{-6}$	1/2	-0.55529(3)	3.725(2)	$1.566(3) \cdot 10^{-9}$	$2.01 \cdot 10^{-19}$
<sup>29</sup> Si XIV	$1.7 \cdot 10^{-6}$	1/2	-0.55529(3)	0.38165(7)	$1.4557(8) \cdot 10^{-6}$	$2.01 \cdot 10^{-19}$
<sup>33</sup> S XIV	$1.6 \cdot 10^{-7}$	3/2	+0.6438212(14)	3.123(2)	$1.328(3) \cdot 10^{-9}$	$5.05 \cdot 10^{-19}$

nuclear charge  $Z$  is seen. Radiation transition probability depends on  $Z$  even more sharply (proportional to  $\Delta E_{HFS}^3$ , therefore to  $Z^9$ , see below), that makes HFS transitions in high- $Z$  ions competitive to hydrogen 21 cm transition even despite their much smaller isotopic abundances.

More precise wavelengths of hyperfine structure transitions are taken from Shabaev et al. (1995, 1997), except for H-like ions <sup>25</sup>Mg XII and <sup>29</sup>Si XIV where formulas given in Shabaev (1994) were utilized directly. Transition rates are then computed using well-known formula (Sobelman et al., 1981) that in case of H-like and Li-like ions takes the form

$$\begin{aligned}
 A(F \rightarrow F-1) &= \frac{I}{I+1} A(F-1 \rightarrow F) = \\
 &= 1.0789 \cdot 10^{-7} \frac{I}{2I+1} \cdot \left( \frac{\lambda}{1 \text{ mm}} \right)^{-3} \text{ s}^{-1},
 \end{aligned}
 \tag{2.1}$$

where  $F$  is the largest of the two sublevel total atomic angular momenta and  $\lambda_{\text{mm}}$  is the transition wavelength expressed in mm. Note that in case of negative nuclear magnetic moment  $\mu$  the sublevel with total angular momentum  $F-1$  has energy larger than one of  $F$ .

Absorption cross-section  $\sigma$  is (Sobolev, 1963):

$$\sigma = \frac{\lambda^2}{8\pi} \frac{g_u}{g_l} \phi(\nu) A_{ul},
 \tag{2.2}$$

where  $g_u$  and  $g_l$  are hyperfine sublevel weights,  $\phi(\nu)$  is a spectral line profile, normalized such that  $\int_{-\infty}^{\infty} \phi(\nu) d\nu = 1$  and  $A_{ul}$  is the spontaneous transition rate from the upper hyperfine sublevel  $u$  to the lower  $l$ .

Near the center of a spectral line  $\phi(\nu) \approx (\sqrt{\pi}\Delta\nu_D)^{-1}$ , where the Doppler line width  $\Delta\nu_D$  is arising due to thermal and turbulent motions of particles in plasma (thermal motion velocity  $v_{th}$  of nitrogen ions at temperature  $10^6$  K is about 34 km/s). Inserting this expression into equation (2.2), we obtain:

$$\sigma = \frac{\lambda^3}{8\pi^{3/2}} \frac{g_u}{v g_l} A_{ul}. \quad (2.3)$$

It is seen that the absorption cross-section is not dependent directly on the nuclear charge, as the radiative transition rate dependence on the wavelength is canceled by the  $\lambda^3$  factor.

In Table 2.1 we present parameters of HFS transitions, such as wavelengths, transition rates and absorption cross-sections. Abundances of ions (taken from Mazzotta et al. (1998)) of isotopes of interest as functions of temperature are shown on Figure 2.1.

HFS sublevel electron collisional excitation collision strength values for  $^{13}\text{C}$  VI and  $^{14}\text{N}$  VII are given by Zhang & Sampson (1997). For other H-like ions they were obtained by scaling along isoelectronic sequence (Beigman, private communication). Respective electron-impact fine-structure excitation cross-sections for lithium-like ions were taken from Fisher et al. (1997). Already Sunyaev & Churazov (1984) noticed that this is the main channel of the ground-state HFS excitation in Li-like ions.

Spectral line emissivity was then computed as

$$\varepsilon = D(T_R, n_e) X_{ion}(T) X_{iso} C_{lu}(T),$$

where  $D(T_R, n_e)$  is the correction factor defined below,  $X_{ion}(T)$  is ionic abundance (taken from Mazzotta et al. (1998)),  $X_{iso}$  is absolute isotopic abundance relative to hydrogen and  $C_{lu}(T)$  is the excitation rate coefficient from level  $l$  to level  $u$ , obtained either from excitation cross-sections or from collision strengths. Resulting line emissivities as functions of temperature are shown on Figure 2.2.

### 2.2.1 Optical depth and emissivity corrections

Computing line emissivity as well as line optical depth, one has to account for change in the hyperfine sublevel population due to interaction with cosmic microwave background (CMB) radiation and collisional processes. Both these effects diminish spectral line emissivity and line optical depth (see below).

If we characterize external radiation fields with effective temperature  $T_R$  at the frequency of transition (in the majority of cases it will be equal to the CMB temperature<sup>1</sup>), the stationary upper-to-lower hyperfine sublevel population ratio is expressed as (e.g., D'Cruz et al. (1998); Liang et al. (1997))

$$\frac{n_u}{n_l} = \frac{g_u}{g_l} \frac{N + n_e/n_{cr}}{1 + N + n_e/n_{cr}}, \quad (2.4)$$

---

<sup>1</sup>In the vicinity of strong radio sources this effective temperature will be somewhat higher. For the specific sources we are considering, the highest effective temperature is in the Cas A supernova remnant additionally contributing at wavelength 6.5 mm about 1 K to the CMB (Baars et al., 1977).

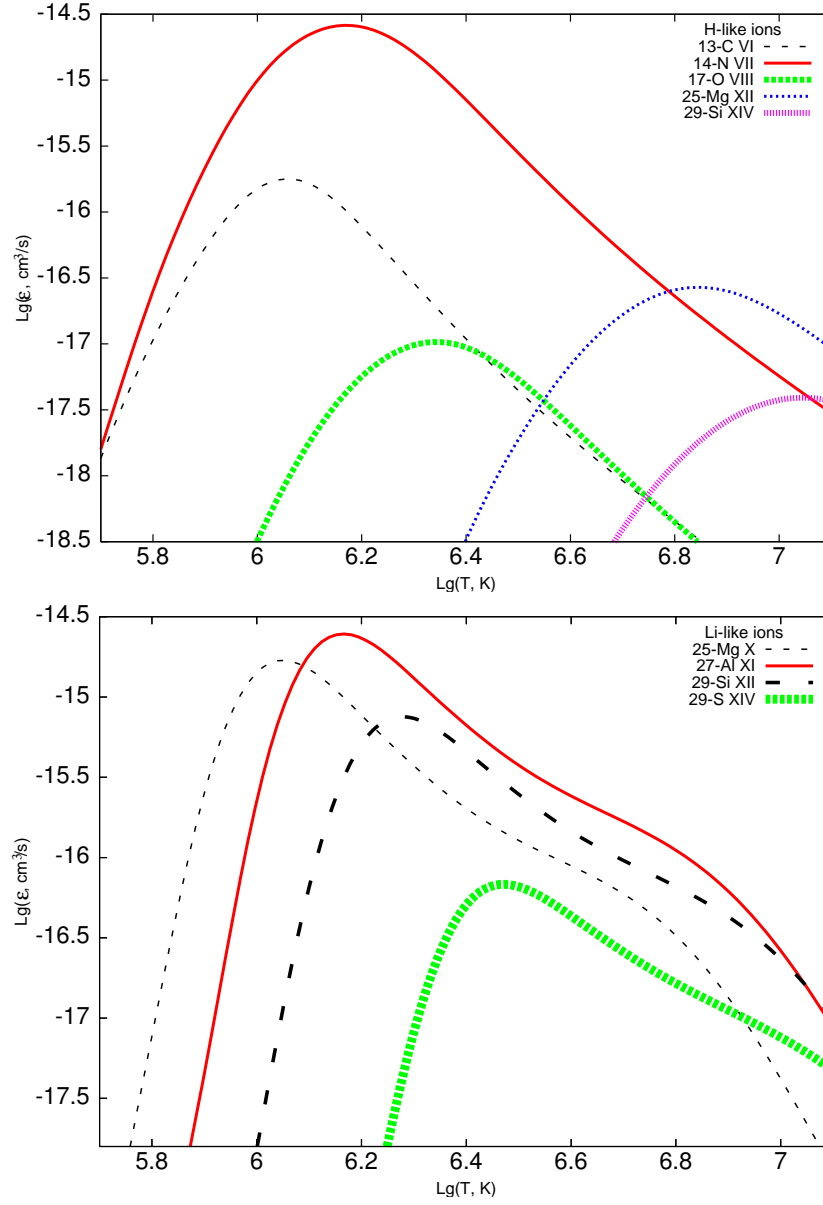


Figure 2.2: Emissivity  $\varepsilon$ ,  $\text{cm}^3/\text{s}$ , of hyperfine structure transitions of discussed ions. Curves are valid for negligibly low electron density and take into account CMB radiation field at redshift  $z = 0$ . Left and right panels present data on H-like and Li-like ions respectively.

where  $n_e$  denote the electron number density, and the photon occupation number is  $N = \left[ \exp\left(\frac{h\nu}{kT_R}\right) - 1 \right]^{-1}$ . Here

$$n_{\text{cr}} \equiv \frac{A_{ul}}{C_{ul}} = \frac{g_u}{g_l} \cdot \frac{A_{ul}}{C_{lu}}$$

define critical electron number density. Its values for HFS transitions are given in Table 2.2 for isotopes with  $n_{\text{cr}} < 500 \text{ cm}^{-3}$ . HFS level population ratio  $n_u/n_l$  as a function of electron number density is shown in Figure 2.3.

Then the intensity and optical depth multiplicative correction factor is

$$D(T_R, n_e) = \frac{1}{1 + \left(1 + \frac{g_u}{g_l}\right) \left(N + \frac{n_e}{n_{\text{cr}}}\right)}. \quad (2.5)$$

In case of  $n_e \ll n_{\text{cr}}$  this expression reduces to

$$D(T_R, 0) = \frac{1 - \exp(-h\nu/kT_R)}{1 + \frac{g_u}{g_l} \exp(-h\nu/kT_R)}. \quad (2.6)$$

Correction coefficients for zero redshift are given in Table 2.2 and Figure 2.4, using  $T_{R0} = 2.725 \text{ K}$ . We also present correction coefficient as a function of redshift  $z$  for some of relevant transitions on Figure 2.5.

In the opposite case of  $n_e \gg n_{\text{cr}}$

$$D(T_R, n_e \rightarrow \infty) = \frac{n_{\text{cr}}}{n_e} \cdot \frac{1}{1 + g_u/g_l}, \quad (2.7)$$

hence the absorption line optical depth depends only on the path length and not on the actual density value. This means that there is a lower limit on absorbing medium path length  $l_{\text{min}}$ , that may give rise to a given optical depth  $\tau$ . Its approximate values for  $\tau = 0.1\%$  are given in Table 2.2. To determine it, we assume solar elemental abundances and maximum ionization fractions (respectively, 0.3 for Li-like and 0.5 for H-like ions). From this Table it can be seen immediately that only larger objects, such as WHIM filaments or large amounts of hot ISM, are observable in absorption. We note that intensities of  $^{14}\text{N}$  V and  $^{17}\text{O}$  VI hyperfine lines are strongly diminished due to small critical densities of corresponding transitions.

The same effect will make the emission line intensity in high-density environments to be proportional not to emission measure  $\int n_e^2 dl$ , but to  $\int n_e n_{\text{cr}} dl$ , thus relatively diminishing contribution from the denser regions. This allows one in principle to separate highly-charged ion line emission of the heliospheric and geocoronal charge-exchange reactions from the Galactic halo or Local Bubble emission, that is now virtually impossible for soft X-ray observatories (see also below).

Emissivity of HFS lines of Li-like ions, from the other side, can be enhanced by the resonance excitation by the fine structure lines of the same ions (Field, 1958; Sunyaev & Churazov, 1984) situated in the far ultraviolet and having large resonance scattering cross-sections.

Table 2.2: Radiative correction coefficients (for redshift  $z = 0$ ) and critical density values (at  $T = 10^6$  K) for relevant HFS transitions. The last column contains minimum path length necessary for achieving optical depth of 0.1%.

Isotope, ion	$D(T_{R0}, 0)$	$n_{\text{cr}}, \text{cm}^{-3}$	$l_{\text{min}}, \text{kpc}$
$^{13}\text{C VI}$	0.421	4.1	0.3
$^{14}\text{N V}$	0.0252	$8.5 \cdot 10^{-5}$	900
$^{14}\text{N VII}$	0.340	1.7	0.03
$^{17}\text{O VI}$	0.247	0.0017	9000
$^{17}\text{O VIII}$	0.991	380	0.03
$^{25}\text{Mg X}$	0.413	0.034	50
$^{27}\text{Al XI}$	0.970	10.2	0.10
$^{29}\text{Si XII}$	0.701	0.18	25
$^{33}\text{S XIV}$	0.624	1.77	18

## 2.3 Emission lines from hot ISM and supernova remnants

### 2.3.1 Overview of the brightest objects

To be bright in hyperfine structure emission lines, the plasma should have high emission measure and appropriate temperature. Besides, among objects of equal emission measure the *least dense* will be the brightest due to diminishing of the  $D(T_{\text{R}}, n_{\text{e}})$  with density, as described in the previous section.

Therefore the main types of objects with expected bright emission lines are young and middle-aged supernova remnants (SNR) and the hot interstellar medium (ISM) including galactic halos. As the same H-like ions that we are considering have spectral lines in the soft X-ray band, the objects with bright X-ray lines should also be bright in HFS lines.

According to these selection criteria, we have chosen several objects with parameters given in the Table 2.3. They include Vela XYZ (Lu & Aschenbach, 2000), Cygnus Loop (Decourchelle et al., 1997) and Cassiopeia A (Lazendic et al., 2006) Galactic supernova remnants, bright supernova remnant N157B (Chen et al., 2006) in Large Magellanic Cloud and hot interstellar gas in the Local Hot Bubble, cool Galactic halo and North Polar Spur (Willingale et al., 2003b). All of the bright spots considered in these objects are diffuse (i.e., larger than or comparable to the radio telescope angular resolution), therefore we use the notion of differential brightness temperature  $T_b$  in our analysis.

Young supernova remnant Cassiopeia A (Cas A) stands separate in this list as its brightest regions contain material strongly enriched in the supernova explosion. In the considered regions R1, R3 and R4 from Lazendic et al. (2006) the oxygen ions are dominant (constituting more than 80 – 90% by mass), hence the abundances of oxygen, magnesium, silicon and sulphur isotopes of interest may be about three orders of magnitude higher than

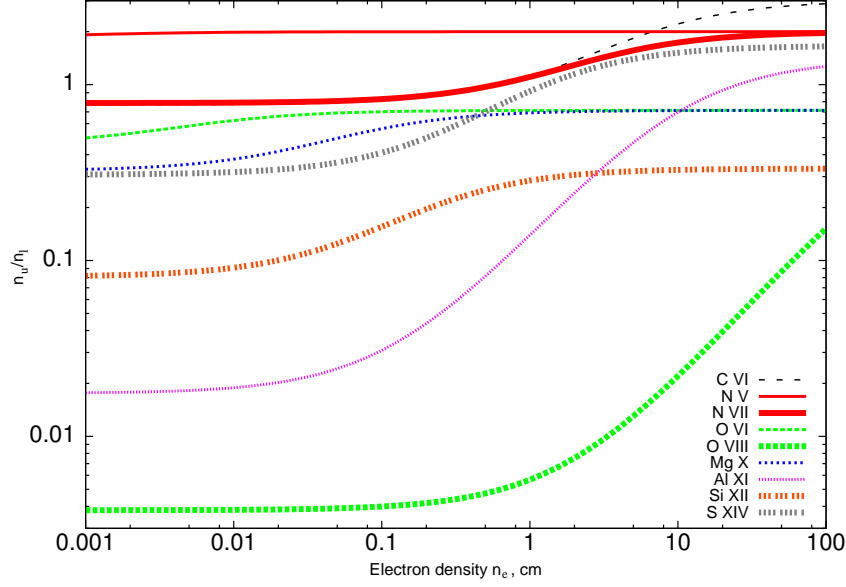


Figure 2.3: Upper-to-lower hyperfine sublevel population ratio  $n_u/n_l$  as a function of electron number density  $n_e$  at  $z = 0$ . Behavior in the limiting case of low  $n_e$  is determined by CMB radiation field (see Eq. (2.6)).

Table 2.3: Objects expected to be bright in HFS lines and discussed further include several supernova remnants, such as Vela XYZ, N157B, Cygnus Loop (CL) and Cassiopeia A and some galactic objects such as as Local Hot Bubble (LHB), cool Galactic halo (CGH) and North Polar Spur (NPS). Rough estimates for hot interstellar medium (HISM) in the plane of the Milky Way is also given. Table includes distance to the object  $d$ , bright fragment angular size  $\theta$ , its average electron density  $n_e$  and temperature  $T_e$ , linear extent  $l$ , emission measure  $n_e^2 l$  and equatorial J2000 coordinates.

	LHB	CGH	NPS	Vela	N157B	CL	Cas A	HISM
$d$ , kpc	—	0.4	0.1	0.25	50	0.44	3.4	—
$\theta$	30'	30'	30'	$> 5'$	1'	5'	5"	—
$n_e$ , $\text{cm}^{-3}$	0.010	0.010	0.031	0.5	3.8	5.5	160	0.01
$kT_e$ , keV	0.10	0.10	0.26	0.12	0.23	0.12	0.77	0.10
$l$ , pc	60	1000	160	8	14	1.2	0.08	3000
RA, J2000	16 <sup>h</sup> 42 <sup>m</sup>	16 <sup>h</sup> 26 <sup>m</sup>	16 <sup>h</sup> 26 <sup>m</sup>	08 <sup>h</sup> 57 <sup>m</sup>	05 <sup>h</sup> 37 <sup>m</sup> 54 <sup>s</sup>	20 <sup>h</sup> 50 <sup>m</sup>	23 <sup>h</sup> 23 <sup>m</sup> 35 <sup>s</sup>	—
Dec, J2000	02°19'	03°11'	03°11'	-45°00'	-69°09' 50"	32°11'	58°50'05"	—
$n_e^2 l$ , $\text{cm}^{-6}$ pc	0.005	0.088	0.13	2.2	200	35	1000	0.3



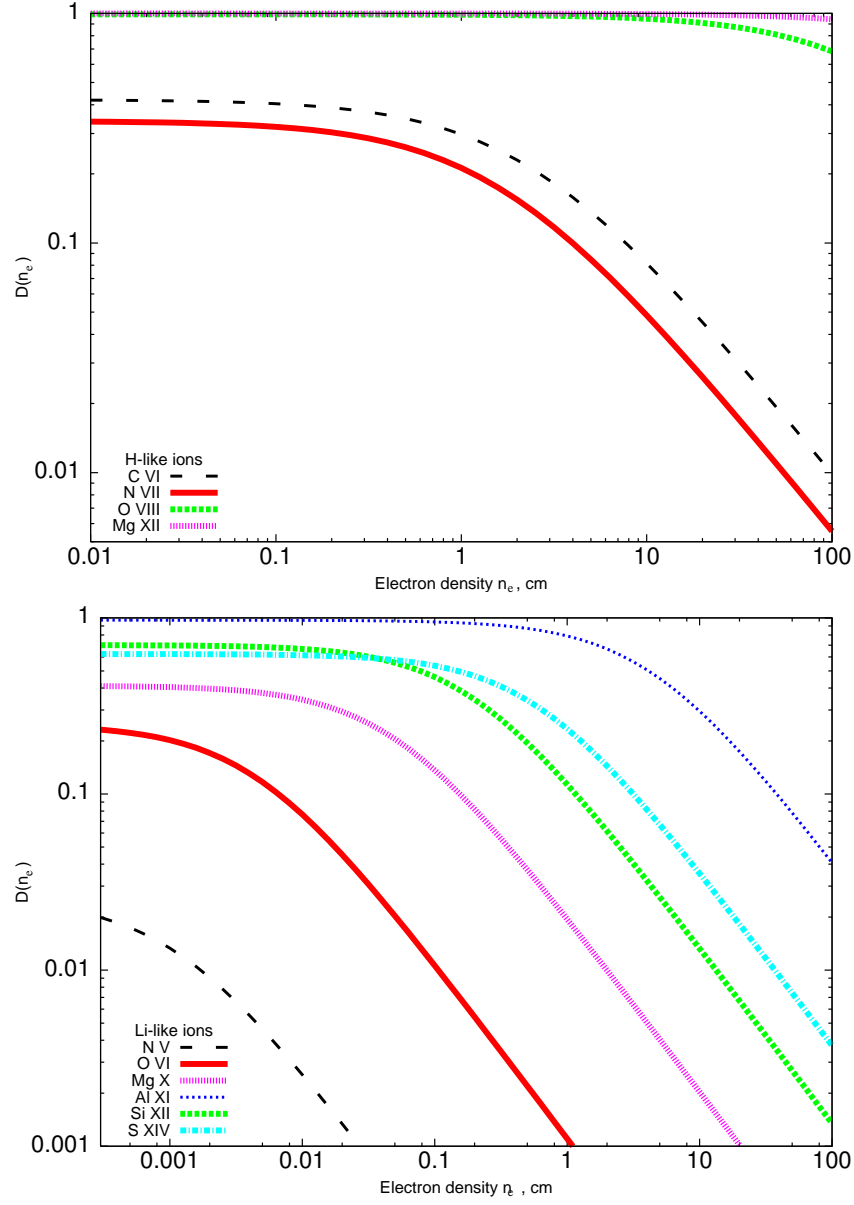


Figure 2.4: Correction coefficient  $D(T_{R0}, n_e)$  as a function of electron density  $n_e$  for zero redshift, i.e. for  $T_{R0} = 2.725$  K. Left and right panels present data on H-like ions and Li-like ions respectively.

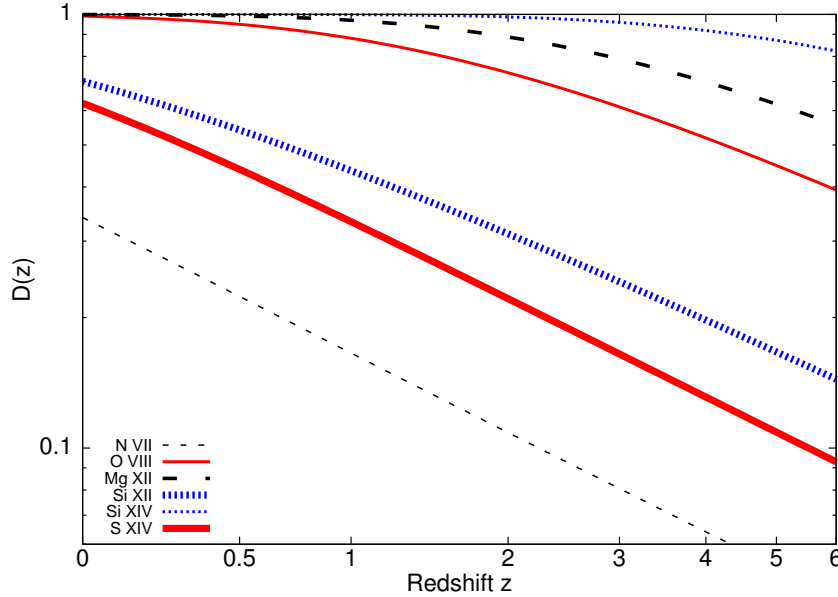


Figure 2.5: Correction coefficient  $D(T_R, n_e)$  as a function of redshift  $z$  for some HFS transitions. The horizontal scale is linear in  $\lg(1+z)$ .

in other cases, if making rather natural assumption of Earth isotopic mole fractions. This is the main reason of high-intensity signal coming from Cas A (see Table 2.4). Detection of these isotopes will give important information about nuclear processes leading to formation of isotopes of  $\alpha$ -elements before and during a supernova explosion.

We use a simple model to estimate emission and absorption in the hot interstellar medium (HISM) of the Milky Way. For this we assume the same temperature and density as in the Local Hot Bubble (see Table 2.3), but take the path length of 3 kpc (from the total path through the Galaxy of 15 kpc and hot ISM filling fraction of 20%).

### 2.3.2 Emission line intensity estimates

From the beginning let us discuss the  $^{14}\text{N}$  VII emission line arising in distant ( $z > 0$ ) sources. First let us estimate a possibility of its detection from halo of a spiral galaxy. Assuming Milky Way parameters (see above), galactic halo volume emission measure is  $n_e^2 V \approx 1 \cdot 10^{63} \text{ cm}^{-3}$ . HFS line emissivity for temperature  $T \approx 1.5 \cdot 10^6 \text{ K}$  is  $3 \cdot 10^{-15} \text{ cm}^3/\text{s}$  (see Figure 2.2). Assuming solar nitrogen abundance, the luminosity in the  $^{14}\text{N}$  VII spectral line is about  $1 \cdot 10^{33} \text{ erg/s}$ .

Another sources of the  $^{14}\text{N}$  VII HFS emission are supernova remnants (this has been suggested already by Sunyaev & Churazov (1984)) at age between one and ten thousand years. As a numeric example, let us take bright SNR Puppis A (Hwang et al., 2005). Its studies indicate hot gas emission measure of  $n_e^2 V \approx 2 \cdot 10^{59} \text{ cm}^{-3}$ . Accounting for some

diminishing of the correction factor, the luminosity in the spectral line is about  $1 \cdot 10^{29}$  erg/s.

Observing the polar cap of nearby galaxy M82 having high star formation rate (3.6 solar masses per year) and apparently being in the process of merger, *Suzaku* and *XMM-Newton* orbital telescopes have discovered the gas in the temperature range  $(2 - 6) \cdot 10^6$  K (Tsuru et al., 2007) optimal for the  $^{14}\text{N}$  VII line detection. It is argued that this gas is moving from the galaxy with hyperbolic velocity.

In a starburst galaxy the star formation rate may be as high as 500 solar masses per year or even higher. This corresponds to supernova rate of about ten per year, therefore the total number of supernova of age below  $10^4$  years should be several tens of thousands. Note that a lot of gas reside in a starburst galaxy, hence supernovae will explode in dense medium forming a lot of bright high density supernova remnants. In such galaxy the total luminosity in line may be as high as  $10^{34} - 10^{35}$  erg/s.

At the redshift of  $z = 0.15$  luminosity in line of  $1 \cdot 10^{34}$  erg/s corresponds to signal of only about  $3 \mu\text{Jy}$  in the line of about 40 km/s width, showing that the emission signal from this class of objects is difficult to detect using existing instruments. Though, the next generation instruments such as *SKA* should be able to observe it from high-redshift ( $z > 1.1$ ) star-forming galaxies.

As the zenith atmospheric transmission at 53 GHz at the height of Chajnantor plane reaches up to 50%, telescopes such as *APEX* and, later, *ALMA* will be able to conduct the first observations of the  $^{14}\text{N}$  VII line from supernova remnants such as N157B which is especially bright in this spectral line.

In case of observations from Chajnantor plane or in case of of emission lines in atmospheric transparency bands, it is preferable to observe first the brightest sources of our Galaxy. In this case the received flux will accordingly rise. Estimates of brightness temperature  $T_b$  in hyperfine structure lines from mentioned objects of the Galaxy and its neighborhood are given in Table 2.4. Solar elemental abundances are assumed everywhere, except for O, Mg, Si and S ions in Cas A supernova remnant, where they are known from Lazendic et al. (2006). Differential brightness temperature of the same order of magnitude is expected as long as the observed object (for example, a galaxy) is larger than the angular resolution of the radio telescope.

We estimate  $T_b$  in the  $^{25}\text{Mg}$  X HFS line arising in the Milky Way halo, Vela, N157B and Cygnus Loop supernova remnants to be about 5–15  $\mu\text{K}$ . As another example, in younger and hotter oxygen-rich Cas A supernova remnant the brightness temperature in mm-band  $^{27}\text{Al}$  XI,  $^{29}\text{Si}$  XII and  $^{33}\text{S}$  XIV hyperfine transition lines is estimated to constitute about 40–80  $\mu\text{K}$ . Accounting for resonance excitation due to significant optical depth in the Si XII and S XIV ionic fine structure transitions in the bright Cas A fragments, HFS lines of isotopes of these ions will be enhanced by factors of 1.5 and 2, respectively (in the Table 2.4 we give values accounting for this increase). For other described sources there is no strong enhancement of HFS line intensity (for example, in N157B the resonance excitation contributes additionally about 20%, assuming solar elemental abundances).

Sub-millimeter lines of  $^{25}\text{Mg}$  XII and  $^{29}\text{Si}$  XIV arising in Cas A are of the same order of brightness reaching about 50  $\mu\text{K}$ . Unfortunately, there is significant atmospheric ob-

Table 2.4: Brightness temperature  $T_b$ ,  $\mu\text{K}$ , in hyperfine structure emission lines from the bright fragments of objects from the Table 2.3. Values less than  $0.01 \mu\text{K}$  are not shown. Unless noted otherwise, solar elemental abundances are assumed.

Isotope	$\lambda$ , mm	LHB	CGH	NPS	Vela	N157B*	CL	Cas A	HISM
$^{13}\text{C}$ VI	3.8740(8)	0.01	0.15	—	1.7	4	13	—	0.4
$^{14}\text{N}$ VII	5.6519(11)	0.2	3.5	1.0	70	700	400	7	20
$^{17}\text{O}$ VIII	1.0085(2)	—	—	—	0.01	0.8	0.08	8*	—
$^{25}\text{Mg}$ X	6.680(4)	0.3	5.1	0.4	8.0	15	14	1.0*	15
$^{25}\text{Mg}$ XII	0.65809(13)	—	—	—	—	—	—	40*	—
$^{27}\text{Al}$ XI	1.2060(7)	0.01	0.1	0.06	4.2	50	40	1	0.8
$^{29}\text{Si}$ XII	3.725(2)	—	0.04	0.30	1.2	30	3.0	120*	0.7
$^{29}\text{Si}$ XIV	0.38165(7)	—	—	—	—	—	—	40*	—
$^{33}\text{S}$ XIV	3.123(2)	—	—	0.15	—	10	—	150*	—

\* elemental abundances are known from observations

scuration on frequencies of these lines at zero redshift, that may give rise to difficulties in the ground-based detection. Simple estimates of *ALMA* sensitivity, taking its system temperature from sensitivity calculator<sup>2</sup> to be 1600 K give  $3\text{-}\sigma$  detection limit on the order of  $0.4 \text{ mK}$  at  $658 \mu\text{m}$  (wavelength of  $^{25}\text{Mg}$  XII line) that is about one order of magnitude above the predicted emission line intensities.

Estimates of emission line intensity from WHIM filaments, similar to discussed above, give differential brightness temperature significantly below  $1 \mu\text{K}$  due to their low emission measure.

Most of the bright spots we are discussing have angular sizes of the order of arcminute that is similar to the angular resolution of PSPC detector aboard *ROSAT* and of a 10-meter-class radio telescope. Computing total luminosity of a bright spot it is sometimes comfortable to use its flux  $S$  that is connected with the brightness temperature from Rayleigh-Jeans formula as

$$S = 0.23 \cdot \left( \frac{T_b}{1 \mu\text{K}} \right) \cdot \left( \frac{\lambda}{1 \text{ mm}} \right)^{-2} \cdot \left( \frac{\theta}{1'} \right)^2 \text{ mJy},$$

where  $\theta$  denote the brightest spot angular size.

### 2.3.3 Resonant scattering in the surroundings of quasar

Detection of emission lines arising in the process of the resonant scattering of the quasar radio emission in the hot and warm gas surrounding the quasar (Sazonov et al., 2004;

<sup>2</sup><http://www.eso.org/projects/alma/science/bin/sensitivity.html>

Kallman & McCray, 1982) might be especially interesting. Discovery of a line formed by the resonantly scattered radiation may shed light upon the quasar radiation beam width, as for the narrow beam much less gas is irradiated (Cramphorn et al., 2004).

As in the quasar neighborhood the photon density might highly exceed one of the CMB radiation, the correction coefficient will decrease there (see Eq. 2.5). Despite this, arising line brightness is of the same order of magnitude as of the lines described above.

We show it on example of 3C 273 ( $z = 0.158$ ) quasar, having flux about 30 Jy on the wavelength of  $^{14}\text{N VII}$  ion line. The quasar radiation photon occupation number at the line frequency exceeds the one due to the CMB inside central 70 kpc. Even so, despite the very low average value of  $D \approx 3 \cdot 10^{-3}$ , the additional flux due to resonant scattering in the line center will constitute about 0.5 mJy (assuming gas cloud parameters similar to ones observed around elliptical galaxies). A large number of young supernova remnants is expected to exist in the central region of galaxy surrounding a quasar. Gas of these SNRs will resonantly scatter quasar radiation, additionally increasing the signal.

### 2.3.4 Disentangling Local Bubble and heliospheric emission

One of serious problems in studying the Local Bubble — the hot gas cavity around the Solar System — is difficulty of separation of its soft X-ray line radiation from foreground contribution arising in the solar wind and the Earth corona (respectively, heliospheric and geocoronal emission). The latter arise in charge-exchange collisions (Cox, 1998) that are so effective that intensity of e.g. O VIII line may significantly exceed one of the Local Bubble (Smith et al., 2005).

There is an intrinsic difficulty in disentangling these two spectral line contributions in soft X-rays, as both these sources are diffuse. Though, using simultaneous observations of soft X-ray and HFS lines it becomes possible to separate them, as the HFS line emissivity is dependent on density (see Figure 2.4) and for some ions the correction coefficient is significantly different in dilute Local Bubble gas ( $n_e \approx 0.01 \text{ cm}^{-3}$ ), denser solar wind ( $n_H \approx 0.1 \text{ cm}^{-3}$ ) and geocorona ( $n_H \approx 10 \text{ cm}^{-3}$ ). In the last two cases we give the neutral hydrogen number density as it is the primary source of electrons participating in the charge-exchange collisions.

As a tool for such density diagnostics one may take  $^{25}\text{Mg X}$  line having critical density of about  $0.03 \text{ cm}^{-3}$ , that is less than electron density in the Solar System. Hence its line emissivity will be suppressed by a factor of roughly  $n_e/n_{\text{cr}}$ , this factor being dependent on the distances to Sun and to Earth.

For estimates of separate source contributions we use simple models of neutral hydrogen distribution in heliosphere and geocorona and rates of charge-exchange reactions from Greenwood et al. (2001) and Cravens et al. (2001). It follows that the main part of heliospheric emission arises at distances larger than 1 a.u. where the solar wind densities fall down to about  $0.1 - 1 \text{ cm}^{-3}$ . Hence  $^{25}\text{Mg X}$  line emissivity in heliosphere is suppressed by a factor of several (about three) as compared to the Local Hot Bubble. Geocoronal emission mostly arises in regions where electron density is much more than  $1 \text{ cm}^{-3}$ . Therefore its  $^{25}\text{Mg X}$  line emission is suppressed much stronger (by factor of about 100) and is

virtually unobservable.

The practical problem of this method, however, is an extremely low brightness temperature from each of these sources. As indicated in Table 2.4, expected  $T_b$  from the Local Bubble is below  $1\ \mu\text{K}$ ; expected contribution from the Solar System is of the same order of magnitude.

## 2.4 Absorption lines in WHIM and hot ISM

### 2.4.1 Warm-hot intergalactic medium

The prospects of detection of highly-ionized oxygen O VII and O VIII ion absorption X-ray lines from the WHIM are being widely discussed now (e.g., Hellsten et al. (1998); Chen et al. (2003); Cen & Fang (2006)). We estimate below the feasibility of detection of the  $^{14}\text{N}$  VII ion HFS absorption line from this medium. Only this isotope is considered, as other HFS absorption lines (e.g., of  $^{25}\text{Mg}$  X,  $^{29}\text{Si}$  XII) will be at least one order of magnitude weaker due to smaller isotopic abundances (see Figure 2.1).

Absorption cross-sections of O VII and O VIII X-ray transitions around  $20\ \text{\AA}$  are  $\sigma \approx (2-5) \cdot 10^{-16}\ \text{cm}^2$ , i.e. about three orders of magnitude larger than of HFS transitions. Moreover, optical depth  $\tau$  of HFS transition is additionally diminished due to population of upper hyperfine sublevel in the field of the CMB radiation. Resulting rough estimate of  $^{14}\text{N}$  VII HFS line optical depth corresponding to O VII or O VIII soft X-ray line  $\tau(\text{O}) \approx 1$  is only about  $\tau(^{14}\text{NVII}) \approx (3-10) \cdot 10^{-5}$ .

Note that weak emission lines of comparable magnitude have already been detected on *GBT*. As an example, HCN molecular line with line width of  $\Delta v = 140\ \text{km/s}$  was observed by Vanden Bout et al. (2004) in emission from galaxy at  $z = 2.28$  at frequency  $27.0\ \text{GHz}$  with  $1\text{-}\sigma$  flux uncertainty of  $0.1\ \text{mJy}$ . This flux corresponds to optical depth of only  $1 \cdot 10^{-5}$ , if observed from the source with flux of  $10\ \text{Jy}$ .

To assess frequency of occurrence of  $^{14}\text{N}$  VII absorption lines in WHIM, we use the distribution function of O VIII X-ray absorption line equivalent width from Cen & Fang (2006) and correspondence between the equivalent width and ionic column density from Chen et al. (2003) cosmological simulations. As a first approximation, we also assume that in WHIM conditions the ionization equilibrium curve of O VIII atoms is the same as of N VII atoms<sup>3</sup> and their relative abundance N/O is solar. Then on average in one sight line in the redshift intervals  $z = 0.15 - 0.30$  and  $z = 0.3 - 0.6$  there is expected one  $^{14}\text{N}$  VII HFS line with  $\tau \geq 2 \cdot 10^{-5}$  and  $\tau \geq 3 \cdot 10^{-5}$ , respectively. In case of reported N VII soft X-ray line detection by Nicastro et al. (2005) with ionic column density of  $1.5 \cdot 10^{15}\ \text{cm}^{-2}$  the optical depth in absorption HFS line would constitute about  $\tau = 3 \cdot 10^{-4}$ .

---

<sup>3</sup>In collisional ionization equilibrium conditions, N VII is abundant at slightly lower temperatures than O VIII. But in the low-density environments ionic abundances change due to photo-ionization and, as a result, N VII abundance widens and becomes rather similar to one predicted for O VIII ion (Chen et al., 2003).

Table 2.5: HFS absorption line optical depth  $\tau$  estimate from Cygnus X-3. The last column contains corresponding absorbed flux assuming source brightness of 20 Jy at 10 GHz and spectral index of  $\alpha = -0.5$ . Only lines with resulting optical depth of more than  $3 \cdot 10^{-6}$  are shown.

Isotope, ion	$\lambda$ , mm	$\tau$	$-S_{abs}$ , mJy
$^{13}\text{C VI}$	3.8740(8)	$3 \cdot 10^{-5}$	0.17
$^{14}\text{N VII}$	5.6519(11)	$3 \cdot 10^{-4}$	2.0
$^{25}\text{Mg X}$	6.680(4)	$1 \cdot 10^{-5}$	0.10
$^{27}\text{Al XI}$	1.1060(7)	$1 \cdot 10^{-5}$	0.04

### 2.4.2 Hot interstellar medium

Another case of interest concerns absorption by the hot ISM of a spiral galaxy with strong radio source in it. For example, every several years exceptionally luminous radio sources (so-called microquasars) burst in the Milky Way. They retain their outstanding brightness for the time period of several weeks and are thus good candidates to study absorption lines in the hot ISM.

As a specific example of a luminous outburst, there has been observed a brightening of Cygnus X-3 with flux as high as 20 Jy at 10.5 GHz (Gregory et al., 1972) and spectral index estimate of  $\alpha \geq -0.5$ . Cygnus X-3 lies in the galactic plane at a distance of about 9 kpc. Taking the Milky Way parameters as discussed above, the column density of hydrogen ions in hot ISM in the direction of Cygnus X-3 is about  $6 \cdot 10^{19} \text{ cm}^{-2}$ . Resulting HFS line optical depths and respective absorption line (negative) fluxes are given in Table 2.5.

### 2.4.3 Gamma-ray burst afterglows

Significant part of bright gamma-ray afterglows originates from the star-forming regions or star-forming galaxies. The lifetime of afterglow in radio band is longer than days or even weeks. This opens a unique possibility to measure absorption lines in their spectra connected with hot ISM of the parent galaxy, hot intracluster medium of the corresponding cluster of galaxies (if any) and the WHIM along the whole path of radio waves to the source.

The optical depth of the absorption features should not diminish significantly with redshift. Though, the flux from gamma-ray burst radio afterglows (several mJy) is weaker than of brightest high- $z$  quasars by about three orders of magnitude that makes the detection of HFS absorption lines a task for the next generation of interferometers such as *SKA*.

### 2.4.4 Estimates of HFS line detectability

Now let us estimate a modern telescope abilities on example of the *Green Bank Telescope* (*GBT*) observing absorption line from 3C 279 – one of the the strongest radio sources at

40 GHz with flux of about 15 Jy – with integration time 10 hours and frequency resolution of 1 MHz.

As an example, we assume line redshift of  $z = 0.3$  so that the observed  $^{14}\text{N}$  VII line is shifted from the atmospheric absorption region. The *GBT* telescope system temperature near 40 GHz is about 75 K, therefore during the integration time the  $1\text{-}\sigma$  flux RMS is on the order of 0.1 mJy. Hence, neglecting systematic effects, the  $3\text{-}\sigma$  detection limit of the optical depth will be of the order of  $0.3\text{ mJy}/15\text{ Jy} \approx 2 \cdot 10^{-5}$  which is of the same order as the N VII HFS line optical depth estimates in WHIM or galactic halo.

As another example, we estimate detection feasibility of the same line in the spectrum of high- $z$  quasar 2134+004 ( $z = 1.934$ ). Its flux density on 18 GHz (redshifted frequency of  $^{14}\text{N}$  VII) line is about 5 Jy that allows to detect with similar observation parameters (10 hours integration time, velocity resolution 10 km/s) absorption lines of  $\tau \approx 6 \cdot 10^{-5}$  on  $3\text{-}\sigma$  level.

From this we conclude that the 5.65 mm  $^{14}\text{N}$  VII hyperfine structure line in redshifted WHIM filaments might be detectable in absorption using existing ground-based instruments. Searching for it, it is natural to start from the extragalactic sources brightest in mm band and having redshift  $z > 0.15$ , such as 3C 273, 3C 279, 3C 345, 3C 454.3 and 2145+067.

Two more notes would be helpful here. First, from observations of one absorption spectral line it is difficult to both determine redshift and identify the line. Hence observations of known objects or combined with other wavelength data would be desired. Second, HFS absorption line with the same optical depth is easier to detect at higher redshifts, as observed line wavelength moves to lower frequencies where the illuminating background source flux is stronger and telescope sensitivity becomes higher. Opposing it is the factor  $D(T_R, n_e)$  that is decreasing optical depth in similar gas clouds with redshift  $z$  for  $^{14}\text{N}$  VII line approximately as  $(z + 1)^{-1}$  (see Figure 2.5).

## 2.5 Conclusions

We discuss the feasibility of the emission and absorption hyperfine structure line observations from astrophysical objects in temperature range of  $10^5 - 10^7$  K. We find that thanks to  $^{14}\text{N}$  high isotopic abundance in interstellar and intergalactic gas the line of  $^{14}\text{N}$  VII is the most prospective to be observed in absorption in spectra of brightest mm-band extragalactic radio sources with  $z > 0.15$ . Typical optical depth predicted for WHIM filaments is about  $10^{-4}$  that is within the reach of the existing instruments. Other HFS lines in absorption will only be detectable with the next generation radio telescopes.

We estimate the  $^{14}\text{N}$  VII brightness temperature in emission from several Galactic supernova remnants to constitute up to 700  $\mu\text{K}$ . Brightness temperature in other lines of  $^{25}\text{Mg}$ ,  $^{27}\text{Al}$ ,  $^{29}\text{Si}$  and  $^{33}\text{S}$  reaches up to 100  $\mu\text{K}$  in oxygen-rich SNR Cas A, the level on the limit of sensitivity of the existing instruments and accessible to future observatories.



Observations of hyperfine structure lines might provide additional information on isotopic composition of supernova remnants, help to discover obscured Galactic SNRs, allow studying star-forming galaxies and superwinds, discriminating between heliospheric and Local Bubble contribution to diffuse soft X-ray background. They might also allow to measure hyperfine splitting experimentally with high precision, thus letting to choose between theoretical highly-charged heavy ion hyperfine splitting computation models and to precise isotopic nuclear magnetic moments.

## Acknowledgements

Authors are grateful to I.L. Beigman, L.A. Vainshtein and E.M. Churazov for their useful remarks and to B. Aschenbach, T. Dotani, R. Mushotsky and R. Smith for information about the brightest objects of the soft X-ray sky.



## Chapter 3

# Optical and near-infrared recombination lines of oxygen ions from Cassiopeia A knots

*Astronomy & Astrophysics*, 2008, accepted  
D. Docenko and R.A. Sunyaev

## Abstract

**Context:** Fast-moving knots (FMK) in the Galactic supernova remnant Cassiopeia A consist mainly of metals and allow us to study element production in supernovae and to investigate shock physics in great detail.

**Aims:** We discuss and suggest observations of a previously unexplored class of spectral lines, the metal recombination lines in optical and near-infrared bands, emitted by the cold ionized and cooling plasma in fast-moving knots.

**Methods:** By tracing ion radiative and dielectronic recombination, collisional  $l$ -redistribution and radiative cascade processes, we compute resulting oxygen, silicon and sulphur recombination line emissivities. This allows us to determine the oxygen recombination line fluxes, based on a fast-moving knot model that predicts the existence of highly-ionized ions from moderate to very low plasma temperatures.

**Results:** The calculations predict oxygen ion recombination line fluxes detectable with modern optical telescopes in the wavelength range from 0.5 to 3  $\mu\text{m}$ . Recombination line flux ratios to collisionally-excited lines will allow us to probe in detail the process of rapid cloud cooling after the passage of a shock front, to test high abundances of  $\text{O}^{4+}$ ,  $\text{O}^{5+}$  and  $\text{O}^{6+}$  ions at low temperatures and measure them, to test existing theoretical models of FMK and to build more precise ones.

**Keywords:** atomic processes - supernovae: individual: Cassiopeia A - infrared: ISM

Tables 5 to 23 are only available in electronic form at the CDS (Centre de Données astronomiques de Strasbourg) via anonymous ftp to [cdsarc.u-strasbg.fr](ftp://cdsarc.u-strasbg.fr) (130.79.128.5) or via <http://cdsweb.u-strasbg.fr/cgi-bin/qcat?J/A+A/>

### 3.1 Introduction

The brightest source on the radio sky, the supernova remnant Cassiopeia A, is so close and so young that modern instruments are able to observe exceptionally fine details in its rich structure in different spectral bands. One of the most interesting phenomena are dense ejecta blobs of the supernova explosion, observed as numerous bright optical “fast-moving knots” (FMKs). These knots radiate mostly in the [O III] doublet near 5000 Å and in other forbidden lines of oxygen, sulphur, silicon and argon.

Early observations using the 200-inch telescope on Mount Palomar (Baade & Minkowski, 1954; Minkowski & Aller, 1954; Minkowski, 1957) demonstrated that the emitting knot plasma has temperatures of about  $2 \times 10^4$  K and electron densities of about  $10^4$  cm<sup>-3</sup>. Very unusual spectra of the fast-moving knots lead Shklovskii (1968) to the suggestion, later confirmed by detailed measurements and analysis (Peimbert & van den Bergh, 1971; Chevalier & Kirshner, 1978, 1979), that they have extremely high abundances of some of heavy elements. Some of the knots consist of up to 90% of oxygen, others contain predominantly heavier elements, such as silicon, sulphur, argon and calcium (Chevalier & Kirshner, 1979; Hurford & Fesen, 1996).

It was also discovered that a typical lifetime of a FMK is of the order of 10–30 years (Kamper & van den Bergh, 1976). Existing knots disappear, but other bright knots appear on the maps of Cassiopeia A (hereafter Cas A).

Detailed Chandra observations (Hughes et al., 2000; Hwang et al., 2004) revealed the presence of similar knots in X-rays, being very bright in spectral lines of hydrogen- and helium-like ions of silicon and sulphur and showing traces of heavily absorbed oxygen X-ray lines.

Similar bright optical knots are observed in other oxygen-rich supernova remnants (e.g., Puppis A, N132D, etc., Sutherland & Dopita (1995a)), but the case of Cas A is the most promising for further investigations.

Chevalier & Kirshner (1978, 1979) were the first to treat the FMK optical spectra as a shock wave emission. Subsequently it was understood that the shock models used, that assumed solar abundances, are inappropriate for the case of the FMK plasma, as its high metal abundances result in a different shock structure.

There have been several theoretical models published describing the shock emission in pure oxygen plasmas (Itoh, 1981a,b; Borkowski & Shull, 1990) and oxygen-dominated plasmas (Sutherland & Dopita, 1995b, hereafter SD95). In these models, the reverse shock of the supernova remnant encounters a dense knot and decelerates on entering its dense medium (Zel’dovich & Raizer, 1967; McKee & Cowie, 1975) to velocities of several hundred km/s. Shortly after the shock wave enters the cloud, the material ahead of the shock front is ionized by the radiation from the heated gas behind the shock front. All the theoretical models assume shock wave propagation with a constant velocity through a constant density cloud.

The optical emission is formed in two relatively thin layers: one immediately following the shock front, where plasma rapidly cools from X-ray emitting temperatures of about  $5 \times 10^6$  K to below  $10^3$  K and another at the photoionization front before the shock wave.

The relatively cold layers with temperatures below  $10^5$  K contribute most strongly to the line emission, as approximate pressure equilibrium results in much higher densities and emission measures of these regions.

An important detail is that *the recombination time is much longer than the plasma cooling time*. Therefore recombining and cooling plasma simultaneously contains ions in very different ionization stages at all temperatures down to several hundred Kelvin – the plasma is in a non-equilibrium ionization state. It is very important to find a way to confirm experimentally this prediction of the computational models.

Predictions of various theoretical models differ in many ways. For example, as we show in an accompanying article (Docenko & Sunyaev, to be submitted), the model predictions of the fine-structure far-infrared line intensities differ by several orders of magnitude. We also show there that the models of SD95 and of Borkowski & Shull (1990) are the best available ones in reproducing the far-infrared line emission of the fast-moving knots, although each is only precise up to a factor of a few.

Nevertheless, these two theoretical models still have many differences. For example, in the Borkowski & Shull (1990) models the  $O^{4+}$  and higher-ionized species are essentially absent, whereas in the SD95 model  $O^{6+}$  is the dominant ion after the shock at temperatures above about 5000 K. Unfortunately,  $O^{4+}$ ,  $O^{5+}$  and  $O^{6+}$  ions have no collisionally-excited lines in visible and infrared ranges, and their ultraviolet and soft X-ray lines are almost or completely undetectable due to high interstellar absorption on the way from Cas A.

From the large differences between the theoretical model predictions it is clear that they lack observational constraints and more diagnostic information in the form of various line ratios is needed to pin down the true structure of fast-moving knots. Some of such information can be obtained from the far-infrared lines.

In this paper we argue that still more information may be obtained from metal recombination lines (RL) in optical and near-infrared spectral ranges. These lines arise in the transitions between highly-excited levels (principal quantum number  $n \approx 5-10$ ) populated by the processes of dielectronic and radiative recombination. The RLs are emitted by *all* ionic species, including, for example,  $O^{4+}$  and  $O^{5+}$  that have no other lines detectable from Cas A.

Unfortunately, the collisional excitation process, that is much more efficient at exciting lines corresponding to transitions between lowest excited states, is negligibly weak at the excitation of high- $n$  levels. Therefore, emissivities of the RLs are normally several orders of magnitude weaker than those of the collisionally-excited lines, but, as we show in this article, intensities of the recombination lines from the FMKs do reach detectable levels.

For oxygen-dominated knots, using plasma parameters (electron temperature, density and emission measure of the gas at different distances from the shock wave) from the SD95 model with a 200 km/s shock speed we have computed the spectrum in the optical and near-infrared bands accessible by modern ground-based telescopes. The cloud shock speed in the Cas A FMKs of about 200 km/s is determined by SD95 from the comparison of observed optical spectra with their model predictions. Although a similar analysis based on the Borkowski & Shull (1990) model would also be valuable, the original article does

not give enough information to allow us to compute the RL fluxes (e.g., the ionization state distributions as functions of temperature cannot be resolved from the plots in the regions significantly contributing to the recombination line emission).

The lines under consideration are predicted to be 200 – 1000 times weaker than e.g. the [O III] line at 5007 Å. However, their fluxes are well above the sensitivity of the best present-day telescopes. These fluxes are only 2–5 times weaker than the detection limits of observations done in the 1970s and later, on the 200-inch and smaller telescopes (Peimbert & van den Bergh, 1971; Chevalier & Kirshner, 1979; Hurford & Fesen, 1996). Observations of these lines do not demand high spectral resolution due to velocity spreads and turbulence in the shocked plasma, as well to intrinsic line splitting.

The recombination lines discussed below are radiated by all coexisting ionized oxygen species, from  $O^+$  to  $O^{6+}$ . Study of these lines will permit us to observe in detail the process of the non-equilibrium cooling and recombination of the pre- and post-shock plasmas overabundant in oxygen or sulphur and silicon.

The discussed spectral lines allow us to observe the coldest ionized pre-shock and post-shock regions in the FMK, that are not detectable using the ground-based observations by any other means. The fine-structure far-infrared emission lines are also able to give such information, but demand an observatory located outside the atmosphere and cannot reach angular resolutions sufficient to distinguish individual knots.

Observations of recombination lines of elements other than oxygen will allow us to improve our knowledge of many yet unknown physical parameters characterizing the Cas A ejecta.

The metal recombination lines are a promising tool also for studies of other oxygen-rich supernova remnants like Puppis A, N132D, G292+1.8, etc.

The paper structure is the following. In the second Section we describe our method of recombination line flux computation. In Section 3.3 we apply the method to predict the optical and near-infrared line fluxes from the optical knots in Cassiopeia A and compare them with existing observational constraints. A description of the recombination line sub-structure allowing one to identify the parent ion is given in the Section 3.4. In Section 3.5 we discuss ways to obtain information about physical parameters of the emitting region from the line ratios. In Section 3.6 we conclude.

## 3.2 Computation of recombination line fluxes

In the process of radiative recombination, especially at low temperatures (when  $kT$  is at least several times below the ionization potential), a significant part of the electrons recombine into excited states. Dielectronic recombination for the majority of heavy ions populate excited states even more efficiently than radiative recombination.

In low-density plasmas, such recombination into excited states, characterized by quantum numbers ( $nl$ ), is followed by the electron radiative cascade to the ground state and emission of multiple photons in the course of the cascade. In the case of recombining

highly-charged ions, these photons are emitted in microwave, infrared, optical and ultra-violet spectral bands.

In this paper we describe the lines produced as a result of such a radiative cascade, when both collisional and induced transitions of the type  $(nl) \rightarrow (n'l')$  are unimportant. The only non-radiative process influencing the electron cascade in our model is the collisional  $(nl) \rightarrow (n'l')$  transitions, as they have much higher cross sections and more significantly affect the level populations at relatively low  $n$ . They also are the main reason for changes of the recombination line emissivities with electron density.

We show in Appendix A.1 that the  $n$ -changing transitions may be neglected in computations of optical recombination line fluxes, while still retaining reasonable accuracy of the results (better than 20%).

### 3.2.1 Elementary processes

In the current work we account for the following processes:

- Radiative recombination (RR). Its level-specific rates  $q_{\text{RR}}(nl; T_e)$  were computed as described in Appendix A.2.
- Dielectronic recombination (DR). Its level-specific rates  $\sum_{\gamma} q_{\text{DR}}(\gamma, nl; T_e)$  were computed as described in Appendix A.3.
- Radiative transitions. Their rates  $A_{nl,n'l'}$  were computed using hydrogenic formulae with radial integral expressions from Gordon (1929). This may not be accurate for non-hydrogenic ions at  $l < 3$ , but electrons recombined to those low- $l$  states mostly transit to  $n' \approx l$  and do not contribute to the optical RL emission<sup>1</sup>.
- Collisional  $l$ -redistribution. Its rates  $C_{nl,nl'}$  were computed using sudden collision approximation expressions from Pengelly & Seaton (1964) and Summers (1977), in the region of their applicability. Outside it (where the maximum cut-off parameter  $r_{\text{max}}$  becomes less than the minimum one  $r_{\text{min}}$ ), we approximated the Vrinceanu & Flannery (2001) classical expressions introducing a cut-off at large impact parameters equal to  $r_{\text{max}}$ . Details of this approximation are of minor importance, since the cross sections are proportional to  $r_{\text{max}}^2$ , therefore being relatively small. Energies of  $(nl)$ -levels and their differences determining the collisional rates in many cases were computed as described in Appendix A.5.

The usage of the hydrogenic approximation does not allow us to reliably compute emissivities and wavelengths of the lines corresponding to transitions involving levels  $n < 4$ . Therefore we do not provide the results concerning these levels.

Details of the atomic physics and approximations utilized for computations of the line emissivities are given in Appendix A.

---

<sup>1</sup>After all computations were performed, we learnt about a more elegant and modern way of hydrogenic radial integral computation using associated Laguerre polynomials (Malik et al. (1991); note that there is a typographical error in one of their equations, which is rectified in the appendix of Heng & McCray (2007)).



### 3.2.2 Cascade and $l$ -redistribution equations

The equation describing the radiative cascade of a highly-excited electron, accounting for the collisional  $l$ -redistribution, is

$$\begin{aligned} N_{nl} \left( \sum_{n' < n} \sum_{l' = l \pm 1} A_{nl, n'l'} + \sum_{l' \neq l} C_{nl, nl'} \right) = \\ = n_e n_+ \left( q_{\text{RR}}(nl) + \sum_{\gamma} q_{\text{DR}}(\gamma, nl) \right) \\ + \sum_{n' > n} \sum_{l' = l \pm 1} N_{n'l'} A_{n'l', nl} + \sum_{l' \neq l} N_{n'l'} C_{n'l', nl}, \end{aligned} \quad (3.1)$$

where  $n_e$ ,  $n_+$  and  $N_{nl}$  are the number densities of electrons, recombining ions and recombined ions with electrons on the level  $(nl)$ .

An analytic solution of this coupled system of equations involves inversion of large matrices of sizes of up to several tens of thousands and is not feasible.

We solved the problem the following way. Starting from some maximum  $n = n_{\text{max}}$  relevant for the problem (defined in Appendix A.1), we neglected its cascade population. Knowing the level-specific recombination and  $l$ -redistribution rates, we computed the resulting populations of levels  $(nl)$  by numerical solution of the system of linear equations (3.1) for  $n = n_{\text{max}}$ .

Using level-specific radiative rates, we could compute the  $l$ -resolved cascade population of the levels  $(nl)$  for  $n = n_{\text{max}} - 1$ . Having computed total population rates, we solved the system (3.1) for this  $n$ . In such a way, moving downwards in  $n$ , populations of all levels were computed.

### 3.2.3 Recombination line emissivities

Having obtained level populations  $N_{nl}$ , we computed recombination line emissivities  $\varepsilon(nl, n'l')$ ,  $\text{cm}^3/\text{s}$ , defined as

$$\varepsilon(nl, n'l') = \frac{d\mathcal{N}(nl \rightarrow n'l')}{dV dt} \frac{1}{n_e n_+} = \frac{N_{nl}}{n_e n_+} A_{nl, n'l'}, \quad (3.2)$$

where  $d\mathcal{N}(nl \rightarrow n'l')/dV dt$  is the number of transitions from level  $(nl)$  to  $(n'l')$  per second in the unit volume.

As an example, the predicted O v  $8\alpha$  line<sup>2</sup> low-density emissivity with  $l$ - and  $l'$ -components summed is shown in Figure 3.1 as a function of temperature for different approximations.

Emissivities of recombining O<sup>5+</sup> optical and near-infrared recombination lines are given in Table 3.1 as functions of temperature in the low-density limit.

Approximate wavelengths<sup>3</sup> of the brightest lines of all ions as functions of ionization stage are given in Table 3.2. They can be easily estimated using hydrogenic expressions

<sup>2</sup>As usual, by  $n\alpha$  we denote a spectral line formed by electronic transition from level  $n + 1$  to level  $n$ , by  $n\beta$  – from  $n + 2$  to  $n$ , etc.

<sup>3</sup>Here and everywhere below we present the vacuum wavelengths.

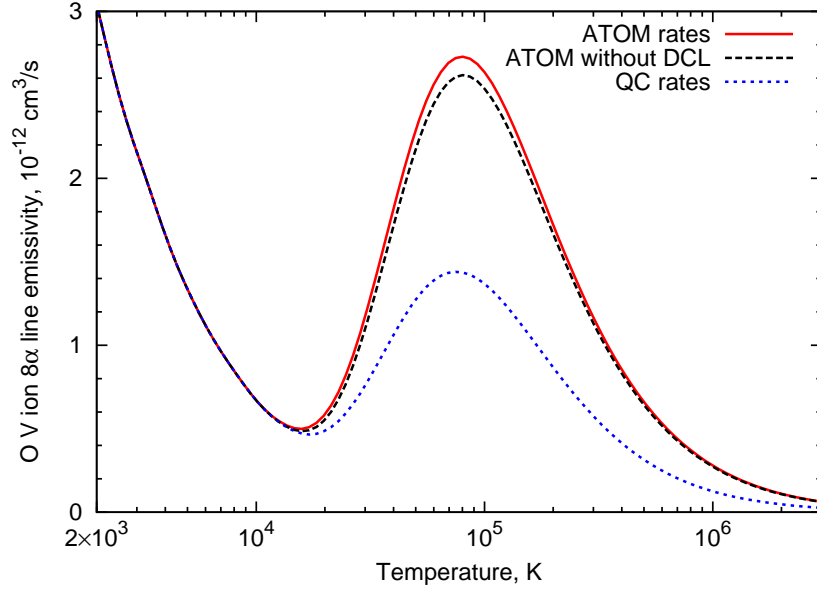


Figure 3.1: Temperature dependence of the O V  $8\alpha$  recombination line emissivity in the low-density limit. The lower curve corresponds to DR rate computations using quasi-classical autoionization rates, the upper curve – to the ATOM rates (for details see Appendix A.3), the middle curve does not account for the process of line emission without recombination (DCL), described in Appendix A.7. At low temperatures the emissivity increase is determined by the radiative recombination, but the peak around  $10^5$  K arises due to the dielectronic recombination.

for any recombination line arising in transition  $n \rightarrow n'$  between levels with  $n' > 3$ ,  $l > 2$  as

$$\lambda(n \rightarrow n') \approx \frac{0.091127}{Z^2} \left( \frac{1}{n'^2} - \frac{1}{n^2} \right)^{-1} \mu\text{m}, \quad (3.3)$$

where  $Z$  is the recombining ion charge.

### 3.2.4 Resulting line fluxes

Fluxes  $I(nl, n'l')$ , erg/cm<sup>2</sup>/s, of the lines were computed by integrating along the line of sight

$$I(nl, n'l') = h\nu \frac{S}{4\pi R^2} \int \varepsilon(nl, n'l'; T_e(r)) n_e(r) n_+(r) dr, \quad (3.4)$$

where  $h\nu$  is the photon energy,  $R$  is the distance from the observer to the emitting region and  $S$  is the emitting region area.

Table 3.1: Wavelengths  $\lambda$  and emissivities  $\varepsilon$  of several O V optical and near-infrared recombination lines in the low-density limit.

Line	$\lambda, \mu\text{m}$	Emissivity $\varepsilon, \text{cm}^3/\text{s}$ , for electron temperature $T_e$			
		$1 \cdot 10^3 \text{ K}$	$3 \cdot 10^3 \text{ K}$	$1 \cdot 10^4 \text{ K}$	$3 \cdot 10^4 \text{ K}$
$5\alpha$	0.298	$9.4 \cdot 10^{-12}$	$4.1 \cdot 10^{-12}$	$3.5 \cdot 10^{-12}$	$5.9 \cdot 10^{-12}$
$6\alpha$	0.495	$7.6 \cdot 10^{-12}$	$3.2 \cdot 10^{-12}$	$1.2 \cdot 10^{-12}$	$3.0 \cdot 10^{-12}$
$7\alpha$	0.762	$6.3 \cdot 10^{-12}$	$2.5 \cdot 10^{-12}$	$8.8 \cdot 10^{-13}$	$1.9 \cdot 10^{-12}$
$8\alpha$	1.112	$5.2 \cdot 10^{-12}$	$2.0 \cdot 10^{-12}$	$6.7 \cdot 10^{-13}$	$1.3 \cdot 10^{-12}$
$9\alpha$	1.554	$4.4 \cdot 10^{-12}$	$1.7 \cdot 10^{-12}$	$5.2 \cdot 10^{-13}$	$8.8 \cdot 10^{-13}$
$10\alpha$	2.100	$3.7 \cdot 10^{-12}$	$1.4 \cdot 10^{-12}$	$4.1 \cdot 10^{-13}$	$6.0 \cdot 10^{-13}$
$11\alpha$	2.761	$3.2 \cdot 10^{-12}$	$1.1 \cdot 10^{-12}$	$3.3 \cdot 10^{-13}$	$4.0 \cdot 10^{-13}$
$12\alpha$	3.548	$2.7 \cdot 10^{-12}$	$9.3 \cdot 10^{-13}$	$2.6 \cdot 10^{-13}$	$2.6 \cdot 10^{-13}$

Table 3.2: Hydrogenic vacuum wavelengths,  $\mu\text{m}$ , of some optical and near-infrared recombination  $\alpha$ -lines for several ionization stages, denoted by the ion spectroscopic symbol after recombination.

Line	I	II	III	IV	V	VI
$4\alpha$	4.0501	1.0125	0.4500	0.2531	0.1620	0.1125
$5\alpha$	7.4558	1.8640	0.8284	0.4660	0.2982	0.2071
$6\alpha$	12.365	3.0913	1.3739	0.7728	0.4946	0.3435
$7\alpha$	19.052	4.7629	2.1168	1.1907	0.7621	0.5292
$8\alpha$	27.788	6.9471	3.0876	1.7368	1.1115	0.7719
$9\alpha$	38.849	9.7122	4.3165	2.4281	1.5540	1.0791
$10\alpha$	52.506	13.127	5.8340	3.2817	2.1003	1.4585
$11\alpha$	69.035	17.259	7.6705	4.3147	2.7614	1.9176
$12\alpha$	88.707	22.177	9.8563	5.5442	3.5483	2.4641

The integral over distance in the plane-parallel approximation can be easily transformed into an integral over temperature by substitution

$$dr = \frac{dr}{dt} \frac{dt}{dT} dT = v_{\text{shock}} \frac{n_{0,t}}{n_t} \frac{3/2(n_t + n_e)k_B}{n_t n_e \Lambda_N} dT,$$

where  $v_{\text{shock}}$  is the shock front speed,  $\Lambda_N$  is a cooling function and  $n_t$  and  $n_{0,t}$  are the total number densities of all ions in a given point and in the pre-shock region.

The parameters of this equation – cooling function, electron and ion densities as functions of temperature – were taken from the SD95 200 km/s shock model, described in more detail in Section 3.3 below.

For the purpose of qualitative analysis, we introduce below the oxygen differential emission measure per logarithmic temperature interval

$$\frac{dE_O}{d(\log T_e)} = T_e \frac{n_O n_e dr}{dT_e},$$

where  $n_O$  is the total oxygen ion number density. It shows the contribution of a given logarithmic temperature interval to the total emission measure, showing where most of the line emission originates. Using this notion, we can express the line flux from Eq. (3.4) as

$$I(nl, n'l') = h\nu \frac{S}{4\pi R^2} \int \varepsilon(nl, n'l'; T_e) \frac{dE_O}{d \log T_e} \frac{n_+}{n_O} T_e dT_e.$$

Here the fraction  $n_+/n_O$  is the abundance of a given ionic species and is also dependent on temperature.

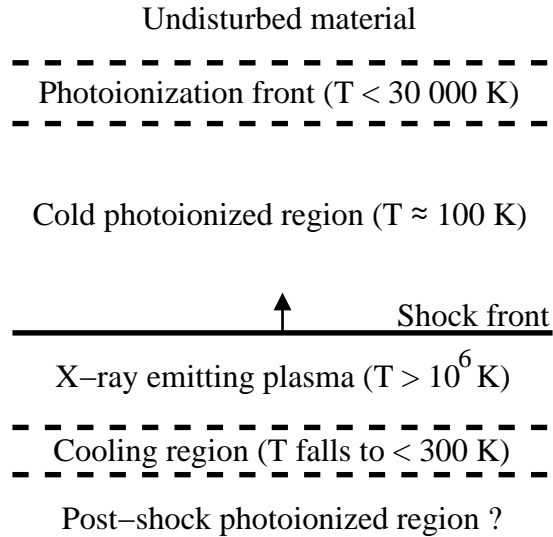
In our computation of the post-shock recombination line emission, we artificially stop integrating expression (3.4) when the plasma temperature drops below 1000 K. This results in some, possibly significant, underestimation of the cooling region line fluxes arising from recombinations of  $O^{2+}$  ions. However, as we show below, the  $O\text{ II}$  recombination lines from the photoionized region are expected to be much brighter.

*It should be remembered* that, e.g.,  $O\text{ V}$  recombination lines arise in the radiative cascade in the  $O^{4+}$  ion triggered by the recombination of the  $O^{5+}$  ion, so the line fluxes are proportional to the ionic abundance of  $O^{5+}$ , not  $O^{4+}$ .

### 3.3 Astrophysical application: FMKs in Cassiopeia A

The SD95 model describes fast-moving knot emission as arising in the interaction of the oxygen-dominated dense cloud with the external shock wave, entering the cloud and propagating through it (see Figure 3.2). The heated region just after the shock front produces a high flux of ionizing radiation that results in the appearance of two photoionized regions: before and after the shock front.

The plasma after the shock front passage cools rapidly and, at temperatures of  $(0.5 - 5) \times 10^4$  K, emits the lines observable in the visible (Chevalier & Kirshner, 1978, 1979;



### 3.3.1 Cooling region after the shock front

It is useful to make order-of-magnitude estimates of some timescales in the post-shock rapidly cooling plasma at temperatures between several hundred and  $3 \times 10^4$  K, where the recombination line emission occurs (see below). As derived from the SD95 model, the plasma cooling time is roughly equal to

$$\tau_{\text{cool}} = \frac{3}{2} \frac{(n_t + n_e) k T_e}{n_t n_e \Lambda} \approx 2 \times 10^4 \text{ s } T_4^{1/2} n_{t,5}^{-1},$$

where  $T_e = 10^4 T_4$  K and  $n_t = 10^5 n_{t,5} \text{ cm}^{-3}$ . It should be compared with the time needed to reach the collisional ionization equilibrium (CIE), that is in our case approximately equal to the recombination timescale  $\tau_{\text{rec}}$ . For example, for ion  $\text{O}^{2+}$  and  $\text{O}^{6+}$  the recombination time is

$$\begin{aligned} \tau_{\text{rec}}(\text{O}^{6+}) &= (n_e q_{\text{RR}, \text{O}^{6+}}(T_e))^{-1} \approx 4.7 \times 10^5 \text{ s } T_4^{0.64} n_{e,5}^{-1}, \\ \tau_{\text{rec}}(\text{O}^{2+}) &= (n_e q_{\text{RR}, \text{O}^{2+}}(T_e))^{-1} \approx 4.9 \times 10^6 \text{ s } T_4^{0.64} n_{e,5}^{-1}, \end{aligned}$$

where  $n_e = 10^5 n_{e,5} \text{ cm}^{-3}$  and  $q_{\text{RR}, \text{O}^{2+}}$  is the total radiative recombination rate for this ion, taken from Pequignot et al. (1991). It is easy to see that the recombination timescale in this temperature interval is always longer than the cooling time for any abundant ion. Therefore the plasma is strongly overionized for its temperature, which results in high emissivities of the recombination lines.

The quantitative comparison of these timescales in the model is given in Figure 3.3, where ionization and recombination timescales for several ions are compared with the cooling time. At high temperatures the cooling timescale is longer than the ionization timescales and the material has enough time to converge to the CIE. At  $T_e < 10^6$  K the cooling is much faster than the recombination down to temperatures of several hundred Kelvin and the high ionization state stays “frozen” until very low temperatures are reached.

Let us now compare the thermalization timescales and mean free paths to the quantities determined above. Following Spitzer (1956), the electron or ion self-collision timescale is equal to

$$\tau_c = 114 \text{ s } \frac{A^{1/2} T_4^{3/2}}{n_5 Z^4 \ln \Lambda_C},$$

where  $A$  is the atomic weight (equal to  $m_e/m_p \approx 1/1836$  for electrons),  $Z$  is the particle charge,  $n = 10^5 n_5 \text{ cm}^{-3}$  is the particle concentration and  $\Lambda_C \approx 3.92 \times 10^7 n_{e,5}^{-1/2} T_4^{3/2}$ . In our case of the highly-charged plasma having  $Z \gg 1$  the timescale of the ion-ion collisions is even shorter than for the electron-electron collisions.

Nevertheless, the mean free path even for electrons  $\lambda_e$  stays significantly below any other characteristic scale, including the typical temperature change length scale of the order of  $10^9 - 10^{10} \text{ cm}$ :

$$\lambda_e = \tau_{c,e} \sqrt{3kT_e/m_e} \approx 1 \times 10^7 \text{ cm } T_4^2 n_{e,5}^{-1}.$$

For an illustration of the characteristic conditions after the passage of the shock front, in Figure 3.4 we show the Li-like  $\text{O}^{5+}$  ion density as function of plasma temperature for

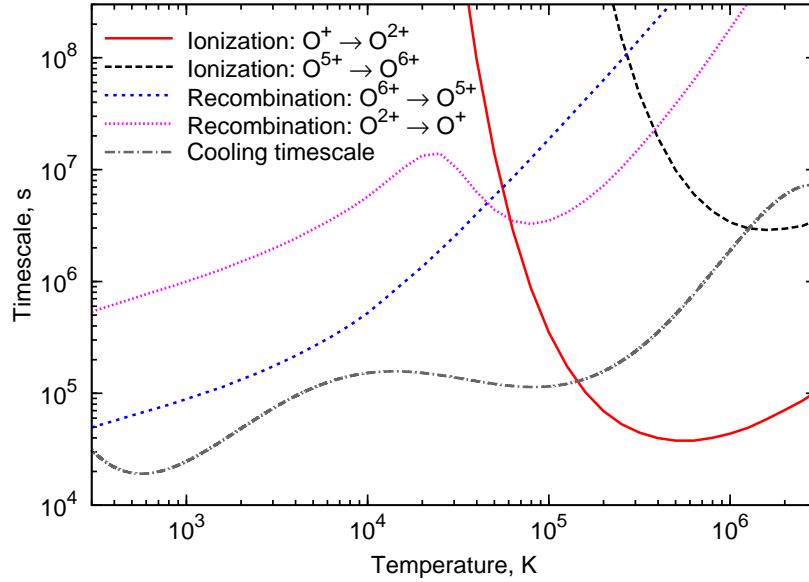


Figure 3.3: Oxygen ion  $O^{6+}$  and  $O^{2+}$  recombination and ionization timescales compared to the plasma cooling time using the electron density dependence on temperature and the cooling function from the SD95 model with a 200 km/s cloud shock speed.

this region<sup>4</sup>. The figure demonstrates overly high abundance of this ion in relatively dense plasma with  $T < 3 \times 10^4$  K after the shock front, much higher than in the CIE, where this ion exists only in a narrow temperature range  $T_e = (2 - 7) \times 10^5$  K (Mazzotta et al., 1998).

In the same figure we also present the oxygen emission measure distribution over temperature  $d(EM)/d(\log T_e)$  in the SD95 model. This distribution together with the line emissivity dependence on temperature (e.g., Fig. 3.1) allows one to calculate the relative contributions to the total line flux from different temperature intervals (see Section 3.2.4 above).

Such line flux distributions for the prominent [O III] line at 5007 Å and  $8\alpha$  recombination lines of different oxygen ions are shown in Figure 3.5. Note that at low temperatures (below 4000 K), the [O III] 5007 Å line emission is dominated by the contribution from the recombination cascades, not the collisional excitation. The cascade contribution to the post-shock intensity of this line reaches about 20%.

Because of high  $O^{6+}$  abundances at both low and high temperatures, the distribution of the O VI  $8\alpha$  line emission is much wider than that of the collisionally-excited optical [O III]

<sup>4</sup> We made our own computations of the post-shock plasma recombination and discovered that our oxygen ion distribution over ionization stages is rather similar to the one presented in the lower panel of Figure 3 of SD95, but only if the ion spectroscopic symbols on that figure are increased by unity. Therefore we assume that Figure 3 of SD95 has a misprint and the ion spectroscopic symbols should be read, e.g., “O VII” instead of “O VI”, “O VI” instead of “O V”, etc.

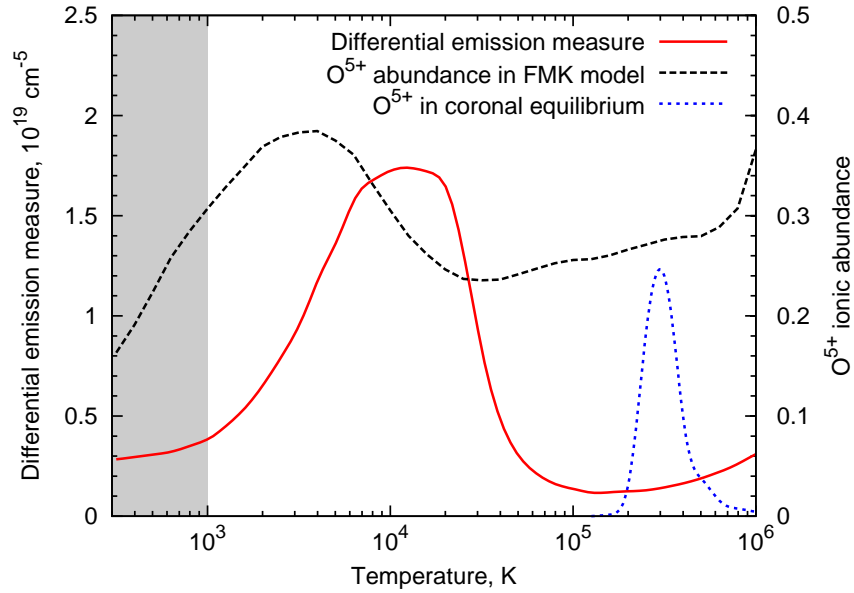


Figure 3.4: Differential oxygen emission measure per logarithmic temperature interval  $dE_O/d(\log T_e)$  in the post-shock cooling region of the SD95 FMK model. Ionic abundances  $n(O^{5+})/n(O)$  of the  $O^{5+}$  ion in the FMK model and in the collisional ionization equilibrium in low-density plasmas (Mazzotta et al., 1998) are also shown. The temperature range not taken into account in our calculations is shaded.

line and has 90% of its area within the temperature range  $5 \times 10^2 - 2 \times 10^4$  K. Note that the dielectronic recombination contributes less than 30% to the resulting line intensity for any of the oxygen ions in the discussed SD95 model.

The O V and O VI lines are the brightest expected ones. Lines of O III and O IV from this region are predicted to be dimmer by a factor of about three, and the O II lines by a factor of about ten.

In Figure 3.6 we show the predicted oxygen recombination line fluxes from the post-shock region of a model FMK. The brightest recombination lines around  $1 \mu\text{m}$  are about 2000 times less intense than the reddened [O III] 5007 Å line. Expected flux values are given in Table 3.3.

### 3.3.2 Cold photoionized region

The ions in the photoionized region before the shock front are rapidly recombining because of their low temperature. This results in rather bright recombination lines, with fluxes proportional to the distance  $d$  between the ionization front and the shock wave.

The plane-parallel SD95 model does not determine this distance. The assumption of small optical depth of material between the shock wave and the ionization front results in



Table 3.3: Brightest recombination line  $l$ -summed emitted and reddened fluxes  $I$  and  $F$  from the post-shock cooling region computed following the SD95 model. The optical [O III] 5007 Å line flux is also given. The last column contains the flux part in the strongest unresolved line component  $f_s$ . The wavelength  $\lambda$  corresponds to the strongest line component.

Ion	Line	$\lambda, \mu\text{m}$	$I, \text{erg/cm}^2/\text{s}$	$F, \text{erg/cm}^2/\text{s}$	$f_s$
O VI	7 $\alpha$	0.5293	$1.16 \times 10^{-17}$	$1.34 \times 10^{-19}$	0.99
O VI	8 $\alpha$	0.7720	$7.73 \times 10^{-18}$	$4.52 \times 10^{-19}$	0.99
O VI	9 $\alpha$	1.0792	$4.32 \times 10^{-18}$	$8.98 \times 10^{-19}$	1.31*
O VI	12 $\beta$	1.3740	$9.15 \times 10^{-19}$	$3.10 \times 10^{-19}$	0.99
O VI	10 $\alpha$	1.4586	$2.52 \times 10^{-18}$	$9.32 \times 10^{-19}$	1.00
O VI	13 $\beta$	1.7189	$6.18 \times 10^{-19}$	$2.76 \times 10^{-19}$	1.00
O VI	11 $\alpha$	1.9177	$1.54 \times 10^{-18}$	$7.58 \times 10^{-19}$	1.00
O VI	12 $\alpha$	2.4642	$9.69 \times 10^{-19}$	$5.69 \times 10^{-19}$	1.00
O V	6 $\alpha$	0.4943	$1.82 \times 10^{-17}$	$1.14 \times 10^{-19}$	0.62
O V	7 $\alpha$	0.7618	$8.68 \times 10^{-18}$	$4.89 \times 10^{-19}$	0.81
O V	8 $\alpha$	1.1114	$4.53 \times 10^{-18}$	$1.01 \times 10^{-18}$	0.89
O V	10 $\beta$	1.1929	$1.22 \times 10^{-18}$	$3.20 \times 10^{-19}$	0.92
O V	9 $\alpha$	1.5538	$2.51 \times 10^{-18}$	$1.00 \times 10^{-18}$	1.21*
O V	12 $\beta$	1.9784	$5.05 \times 10^{-19}$	$2.55 \times 10^{-19}$	0.96
O V	10 $\alpha$	2.1002	$1.45 \times 10^{-18}$	$7.65 \times 10^{-19}$	0.94
O V	11 $\alpha$	2.7613	$8.72 \times 10^{-19}$	$5.43 \times 10^{-19}$	0.97
O IV	7 $\alpha$	1.1902	$8.82 \times 10^{-19}$	$2.32 \times 10^{-19}$	0.80
O IV	8 $\alpha$	1.7363	$4.58 \times 10^{-19}$	$2.07 \times 10^{-19}$	0.74
O III	5 $\alpha$	0.8262	$1.88 \times 10^{-18}$	$1.42 \times 10^{-19}$	0.25
O III	6 $\alpha$	1.3727	$8.23 \times 10^{-19}$	$2.78 \times 10^{-19}$	0.25
O III	7 $\alpha$	2.1149	$3.96 \times 10^{-19}$	$2.10 \times 10^{-19}$	0.76
[O III]		0.5007	$5.78 \times 10^{-15}$	$3.90 \times 10^{-17}$	
[O III]**		0.5007	$2.72 \times 10^{-13}$	$1.84 \times 10^{-15}$	

\* Including the 11 $\beta$  line that overlaps with 9 $\alpha$

\*\* Including the pre-shock photoionized region contribution

*Note.* Assumed cloud area is  $1 \times 10^{34} \text{ cm}^2$  (size about  $2''$ ). Reddening was applied using the Schild (1977) reddening curve and  $E(B - V) = 1.5$  (Hurford & Fesen, 1996). The brightest knots are a factor of 5–20 more intense in the [O III] 5007 Å line than the values given in the table. The  $f_s$  values were determined from simulated spectra having a 200 km/s Doppler line width at the half maximum level (FWHM), that is equal to the optical line widths observed in the Cas A knots (van den Bergh, 1971); see also Section 3.4.

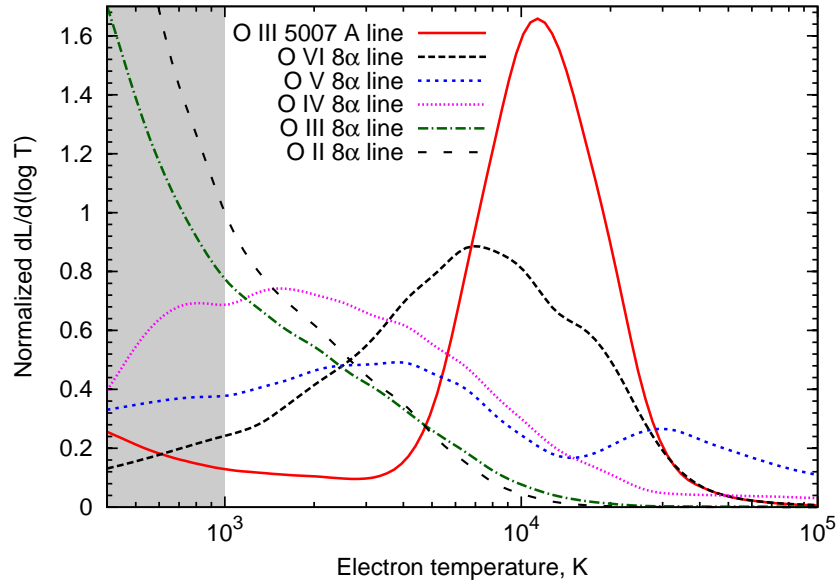


Figure 3.5: Differential luminosity distribution per logarithmic temperature interval according to the SD95 model for several spectral lines, including the prominent 5007 Å [O III] line and predicted O II – O VI 8 $\alpha$  lines. Curves are normalized so that the area enclosed under each of them equals one. The temperature range not taken into account in our calculations is shaded.

restriction of  $d < 10^{17}$  cm for relevant cloud models for a preshock ion number density of  $100 \text{ cm}^{-3}$  (illustrated in Figure 12 of SD95). Below we conservatively take  $d = 10^{15}$  cm, keeping in mind that the line fluxes scale linearly with it.

The cloud model also does not determine the exact temperature in the photoionized region. We take  $T_e = 1 \times 10^3$  K as a reference value, but Dopita et al. (1984) mention that it may be as low as 100 K. If the real temperature in the region is less than our assumed value, recombination line emissivities are respectively higher (see Section 3.5.1 below for quantitative dependences).

Predicted oxygen line fluxes for the SD95 model OP200 with a shock speed of 200 km/s and total preshock ion number density of  $100 \text{ cm}^{-3}$  are shown in Figure 3.7 and given in Table 3.4. It is seen that even with our quite conservative assumptions, the resulting line fluxes are noticeably stronger than from the shock front. Indeed, the predicted line brightest components are on the level of a percent of the [O III] 5007 Å line.

If this would be the case, the lines would have been detected in spectroscopic observations of the fast-moving knots (see discussion on existing observation limits in Section 3.3.4 below).

Our estimate of the observational limit on the O III 5 $\alpha$  recombination line flux at  $0.83 \mu\text{m}$  based on the data by Hurford & Fesen (1996) of  $0.005 \times F(5007 \text{ Å})$  may be trans-

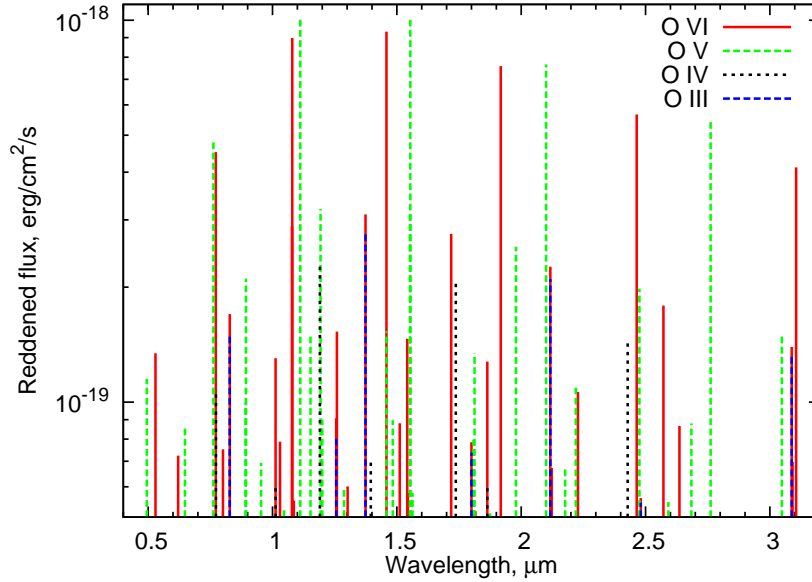


Figure 3.6: Reddened recombination line  $l$ -summed fluxes  $F$  from the post-shock cooling region. Details are as in note to Table 3.3. Here the lines are represented as “infinitely thin”; their fine structure is discussed in Section 3.4.

formed into a joint constraint on the thickness of the photoionized region  $d$ , its temperature  $T_e$  and total ion density  $n_t$ :

$$\left(\frac{n_t}{100 \text{ cm}^{-3}}\right)^2 \left(\frac{10^3 \text{ K}}{T_e}\right) \left(\frac{d}{10^{15} \text{ cm}}\right) < 1,$$

assuming  $E(B - V) = 1.5$  and  $\text{O}^{3+}$  ionic abundance after the ionization front of 0.6.

From this example it is easy to see that detection of the lines or even tight upper limits will allow us to perform detailed observational tests of the SD95 and other FMK models.

### 3.3.3 Separating pre- and post-shock spectral lines

Observationally, the lines formed in the regions before and after the shock wave will be distinguishable because of two effects. Firstly, the lines arising in the photoionized region still dynamically undisturbed by the shock wave should be very narrow intrinsically, but the lines arising in the post-shock region are expected to be Doppler-broadened by turbulence.

Secondly, the spectral lines arising in the post-shock region should be shifted with respect to the pre-shock lines. The relative Doppler shift between these two line families appears due to motion of the post-shock gas relative to the initial knot speed induced by the shock wave. In the strong-shock limit this velocity difference equals  $3/4 v_{\text{shock}}$  for the specific heat ratio  $\gamma = 5/3$  (Zel’dovich & Raizer, 1967), i.e. up to 150 km/s in the SD95

Table 3.4: Brightest recombination line  $l$ -summed emitted and reddened fluxes  $I$  and  $F$  from the photoionized region before the shock front, computed following the SD95 model. Details are as in the note to Table 3.3. The photoionized region thickness is  $10^{15}$  cm. The last column contains the flux part in the strongest unresolved line component  $f_s$  for a FWHM of 200 km/s (see Note to Table 3.3). The wavelength  $\lambda$  corresponds to the strongest line component.

Ion	Line	$\lambda, \mu\text{m}$	$I, \text{erg/cm}^2/\text{s}$	$F, \text{erg/cm}^2/\text{s}$	$f_s$
O III	$5\alpha$	0.8262	$4.13 \times 10^{-16}$	$3.26 \times 10^{-17}$	0.26
O III	$6\beta$	0.8327	$1.05 \times 10^{-16}$	$8.48 \times 10^{-18}$	0.31
O III	$7\beta$	1.2552	$6.09 \times 10^{-17}$	$1.77 \times 10^{-17}$	0.73
O III	$6\alpha$	1.3727	$1.95 \times 10^{-16}$	$6.61 \times 10^{-17}$	0.27
O III	$8\beta$	1.7998	$3.69 \times 10^{-17}$	$1.72 \times 10^{-17}$	0.86
O III	$7\alpha$	2.1149	$1.00 \times 10^{-16}$	$5.32 \times 10^{-17}$	0.82
O III	$9\beta$	2.4804	$2.32 \times 10^{-17}$	$1.36 \times 10^{-17}$	1.32*
O III	$8\alpha$	3.0871	$5.50 \times 10^{-17}$	$3.59 \times 10^{-17}$	0.91
O II	$5\alpha$	1.8645	$4.03 \times 10^{-17}$	$1.94 \times 10^{-17}$	0.24
O II	$6\alpha$	3.0922	$1.90 \times 10^{-17}$	$1.24 \times 10^{-17}$	0.59

\* Including the  $10\gamma$  line that overlaps with  $9\beta$

model, but the relative Doppler shift will also depend on the angle between the shock front and the direction towards the observer.

Both collisionally-excited and recombination lines should display these features, but for the former group such differences should be easier to detect because of their higher line intensities.

The observations with higher spectral resolution ( $\lambda/\Delta\lambda \lesssim 20\,000$ ) could also result in detection of several narrow components forming a line. They could arise from the individual vortice or velocity component emission, if there is only one or a few of them dominating the plasma motion after the shock, as observed in laser experiments simulating cloud-shock interaction in supernova remnants (Klein et al., 2003). The resulting spectral line profile might be quite complicated (e.g., Inogamov & Sunyaev (2003)), but such observations will provide data on the post-shock dynamics of the fast-moving knot that is presently poorly constrained from observations.

### 3.3.4 Existing observational limits

As is seen from Figures 3.6 and 3.7, the brightest recombination lines are expected to lie in the wavelength range between 0.7 and 3  $\mu\text{m}$ . Several detailed spectroscopic investigations have already been performed in this range and could have found these lines, provided that they had low enough detection limits. Below we discuss such existing optical and

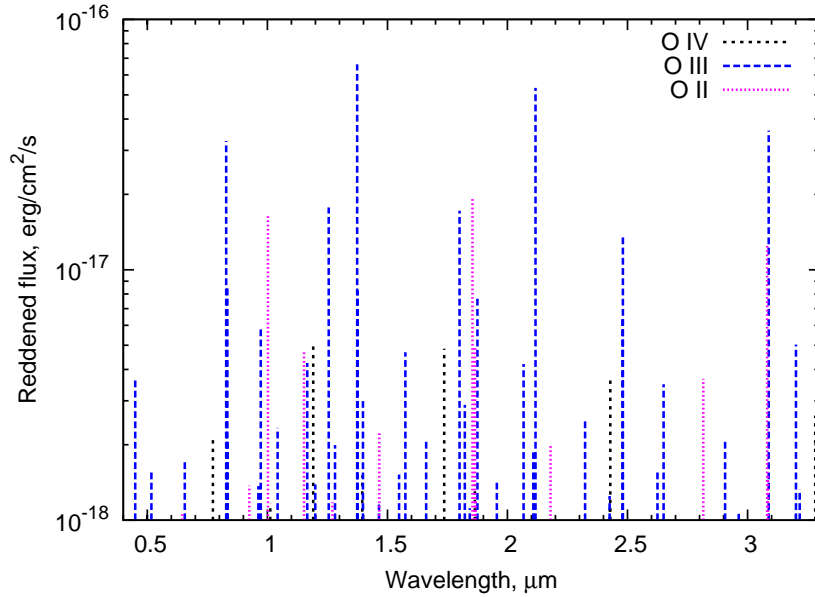


Figure 3.7: Recombination line  $l$ -summed reddened fluxes expected from the photoionized region before the shock front computed following the SD95 ionization front model. Details are as in the note to Table 3.3. The photoionized region thickness is  $10^{15}$  cm.

near-infrared limits on the line fluxes and compare them with the SD95 model predictions.

Optical spectra of fast-moving knots with wide spectral coverage were obtained, e.g., by Chevalier & Kirshner (1979) and Hurford & Fesen (1996). According to the authors, the detection limits around  $0.75\text{--}0.85\text{ }\mu\text{m}$  are about 200–300 times less than the [O III] 5007 Å line flux for the brightest observed features.

Our results give flux ratios of the reddened 5007 Å line to the brightest components of the O VI  $8\alpha$ , O V  $7\alpha$  and O III  $5\alpha$  lines of about 200–2000 (see Figures 3.6 and 3.7 and Tables 3.3 and 3.4). These values show that the model is on the boundary of consistency with the observational results. They also imply that oxygen recombination line detection should be possible, provided that the physics in the post-shock and pre-shock regions corresponds to that described by the SD95 model.

Recently, near-infrared ( $0.95\text{--}2.5\text{ }\mu\text{m}$ ) spectra of Cas A fast-moving knots, obtained with the 2.4 m Hiltner telescope, were published by Gerardy & Fesen (2001). It is more difficult to compare their detection limits with our predictions, as there is only one oxygen O I line blend present around  $1.129\text{ }\mu\text{m}$ . It arises in transitions between excited states of neutral oxygen and is also blended with the [S I] line. If we assume that the overlapping [S I] line emission is negligible, our estimate of the observational detection limit corresponds to about 1/100 of the reddened optical [O III] line flux. This value is again similar to or a factor of several higher than the predicted fluxes of the O VI  $9\alpha$ , O V  $8\alpha$  and O III  $6\alpha$  and  $7\alpha$  lines, also showing the feasibility of the line detection.

### 3.4 Individual line substructure

In the non-relativistic hydrogenic approximation, level energies depend only on the ion charge and the principal quantum number  $n$  of the level. Though, this approximation is not fully applicable for the description of the spectral lines corresponding to transitions between the levels with  $n \approx 10$ , as other effects start playing a role. They arise due to energy level shifts, described in Appendix A.5, resulting in the “fine” structure appearing in the spectral lines. As a result, these effects help to distinguish lines of different elements having equal ionization stages and initial and final  $ns$ .

We calculated the line  $l$ - and  $K$ -substructure following the method outlined in Appendix A.6 ( $K$  is the quantum number used to characterize additional interaction of the highly-excited electron orbital momentum with the total angular momentum of other electrons, present in O II, O III, S II and S III lines). The results are shown in Figure 3.8 for the most interesting cases, assuming recombination lines having widths around 200 km/s (full width at half maximum level, FWHM), of the same order as the observed widths of forbidden optical lines (van den Bergh, 1971).

It is easily seen that high- $l$  levels have both smaller quantum defects and smaller  $K$ -splitting. When  $K$ -splitting is present, a complicated line structure results in weaker individual line fluxes, making them more difficult to detect.

The spectral lines arising in the transitions between lower- $n$  levels have higher  $K$ - and  $l$ -splittings. Therefore the line components have larger separations and the number of individual components increases even more, with each of them being less intense. The near-infrared lines are therefore more promising for the detection than the optical ones, as they have less substructure (compare panels (b) and (c) in Figure 3.8).

The substructure of the  $6\alpha$  recombination lines of Mg I, Al I and Si I have been observed in solar spectra near 12  $\mu\text{m}$  and explained using similar, although somewhat more elaborate, theoretical descriptions (Brault & Noyes, 1983; Chang & Noyes, 1983; Chang, 1984). We have used these observations as the test cases for our line substructure computation code.

In Tables 5–15, available as an electronic supplement at CDS, we give O II – O VI, S II – S V, Si II and Si III recombination line component vacuum wavelengths, emissivities and relative intensities in the  $(nlK) \rightarrow (n'l'K')$  resolution for several temperatures ( $\lg(T_e, \text{K}) = 3.0, 3.5, 4.0, 4.5$  and  $5.0$ ) in the low-density limit. The first seven columns characterize the quantum numbers of the transition (total recombining ion electronic angular momentum  $J_c$  and highly-excited electron quantum numbers before and after the transition  $n, l, K, n', l', K'$ ), Column 8 gives the line component wavelength in microns, the next columns in pairs give the line component emissivity in  $\text{cm}^3/\text{s}$  and the intensity ratio of this component with respect to the  $K$ - and  $l$ -summed emissivity  $\varepsilon(J_c, nlK, n'l'K')/\varepsilon(n, n')$ . Only the lines most likely to be detected are given in these tables, selected by the following parameters – only  $\alpha, \beta$  and  $\gamma$  lines having wavelengths between 0.3 and 5.0  $\mu\text{m}$ .

Tables 16–23, also available at CDS, contain similar information on predicted oxygen line component fluxes in the SD95 200 km/s shock model. The fluxes from the cooling and photoionized regions are given separately in Tables 16–20 (for O II – O VI) and 21–23 (for O II – O IV), respectively. The first eight columns again contain the quantum numbers

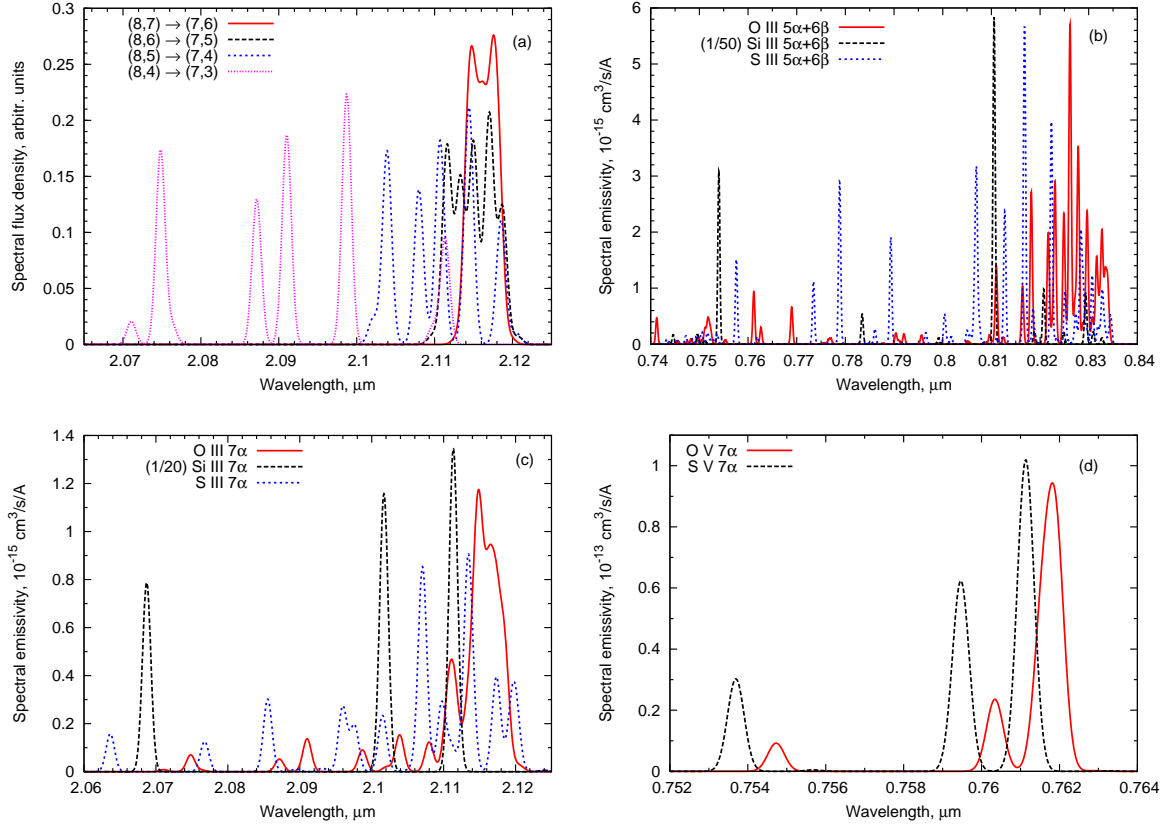


Figure 3.8: Fine structure of recombination lines. A Doppler FWHM of 200 km/s is assumed. (a): O III 7α line  $(8, l) \rightarrow (7, l - 1)$  component structure for  $l \geq 4$ . The sum of all components is set to be equal for each  $l$ . Emissivities of the  $(8, l) \rightarrow (7, l + 1)$  components are much weaker and the structure of the resulting lines is not shown. (b),(c): Spectral emissivity  $d\varepsilon/d\lambda$ , cm<sup>3</sup>/s/Å of the simulated O III, Si III and S III 5α + 6β and 7α line structure for low-density case and temperature  $T_e = 2 \times 10^4$  K. Note that Si III lines have been scaled down to fit on the same scale. (d): Spectral emissivity for the simulated O V and S V 7α line structure in the same conditions. Absence of  $K$ -splitting results in much simpler profiles.

characterizing the transition and the line wavelength, Column 9 lists the line component flux in  $\text{erg}/\text{cm}^2/\text{s}$ , Column 10 contains the intensity ratio of this component with respect to the  $K$ - and  $l$ -summed emissivity.

As discussed in Appendix A.5, the input atomic data are precise to about 10% and we cannot expect better precision of the resulting line wavelength differences from the hydrogenic values.

A sample region from the total resulting model spectrum is shown in Figure 3.9. It shows the variety of the spectral shapes as well as illustrates the diminishing of the peak intensity due to  $K$ -splitting for O III lines.

The line substructure changes with density and temperature because of changes in the relative populations of the  $l$ -states. At low temperatures the main population mechanism is the radiative recombination, which is populating high- $l$  levels relatively efficiently. When the electron density increases,  $l$ -redistribution modifies high- $l$  populations for  $n$  greater than about 20, but for  $n < 15$  the changes are generally smaller.

At higher temperatures, DR populates relatively lower  $l$  states having higher quantum defects and low probabilities of  $\alpha$ -line emission. Therefore a recombination line is split into many components and its emissivity is relatively low. In this case,  $l$ -redistribution mostly shifts the recombined electrons to higher- $l$  states, simplifying the line profile and significantly increasing its emissivity.

In Figure 3.10 we show the change of the O III  $7\alpha$  line fine structure with temperature and density, illustrating the described effects.

Another effect arising at low temperatures and electron densities is lower populations of excited  $J_c$  core states. For O II, O III, S II and S III lines this results in the damping of the  $K$ -splitting, as it arises only from recombination of excited ions. All the flux from  $(nlK) \rightarrow (n'l'K')$  components in this case will be redistributed into the central  $(nl) \rightarrow (n'l')$  components and only the  $l$ -splitting will remain.

## 3.5 Plasma diagnostics using recombination lines

### 3.5.1 Temperature diagnostics

The line emissivity dependence on temperature is shown for several bright optical and near-infrared oxygen recombination lines in the low-density limit in Figure 3.11. Corresponding line wavelengths are given in Table 3.2 above. This figure allows us to compute the recombination line fluxes for other models of the multi-temperature plasma with an emission measure distribution different from the discussed SD95 model.

The curves in Figure 3.11 have two distinct regions. At low temperatures the emissivity is determined by the radiative recombination and changes smoothly from ion to ion. At temperatures higher than several tens of thousands Kelvin the dielectronic recombination starts to dominate the recombination rates (except for the O VI lines due to the absence at low temperatures of dielectronic recombination channels in the He-like ion  $\text{O}^{6+}$ ) and line emissivities of different ions become determined by the lowest excited states of the



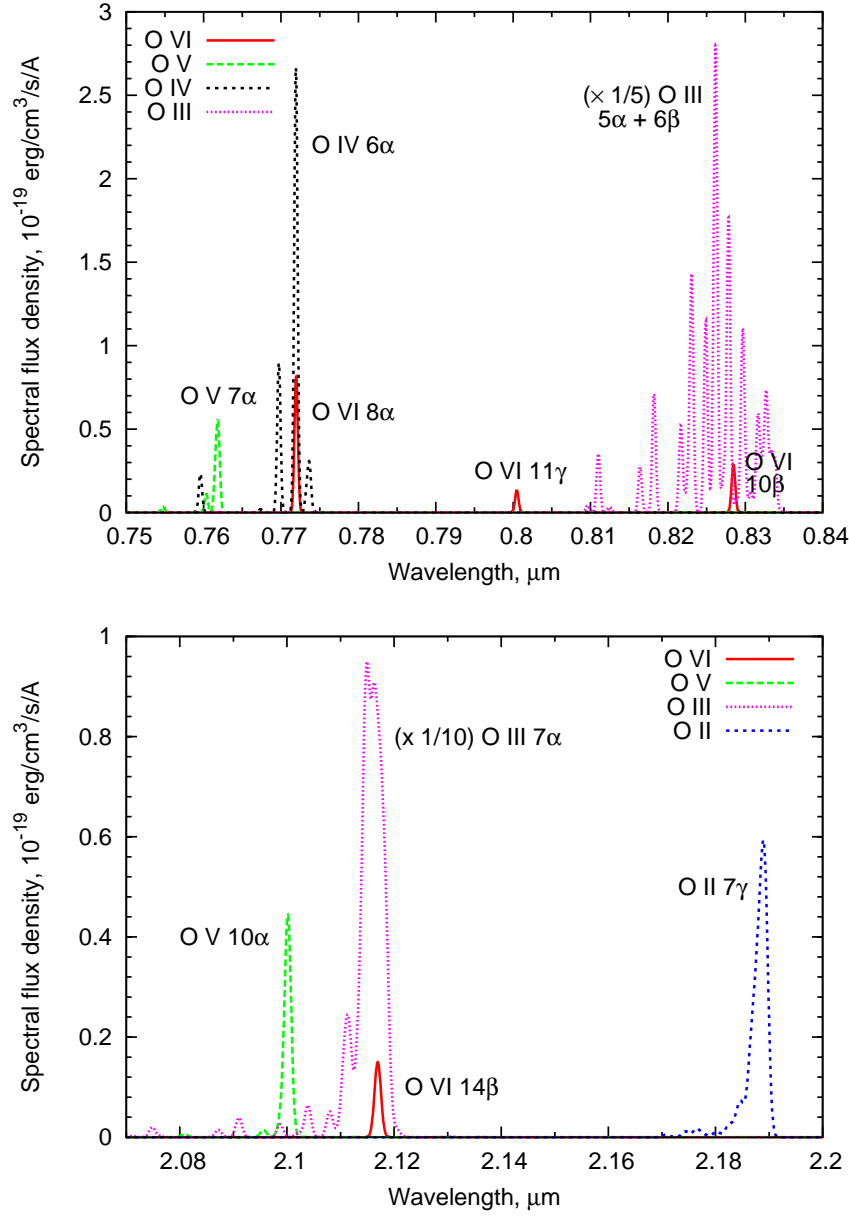


Figure 3.9: Model spectra near 0.8 and 2.1  $\mu$ m containing recombination lines of O II–O VI computed based on the SD95 200 km/s shock model. Contributions of cooling and photoionized regions are added. It is seen that at longer wavelengths the line profiles are less influenced by the substructure. Note that O III line fluxes are diminished to fit on the same scale. A line FWHM of 200 km/s is assumed.

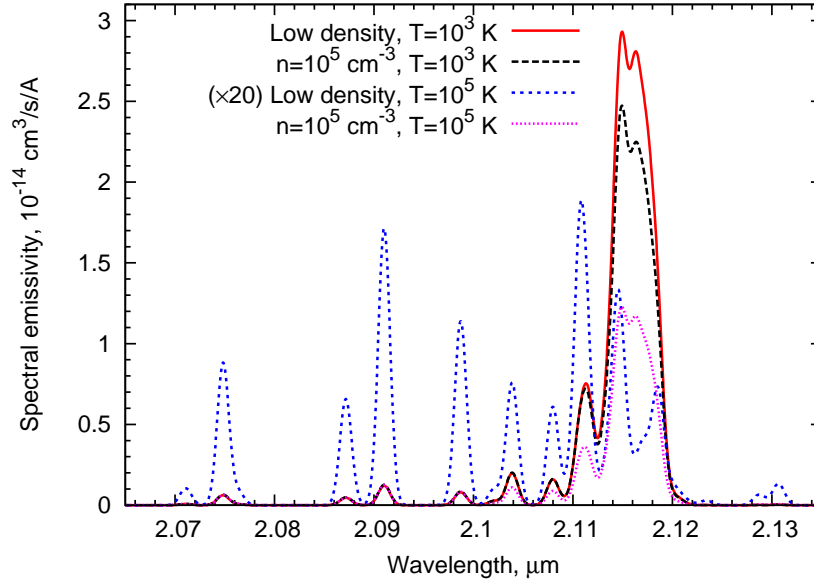


Figure 3.10: Variation of the fine structure of the O III  $7\alpha$  line at  $2.1 \mu\text{m}$  with temperature and density. Line FWHM of 200 km/s is assumed. Note that the low-density curve for  $T_e = 10^5 \text{ K}$  is multiplied by 20 to be visible on this scale.

recombining ion, as described in Appendix A.3. The temperature of the strong emissivity rise is proportional to the typical energy of such excited states. The amplitude of the rise is proportional to the lowest excited state decay rate.

For the discussed SD95 200 km/s shock model the high-temperature region where the DR dominates is important only for O V lines, but it is easy to imagine other ionic abundance distributions where it also will affect ions in lower ionization stages.

The dependence of individual O V recombination  $\alpha$ -line ratios on temperature is shown in Figure 3.12. Again, the two distinct regions are seen at low and high temperatures corresponding to RR- and DR-dominated recombination.

In the intermediate temperatures, the lines corresponding to transitions at lowest  $n$ s become relatively brighter. The reason for such dependence, especially clearly visible in the  $6\alpha/7\alpha$  line ratio, is the following. As follows from Appendix A.3, at low temperatures the dielectronic recombination rate is damped by the factor  $\exp(-\mathcal{E}/kT_e)$ . For the low  $n$  levels the doubly excited state energy  $\mathcal{E}$  may be significantly lower than the core excitation energy and at low temperatures this makes a difference and the dielectronic recombination populates mostly low- $n$  levels, increasing emissivities of low- $n$  recombination lines.

The described effect is most pronounced for recombination lines of O V, Si III and S V, although in all cases the most temperature-sensitive line – the  $\alpha$ -line formed by the transition from the lowest level, into which the DR is possible – is situated around 2000–3000 Å. Though, as can be seen from Figure 3.12, the next recombination line of these ions around

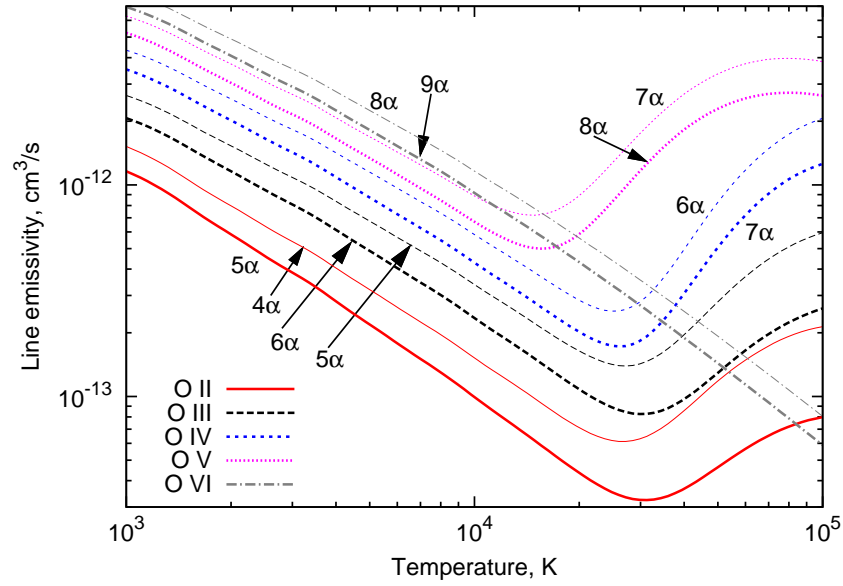


Figure 3.11: Low-density  $l$ -summed emissivities of oxygen ion optical and near-infrared recombination lines. Different colors represent different ions, plotted line thickness increases with the spectral line wavelength.

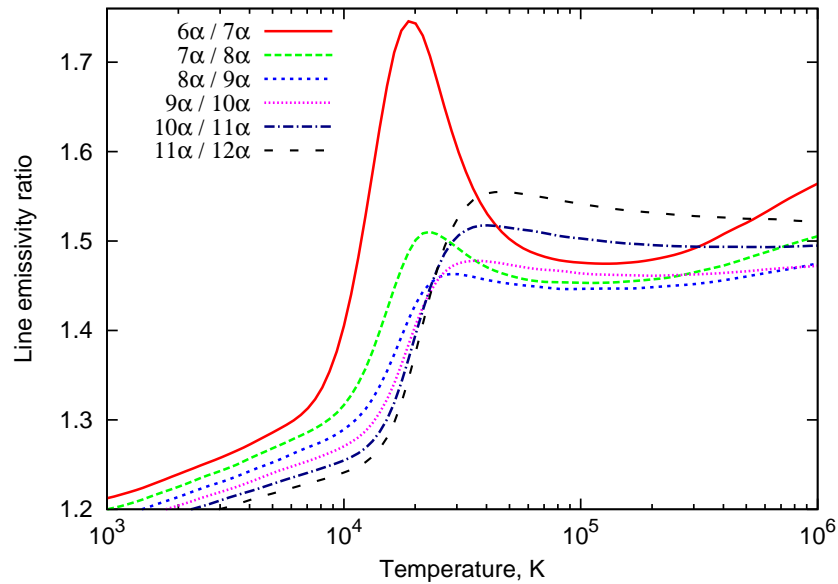


Figure 3.12: Low-density  $l$ -summed O V recombination line emissivity ratios as functions of electron temperature.

4500–5000 Å also can be a useful diagnostic tool, being relatively much brighter in a narrow temperature interval.

### 3.5.2 Recombination lines as density diagnostics

Recombination line flux ratios in principle allow us also to determine density of the emitting region, as their dependences on density and temperature differently affect the relative line fluxes.

As an example, in Figure 3.13 we plot the O V  $7\alpha$  line emissivity as a function of the electron density for different temperatures between  $10^3$  and  $10^5$  K. For better representation, emissivity ratios to their low-density values are shown. Clearly, the density dependences are weak and can probably be neglected in the first stage of the qualitative analysis, especially at low temperatures.

Two distinct regions are seen once again. At low temperatures where only radiative recombination determines the level populations, emissivities decrease with density, but at higher temperatures they increase. The difference is explained by different initial populations of the levels.

Dielectronic recombination predominantly populates states with  $l \lesssim 10$  (see, e.g., Appendix A.3). Collisions in this case mostly transfer recombined electrons to higher  $l$ s, increasing the probability of  $\Delta n = 1$  transitions and, therefore,  $\alpha$ -line emissivities.

Radiative recombination, especially at low temperatures, populates high- $l$  states much more efficiently. In this case, populations of low- $l$  levels relatively increase as a result of the  $l$ -changing collisions, and recombination line emissivities somewhat decrease.

In Figure 3.14 we show the O V recombination line emissivities relative to their low-density values as a function of electron density at temperature 30 000 K. Lines arising in transitions between higher levels increase relatively more, but in absolute terms the increase in emissivity is approximately constant, determined by the  $l$ -redistribution in the high- $n$  levels.

### 3.5.3 Recombination lines of other elements

Our previous analysis mainly examined the oxygen recombination line emission, as the SD95 model allows us to make quantitative predictions about their fluxes and line ratios to the observed collisionally-excited lines. For other elements, no model results for ionic abundance distribution are available. Thus to predict their line fluxes it is necessary to solve a separate problem of non-equilibrium plasma cooling and recombination after the shock front for dense clouds of different compositions. Such an analysis is outside the scope of this paper.

Nevertheless, it seems valuable to provide data on the recombination line emissivities as functions of temperature for the most typical elements. Then, from measured line ratios, it will be possible to reconstruct characteristic conditions in the emitting regions. As the two most typical examples of elements composing FMKs in Cas A, we concentrate on the

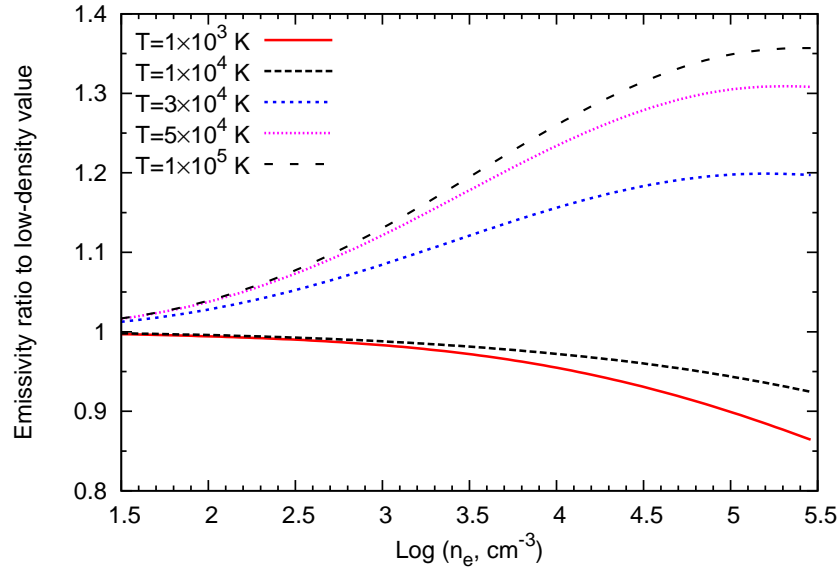


Figure 3.13: Dependence of O V  $7\alpha$  line emissivity on electron density for different electron temperatures  $T_e$ . Values are normalized to the low-density emissivity.

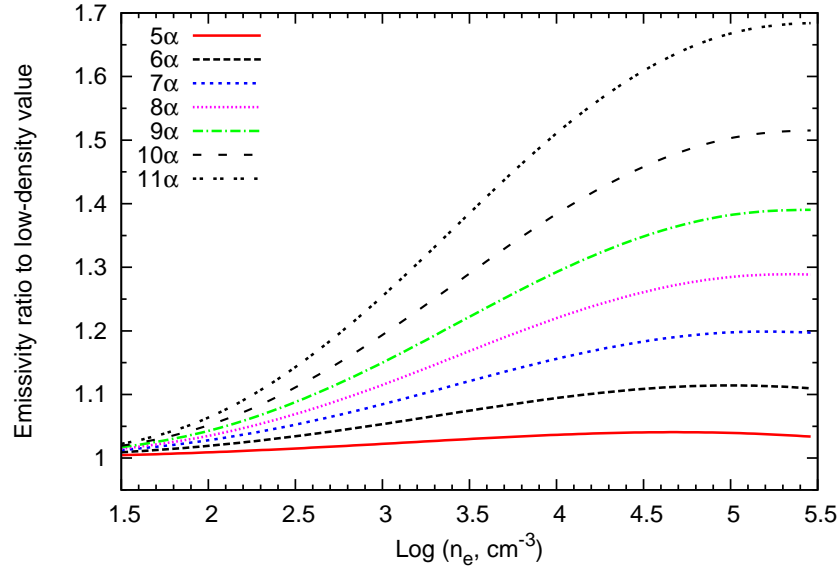


Figure 3.14: Increase of O V  $\alpha$ -line emissivities with electron density at temperature  $T_e = 3 \times 10^4$  K.

recombination lines of silicon and sulphur. Approximate wavelengths of their recombination lines are given in Table 3.2 above.

Figure 3.15 presents low-density emissivities of the brightest optical and near-infrared recombination lines of silicon and sulphur ions expected to exist in the fast-moving knots. Note that Si IV and S VI lines are much weaker than of the other ions at  $T_e > 10^4$  K due to the weakness of dielectronic recombination channels at these temperatures. Note also that the line emissivities in Si II and Si III ions start to increase sharply at about 12 000 K.

Thus these ions are the most sensitive tracers of plasma at temperatures between 15 000 and 30 000 K, when emissivities of O and S ions are still relatively weak. This is also seen in Figure 3.8(b,c), where the emissivities of the lines of Si III are a factor of 20-50 higher than that of O III and S III in the same conditions.

Similar to the case of oxygen recombination lines, the density dependences are not pronounced.

### 3.5.4 Recombination line flux ratios to collisionally-excited lines

The comparison of metal recombination line fluxes with the “traditional” collisionally-excited lines may also be a useful tool for plasma diagnostics.

As these two types of lines have different origins, their emissivity dependences on temperature and density are rather different. For example, collisionally-excited line emissivities exponentially decrease at temperatures below about  $h\nu/k_B$ , as thermal electron energies are not sufficient to excite the ion electronic transition. In contrast, recombination line emissivities at low temperatures increase with decreasing temperature.

Another useful property is that, even in the case when the recombination lines are not detected at all, from the limits of the ratios to the collisional lines it is possible to place constraints on the plasma parameters.

In Figure 3.16 we give ratios to several brightest collisionally-excited optical lines. The exponential increase of the ratios at low temperatures is clearly seen. Collisional line emissivities have been computed using the Chianti atomic database (Dere et al., 1997; Landi et al., 2006)

Recombination line flux ratios to the fine-structure far-infrared line emissivities are given in Figure 3.17. As the Chianti database does not allow one to compute line emissivities down to 100 K, we computed them by extrapolating fine-structure transition electronic excitation collision strengths to low temperatures by a constant that should be reliable to within a factor of two. The collision strength values were adopted from calculations by Lennon & Burke (1994); Blum & Pradhan (1992); Tayal & Gupta (1999); Tayal (2000, 2006).

We note that observations of the far-infrared lines in the spectral range from 10 to 100  $\mu\text{m}$  are impossible from the ground. But even from space, observations of these very intense lines cannot be performed with an angular resolution sufficient to resolve individual knots. They can result only in a signal integrated over many individual emitting objects.

The density dependences of recombination and collisionally-excited lines are also different. Forbidden line emissivity starts decreasing as  $1/n_e$  at some critical density, whereas the

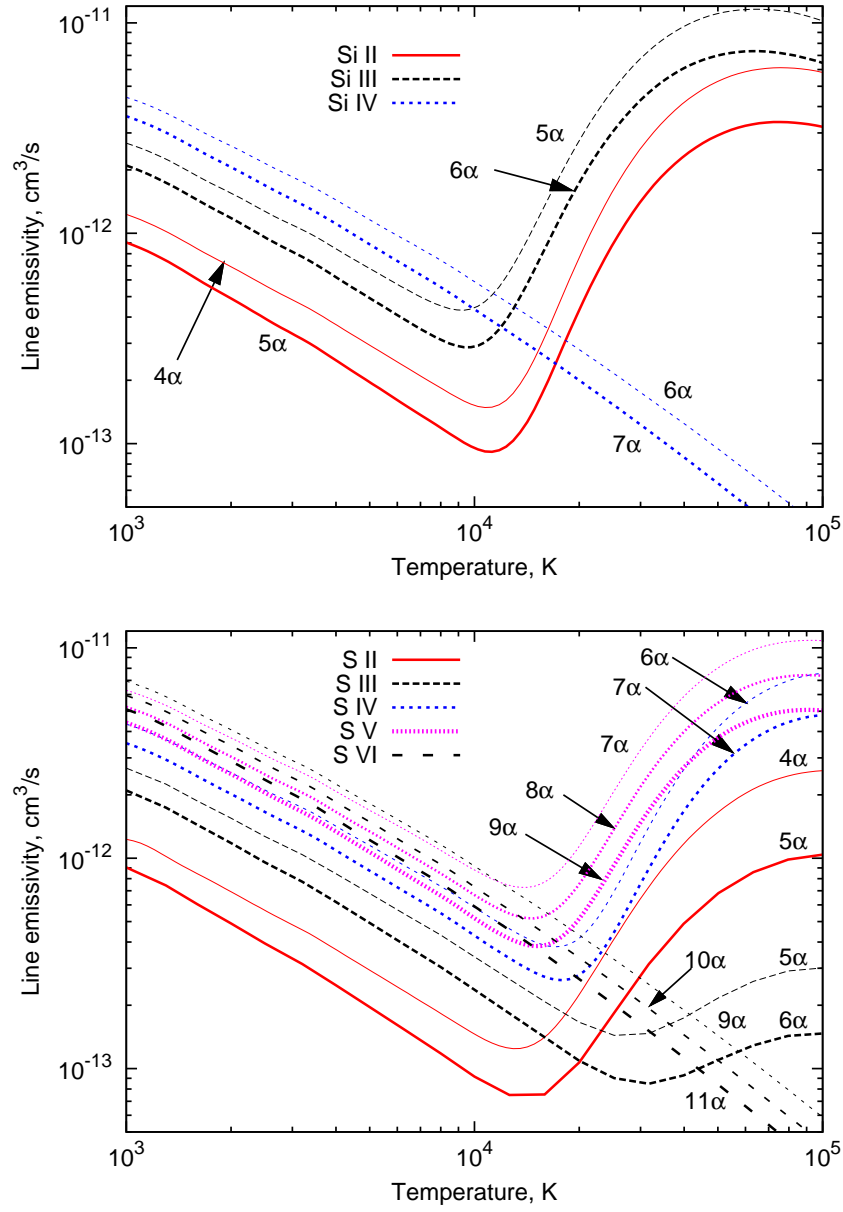


Figure 3.15: Low-density  $l$ -summed emissivities of several optical and near-infrared silicon and sulphur recombination lines. Different colors represent different ions, plotted line thickness increases with spectral line wavelength.

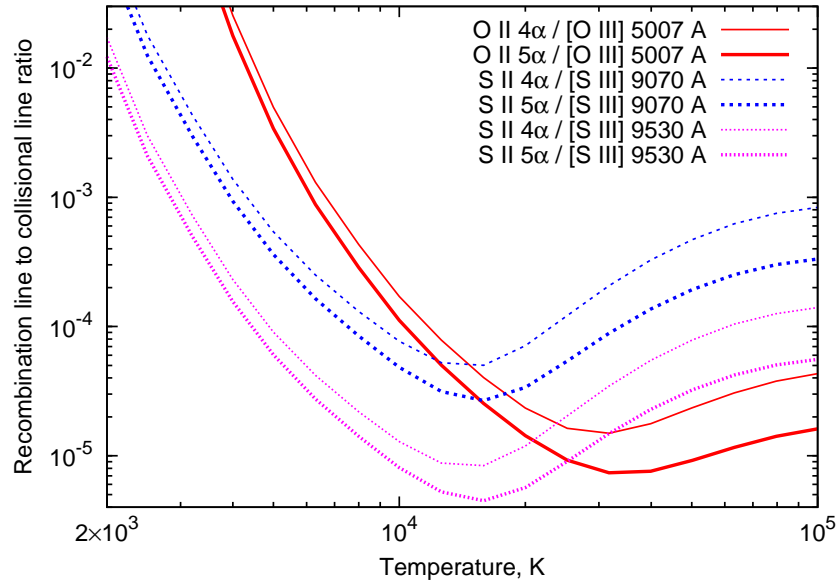


Figure 3.16: Low-density emissivity ratios of recombination lines to several brightest optical collisionally-excited lines.

recombination line emissivities may both decrease and increase depending on the plasma temperature (see above).

The best density indicators for relatively low temperatures and densities in the fast-moving knots are obviously ratios of different optical and near-infrared lines to the far-infrared lines that have critical densities of the order of  $100 - 10^4 \text{ cm}^{-3}$ . In an accompanying paper (Docenko & Sunyaev, to be submitted), we present such an analysis based on existing experimental data and compare the results to our predictions based on the SD95 model.

### 3.6 Conclusions

We have developed in detail a new method of rapidly recombining plasma diagnostics based on measurements of optical and near-infrared recombination lines of multiply-ionized metal atoms.

As an example, we have applied our method to the SD95 theoretical model of fast-moving knots in the Cassiopeia A supernova remnant and computed expected oxygen line fluxes from a single FMK of average size and the resulting recombination line ratios. Both the cold photoionized region before the shock front and the rapidly cooling region immediately after the shock front produce oxygen recombination lines strong enough to be observed with modern optical telescopes in the wavelength range between  $0.5$  and  $3 \mu\text{m}$ .

At shorter wavelengths, two factors hamper the line observations: high absorption in



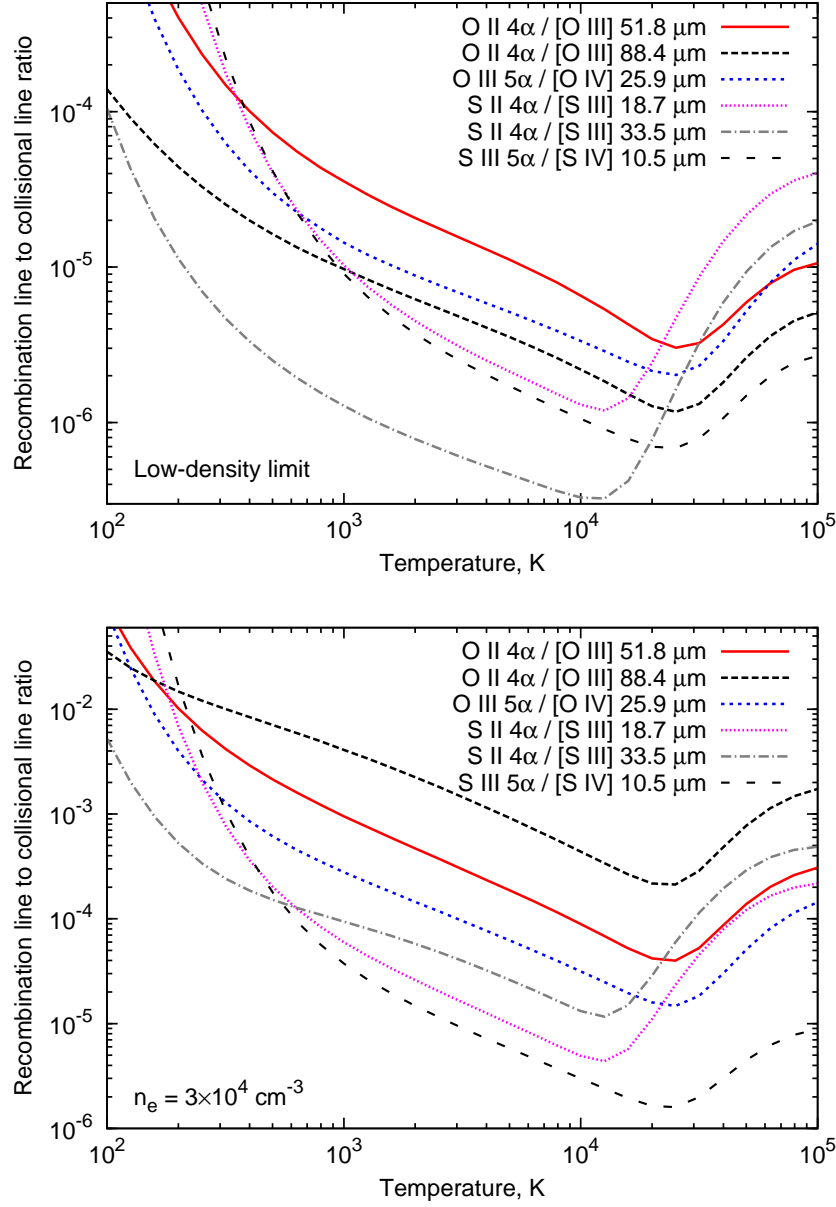


Figure 3.17: Emissivity ratios of recombination lines to several far-infrared collisionally-excited lines. Upper and lower panels show emissivity ratios in the low-density limit applicable for the cold photoionized region (except for the 88.4  $\mu\text{m}$  line) and the case of  $n_e = 3 \times 10^4 \text{ cm}^{-3}$  typical for the cooling region after the shock front.

the interstellar medium on the way from Cas A and the line splitting into widely separated multiple components with consequently lower intensities in each of them. The lines  $n\alpha$  corresponding to transitions between  $n \geq 6$  levels are the most promising, as they are not so strongly split and have 50-90% of the  $l$ -summed intensity in one or a few narrow components.

The precision of our RL flux estimates from Cas A is not expected to be better than a factor of several, as inconsistencies of similar magnitude are observed between the SD95 model predictions and far-infrared oxygen line observations (Docenko & Sunyaev, to be submitted).

Nevertheless, when detected, the recombination lines will allow us to determine the details of the photoionization and rapid cooling processes in the FMKs from the line intensities, intensity ratios to each other and to forbidden collisionally-excited lines and from the recombination line fine structure measurements. The measurements of the line structure demand higher signal-to-noise ratios that can nevertheless be achieved by modern telescopes in a reasonable integration time of a few hours.

One very interesting result is that the predicted O V and O VI recombination lines, being brightest in the cooling region recombination line spectra, arise in the temperature range significantly below  $10^5$  K, where there are essentially no  $O^{5+}$  and  $O^{6+}$  ions in collisional ionization equilibrium conditions.

It also would be very interesting to observe the recombination lines from the knots consisting mostly of silicon and iron. The existence of high-temperature shock-heated plasma having such a chemical composition has been proven by X-ray spectral observations (e.g., Hughes et al. (2000); Hwang et al. (2004)), but detailed theoretical predictions of the cooling and ionization structure of such clouds have not yet been developed.

One of the purposes of this article is to attract attention to metal recombination lines radiated by plasma far out of the collisional ionization equilibrium and having highly-charged ions at low temperatures. Besides the supernova remnants, such plasma producing detectable metal recombination lines may exist in planetary nebulae, as well as near quasars and active galactic nuclei.

## Acknowledgements

We are grateful to L.A. Vainshtein for valuable advices, providing results from the ATOM computer code and permission to use it. We also thank the anonymous referee for remarks making the paper easier to understand and for a useful reference on computation of hydrogenic radiative transition rates.

# Chapter 4

## Fine-structure infrared lines from the Cassiopeia A knots

*Astronomy & Astrophysics*, 2008, submitted  
D. Docenko and R.A. Sunyaev

## Abstract

**Aims:** Archival observations of the infrared fine-structure lines from the young Galactic supernova remnant Cassiopeia A allow to test existing models and to determine the physical parameters of various regions of the fast-moving knots – metal-dominated clouds of the material ejected in the supernova explosion.

**Methods:** The fluxes of the far-infrared [OI] and [OIII] lines are extracted from the previously unpublished archival ISO data. The archival *Spitzer* data are used to determine the fluxes of the O, Ne, Si, S, Ar and Fe ion fine-structure lines originating in the fast-moving knots. The ratios of these line fluxes are used for the plasma diagnostics. We also determine the infrared line flux ratios to the optical [OIII] 5007 Å line in the knots having previously measured reddening.

**Results:** We show that the infrared oxygen line flux predictions of all existing theoretical models are correct only to within a factor of several. Comparison of the model predictions shows that to reproduce the observations it is essential to include the electron conductivity and effects of the dust. Detailed analysis of the diagnostic line ratios of various ions allows us to qualitatively confirm the general model of the FMK emission and to determine observationally the physical conditions in the photoionized region after the shock front for the first time. We also infer from the results that the pre-shock cloud densities are higher than in the existing theoretical models and most probably constitute several hundred particles per cm<sup>3</sup>. We determine also the Cas A luminosities in the infrared continuum and lines.

**Keywords:** atomic processes - ISM: supernova remnants: individual: Cassiopeia A - infrared: ISM

## 4.1 Introduction

The young Galactic supernova remnant Cassiopeia A (Cas A) is one of only a few objects where the inner composition of the supernova progenitor may be studied directly, as the explosion ejecta have not yet mixed with the surrounding medium. In places where these ejecta are being crossed by the reverse shock wave, they are observable as compact knots emitting optical forbidden lines of ions of oxygen, sulphur, argon and other elements. Due to their high density, such ejecta knots are not strongly decelerated by the reverse shock wave and, as a result, have high proper motions, that motivated to name them as the fast-moving knots (FMKs). Studies of Peimbert & van den Bergh (1971) and Chevalier & Kirshner (1978, 1979) have firmly established that the FMKs are an observational manifestation of the supernova ejecta.

In the FMKs we therefore deal with very unusual situation in astrophysics where oxygen comprises 80%-90% of all atoms in the plasma, other components being mostly Ne, Si, S, Ar and Fe. The hydrogen and helium abundances are, in contrast, thought to be negligibly low. Optical observations have shown that some knots consist even of essentially pure oxygen (so-called [O III] filament, Chevalier & Kirshner (1979)).

Theoretical interpretation of the optical observations has proven that the plasma heated up to temperatures of several million degrees is rapidly cooling due to its high density and anomalous chemical composition of the gas. At the same time the ionization degree is lagging behind the rapid cooling rate. This results in a unique situation where atoms with strongly different ionization degrees coexist at low temperatures from  $10^4$  K to several hundreds Kelvin. Just because of that, as we show below, the lines of highly-charged ions, such as [Si x] and [Ar v], originate at temperatures about  $10^4$  K and lower<sup>1</sup>.

Traditionally, theoretical models of the fast-moving knot emission were compared only with the optical line observations. As there is only a very limited number of informative line ratios in the optical spectrum, the FMK theoretical models are both difficult to construct and to compare with optical observations. Most well-known models are the ones constructed by Itoh (1981a,b); Borkowski & Shull (1990) and Sutherland & Dopita (1995b).

Recent paper by Docenko & Sunyaev (2008) has shown one way to constrain the theoretical models using prospective observations of the optical and near-infrared recombination lines of highly-charged oxygen ions.

In this paper we demonstrate how the existing archival infrared observations can discriminate between the existing models and set strong constraints for the construction of the future ones. We compare the model predictions of the far-infrared (FIR) fine-structure oxygen line flux ratios to the flux in the optical [O III] 5007 Å line with their observational values and show that all of the predictions are in error by a factor of several for one or several flux ratios. It should be remembered, however, that the theoretical models predict the deviations of ionic abundances from their collisional equilibrium values by orders of

---

<sup>1</sup>The [Si x] line have been detected also in spectra of several active galactic nuclei (Thompson, 1996; Riffel et al., 2006), where it is apparently formed in the photoionized region. Even so, the models predict the line-forming region temperatures around  $10^5$  K (Ferguson et al., 1997).

magnitude. Therefore inconsistencies of the observed order suggest that some corrections should be applied to the existing models, while the general picture described in the models is entirely correct.

The infrared fine-structure line flux ratios of other element (in addition to oxygen) ions are currently the best tool available for direct studies of the physical parameters in the FMKs. We made an attempt to estimate these parameters using available observational data. As a result, parameters of the post-shock photoionized region are estimated observationally for the first time, confirming qualitatively the predictions of the theoretical models, but again showing some quantitative differences.

The FIR lines will be even more important probe in future, as several far-infrared observatories, such as Herschel Space Observatory and SOFIA, will start their operation soon. They will provide much better FIR data with higher sensitivity and angular resolution, allowing to further constrain the FMK models.

Results of this study are important also for better understanding of the small-scale structure of other oxygen-rich supernova remnants, such as Puppis A, N132D, G292+1.8, etc.

The paper structure is following. In the next Section we briefly describe the existing theoretical models of the FMKs and estimate oxygen infrared line fluxes from one of them. Section 4.3 is devoted to description of the archival infrared observations of the Cas A and their analysis. In Section 4.4 we estimate the physical conditions and abundances in the different regions of FMKs from the observed line flux ratios. In Section 4.5 we discuss these results and compare them with the values predicted by the models. Finally, in Section 4.6 we conclude the article.

## 4.2 Theoretical models of the fast-moving knots

The first detailed model of a fast-moving knot emission, describing it as arising in the passage of a shock wave through the pure oxygen medium, was constructed by Itoh (1981a,b). His model H results were compared with the [O III] filament optical spectrum in the northern part of the Cas A supernova remnant (SNR) shell and reproduced all four measured oxygen [O I], [O II] and [O III] optical line flux ratios to within a factor of two. The infrared line ratios to the [O III] 5007 Å line<sup>2</sup> for this theoretical model (denoted I-H) and other models described below are given in Table 4.1.

In this and other theoretical models, the rapidly cooling region just after the shock front produces high flux of the ionizing radiation that results in appearance of two photoionized regions (PIRs): before and after the shock front (see Figure 4.1).

Later, Itoh (1986) discussed that the model neutral oxygen optical line intensities arising in the PIR after the shock front are much too high when compared to the observed spectra

---

<sup>2</sup>The 5007 Å line is three times brighter than the other [O III] doublet component at 4959 Å (e.g., Osterbrock & Ferland (2006)). Note that in some papers the line intensities are compared to the sum of the doublet components.

Table 4.1: Far-infrared line flux ratios to the dereddened 5007 Å line as derived from different theoretical models and observations. See text for details.

	$\lambda, \mu\text{m}$	$I/I(5007)$					$f_{\text{PIR}}$ SD-200*
		I-H	BS-F	BS-DC	SD-200*	Observed**	
[O IV]	25.91	0.0051	5.0	0.53	8.1	0.20	0.995
[O III]	51.81	0.031	1.34	0.72	0.67	0.25	0.999
[O I]	63.19	1.30	170	12	—	0.07	—
[O III]	88.36	0.028	0.22	0.11	0.55	0.10	0.999
[O I]	145.5	0.038	7.8	0.75	—	<0.0024	—

\* Derived in Sections 4.2.1 and 4.2.2.

\*\* Obtained in Sections 4.3.1 and 4.3.2.1.

*Notes.* The last column lists contribution to the line flux in the SD-200 model arising from the photoionized region (PIR) before the shock wave. Derivation of the observed line flux ratio values is described in Section 4.3. The model-predicted [O I] lines are sensitive to the pre-shock ion number density in the model, see Section 4.4.1.2.

of the oxygen-rich supernova remnant Cas A and Puppis A ejecta. He suggested that emission from this region is damped because the region itself is truncated due to some hydrodynamical phenomena. It affects essentially only neutral oxygen lines, as all the other ions have already recombined in the dense post-shock plasma before reaching the photoionized region. This possibly makes the [O I] lines least reliable for direct comparison with model predictions, as all existing models are one-dimensional.

Another group of theoretical FMK models was proposed by Borkowski & Shull (1990). In contrast to the Itoh models, some of them accounted for the electron conductivity that changed the line fluxes considerably. One more difference is that the Borkowski & Shull (1990) models do not account for the emission from the PIR before the shock wave. The models best describing the Cas A FMK optical spectra are F and DC (respectively, denoted as BS-F and BS-DC in Table 4.1 and below). Note that only the BS-DC model takes into account the electron conductivity.

Both Itoh (1981a,b) and Borkowski & Shull (1990) describe the emission arising in the pure oxygen plasma. However, it was shown by Dopita et al. (1984) that inclusion of other elements in the model significantly changes the plasma thermal structure and emission, especially in the cold PIRs, where a number of fine-structure transitions in ions of other elements can effectively cool plasma to temperatures of about one hundred Kelvin. Following this line of reasoning, another group of the FMK models was published by Sutherland & Dopita (1995b). It describes emission arising in the interaction of the dense cloud with the external shock wave, entering the cloud and propagating through it. The expected far-infrared line intensities are not published and we estimate them in the Section 4.2.1 and 4.2.2 for the model with 200 km/s shock speed and pre-shock ion number density of  $100 \text{ cm}^{-3}$  (denoted as SD-200 in Table 4.1 and below), that is best reproducing

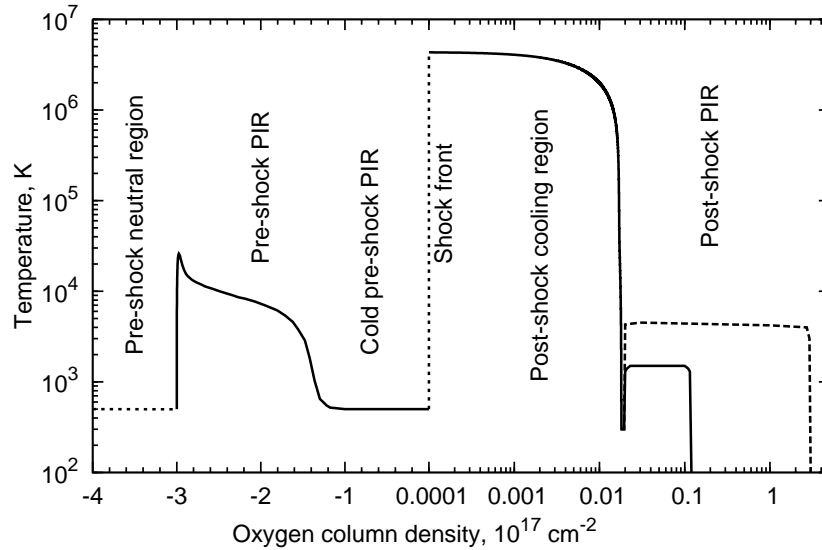


Figure 4.1: Schematic representation of the FMK temperature structure, induced by its interaction with the reverse shock. Negative column densities corresponding to the pre-shock regions are in linear scale; positive (post-shock) column densities are in logarithmic scale. The post-shock photoionized region (PIR) parameters are given as derived in Section 4.5.2 (solid line) and according to the Borkowski & Shull (1990) models (dashed line). Shock is moving to the left. Due to the FMK high density the reverse shock in it is slowed down to about 200 km/s.

the optical spectra of Cas A fast-moving knots, as demonstrated by Sutherland & Dopita (1995b).

As compared to the models of Itoh (1981a,b) and Borkowski & Shull (1990), the SD-200 model does not include the PIR after the shock front, as it is constructed to describe the FMK optical spectrum and the temperature of this post-shock PIR is estimated to be too low to contribute significantly to the optical line emission.

All described models nevertheless share a lot of similar features (see Figure 4.1). In all of them the plasma after the shock front passage is rapidly cooling and, at temperatures of  $(5 - 50) \times 10^3$  K, emitting the high-ionization lines observable in the visible and near-infrared spectra (Chevalier & Kirshner, 1978, 1979; Hurford & Fesen, 1996; Gerardy & Fesen, 2001). Thickness of this emitting layer is extremely small (about  $10^{10}$  cm for the pre-shock ion density of  $100 \text{ cm}^{-3}$ ), but due to the high electron density in the cooling material at  $T < 10^5$  K (more than  $10^5 \text{ cm}^{-3}$ ) the emission measure is enough to produce or contribute to bright emission lines of highly-charged ionic species, such as [O III] lines near 5000 Å.

In all these models the visible line emission of weakly-ionized ionic species (e.g., [O I]



and [O II]) is arising in photoionized regions before and after the shock front.

Although all of the theoretical models describe optical spectrum relatively well, with discrepancies in relative intensities not exceeding factors of about two, predictions for the infrared lines differ by several orders of magnitude (see Table 4.1). It is therefore clear that the models have lack of constraints and more diagnostic information in form of various line flux ratios is needed to pin down the true structure of the fast-moving knots. Part of such information may be obtained from the far-infrared line archival observations, and we present such analysis in the Section 4.3 below.

### 4.2.1 Infrared lines from the SD-200 model

Because of lack of published values, we had to make our own estimates of the far-infrared line fluxes and their ratios to the [O III] 5007 Å line in the SD-200 model. Fortunately, all the data necessary for such calculation – ionic abundances of all oxygen ions, temperature and density structure of the post-shock region and temperature structure of the pre-shock photoionization front – are known for the SD-200 model<sup>3</sup>.

Note that the FMK structure calculations in the SD-200 model are based on the plasma composition that is slightly different from the composition inferred from the X-ray and optical observations. Specifically, it is dominated by O (63% by number) and Ne (29%) and contains minor amounts of C, Mg and Si. In contrast, the observations show that the major part of the currently bright X-ray and optical plasma contains about 90% of oxygen with other abundant elements being not only Ne, but also Si and S.

On Figure 4.2 we demonstrate how strongly different is the ionization state distribution in the SD-200 model as compared to the collisional ionization equilibrium (CIE, Mazzotta et al. (1998)) on examples of the  $O^{2+}$  and  $O^{3+}$  ions producing bright FIR lines. It is seen that in the rapidly cooling plasma these ions are abundant at significantly lower temperatures (down to 300 K and below) than in the CIE due to very rapid plasma cooling via the line emission.

On the same figure we present the oxygen ion emission measure distribution over temperature  $dE_O/d(\log T_e)$  in the SD-200 model, defined in Equation (4.3). This distribution together with the line emissivity dependence on temperature allows one to calculate the relative contributions to the total line flux from different temperature intervals (see Section 4.2.2).

---

<sup>3</sup>We made our own computations of the post-shock plasma recombination and discovered that our oxygen ion distribution over ionization stages is rather similar to the one presented on the lower panel of Figure 3 of the Sutherland & Dopita (1995b), but only if the ion spectroscopic symbols on that figure are increased by unity. Therefore we assume that the Figure 3 of Sutherland & Dopita (1995b) has a misprint and the ion spectroscopic symbols should be read, e.g., “O VII” instead of “O VI”, “O VI” instead of “O V”, etc. Therefore, the SD-200 model values for the neutral oxygen abundances are not known and we do not provide estimates of the FIR [O I] line intensities.

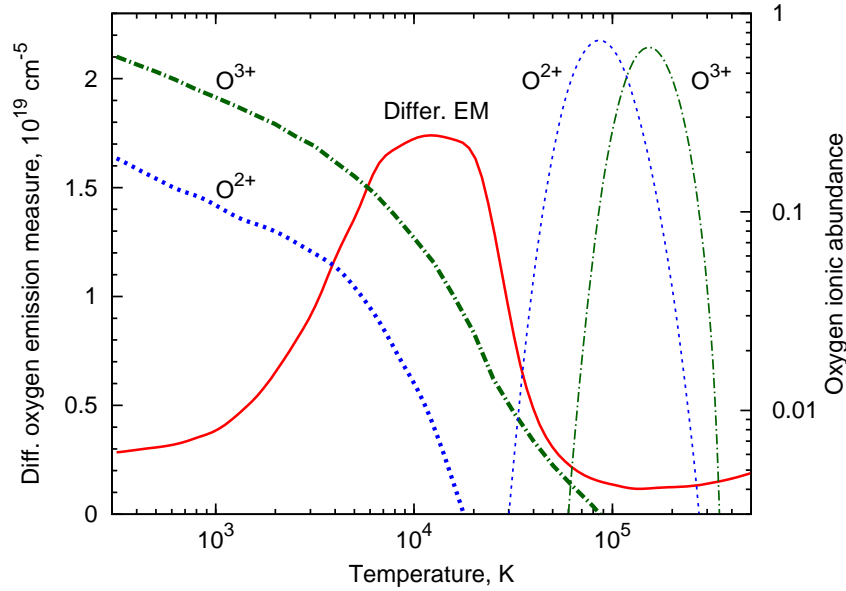


Figure 4.2: Comparison of ionic abundances of oxygen ions  $O^{2+}$  and  $O^{3+}$  in the collisional ionization equilibrium (thin curves) and in the cooling post-shock region of the SD-200 model (thick curves of the same color). The differential oxygen emission measure per logarithmic temperature interval  $dE_O/d\log T_e$  is shown with the red solid line.

### 4.2.2 Line flux computation

The emissivity,  $\text{cm}^3/\text{s}$ , of a spectral line corresponding to transition from level  $u$  to level  $l$  is defined as

$$\varepsilon(u, l) = n_u A_{ul} / n_e n_i, \quad (4.1)$$

where  $n_e$ ,  $n_i$  and  $n_u$  are the number densities of electrons, corresponding ionic species and ions in the state  $u$ , respectively, and  $A_{ul}$  is the spontaneous  $u \rightarrow l$  transition rate.

For oxygen ions at temperatures above 1000 K the line emissivities  $\varepsilon$  were obtained from the Chianti atomic database (Dere et al., 1997; Landi et al., 2006). For lower temperatures and other ions, we have computed emissivities using a standard approach, i.e., calculating the level populations by solution of a system of linear equations describing transitions between the lowest ionic levels using electronic excitation effective collision strength data from literature and spontaneous transition rates from the Ralchenko et al. (2007) database<sup>4</sup> and MCHF/MCDHF collection<sup>5</sup>, and then applying Eq. (4.1) to derive the line emissivities.

The electronic collisional excitation effective collision strength values were taken from Dufton & Kingston (1991); Blum & Pradhan (1992); Zhang et al. (1994); Butler & Zeippen (1994); Lennon & Burke (1994); Galavis et al. (1995); Pelan & Berrington (1995); Berrington et al.

<sup>4</sup>Available online at <http://physics.nist.gov/asd3>

<sup>5</sup><http://atoms.vuse.vanderbilt.edu/>

(1998); Tayal & Gupta (1999); Griffin & Badnell (2000); Griffin et al. (2001); Tayal (2006) and Ramsbottom et al. (2007) and extrapolated to lower temperatures by a constant, if needed.

Line fluxes  $I(u, l)$ , erg/cm<sup>2</sup>/s, were computed by integrating along the line of sight

$$I(u, l) = h\nu \frac{S}{4\pi R^2} \int \varepsilon(u, l; T_e(r)) n_e(r) n_i(r) dr, \quad (4.2)$$

where  $h\nu$  is the photon energy,  $R$  is the distance from the observer to the emitting region (3.4 kpc, Reed et al. (1995)) and  $S$  is the emitting region area. From this expression it is seen that the line emission is mostly arising in regions having highest emission measure  $n_e n_O dr$ , ionic abundance  $n_i/n_O$  and emissivity  $\varepsilon$  (here  $n_O$  is the total number density of all oxygen ions).

The integral over distance in the post-shock cooling region can be easily transformed into integral over temperature by substitution

$$dr = \frac{dr}{dt} \frac{dt}{dT} dT = v_{\text{shock}} \frac{n_{0,t}}{n_t} \frac{3/2(n_t + n_e)k_B}{n_t n_e \Lambda_N} dT,$$

where  $v_{\text{shock}}$  is the shock front speed,  $\Lambda_N$  is the cooling function (Sutherland & Dopita, 1993) and  $n_t$  and  $n_{0,t}$  are the total number densities of all ions in plasma at a given point and before the shock (i.e., in the SD-200 model  $n_{0,t} = 100 \text{ cm}^{-3}$ ). It is assumed here that the photon heating is insignificant compared to the energy losses. Parameters of this equation – cooling function, electron and ion densities as functions of temperature – were taken from the SD-200 model.

For purpose of qualitative analysis, we introduce the oxygen differential emission measure per logarithmic temperature interval

$$\frac{dE_O}{d(\log T_e)} = T_e \frac{n_O n_e dr}{dT_e}. \quad (4.3)$$

It shows contribution of a given logarithmic temperature interval to the total emission measure, showing where most of the line emission originates. Using this notion, we can express the line flux from Eq. (4.2) as

$$I(u, l) = h\nu \frac{S}{4\pi R^2} \int \varepsilon(u, l; T_e) \frac{dE_O}{d \log T_e} \frac{n_i}{n_O} \frac{dT_e}{T_e}.$$

Contributions from different temperature intervals to the emission of the post-shock cooling region in the oxygen lines are illustrated on Figure 4.3, where we plot the normalized line luminosities per logarithmic temperature interval. It is seen that the post-shock contribution to the visible [O III] line emission is arising at temperatures of  $(5 - 20) \times 10^3 \text{ K}$ , whereas the infrared lines are emitted mostly at lower temperatures. They also have much broader range of temperatures contributing to the line emission because of lower excitation energies.

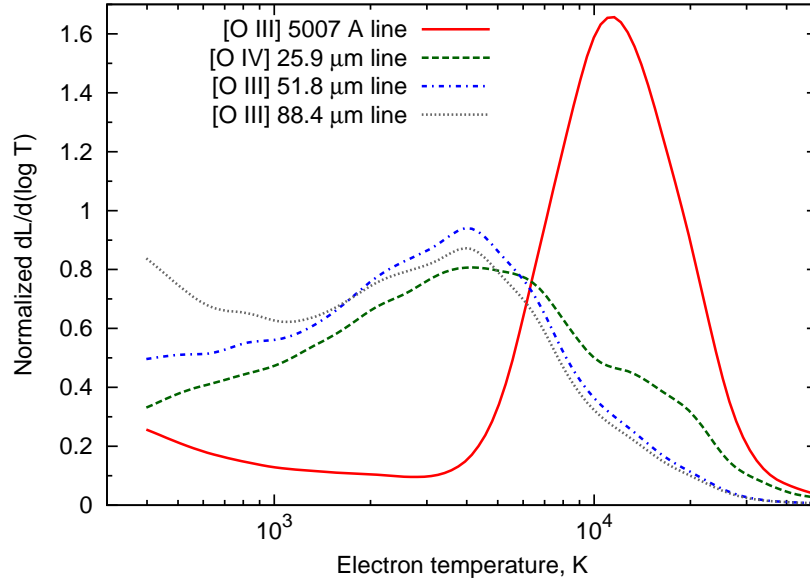


Figure 4.3: Differential luminosity contribution per logarithmic temperature interval for the optical [O III] 5007 Å line and discussed infrared lines in the cooling post-shock region according to the SD-200 model. Curves are normalized so that the area enclosed under each of them equals one. Low-temperature (below 4000 K) contribution to the optical [O III] line is due to recombination.

In our analysis, we artificially stop integrating expression (4.2) in the post-shock region when the plasma temperature drops below 300 K, as the SD-200 model does not contain data for lower temperatures. This should not influence much the total FIR line intensities, as the model predicts them to be mainly emitted in the pre-shock region.

In the pre-shock PIR the ion density is constant and temperature dependence on time for the SD-200 model is known explicitly. Therefore the Eq. (4.2) was applied directly to compute the line fluxes from this region.

Resulting line flux ratios are given in Table 4.1.

### 4.3 Archival observations of the FIR lines

The first search for the [O I] 63.19 μm line was performed by Dinerstein et al. (1987), who observed the northern part of the Cas A using the NASA Kuiper Airborn Observatory. This search resulted in a 3-σ upper limit of reddening-corrected flux ratio  $I(63.19 \mu\text{m})/I(5007 \text{ Å})$  of about 0.3, already constraining some theoretical models.

Later, the far-infrared lines of O, Ne, Si, S and Ar ions were detected by the Infrared Space Observatory (ISO, Arendt et al., 1999). We describe our analysis of some of these

archival observations in Section 4.3.1.

Recently, the *Spitzer* Space Telescope has spectrally mapped this supernova remnant (Ennis et al., 2006; Rho et al., 2008). In Section 4.3.2, we determine the line ratios<sup>6</sup> of O, Ne, Si, S, Ar and Fe lines to the [O III] 5007 Å line.

To determine these ratios, we compare the infrared observations of ISO and *Spitzer* with the optical images of the Hubble Space Telescope. The best method for comparison of these observations would be an analysis of the properties of individual knots but, unfortunately, the ISO data have insufficient angular resolution (about 40"). The angular resolution of the *Spitzer* data is much better (2"–8"), but also too coarse for isolating contributions of *individual* knots distinguishable on the optical maps (0".2–1", corresponding to  $(3 - 15) \times 10^{16}$  cm at 3.4 kpc).

As the optical observations show, the bright FMK lifetime is of the order of 30 years (Kamper & van den Bergh, 1976) that is determined by the time needed for the shock wave to cross the cloud. After that the knots fade, but other ones gradually appear on the maps of the Cas A. Therefore one may directly compare either observations performed with a small time difference between them (as it is the case with the Hubble Space Telescope observations compared with the *Spitzer* data), or averaged over large area (as it is the case with ISO data).

### 4.3.1 ISO observations

The Infrared Space Observatory<sup>7</sup> Long Wavelength Spectrometer (ISO LWS) observations of the Cassiopeia A supernova remnant have been performed in 1996 and 1997. Here we do not discuss observations at shorter wavelengths ( $\lambda < 40 \mu\text{m}$ ), as more recent data from the *Spitzer* observatory is available, having significantly higher angular resolution.

To determine the line fluxes, we used the ISO LWS calibrated data from a highly-processed data product "Uniformly processed LWS L01 spectra" available at the ISO data archive<sup>8</sup>.

There are seven LWS observations in L01 mode each covering full instrument spectral range between 43 and 170  $\mu\text{m}$  with medium spectral resolution ( $\lambda/\Delta\lambda$  between 150 and 200). The regions observed by ISO are shown on Figure 4.4 overlaid with the Hubble Space Telescope Advanced Camera for Surveys (HST ACS) Cas A image in filter F475W, containing [O III] 4959 and 5007 Å lines (Obs.ID 10286, observations made in December 2004, Fesen et al. (2006)).

The ISO LWS observational data are summarized in Table 4.2 and the spectral cuts containing the discussed lines are presented on Figure 4.5.

To compute the far-infrared spectral line fluxes, we subtracted the background continuum flux and averaged over three scans of the same detector weighting the data corre-

<sup>6</sup>Here and everywhere below the "line ratio" denotes the ratio of the line fluxes in energy units.

<sup>7</sup>Results in this section are based on observations with ISO, an ESA project with instruments funded by ESA Member States (especially the PI countries: France, Germany, the Netherlands and the United Kingdom) and with the participation of ISAS and NASA.

<sup>8</sup> <http://www.iso.vilspa.esa.es/ida/>

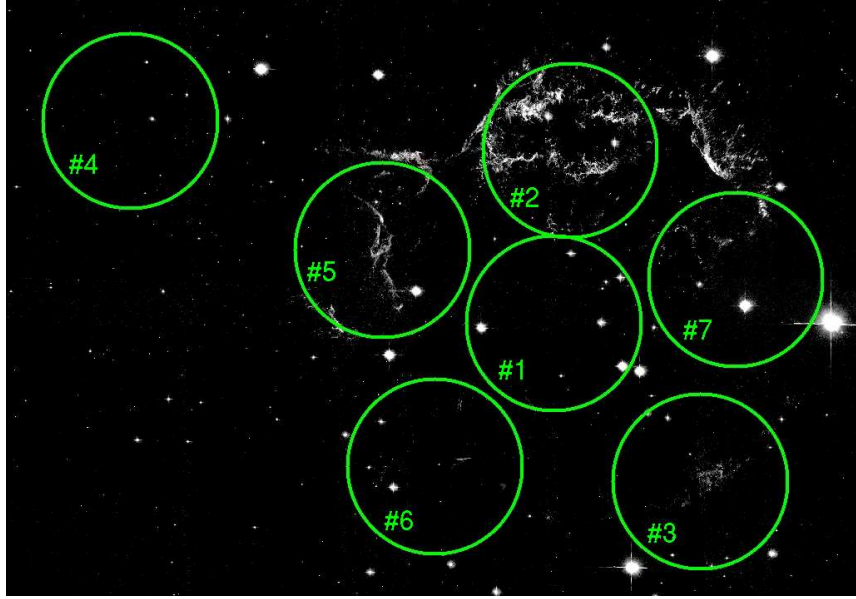


Figure 4.4: ISO LWS apertures (green circles) overlaid on the Hubble Space Telescope 2004 ACS image of Cas A in F475W filter (Fesen et al., 2006). North is upwards and East is to the left.

Table 4.2: Summary of the ISO LWS archival observations of the Cassiopeia A.

ID	Date	Exposure	R.A.	Dec.
Cas A #1	1996 Jun 24	1054 s	350.8656	+58.8130
Cas A #2	1996 Jun 24	1052 s	350.8614	+58.8361
Cas A #3	1996 Jun 24	1054 s	350.8279	+58.7919
Cas A #4	1996 Jun 24	1054 s	350.9748	+58.8400
Cas A #5	1997 Jun 09	1612 s	350.9097	+58.8228
Cas A #6	1997 Jun 09	1612 s	350.8963	+58.7939
Cas A #7	1997 Jun 02	1614 s	350.8186	+58.8188

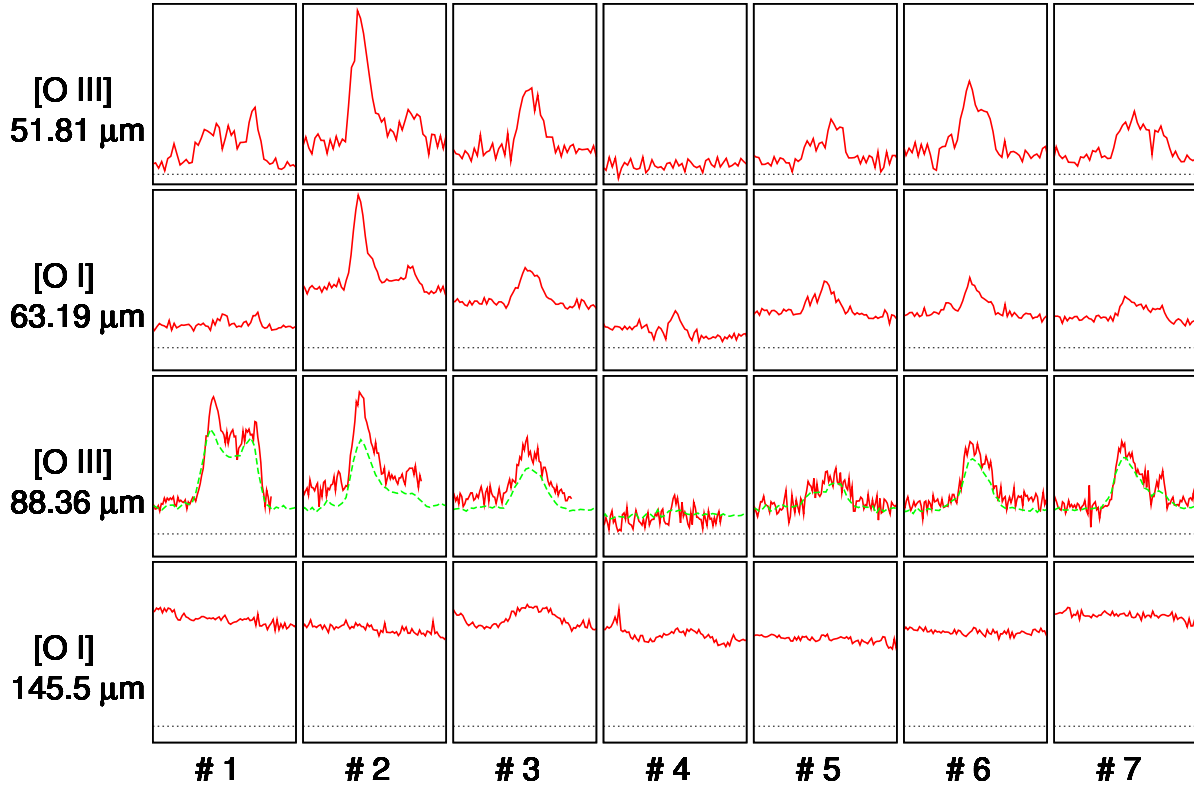


Figure 4.5: ISO LWS spectral cuts containing oxygen far-infrared lines discussed in the text (averages over three scans weighted according to their uncertainties). Continuum emission is not subtracted. Two curves for the 88.36  $\mu\text{m}$  line correspond to measurements by two different ISO detectors. The short-dashed line denotes zero level; maximum intensity corresponds to  $1.7 \times 10^{-10}$ ,  $0.7 \times 10^{-10}$ ,  $0.7 \times 10^{-10}$  and  $0.10 \times 10^{-10}$   $\text{erg}/\text{cm}^2/\mu\text{m}$  for [O III] 51.81  $\mu\text{m}$ , [O I] 63.19  $\mu\text{m}$ , [O III] 88.36  $\mu\text{m}$  and [O I] 145.5  $\mu\text{m}$  lines, respectively. Spectral ranges are centered on the rest wavelengths of the respective spectral lines and include velocity range of  $\pm 10^4$  km/s.

Table 4.3: Far-infrared line fluxes from the ISO LWS observations of Cas A. Fluxes from the matched regions in the HST ACS F475W filter are also given. The upper limits are on the  $3\sigma$  level.

Line	#1	#2	#3	#4	#5	#6	#7
FIR line fluxes $F$ , $10^{-11}$ erg/cm <sup>2</sup> /s							
[O III] 52 $\mu$ m	5.4	9.3	5.4	<1.2	3.5	5.0	5.2
[O I] 63 $\mu$ m	<0.6	2.6	1.2	<1.2	1.0	1.0	0.9
[O III] 88 $\mu$ m	7.5	4.2	2.7	0.5	1.9	3.2	3.4
[O I] 145 $\mu$ m	<0.1	<0.09	0.3	0.1	<0.1	<0.1	<0.1
[O III] 4959 + 5007 Å line flux $F$ , $10^{-13}$ erg/cm <sup>2</sup> /s							
	<0.1	25	2.0	<0.1	6.5	0.5	2.9

*Note.* ISO region positions are shown on Figure 4.4. Regions #3, #6 and #7 have higher interstellar absorption column (Bieging & Crutcher, 1986).

sponding to its uncertainties. In case of the [O III] 88.36  $\mu$ m line it was possible to estimate the systematic uncertainties by comparing the flux values obtained from two neighboring detectors. The flux differences are expected to be arising due to two reasons: slightly different apertures of the detectors and systematic errors due to imperfect instrumental calibration (Gry et al., 2003). Our analysis showed that differences between the two detector measurements do not exceed 10–15%, when the line flux determination accuracy is sufficiently high (see Figure 4.5 for visual comparison).

The background-subtracted FIR line fluxes from the observed regions are presented in Table 4.3. It is seen that flux on the level of up to 10% of brightest fields is observed in the 88.36  $\mu$ m from the region #4 situated outside the main supernova remnant shell and having no detected optical [O III] emission and very little diffuse emission in other optical bands. We consider the flux from this region as coming from foreground and/or background of the Cassiopeia A and in our analysis subtract it from the fluxes of other regions.

In the same table we give the total fast-moving knot optical flux in the matched regions in the F475W filter of the discussed HST ACS data. The diffuse emission in this filter is assumed to be coming only in the [O III] 4959 and 5007 Å lines.

From these data we have calculated the line ratios to the [O III] 5007 Å line, given in Table 4.4. Assuming that the FIR line emission observed by ISO is arising in the same spatial regions where the optical line emission originates, these flux ratios are characteristic for the knot emission and may be used for tests of the theoretical models. If significant large-scale diffuse emission in the FIR lines is present, like one observed in the [S III] and [O IV] lines from Spitzer observations (see Section 4.3.2), then the determined line ratios should be interpreted as the upper limits on the values characteristic for the knots.

In Table 4.4 we provide the values corrected for the interstellar absorption of the optical



Table 4.4: Far-infrared line flux ratios to the optical 5007 Å line  $I/I(5007 \text{ Å})$  corrected for the optical line reddening.

Line	#2	#5
[O III] 51.81 $\mu\text{m}$	0.25	0.36
[O I] 63.19 $\mu\text{m}$	0.07	0.10
[O III] 88.36 $\mu\text{m}$	0.10	0.14
[O I] 145.5 $\mu\text{m}$	<0.0024	<0.01

*Note.* The 5007 Å line contribution of 75% to the total FMK emission in the F475W filter is assumed. Optical line attenuation due to reddening of 200 times is assumed in both ISO LWS regions, see text. FIR line attenuation is neglected.

line using an average value from Hurford & Fesen (1996). This level of reddening diminishes observed visible [O III] doublet intensities by a factor of about 200 ( $A_V \approx 5.0$ ) and is characteristic for region #2 and, possibly, region #5 (Bieging & Crutcher, 1986).

For southern and eastern regions (#3, #6 and #7) the reddening is known to be much higher due to absorption in the molecular clouds with peak  $A_V$ 's reaching 10–15 (Bieging & Crutcher, 1986) corresponding to the optical line attenuation up to factors of  $10^4$  and more. Therefore we do not provide dereddened line ratios in these regions. In our further analysis in Sections 4.4 and 4.5.4 we use only the data from the region #2.

There is an eight-year time difference between ISO and HST observations. During this time, which is about 30% of a bright FMK lifetime (Kamper & van den Bergh, 1976), some optical knots may have disappeared, and new ones may have appeared. Though, averaging over large number of optical knots contained in any ISO LWS field of view at least partially cancels changes induced by brightening or fading of individual knots.

### 4.3.2 *Spitzer* Space Telescope observations

Recently, the *Spitzer* Space Telescope has spectrally mapped the Cassiopeia A in the infrared range using its Infrared Spectrograph (IRS) producing low-resolution spectra from 5 to 38  $\mu\text{m}$  (Ennis et al., 2006; Rho et al., 2008) and detected in this spectral band the fine-structure lines of [O IV], [Ne II], [Ne III], [Ne V], [Si II], [S III], [S IV], [Ar II], [Ar III], [Ar V], [Fe II], etc.

We have used basic calibrated data of these publicly available *Spitzer* observations (Program 3310) to construct the data cube over all remnant with the CUBISM software (Smith et al., 2007). The background regions were determined from the 8  $\mu\text{m}$  MIPS images of the supernova remnant (Hines et al., 2004).

The line flux maps were then produced using the parabolic approximation for the background continuum emission. This allowed the maps to be constructed reliably even for the weak lines in the regions of strong continuum dust emission.

As the *Spitzer* spectral maps and the HST images were obtained almost simultaneously

with a time difference of only one month, we could make a direct pixel-by-pixel comparison of the infrared line map with the optical image. For this purpose, we have processed the HST images: removed the stars, convolved with the point spread function (PSF) of a given *Spitzer* spectral map computed as described in Appendix B, and regridded the HST image to match pixels to the IRS module containing given infrared line. Such matched HST images were produced and compared to each of the infrared lines.

#### 4.3.2.1 The oxygen [O IV] 25.91 $\mu\text{m}$ line

The [O IV] 25.91  $\mu\text{m}$  spectral line map of the northern Cas A shell region from *Spitzer* observations is presented on Figure 4.6. Alongside, we show the HST image in F475W filter processed as described above. The northern region is of primary importance as it has well-measured and almost constant interstellar absorption level.

It can be readily seen from the brightest features on the Figure 4.6 that there is a certain difference between the Cas A morphologies in optical and infrared lines. It may originate due to several reasons: variations of the interstellar reddening (Hurford & Fesen, 1996), emitting plasma chemical composition (Chevalier & Kirshner, 1979) and FMK pre-shock density distribution over the remnant.

On Figure 4.7 we present the resulting pixel-by-pixel scatter plot showing interrelation between the [O IV] infrared and [O III] optical line fluxes. From such comparison of the maps we derive the average line ratio between optical and infrared lines, corresponding to an average reddening, FMK density and chemical composition.

In this analysis, “average” reddening was assumed to diminish the observed optical [O III] line emission 200 times, that is an average of the Hurford & Fesen (1996) measurements. As may be inferred from their paper, the small-scale variations of the interstellar reddening in this region change the optical line attenuation within a factor of two. The observed scatter of the line ratio seen on Figure 4.7 is of similar magnitude.

On the same Figure we present also data on five FMKs having reddening measured by Hurford & Fesen (1996). Their positions are shown on Figure 4.7. In these cases, the reddening correction was made according to their measurement results. Four out of five points lie very close to the best fit lines, showing that considerable part of the FMKs have similar excitation conditions. Remaining point (FMK 1) have relatively weaker [O IV] emission, showing that the physical conditions there are different. This region (Filament 1 of Baade & Minkowski (1954)) indeed has composition different from other regions (Chevalier & Kirshner, 1979).

On Figure 4.6 it is also seen that a noticeable infrared emission in the [O IV] line is arising in the central Cas A region having no optical nebulosity (see also Rho et al. (2008)). On Figure 4.7 such infrared-only emission shows up on the left as horizontal branches, corresponding to an approximately constant background surface brightness. Two such branches are apparent, probably corresponding to two different column densities of the  $\text{O}^{3+}$  ion. Pixels forming the lower branch are situated just outside the optical shell, where the optical surface brightness is already fading, but the infrared line emission is still present.

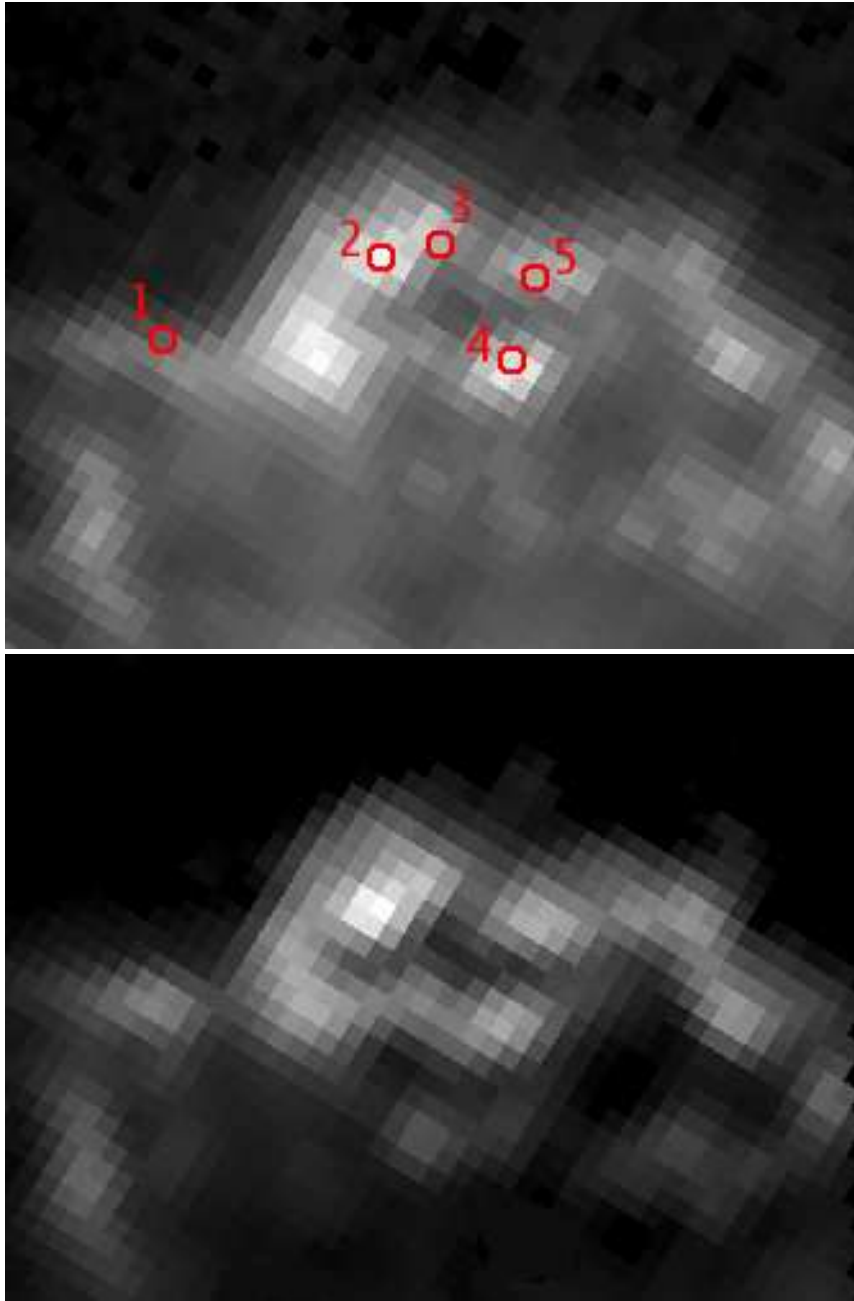


Figure 4.6: The *Spitzer* Space Telescope map of the northern part of the Cas A optical shell rich in FMKs in the [O IV] line at  $25.91\ \mu\text{m}$  (top) compared with the HST image in F475W filter matched in resolution and in pixels (bottom). The red circles denote regions having reddening measured by Hurford & Fesen (1996). Square root scale in intensity is used to enhance weak features. Diffuse infrared [O IV] emission from optically-dark regions is clearly visible.

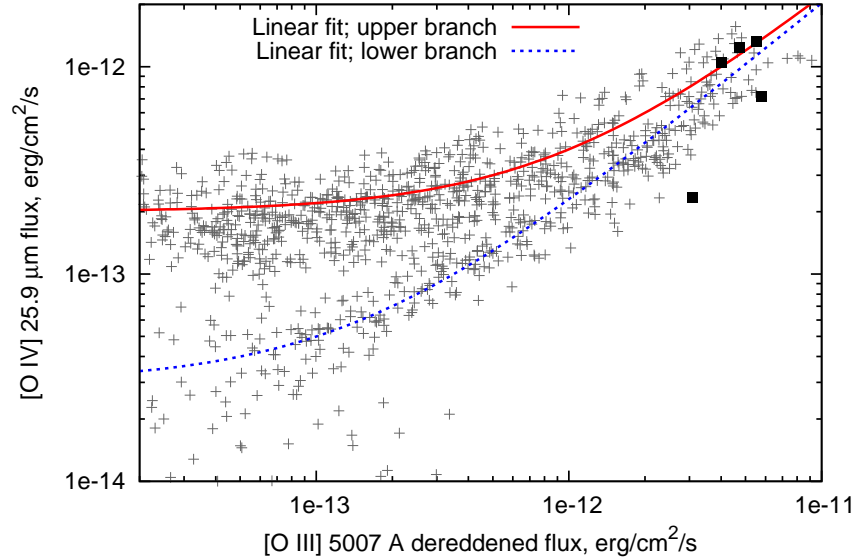


Figure 4.7: Pixel-by-pixel comparison of the dereddened 5007 Å line flux with the infrared [O IV] line map. Fluxes are given per detector pixel, equal to  $(5''.08)^2$  for the IRS LL module containing the infrared oxygen line. Two linear fits, both having the same slope of 0.20, are shown with lines. Filled squares denote FMKs from Hurford & Fesen (1996) having measured reddening.

The upper branch corresponds to the diffuse level emission in the central part of the supernova remnant. Corresponding points on the HST image are partially out of the Figure 4.7 plot range, but the infrared line surface brightness remains on the level of  $(1 - 3) \times 10^{-13}$  erg/cm<sup>2</sup>/s/pix.

This infrared-only line emission hints on the existence of extended cold photoionized regions invisible in optical and X-ray emission near the center of the supernova remnant, possibly connected with the thermal radio absorption observed in the same regions (Kassim et al., 1995; Delaney, 2004).

Note that the [O IV] infrared line at 25.91 μm overlaps with the [Fe II] line at 25.99 μm, but contribution of the latter can be estimated from the comparison with the [Fe II] 17.94 μm line map. Such estimates result in the upper limit on the 25.99 μm [Fe II] line contribution to the total flux of the observed line near 26 μm of 10 – 30% in all regions of the Cas A used for our further analysis. The energy considerations are discussed further in Section 4.3.2.3.

#### 4.3.2.2 Other infrared lines in the *Spitzer* spectral maps

Similar pixel-by-pixel comparisons with the optical image have been performed also for other bright spectral line flux maps. In Table 4.5, we give the derived the flux ratios to the optical [O III] 5007 Å line in five Hurford & Fesen (1996) FMKs and average values of these ratios in the northern part of the Cas A shell. Last digit in brackets in the “Average” column denote observed scatter around the average line flux ratio.

From the table it is seen that different line flux ratios have different scatters around their average values. Small scatter in e.g. Ar, Si and S line ratios to the 5007 Å line corresponds to the Cas A morphology in these lines similar to the optical one. Larger scatter, present in e.g. Ne and Fe line ratios to the 5007 Å line corresponds to different morphologies of the infrared spectral maps, as noted also by Rho et al. (2008).

Obtained line ratios may be further used for tests of the theoretical models and are utilized in the next Section to estimate average abundances and physical conditions in the bright Cas A knots.

From the Table 4.5 it is seen that the full energy flux in the infrared lines detected by *Spitzer* exceeds one of the brightest optical line – [O III] 5007 Å – and is of the same order as the total power in all optical lines summed up.

#### 4.3.2.3 Energetics of the infrared emission

From the analysis of the *Spitzer* archival observations it is straightforward to determine that in the wavelength range from 5 to 35  $\mu\text{m}$  the total Cas A luminosity is  $3.3 \times 10^{37}$  erg/s (the luminosity values are computed assuming a distance to Cas A of 3.4 kpc, Reed et al. (1995)). The total spectral line luminosity in the same range is found to be one order of magnitude smaller, contributing  $3.0 \times 10^{36}$  erg/s.

For the longer wavelengths between 35  $\mu\text{m}$  and 1 mm we have estimated the total Cas A luminosity from data published by Hines et al. (2004) to be about  $1.5 \times 10^{37}$  erg/s. The line contribution to this value in the narrower ISO LWS range between 40 and 200  $\mu\text{m}$  is about  $9 \times 10^{35}$  erg/s, as follows from Table 4.3. Therefore, the total Cas A dust continuum and line luminosities in the infrared range between 5  $\mu\text{m}$  and 1 mm are respectively  $4.7 \times 10^{37}$  and  $3.9 \times 10^{36}$  erg/s.

It is interesting to compare these values with the X-ray and radio luminosities. In radio, the total luminosity at wavelengths longer than 1 mm is about  $1.0 \times 10^{35}$  erg/s that is calculated directly from the spectrum provided by Baars et al. (1977) and Hines et al. (2004), i.e., much lower than in the infrared.

It is not so straightforward to determine the total Cas A luminosity in X-rays because of interstellar and internal X-ray absorption. Various estimates result in values corrected for the absorption of  $(1 - 5) \times 10^{37}$  erg/s (Hartmann et al., 1997; Zombeck, 2007), but are dependent on the assumed spectral model and absorbing material column density.

It is seen from this comparison that the the infrared continuum emission is as important radiative energy loss mechanism from the supernova remnant as the X-rays. Note, however, that the energy contained in the Cas A infrared emission was originally emitted in far-

Table 4.5: Infrared line fluxes  $I$  and their ratios  $I/I(5007 \text{ \AA})$  to the dereddened optical [O III] 5007  $\text{\AA}$  line from the *Spitzer* data. The column “Average” contains the ratio values averaged over northern part of the Cas A and their observed scatter, other columns contain data on the Hurford & Fesen (1996) FMKs.

Line	Line flux $I$ , $10^{-13} \text{ erg/cm}^2/\text{s/pixel}$					Flux ratio $I/I(5007 \text{ \AA})$					
	FMK 1	FMK 2	FMK 3	FMK 4	FMK 5	Average	FMK 1	FMK 2	FMK 3	FMK 4	FMK 5
[Ar II] 6.985 $\mu\text{m}$	3.8	14	17	5.6	11	0.5(1)	0.41	0.75	1.15	0.46	0.79
[Ar III] 8.991 $\mu\text{m}$	0.46	2.0	1.7	0.80	1.5	0.08(3)	0.05	0.13	0.12	0.07	0.12
[S IV] 10.51 $\mu\text{m}$	0.24	1.6	1.4	0.67	0.91	0.07(2)	0.025	0.11	0.10	0.06	0.07
[Ne II] 12.81 $\mu\text{m}$	0.31	0.92	0.89	1.0	0.30	0.10(8)	0.04	0.07	0.07	0.08	0.025
[Ne V] 14.32 $\mu\text{m}$	0.071	0.20	0.18	0.10	0.14	0.012(7)	0.009	0.012	0.012	0.009	0.014
[Ne III] 15.56 $\mu\text{m}$	0.29	2.2	1.2	3.0	0.47	0.05(3)	0.009	0.03	0.03	0.05	0.006
[Fe II] 17.94 $\mu\text{m}$	0.16	0.90	1.3	1.8	0.87	0.03(2)	0.005	0.015	0.03	0.04	0.013
[S III] 18.71 $\mu\text{m}$	0.82	5.0	5.2	2.5	4.2	0.08(2)	0.025	0.08	0.15	0.05	0.06
[O IV] 25.91 $\mu\text{m}$	2.3	13	11	12	7.2	0.20(5)	0.08	0.24	0.26	0.26	0.13
[S III] 33.48 $\mu\text{m}$	0.28	1.9	2.3	0.76	0.6	0.04(1)	0.011	0.05	0.06	0.015	0.015
[Si II] 34.81 $\mu\text{m}$	1.0	3.7	3.9	1.7	1.7	0.07(3)	0.04	0.10	0.11	0.03	0.04

*Notes.* The table contains data on the strongest lines only. The regions are numbered as in Hurford & Fesen (1996) with their positions shown on Figure 4.7. The “Average” column assumes single optical line reddening correction of 200 times. Note that the pixel sizes are different for the IRS LL (5''08,  $\lambda > 15 \mu\text{m}$ ) and SL (1''85,  $\lambda < 15 \mu\text{m}$ ) modules.

ultraviolet and soft X-rays and then absorbed within the emitting knot (see Figure 4.1). Therefore, the infrared luminosity gives us a model-independent lower boundary on the total cooling plasma luminosity between 10 and 200 eV or so (photons of lower energies do not ionize oxygen; photons of higher energies have lower absorption cross-sections and escape from the dense knot).

It is easy to notice that the infrared line-to-continuum emission ratio in the *Spitzer* range is variable over the supernova remnant, as indicated also by the spectra provided by Rho et al. (2008), with a typical value of 0.10. The highest values of this ratio of about 0.22 are characteristic for the central Cas A region. In these regions, the energy losses in the line emission are relatively twice higher than on average, however, still staying significantly below the losses in the infrared continuum.

## 4.4 Physical conditions and abundances in the FMKs

The measured line fluxes may be directly used to determine the ionic abundances<sup>9</sup>, if the model of the emitting region (temperature and density distribution) is known. As the models do not reproduce observations precise enough (see Table 4.1), we cannot suppose that such distribution is known for the FMKs.

Thus the line fluxes cannot be used in such a direct fashion and the inferred ionic abundances will depend on the assumed physical conditions. Fortunately, emissivities of some of the fine-structure lines are only weakly dependent on the electron densities and temperatures in rather wide range, allowing to use these lines for the abundance determination even without detailed knowledge on the line-emitting region properties.

Analysis of the measured flux ratios of the lines of the same ion is a more powerful method. Such line ratios may be used directly to constrain temperature and density of the emitting region, provided that the emitting region is uniform and physically the same for both lines comprising the ratio.

However, these assumptions are not fulfilled in the fast-moving knots for most of the line pairs and we cannot obtain emitting region parameters from, e.g., comparison of optical and infrared lines of [O III]. Even the density-sensitive ratios of two infrared lines should be interpreted carefully, as from the theoretical models it follows that their emission may be arising both in the pre-shock and post-shock regions having comparable emission measures of the order of  $10^{19} \text{ cm}^{-5}$  and temperatures of the order of  $(0.5 - 2) \times 10^4 \text{ K}$ , but densities different by a factor of thousand or more.

More specifically, the pre-shock photoionized region has low electron density (of the order of  $100 - 250 \text{ cm}^{-3}$  in the SD-200 model) and produces lines having approximately low-density limit line ratio, and the post-shock cooling region ( $n_e \approx 10^6 \text{ cm}^{-3}$ ) produces lines having high-density limit line ratio (i.e., corresponding level populations are determined by collisional processes). Therefore, instead of determining the density, some of the FIR line ratios determine contributions of high- and low-density regions to the total line emission.

---

<sup>9</sup>In this paper, by abundance we denote a ratio of number density of given ions or atoms to the number density of all oxygen ions (i.e.,  $n/n_{\text{O}}$ ).

In the following subsections we analyze the line flux ratios to infer the physical conditions and the line fluxes to estimate ionic and elemental abundances.

#### 4.4.1 Information from the same ion line flux ratios

In the infrared range probed by the *Spitzer* and the ISO observatories, there are seven line pairs that can be used for plasma diagnostics and have at least one component detected. These line pairs arise in transitions between three lowest fine structure states  $^3P_{0,1,2}$  in the ground  $p^2$  and  $p^4$  electron configurations. Out of these seven diagnostic pairs, three have both components detected ([O III], [S III] and [Ar V] lines) and four have detections of just one component ([O I], [Ne III], [Ne V] and [Ar III] lines).

Measured values of the flux ratios and the inferred physical parameters are summarized in Table 4.6.

##### 4.4.1.1 [O III] FIR line flux ratio

The measured ratios of the far-infrared [O III] lines  $I(51.81 \mu\text{m})/I(88.36 \mu\text{m})$  in different ISO spectra lie between 0.7 and 2.5 (see Table 4.3) with some indication of correlation between the line ratio and the optical line intensity (such correlation is observed also in the [S III] line ratio map constructed from the *Spitzer* data).

In the approximation of two emitting regions (pre-shock and post-shock) we use the following expression to determine the pre-shock PIR contribution to the total line  $b$  flux from the measured  $a$  and  $b$  line flux ratio  $R = I_a/I_b$  (see Appendix C for derivation):

$$f_{\text{PIR},b} \equiv \frac{I_{\text{PIR},b}}{I_{\text{tot},b}} = \frac{R_2 - R}{R_2 - R_1}, \quad (4.4)$$

where  $I_{\text{PIR},b}$  and  $I_{\text{tot},b}$  denote photoionized region and total line  $b$  fluxes, and  $R_1$  and  $R_2$  denote theoretical line ratio values in the pre- and post-shock regions.

The [O III] line ratio of 2.5 observed from the rich in optical knots ISO LWS region #2 may thus be achieved only if 85% of the 88.36  $\mu\text{m}$  line and 40% of the 51.81  $\mu\text{m}$  line are arising in the pre-shock region. Corresponding theoretical line ratios in this case are  $R_1 = 1.1$  and  $R_2 = 9.7$  (see Table 4.6).

As shown by Sutherland & Dopita (1995b), the 5007  $\text{\AA}$  line is mostly arising in the pre-shock region. Now we have determined that this is the case also for the 88.36  $\mu\text{m}$  line. This allows making one further step and using their flux ratio of  $I(88.36 \mu\text{m})/I(5007 \text{\AA}) \approx 0.10$  to estimate the pre-shock physical conditions. This line ratio is sensitive both to density and temperature and corresponds to  $n_e$  of several hundreds  $\text{cm}^{-3}$  for temperatures  $(1.0 - 1.5) \times 10^4$  K (see Table 4.6), i.e., values very similar to, but somewhat different from, ones given by the SD-200 model having  $T_e \approx 1.0 \times 10^4$  K and  $n_e \approx 200 \text{ cm}^{-3}$ . The constraint on the pre-shock region emitting these [O III] lines is shown on Figure 4.8.



Table 4.6: Information from the same ion line flux ratios measured in the FMKs. See text for details.

Spectrum	line <i>a</i>	line <i>b</i>	Flux ratio	Single region		Two regions			
				$T_e$ , K *	$n_e$ , cm <sup>-3</sup>	$R_1$	$R_2$	$f_{\text{PIR},a}$	$f_{\text{PIR},b}$
[O I]	63.19 $\mu\text{m}$	145.5 $\mu\text{m}$	> 30	< 100 200 – $1 \times 10^4$	any > $2 \times 10^5$				
[O III]	51.81 $\mu\text{m}$	88.36 $\mu\text{m}$	2.5	300 – $1.5 \times 10^4$	500 – 1000	1.1	9.7	0.40	0.85
[O III]	88.36 $\mu\text{m}$	5007 Å	0.10	$1.0 \times 10^4$ $1.5 \times 10^4$	800 200			1.0*	1.0*
[Ne III]	36.01 $\mu\text{m}$	15.56 $\mu\text{m}$	< 0.08	any	any				
[Ne V]	24.32 $\mu\text{m}$	14.32 $\mu\text{m}$	< 0.2	< $3 \times 10^4$	> $3 \times 10^4$				
[S III]	33.48 $\mu\text{m}$	18.71 $\mu\text{m}$	0.5	600 – $3 \times 10^4$	1500 – 3000	1.8	0.09	0.85	0.25
[Ar III]	21.83 $\mu\text{m}$	8.991 $\mu\text{m}$	< 0.10	any	any				
[Ar V]	7.914 $\mu\text{m}$	13.07 $\mu\text{m}$	1.6	1500 – $3 \times 10^4$	$(4 - 10) \times 10^4$	1.0	6.7	0.5	0.9
[Fe II]**	1.3209 $\mu\text{m}$	1.2946 $\mu\text{m}$	0.75	any	> $2 \times 10^5$				
[Fe II]**	1.3209 $\mu\text{m}$	17.94 $\mu\text{m}$	0.024	1700–3000** 1700–1800**	any > $1 \times 10^5$ *				

\* Assumed value

\*\* Derived value

\*\*\* The [Fe II] line flux ratios are discussed in Section 4.5.1.

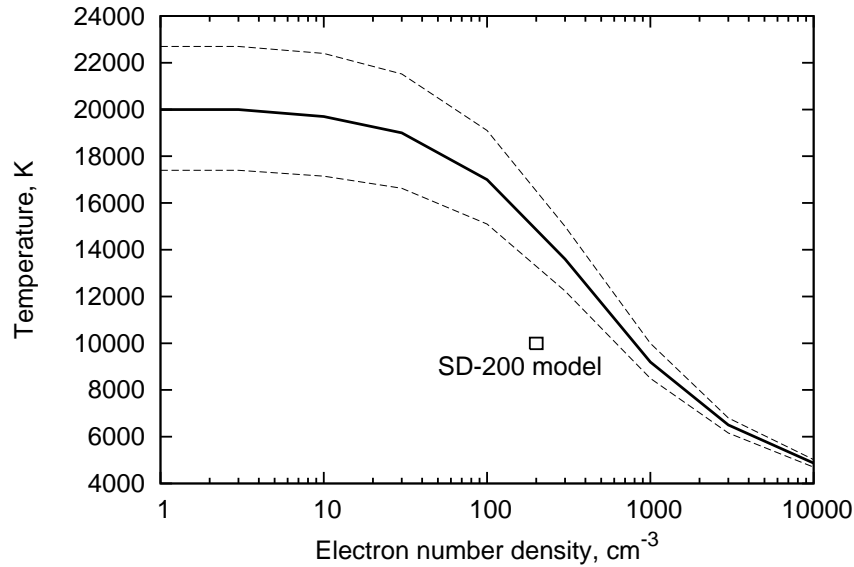


Figure 4.8: The constraints on the pre-shock region emitting the [O III] lines from the average  $I(88.36 \mu\text{m})/I(5007 \text{ \AA})$  line flux ratio (solid line). The dashed lines correspond to the constraints if the line flux ratio is changed by 20%. The square denotes the expected value based on the SD-200 model.

#### 4.4.1.2 [O I] FIR line flux ratio

It is more difficult to use the [O I] line ratio for the quantitative analysis, as only one of the lines is detected. From ISO observations of region #2 we have the  $3\sigma$  lower limit on the  $I(63.19 \mu\text{m})/I(145.5 \mu\text{m})$  line ratio of about 30.

Some information may still be obtained from this lower limit: it corresponds either to extremely low temperatures below 100 K or high electron densities above  $10^5 \text{ cm}^{-3}$  (see Table 4.6).

According to the theoretical models, there is essentially no neutral oxygen in the post-shock cooling region because of slow recombination processes. The models also predict rapid ionization of neutral oxygen in the pre-shock PIR with very low line ratio  $I(63.19 \mu\text{m})/I(5007 \text{ \AA})$  of much less than 0.01 (the observed value is 0.07, see Table 4.4). The pre-shock region as the [O I] line origin is also excluded from the observed value of the  $I(63.19 \mu\text{m})/I(145.5 \mu\text{m})$  line ratio.

From this we conclude that the far-infrared [O I] line emission in the FMKs arises in the dense photoionized region after the shock.

The very high values for this line flux ratio to the 5007 Å line in the models (see Table 4.1) do not contradict such conclusion. Instead, the reason for these differences is the model values for the pre-shock ion densities. For example, the Borkowski & Shull

(1990) models assume very low pre-shock oxygen density of  $1 \text{ cm}^{-3}$ . Taking it higher by two orders of magnitude will decrease the post-shock  $63.19 \mu\text{m}$  line intensity by a similar factor and bring the predicted intensity much closer to the results of ISO observations. The same effect will also lower the predicted  $63.19 \mu\text{m}$  line intensity in Itoh (1981a,b) model that assume a pre-shock oxygen density of  $30 \text{ cm}^{-3}$ .

#### 4.4.1.3 The [Ne III], [Ar III], [Ne V], [Ar V] and [S III] line flux ratios

All these lines are contained in the *Spitzer* data and, thanks to its much higher angular resolution, provide much more information for the analysis.

The upper limits on the [Ne III] and [Ar III] line ratios (see Table 4.6 for details on these and other line ratios) do not constrain much the plasma parameters, as both of them correspond to a wide range of densities and temperatures (Rubin et al., 2001).

Limits on the [Ne V] line ratio are also not too constraining partly because of spectral fringing near  $20 \mu\text{m}$  in the IRS spectra (Ennis et al., 2006) increasing the effective noise level. Nevertheless, the limit on the [Ne V]  $24.32 \mu\text{m}$  line infers that the [Ne V] emission is mostly or fully arising in the post-shock cooling region.

Similarly to the case of [O III], we have derived the fraction of the fine-structure line emission arising in the pre-shock region for [S III] and [Ar V] lines. It turns out that most of the [S III] line at  $33.48 \mu\text{m}$  is arising in the pre-shock region, and we will use this fact for estimation of S abundance in the Section 4.4.2.

Existence of  $\text{Ar}^{4+}$  in the pre-shock region (see Table 4.6) is understandable, given relatively low  $\text{Ar}^{3+}$  ionization potential of 60 eV, comparable to the ionization potential of  $\text{O}^{2+}$  (55 eV). Therefore similar amounts of  $\text{O}^{2+}$  and  $\text{O}^{3+}$  in the pre-shock photoionized region in the SD-200 model give a reason to deduce that  $\text{Ar}^{3+}$  and  $\text{Ar}^{4+}$  ions also have similar number densities. Note that already Chevalier & Kirshner (1979) have shown that the visible [Ar IV] lines are arising in the low-density environment, which we associate with a pre-shock PIR.

#### 4.4.2 Abundances from the flux ratios to the $5007 \text{ \AA}$ line

In general case, ionic and elemental abundances derived from the individual line intensities are strongly dependent on the theoretical model of the fast-moving knots. Such model dependence may be minimized if the spectral lines are known to be emitted in the pre-shock or the post-shock region only.

Some dependence on the underlying model still remains, but the model features used in our further analysis are relatively robust. For example, the peak of the post-shock plasma emission measure around  $10^4 \text{ K}$  is determined by the cooling rate that slows down at  $2 \times 10^4 \text{ K}$  due to closing of the dielectronic recombination channels at lower temperatures. The low-temperature limit of the line-emitting region is computed from the upper transition level excitation energy, which is a simple but reliable estimate.

The ionic abundances in the pre-shock region are stronger dependent on the underlying model, as we estimate them for all elements from average ionization potential of the oxygen

Table 4.7: Estimated FMK post-shock ionic abundances  $n_{\text{ion}}/n_{\text{O}}$ . See text for details.

Line	$I/I(5007 \text{ \AA})$	$T_e, \text{ K}$	$\varepsilon, \text{ cm}^3/\text{s}$	$\Delta t, \text{ s}$	$n_{\text{ion}}/n_{\text{O}}$	$n_{\text{ion}}/n_{\text{O}} \text{ (model)}^*$
[Si x] 1.430 $\mu\text{m}$	0.0016	$2 \times 10^4$	$2.5 \times 10^{-8}$	2000	$1.5 \times 10^{-4}$	$2 \times 10^{-4}$
[Si vi] 1.964 $\mu\text{m}$	0.004	$1 \times 10^4$	$2.0 \times 10^{-9}$	2000	0.003	0.01
[Mg v] 5.608 $\mu\text{m}$	$< 0.003$	$5 \times 10^3$	$8.0 \times 10^{-9}$	2000	$< 0.002$	0.002
[Ar v] 7.914 $\mu\text{m}$	0.005**	$1 \times 10^4$	$5.0 \times 10^{-8}$	2000	0.004	$3 \times 10^{-5}$
[Ne v] 14.32 $\mu\text{m}$	0.015	$1 \times 10^4$	$2.0 \times 10^{-9}$	3000	0.08	0.002

\* Estimated based on SD-200 model. The following elemental abundances are assumed to deduce the model ionic abundances with respect to oxygen:  $n(\text{Ne})/n(\text{O})=0.04$ ,  $n(\text{Mg})/n(\text{O})=0.01$ ,  $n(\text{Si})/n(\text{O})=0.05$ ,  $n(\text{Ar})/n(\text{O})=0.005$ . These values are inferred from X-ray and optical measurements by Chevalier & Kirshner (1979); Willingale et al. (2002); Laming & Hwang (2003); Lazendic et al. (2006).

\*\* This line is partly arising in the pre-shock region. As follows from Table 4.6, the post-shock region contribution is  $I/I(5007 \text{ \AA}) \approx 0.0025$ .

ions in the SD-200 model. Thus the pre-shock abundances may be incorrect up to a factor of several.

As follows from the theoretical models, spectral lines of singly ionized species (e.g., [Ar II], [Si II], etc.) arise mostly in the photoionized regions, whereas ones of highly-ionized species (e.g., [Ne V], [Mg V], etc.) arise mostly in the post-shock cooling regions. The only exception is the [Ar V], but the pre-shock region contribution to its lines have been already estimated above.

Below we discuss these two line groups separately and summarize the results in Tables 4.7 and 4.8.

#### 4.4.2.1 High-ionization ionic species from the post-shock cooling region

An easy estimate of the plasma composition may be done if the problem is simplified by assumption of emission arising in a single layer with given temperature and electron density. In this case one can estimate relative number densities of two types of ions from their line fluxes. The line flux ratio is then expressed from Eq. (4.2) as

$$\frac{I_1}{I_2} = \frac{\nu_1 \varepsilon_1 n_{\text{ion},1} \Delta t_1}{\nu_2 \varepsilon_2 n_{\text{ion},2} \Delta t_2}, \quad (4.5)$$

where  $n_{\text{ion}}$  is ionic number density,  $\Delta t$  is the line emission duration in the post-shock cooling plasma element, and it is assumed that the electron densities are the same for regions emitting both lines (as it is the case in the SD-200 model). The line emissivities entering Eq. (4.5) are computed as described in Section 4.2.2.

Equation (4.5) may be inverted to express relative ionic abundances via the observed line ratios. In it, we always take the second line in the ratio to be the [O III] 5007  $\text{\AA}$  line.

Table 4.8: Estimated FMK pre-shock ionic abundances  $n_{\text{ion}}/n_{\text{O}}$  computed assuming that the lines are arising only in the pre-shock PIR. See text for details.

Line	$I/I(5007 \text{ \AA})$	$T_{\text{e}}, \text{ K}$	$n_{\text{e}}, \text{ cm}^{-3}$	$\varepsilon, \text{ cm}^3/\text{s}$	IP, eV	$\Delta t, \text{ s}$	$n_{\text{ion}}/n(\text{O})$	$n_{\text{element}}/n(\text{O})^{**}$
[Ar II] 6.985 $\mu\text{m}$	0.5	$2.0 \times 10^4$	100	$4 \times 10^{-8}$	27.6	$5 \times 10^6$	1.0*	0.005
[Ar V] 13.07 $\mu\text{m}$	0.003	7000	250	$8 \times 10^{-7}$	75.1	$5 \times 10^7$	$8 \times 10^{-5}$	0.005
[Ne II] 12.81 $\mu\text{m}$	0.10	$1.5 \times 10^4$	150	$5 \times 10^{-8}$	41.0	$1.4 \times 10^7$	0.06	0.04
[Fe II] 17.94 $\mu\text{m}$	0.03	$2.0 \times 10^4$	50	$1.1 \times 10^{-8}$	16.2	$9 \times 10^5$	5.5*	0.01
[S III] 33.48 $\mu\text{m}$	0.04	$1.5 \times 10^4$	150	$3.0 \times 10^{-7}$	34.8	$1 \times 10^7$	0.015	0.04
[Si II] 34.81 $\mu\text{m}$	0.07	$2.0 \times 10^4$	50	$1.5 \times 10^{-7}$	16.4	$1 \times 10^6$	0.7*	0.05
[O III] 88.36 $\mu\text{m}$	0.10	$1.0 \times 10^4$	200	$4.0 \times 10^{-8}$	54.9	$3 \times 10^7$	1.1	1.0

\* Shown to arises mostly in the post-shock photoionized region; see Section 4.5.2.

\*\* Atomic number densities with respect to oxygen from X-ray and optical measurements by Chevalier & Kirshner (1979); Willingale et al. (2002); Laming & Hwang (2003); Lazendic et al. (2006).

In the following, we use the SD-200 model with the post-shock  $O^{2+}$  abundance in the line emitting region of  $n(O^{2+})/n(O) \approx 1\%$ . We account also for the fact that only about 2% of the total 5007 Å line emission is arising in the post-shock plasma according to the SD-200 model. This fraction is uncertain up to a factor of about two, thus introducing a systematic error of similar magnitude in all post-shock ionic abundance determinations.

There are no published results concerning theoretically predicted abundances of ions other than oxygen in the post-shock cooling region of the FMKs. To estimate them, we have utilized the electron and ion densities and the cooling function from the Sutherland & Dopita (1995b) and traced the ion ionization and recombination processes in the post-shock cooling phase using atomic data compiled by Dima Verner<sup>10</sup> for the Cloudy code (Ferland et al., 1998).

Another source of uncertainty in the ionic abundance determination using our method are the model-dependent values of  $\Delta t$ , which were also computed by tracking the plasma cooling and recombination. However, calculations show that for different ions and lines the  $\Delta t$  values differ by no more than approximately a factor of two, that is determined by the general emission measure behavior.

Resulting model abundances are compared with the observational results in Table 4.7. It is seen that the abundances inferred from the SD-200 model seem to be generally consistent with the results of observations, showing that the model in general correctly represents the temperature and density evolution in the post-shock cooling region. The [Ar v] and [Ne v] lines are the only ones showing significant differences with respect to the model expectations, although the derived ionic abundances do not exceed significantly the corresponding elemental abundances.

Note that the two highest ionization fine-structure lines of [Si x] and [Si vi] observed from the fast-moving knots have not been observed by *Spitzer*, but detected in the near-infrared spectra by Gerardy & Fesen (2001). We have determined their line flux ratios to the [O iii] 5007 Å line using reddening measurements from the same regions by Hurford & Fesen (1996).

#### 4.4.2.2 Low-ionization ionic species from the pre-shock PIR

The post-shock plasma recombination is so much slower than the cooling, that even at  $T_e \approx 300$  K the post-shock cooling plasma still mostly contains multiply-charged ions, resulting in essentially no infrared line emission from singly ionized atoms at wavelengths shorter than several tens of  $\mu\text{m}$ .

In this Section, we neglect any contribution to the line fluxes from the post-shock *photoionized* region. Its possible existence and physical conditions are discussed in Section 4.5.2.

Then we can write Eq. (4.2) in the form similar to Eq. (4.5) for the pre-shock region:

$$\frac{I_1}{I_2} = \frac{\nu_1 \varepsilon_1 n_{e,1} n_{\text{ion},1} \Delta t_1}{\nu_2 \varepsilon_2 n_{e,2} n_{\text{ion},2} \Delta t_2}. \quad (4.6)$$

---

<sup>10</sup><http://www.pa.uky.edu/~verner/atom.html>

The equation contains also the electron density ratio, as the ions having different ionization potentials exist in regions having different electron densities.

In contrast to the post-shock case, where the emission measure behavior determined approximate equality of the line emission times  $\Delta t$ , here the timescales are determined by the ionization rates and may vary by an order of magnitude or more from ion to ion.

From the SD-200 model we adopt the average ionization potential (IP) as a function of time and compute ionization state distribution for all elements with the simple approximation that this average IP is equal for all of them. We also take the temperature profile from the model, that has some effect on the resulting emissivities. Fortunately, exact temperature values have only minor effect on the obtained abundances, as the infrared line emissivities depend weakly on  $T_e$  above  $10^3$  K or so.

In the pre-shock ionization front of the SD-200 model, each initially neutral atom is consequently ionized with maximum ionic abundance of each ion of the order of 50-100%. Therefore the ionic abundances obtained in Table 4.8 should be quite close to the elemental abundances, provided that the  $\Delta t$  values are estimated correctly and the pre-shock PIR is giving the major contribution to the line intensity<sup>11</sup>.

As a test case, we have also included in the Table 4.8 the similarly computed  $O^{2+}$  abundance from the [O III] 88.36  $\mu m$  line. The result is very close to the expected value of one (in fact, too close, given our uncertainties of about a factor of two), showing reliability of our method.

Although there are several [Fe II] spectral lines in the infrared spectral range probed by *Spitzer* that originate in the low-lying electronic configurations, the two most promising are blended with other stronger lines (one at 25.99  $\mu m$  is blended with [O IV] line at 25.91  $\mu m$  and one at 35.35  $\mu m$  is blended with [Si II] line at 34.81  $\mu m$ ). Therefore in the *Spitzer* wavelength range we have used for our analysis only the [Fe II] line at 17.94  $\mu m$  (see Figure 4.9 for the energy levels of  $Fe^+$  corresponding to these transitions).

From Table 4.8 it is seen that the  $Ar^+$ ,  $Si^+$  and  $Fe^+$  abundances estimated assuming that their fine-structure lines arise exclusively in the pre-shock region are much higher than the corresponding elemental abundance values obtained from optical and X-ray data (Chevalier & Kirshner, 1979; Willingale et al., 2002). The possible solutions of this discrepancy are discussed in Section 4.5.1.

## 4.5 Discussion

### 4.5.1 On too high pre-shock intensities of some lines

Abundances of Ne and S derived assuming that the fine-structure lines of [Ne II] and [S III] are emitted in the pre-shock photoionized region of SD-200 model agree very well with

---

<sup>11</sup>Abundance of  $Ar^{4+}$  estimated from [Ar V] lines is much lower than the Ar elemental abundance, presumably because only some fraction of Ar atoms is ionized as far as  $Ar^{4+}$  in the pre-shock region.

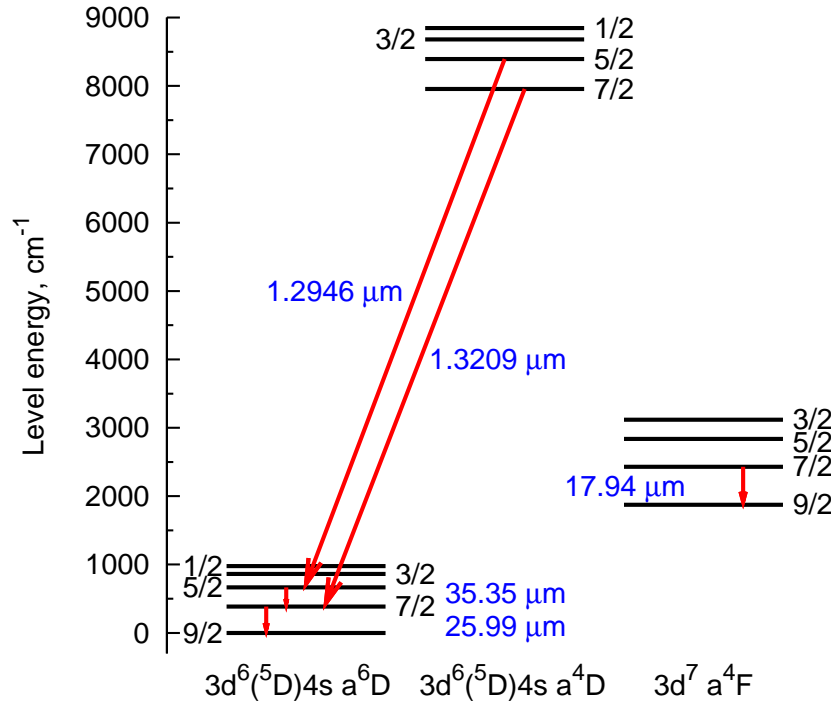


Figure 4.9: Energy diagram of the lowest levels of Fe<sup>+</sup> ion with transitions used in our analysis and corresponding line wavelengths. The electron configurations are given below the diagram; numbers besides the levels denote total angular momentum  $J$ . Data from Ralchenko et al. (2007).

the results of the optical and X-ray observations. Simultaneously, similarly derived abundances of other singly-charged ions (Si<sup>+</sup>, Ar<sup>+</sup>, Fe<sup>+</sup>) are unreasonably high. They are even much higher than the respective elemental abundances obtained both from analysis of optical and X-ray spectra (Chevalier & Kirshner, 1978, 1979; Willingale et al., 2002; Laming & Hwang, 2003; Lazendic et al., 2006).

Within the frame of the SD-200 model, it is difficult to interpret these results and at the same time to comment on absence of other bright infrared lines, such as [Fe III] line at 22.93 μm and many others.

There are several possible solutions of this mismatch between the model predictions and observations.

- The inconsistency might result from the application of the SD-200 model, describing the plasma dominated by C, O, Ne and Mg, to the plasma, containing considerable amounts of S, Si and Ar. However, total abundance of these elements with respect to oxygen reaches only 10-20% that should not significantly alter the shock structure.



- Most of fluxes in the Si and Fe infrared lines might originate in physically separated Fe-dominated clouds. This hypothesis is based on two observations:
  - (a) Cas A in the [Fe II] line have different morphology than in the [O IV] line (Ennis et al., 2006; Rho et al., 2008); and
  - (b) X-ray Chandra observations indicate that hot Si- and Fe-dominated blobs exist in Cas A.

However, the Cas A morphology in the Fe  $K\alpha$  X-ray line is also strongly different from morphology in the [Fe II] 17.94  $\mu\text{m}$  line weakening these arguments. This hypothesis could be tested by observations of the Cas A ejecta with higher spectral resolution, that would allow to determine if the [Fe II] and other infrared lines from the same knots have the same peculiar velocities.

- The [Si II], [Ar II] and [Fe II] lines might originate in separate weakly-ionized photoionized region having high emission measure. It might be situated either before the shock wave (the “far precursor” region of Itoh (1981a,b)) or after it (the post-shock PIR present in models of Itoh (1981a,b) and Borkowski & Shull (1990)). This hypothesis is further discussed below.

It is easy to distinguish between lines emitted by the pre-shock and post-shock PIRs due to their strongly different electron densities, if we use additional constraints on this line-emitting region that can be obtained from the Gerardy & Fesen (2001) observations of the near-infrared [Fe II] lines (see Table 4.6).

The [Fe II] line ratio  $I(1.3209 \mu\text{m})/I(1.2946 \mu\text{m}) < 1$  indicates strongly the electron density being above  $10^5 \text{ cm}^{-3}$  at any temperature, thus weakening the hypothesis of the “far precursor”. In case of lower densities this ratio is always higher, reaching values of 10 – 20 in the low-density limit because of strong difference in the excitation rates of the respective transition upper levels (Ramsbottom et al. (2007), see Figure 4.9 for the transition diagram between the  $\text{Fe}^+$  relevant levels).

Another problem for the pre-shock “far precursor” hypothesis is the observed line ratio of the [Si II] 34.81  $\mu\text{m}$  and [Fe II] 17.94  $\mu\text{m}$  lines of about 2. Both neutral and singly ionized Si and Fe atoms have similar ionization potentials, therefore we might expect that their ionization fractions are similar. Knowing the line emissivities for the low-density pre-shock PIR conditions and average abundance ratio of  $n(\text{Si})/n(\text{Fe}) \approx 5$  (Willingale et al., 2002; Laming & Hwang, 2003) the expected line ratio is as high as 50. We therefore conclude that the PIR contributing to the emission in these lines is likely to extend *after* the shock wave.

### 4.5.2 Post-shock photoionized region

Let us now estimate the properties of this post-shock PIR. It should not affect the optical lines of the [O II] and [Fe II]. This sets an upper limit on this region temperature of  $(5 - 10) \times 10^3 \text{ K}$ . The lower limit on the temperature of about 1000 K is obtained from the requirement that the 25.99  $\mu\text{m}$  [Fe II] emitted by this region should not be too bright (an observational constraint is  $I(25.99 \mu\text{m})/I(17.94 \mu\text{m}) < 2$ ).

The very low value of the near-infrared [Fe II] 1.3209  $\mu\text{m}$  line ratio to the 17.94  $\mu\text{m}$  line corresponds to  $T_e \approx 1700$  K in the high-density limit. However, this ratio is very sensitive to the temperature because of different excitation potentials of the transitions upper levels, so it possibly shows only the upper limit on the temperature with the near-infrared line partially arising in some smaller and slightly hotter region.

The average ionization potential should be below 20 eV, otherwise the [Ne II] infrared line would be enhanced with respect to the pre-shock PIR contribution, but above 8 eV, otherwise the [Fe II] and [Si II] lines would not be enhanced. The average IP is probably lower than 15 eV, as the Ar should be only weakly ionized to reproduce the observed [Ar II] line flux (see below). From these stringent limits it follows that silicon, sulphur and iron should be mostly singly ionized, whereas oxygen and argon are ionized only partially.

Assuming the PIR temperature of 1500 K deduced from the [Fe II] line ratio, we can obtain the electron density estimates also from the limit on the FIR [O I] line ratio, assuming that these lines also originate in the same region (see Section 4.4.1.2).

As in the case of [Fe II] lines, the line ratio corresponds to  $n_e \gtrsim 5 \times 10^5 \text{ cm}^{-3}$ . We assume this value for the electron density and twice larger value  $n_t = 1 \times 10^6 \text{ cm}^{-3}$  for the total ion density (note that in the assumption of constant post-shock pressure this corresponds to a pre-shock total ion number density of about one hundred atoms per  $\text{cm}^3$ ).

Knowing plasma temperature and density, as well as the line fluxes, it is straightforward to estimate the extent of the PIR. To reproduce the [Si II] line intensity with Si elemental abundance of 5% (Laming & Hwang, 2003; Lazendic et al., 2006) and  $\text{Si}^+$  ionic fraction of  $n(\text{Si}^+)/n(\text{Si}) = 50\%$  the post-shock PIR should be  $8 \times 10^9 \text{ cm}$  thick. This corresponds to an oxygen column density of about  $8 \times 10^{15} \text{ cm}^{-2}$  that is one order of magnitude below the value obtained by Borkowski & Shull (1990) in their models.

In the post-shock region the [Si II] 34.81  $\mu\text{m}$  line emissivity is strongly damped due to collisional deexcitation. This allows to obtain similar values for the post-shock PIR thickness from all three remaining lines thought to be arising in it: the [Fe II] 17.94  $\mu\text{m}$ , [Ar II] 6.985  $\mu\text{m}$  and [O I] 63.19  $\mu\text{m}$ , if we take the ionic fractions of 50% for  $\text{Fe}^+$  and  $\text{O}^0$  and 20% for  $\text{Ar}^+$ .

The difference between observationally derived and theoretically predicted thicknesses of the post-shock PIR may arise due to different temperature and ionization structure, as the Borkowski & Shull (1990) models describe pure oxygen plasma. For example, if the temperature falls below 100 K, emissivities of all fine-structure lines are strongly diminished. Though, in this case bright metal recombination lines are formed (Docenko & Sunyaev, 2008) that are at least one order of magnitude brighter than current observational limits of optical observations of Cas A.

Another possibility is a hydrodynamical disruption of the post-shock region, like one proposed by Itoh (1986), resulting in 90% of the ionizing radiation either going through or around the post-shock region. Such disruption have been observed both in numerical simulation of the shock wave interaction with the dense interstellar clouds in supernova remnants (Patnaude & Fesen, 2005) and in the laser experiments emulating such interaction (Klein et al., 2003).

In the next subsection we consider if the presence of the dust may influence the conditions in the post-shock PIR hiding somehow its larger extent.

### 4.5.3 Effects of the dust on the post-shock PIR structure

Using the data from Rho et al. (2008) it is straightforward to estimate the dust mass in each pixel of the *Spitzer* map of the Cas A. Its comparison with the optical image of this supernova remnant allows to determine the dust-to-gas mass ratio in the bright knots using the [O III] line flux predicted by the SD-200 model.

If the emitting dust with temperature  $T_d \approx 100$  K (Rho et al., 2008) is distributed over all volume of the knot, then the dust-to-gas mass ratio is of the order of 2-5%. If, on the other hand, the dust is emitting only in the line-emitting regions, then this mass ratio is of the order of unity. In this case, which will be discussed further, the dust may noticeably influence the physical conditions in the post-shock region.

The dust is highly efficient energy sink decreasing the medium temperature. From the *Spitzer* spectra it is easy to estimate that the flux in the dust continuum is ten times higher than in the infrared lines (see Section 4.3.2.3). This may be the reason why the post-shock PIR temperature inferred from the infrared spectra is approximately twice less than the values predicted by Itoh (1981a,b) and Borkowski & Shull (1990) models.

At lower temperatures the recombination is occurring faster, resulting in shorter extent of the photoionized region and lower ionization degrees. Presence of the dust grains is also known to assist the recombination. If the ion fractions are lower by an order of magnitude than assumed above (e.g., 5% instead of 50%), then the observed size of the post-shock PIR may be reconciled with the Borkowski & Shull (1990) model predictions.

Therefore presence of large amounts of dust will diminish the post-shock PIR optical and infrared line fluxes. However, one would need to perform a more detailed analysis to understand if the quantitative agreement with the observed line-to-continuum flux ratio may be achieved without assumption of the post-shock region disruption, that was initially suggested by Itoh (1986) to explain low intensities of the neutral oxygen optical lines. Such an analysis is outside the scope of this paper.

### 4.5.4 Comparison of the model predictions with observations

As the models provide predictions only of the oxygen line relative intensities, we cannot use observations of lines of other ions for a direct comparison with the models.

Comparing observed far-infrared line ratios with theoretical model results (see Table 4.1), we see that the Itoh (1981a,b) models underestimate the [O III] and [O IV] line fluxes by factors of 3–40, as a result of having much lower average ionization degree after the shock wave passage than in other models. In contrast, Borkowski & Shull (1990) model BS-F and Sutherland & Dopita (1995b) model SD-200 that do not account for the electron conductivity are overpredicting emission in the [O IV] line by factors of 20 – 40.

The remaining model (BS-DC of Borkowski & Shull (1990)) predicts the infrared line fluxes to within a factor of several, except for the neutral oxygen lines, but this problem

is at least partially resolved by increasing the pre-shock density (see Section 4.4.1.2). This strongly suggests that taking into account the electron conductivity is essential for a model to reproduce the observations.

The [O III] far-infrared line ratio  $I(51.81 \mu\text{m})/I(88.36 \mu\text{m})$  in the Borkowski & Shull (1990) models is significantly higher than observed (6 vs. 2.5). This discrepancy arises as they do not include emission from the pre-shock photoionized region. In the SD-200 model, in contrast, the pre-shock region dominates the [O III] infrared line emission and diminishes this infrared line flux ratio to 1.2. Therefore to reproduce the observed line ratio the pre-shock and post-shock contributions should be comparable (see also Table 4.6).

The model I-H is the best in description of the neutral oxygen FIR line ratio. In this model, most of the [O I] emission is arising in the post-shock PIR. The line ratio corresponds to the high-density limit, but the predicted line intensities are about 20 times stronger than observed. As mentioned in Section 4.4.1.2, this discrepancy may be reduced if we assume higher pre-shock atom number density than in the model (for example,  $300 \text{ cm}^{-3}$  instead of  $30 \text{ cm}^{-3}$ ), as in this case the line emissivities will decrease, whereas the ionization parameter and the column density of the PIR will stay the same.

#### 4.5.5 Recombination lines in the infrared range

The metal recombination lines (RLs) are another good tracer of the cold ionized plasma. Their emissivities as functions of temperature have no exponential cutoff at low  $T_e$ 's and increase with decreasing temperature approximately as  $T_e^{-1}$  at  $T_e < 10^4 \text{ K}$ . The line emissivities are only weakly dependent on density.

However, their emissivities are 4 – 6 orders of magnitude less than those of the fine-structure infrared lines in the low-density limit. The infrared RL emissivity ratios to the fine-structure lines increase with electron density due to collisional effects diminishing the fine-structure line emissivities as  $n_e^{-1}$  starting from some critical density. At post-shock electron densities of  $10^6 \text{ cm}^{-3}$  the emissivity ratios are much higher (Docenko & Sunyaev, 2008), but the infrared RLs are nevertheless still much less intense than the fine-structure lines.

As two examples, let us consider infrared RLs near 10 and 60  $\mu\text{m}$ . The brightest regions emitting RLs are the post-shock cooling and photoionized regions (due to their high emission measures  $n_e^2 l$ ) and cold region between the photoionization front and the shock wave (due to its extremely low temperature and large extent).

Let us discuss the O I  $5\alpha$  recombination line at 7.45  $\mu\text{m}$ . It is mostly arising in the post-shock photoionized region and its strongest component emissivity of  $2 \times 10^{-14} \text{ cm}^3/\text{s}$  is about  $5 \times 10^5$  times less than that of the [Ar II] 6.985  $\mu\text{m}$  line. Accounting for the fact that  $\text{O}^+$  is expected to be approximately 500 times more abundant than  $\text{Ar}^+$ , the expected recombination line flux is 1000 times less than that of the 6.985  $\mu\text{m}$  line, or about 10% of the background continuum emission. Estimates show that this limit is achievable with *Spitzer* with exposure of about one hour.

Another example is a O I  $11\alpha$  RL at 69.03  $\mu\text{m}$ . Its emissivity and expected intensity is approximately 5000 times less than that of [O I] fine-structure line at 63.19  $\mu\text{m}$ , or about

$5 \times 10^{-15}$  erg/cm<sup>2</sup>/s from the ISO region #2. This is approximately equal to the expected  $5\sigma$  1-hour point source sensitivity of Herschel PACS instrument (Poglitsch et al., 2006). As the Cas A is not a point source in Herschel resolution (PACS has a 10'' pixel size and most of the emission will be contained in 4-8 PACS pixels), one will need at least few hours to achieve the  $5\sigma$  detection of this recombination line.

The recombination lines of highly-charged oxygen ions from the post-shock cooling region are expected to be about an order of magnitude dimmer than the O I RLs due to lower emission measure in the region emitting these lines.

The metal recombination line observations in the mid- and far-infrared are generally more difficult than in the optical and near-infrared due to lower line emissivities and higher background continuum emission. They are also not able to provide the information about the ion producing the spectral line, but only its electronic charge. However, such observations would allow to determine abundances of ions residing in cold regions and not producing fine-structure lines. Special emphasis should be put on the singly-charged ion lines, as their recombination lines in the optical and near-infrared ranges are split into many weak components, making them more difficult to detect (Docenko & Sunyaev, 2008).

## 4.6 Conclusions

We have performed a comparison of the supernova remnant Cas A fast-moving knot infrared line intensities with the predictions of various theoretical models, that describe the FMK emission as arising in the reverse shock wave interaction with the pure-oxygen or oxygen-dominated clouds. For this comparison we have analyzed archival observational data from ISO and *Spitzer* observatories. We conclude that accounting for the electron conductivity is essential to reproduce the observed line ratios. This is the reason why the Borkowski & Shull (1990) model BS-DC provides the best description of the observed oxygen line relative fluxes, although it is only precise up to a factor of several (the [O I] lines are overpredicted because of too low pre-shock density).

This emphasizes the need for better models describing shock propagation in the oxygen-dominated plasma. In this article, many line flux ratios are derived that will help to construct such future theoretical models. Future far-infrared observations with higher sensitivity and angular resolutions will allow to obtain much more information on the fast-moving knots once the models are constructed. The infrared metal recombination lines are shown to be detectable by the planned far-infrared instruments and useful for derivation of the plasma properties.

Analysis of the infrared lines of O, Ne, Si, S, Ar and Fe ions have confirmed existence of three regions contributing to the infrared and optical line emission:

- Lines of the intermediate- and highly-charged ions arise in the post-shock rapidly cooling region (e.g., [Ne V], [Ar V], [Si VI], [Si X] lines).
- Singly-charged ions with ionization potential of the neutral species below 10 – 15 eV radiate mostly from the post-shock photo-ionized region (e.g., [O I], [Si II], [Ar II],

[Fe II] lines).

- Weakly- and intermediate-charged ion lines arise in the pre-shock photoionized region as well. It gives major contribution to the emission of lines of [Ne II], [O III], [S III], [Ar V], etc.

From the observed line flux ratios it follows that the post-shock photoionized region has temperature  $T_e \approx 1500$  K, electron and ions densities  $n_e \approx 5 \times 10^5$  cm<sup>-3</sup> and  $n_t \approx 1 \times 10^6$  cm<sup>-3</sup> and is approximately  $1 \times 10^{10}$  cm thick, assuming that Si, Ar and Fe atoms are approximately 20%-50% ionized. This is about 10 times less than the thickness predicted in the Borkowski & Shull (1990) model.

From the detailed comparison of observed infrared line intensities with the theoretically expected values, we conclude that

- The theoretical models correctly describe the general structure of the FMKs;
- Accounting for the electron conductivity brings the BS-DC model much closer to the observed oxygen FIR line ratios to the [O III] 5007 Å line than the BS-F and SD-200 models;
- Accounting for the emission from the photoionized region before the shock front is essential to reproduce the FIR [O III] line ratio;
- The FIR [O I] line intensities in the Itoh (1981b) and Borkowski & Shull (1990) models are overestimated due to too low pre-shock atom number densities;
- The pre-shock atom number density is at least 100 cm<sup>-3</sup> and may be as high as 300 cm<sup>-3</sup>;
- The post-shock photoionized region truncation, like suggested by Itoh (1986), may be needed to explain apparent thickness of the post-shock PIR being only 10% of the value predicted by the models, but effects of the dust may also be important in resolving this discrepancy.

## Acknowledgements

DD is thankful to Mike Revnivtsev for many useful advices on data processing.

The version of the ISO data presented in this paper correspond to the Highly Processed Data Product (HPDP) set called 'Uniformly processed LWS L01 spectra' by C. Lloyd, M. Lerate and T. Grundy, available for public use in the ISO Data Archive, <http://www.iso.vilspa.esa.es/ida/>.

Some of the data presented in this paper were obtained from the Multimission Archive at the Space Telescope Science Institute (MAST). They are based on observations made with the NASA/ESA Hubble Space Telescope, obtained from the Data Archive at the Space Telescope Science Institute, which is operated by the Association of Universities for

---

Research in Astronomy, Inc., under NASA contract NAS 5-26555. These observations are associated with program # 10286.

Part of this work is based on observations made with the *Spitzer* Space Telescope, which is operated by the Jet Propulsion Laboratory, California Institute of Technology under a contract with NASA. This research made use of Tiny Tim/Spitzer, developed by John Krist for the Spitzer Science Center. The Center is managed by the California Institute of Technology under a contract with NASA.

CHIANTI is a collaborative project involving the NRL (USA), RAL (UK), MSSL (UK), the Universities of Florence (Italy) and Cambridge (UK), and George Mason University (USA).





# Chapter 5

## Conclusions

In consistence with the goals and tasks of the present work, several new methods for studies of the highly-charged astrophysical plasma were developed and tested for their feasibility for studies of various types of astrophysical objects.

- We have performed the first detailed quantitative studies of expected hyperfine structure line signals from several types of astrophysical objects, such as hot intracluster medium, hot interstellar medium, old supernova remnants and the warm-hot intergalactic medium.

Results of our analysis extend and confirm the earlier theoretical findings and show that the  $[^{14}\text{N VII}]$  HFS line is a feasible probe of several types of  $T \approx 10^6$  K astrophysical plasmas, including the warm-hot intergalactic medium, with the existing radio telescopes. We also present quantitative results on other hyperfine structure line expected signal strengths from the astrophysical plasmas having temperatures from  $10^5$  to  $10^7$  K.

- We have developed a new method to compute precise wavelengths and emissivities of the metal optical recombination lines by explicitly tracing the processes of radiative and dielectronic recombination, radiative cascade and collisional  $l$ -redistribution. This method is universal and readily applicable to any metal ion for  $n > 4$ .

Results of our studies have shown for the first time that these lines are a feasible and rich source of information on the physical conditions in the enriched plasma of the fast-moving knots in the Cassiopeia A supernova remnant using modern ground-based telescopes in optical and near-infrared ranges.

- A detailed analysis of the archival infrared spectra of the Cassiopeia A has allowed us to considerably extend the knowledge of physical conditions in the shock-wave-induced structure formed in a metal-dominated cloud of supernova ejecta. Significant number of diagnostic lines ratios in infrared band resulted in new observational constraints essential for construction of future theoretical models of the fast-moving knots.

From our analysis we have concluded that while the existing theoretical models qualitatively correctly represent the structure of the FMKs induced by the shock passage, there are significant quantitative differences. We also provide the fine structure line intensities constraining the construction of the future theoretical models and deduce for the first time the observation-based properties of the post-shock photoionized region.

### Concluding remarks

- Our work has demonstrated strong potential of several spectral line types that have not been widely used for the astrophysical plasma diagnostics. It may be therefore a good basis for future targeted observations resulting in much better understanding of the nature of the Cassiopeia A ejecta, the intergalactic space shocks and other objects.
- Increased computing capabilities made possible a detailed tracing of the atomic processes without assumption of the equilibrium population. This allowed us to obtain reliable predictions for the optical recombination line emissivities.
- Several more implementations seem to be promising, for example, the theoretical studies of the metal radio recombination lines from the Cas A ejecta and other astrophysical objects. The work in these directions is in progress.

# Appendix A

## Atomic physics for level population computations

### A.1 Determination of the upper cutoff $n_{\max}$

Traditionally, the highly-excited level populations are characterized by the so-called departure coefficients  $b_{nl}$ , defined as the ratio of the actual level population  $N_{nl}$  to its thermodynamic equilibrium value  $N_{nl}^*$ . With  $n$  increasing, at levels  $n > n_1$  the collisional  $l$ -redistribution processes establish an equilibrium population over  $ls$ , i.e.,  $b_n = b_{nl}$ . The value of  $n_1$  depends on the ion, as well as on the electron temperature and number density.

For higher  $ns$ , rates of collisional transitions involving changing  $n$  start rapidly increasing and from some  $n > n_2$  determine the highly-excited level populations. Thus the  $b_n$  curve, itself defined only at  $n > n_1$ , has two distinct ranges as a function of  $n$ : below  $n = n_2$  it is determined by recombination and radiative processes and above it rapidly tends to unity because of the processes relating different  $n$  level populations with each other and with the continuum: collisional  $n$ -redistribution, three-body recombination and collisional ionization. As an example,  $b_{ns}$  of Li-like ion  $O^{5+}$  at temperatures 1000 and 20 000 K and electron density  $50\,000\text{ cm}^{-3}$  are shown in Figure A.1, assuming  $b_n = b_{nl}$ .

In this figure, we also show the departure coefficients, computed accounting only for radiative  $n \rightarrow n'$  transitions. Such an approximation results in population computation errors at levels higher than about  $n_2$ .

Let us now show that the electrons that recombined to levels  $n > n_2$  are contributing relatively weakly to the total recombination and it is safe to introduce an upper cutoff  $n_{\max}$ , neglecting the population of higher levels. Two cases –  $b_{n_2} > 1$  and  $b_{n_2} < 1$  – are discussed separately here.

In the case of  $b_{n_2} > 1$ , not introducing such a cutoff and neglecting  $n \rightarrow n'$  collisions may result in a significant overestimation of the recombination rate – up to a factor of several. The easiest estimate of the cutoff position is the level where the total recombination rate into  $n < n_{\max}$  computed without accounting for  $n \rightarrow n'$  transitions equals the true total recombination rate. It is easy to understand that in this case  $n_{\max} \approx n_2$ , as illustrated in

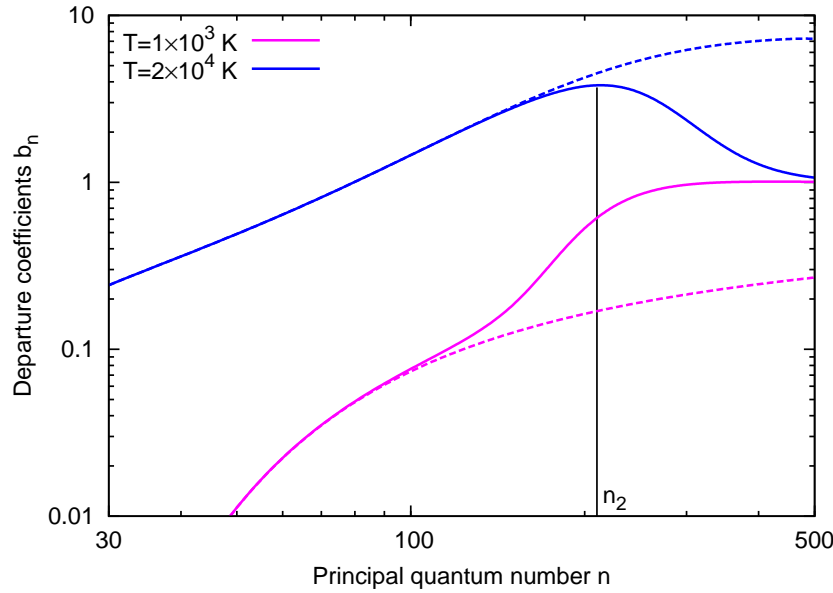


Figure A.1: Departure coefficients  $b_n$  of recombining  $\text{O}^{5+}$  ions computed accounting for all processes (solid lines) and neglecting collisional  $n$ -redistribution, three-body recombination and collisional ionization (dashed lines) at electron temperatures  $T_e = 1 \times 10^3$  K and  $2 \times 10^4$  K and density  $n_e = 5 \times 10^4 \text{ cm}^{-3}$ . At higher temperature dielectronic recombination dominates and significantly increases the level populations.

the lower panel of Figure A.2.

In the case of  $b_{n_2} < 1$  the rates obtained neglecting collisional transitions between high levels will always underestimate the true recombination rates. However, for temperatures above about  $10^3$  K taking the upper cutoff value approximately equal to  $n_2$  does not result in an error of more than about 20% for the relevant ions, as illustrated in the upper panel of Figure A.2. Lower cutoff values will result in more significant underestimates of the total recombination rate and the line emissivities.

In the case of lower densities, when  $n_2$  is very high, another natural limit  $n_{\text{max}} \approx (100 - 200)$  arises from the general dependence of the DR rate on the principal quantum number, see, e.g., Sobelman et al. (1981).

## A.2 Radiative recombination

There are two major recombination processes populating high- $n$  states in low-density plasmas: radiative and dielectronic recombination (RR and DR, respectively). In the radiative recombination process, a free electron directly recombines to a bound state ( $nl$ ). A photon is simultaneously emitted, carrying away the released energy.

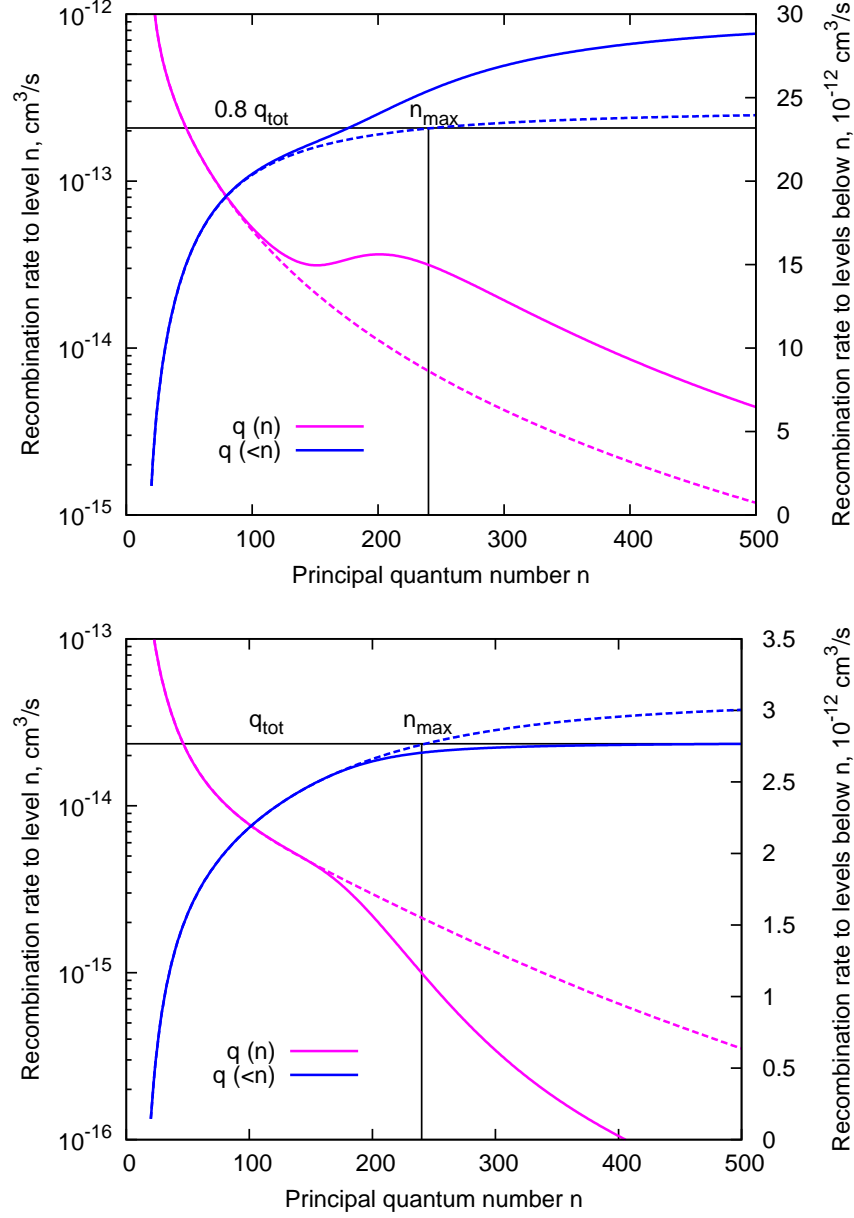


Figure A.2: Recombination rates  $q$  of  $\text{O}^{5+}$  for  $n_e = 5 \times 10^4 \text{ cm}^{-3}$  and  $T_e = 1 \times 10^3$  K (upper panel) and  $2 \times 10^4$  K (lower panel). The meaning of solid and dashed lines is as in Figure A.1. The plot shows both rates for a given  $n$  (magenta curves) and cumulative rates for all levels below  $n$  (blue curves). The vertical line shows the upper cutoff  $n_{\text{max}}$  used for this ion in our calculations.

The radiative recombination level-specific cross sections  $\sigma_{\text{RR}}$  were computed from hydrogenic photoionization cross sections  $\sigma_{\text{PI}}$  by applying the detailed balance relation:

$$\sigma_{\text{RR}}(\mathcal{E} \rightarrow nl) = \frac{\alpha^2 Z^2}{2} \frac{2l+1}{n^2} \frac{\nu^2}{\nu_n(\nu - \nu_n)} \sigma_{\text{PI}}(nl \rightarrow \mathcal{E}), \quad (\text{A.1})$$

where  $\mathcal{E}$  is the electron energy prior to recombination,  $h\nu_n = \text{Ry } Z^2/n^2$  is the level binding energy,  $h\nu = \mathcal{E} + h\nu_n$  is the energy of the emitted photon,  $Z$  is the recombining ion charge and  $\alpha$  is the fine-structure constant. The photoionization cross sections  $\sigma_{\text{PI}}$  were calculated by the computer program of Storey & Hummer (1991).

The level-specific radiative recombination rates  $q_{\text{RR}}(nl; T_e) \equiv \langle \sigma_{\text{RR}}(\mathcal{E} \rightarrow nl) \cdot v(\mathcal{E}) \rangle$  were then computed by numerical integration over the electron Maxwellian energy distribution for the temperature  $T_e$  (here  $v$  denotes the electron velocity).

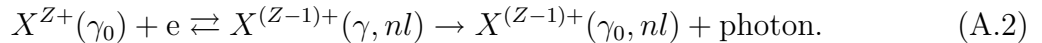
Using expressions from e.g. Spitzer (1956), it may be shown that the electron-electron collision timescale  $\tau_{\text{eec}}$  is always shorter than the cooling time  $\tau_{\text{cool}}$  at temperatures below  $10^5$  K where the line emission occurs, and electrons have enough time to reach the Maxwellian distribution. Roughly,

$$\tau_{\text{eec}} = 2.66 \text{ s} \frac{T_4^{3/2}}{n_{e,5} \ln \Lambda_C} \approx 0.16 \text{ s} \frac{T_4^{3/2}}{n_{e,5}},$$

where  $T_e = 10^4 T_4$  K,  $n_e = 10^5 n_{e,5} \text{ cm}^{-3}$  and  $\Lambda_C \approx 3.92 \times 10^7 n_{e,5}^{-1/2} T_4^{3/2}$ .

### A.3 Dielectronic recombination

The DR is a two-step process (for reviews see, e.g., Beigman et al. (1968); Shore (1969); Seaton & Storey (1976); Sobelman et al. (1981)), illustrated in the simplest case by the following diagram:



The free electron  $e$  is first resonantly captured by the ion  $X^{Z+}$  ( $Z$  denotes the ion charge) with simultaneous core electron excitation from the ground state  $\gamma_0$  to the state  $\gamma$  having excitation energy  $E_c$ . This process is called dielectronic capture. The resulting ion having two excited electrons is unstable with respect to autoionization – the inverse process of dielectronic capture.

The recombined ion then either autoionizes, or its excited core electron transits back to the ground state  $\gamma_0$  and emits a resonant line photon, thus making the ion stable against autoionization.

Therefore the level-specific dielectronic recombination rate  $q_{\text{DR}}(\gamma, nl; T_e)$  is a product of two factors: the dielectronic capture rate and the doubly-excited state stabilization probability. In the simple case described above it is expressed as

$$q_{\text{DR}}(\gamma, nl; T_e) = \left( \frac{2\pi\hbar^2}{mkT_e} \right)^{3/2} \frac{g_\gamma(2l+1)}{g_0} \frac{A_c A_a(\gamma, nl; \gamma_0)}{A_c + A_a(\gamma, nl; \gamma_0)} \exp\left(-\frac{\mathcal{E}}{kT_e}\right), \quad (\text{A.3})$$

where  $\gamma$  and  $\gamma_0$  are the recombining ion ground and excited states,  $g_\gamma$  and  $g_0$  are their statistical weights,  $A_a(\gamma, nl; \gamma_0)$  is the doubly-excited state  $(\gamma, nl)$  autoionization rate with a core electron after the autoionization moving to the ground state  $\gamma_0$ ,  $A_c$  is the core state  $\gamma$  decay rate to the ground state  $\gamma_0$  and  $\mathcal{E}$  is the electron energy prior to the recombination,  $\mathcal{E} = E_c - \text{Ry } Z^2/n^2$ .

We have determined the dielectronic recombination rates using two methods, which differ by the way they compute autoionization rates. In the first method, the autoionization rate is expressed in terms of the photoionization cross section using the dipole approximation for the inter-electronic interaction. A simple expression of this cross section and the autoionization rate in the  $n \gg 1$  limit is then obtained using the quasi-classical (QC) approach (Bureyeva & Lisitsa, 2000).

It is known that the dipole approximation is not applicable for this purpose for  $l \leq 3$  states (Beigman et al., 1981). However, this is not a serious limitation when the dielectronic capture occurs via excitation of the recombining ion core electron without a change of its principal quantum number ( $\Delta n_c = 0$ ). Such transitions are the most important ones in our case, as relevant plasma temperatures are much lower than the  $\Delta n_c > 0$  transition excitation energies.

The second method is based on the use of the program ATOM (Shevelko & Vainshtein, 1993). It computes autoionization rates by extrapolating below the threshold the electronic excitation cross section of the recombining ion core transition. This extrapolation method is based on the correspondence principle and is thus precise in the limit of  $n \gg 1$ . Both in the QC approximation and the ATOM approach, the autoionization rates decrease as  $n^{-3}$ .

Comparison plots of the DR rates of  $\text{O}^{5+}$  forming  $\text{O}^{4+}$  with recombined electrons populating all  $n$ -levels and  $n = 20$  level  $l$ -states are given in Figure A.3. It is seen that in the quasiclassical approximation, electrons populate lower  $l$ s, but higher  $n$ s. As can be inferred from Eq. (A.3), this corresponds to a sharper  $l$ -dependence of the autoionization rates. A comparison of scaled quasiclassical and quantum autoionization rates  $A_a(2p, nl; 2s) \times n^3$  of the doubly-excited oxygen ion  $\text{O}^{4+}$  is shown in Figure A.4, indeed showing the inferred dependence.

It is clear from these data that the two models for the DR rates will result in significantly different line emissivities (see also Figure 3.1). For our final results we use the ATOM rates, where available, as theoretical arguments (Shevelko & Vainshtein, 1993) show that they are more precise than the quasiclassical ones.

For ions  $\text{O}^{5+}$ ,  $\text{O}^{4+}$ ,  $\text{Si}^{4+}$ ,  $\text{Si}^{3+}$ ,  $\text{Si}^{2+}$ ,  $\text{S}^{6+}$ ,  $\text{S}^{5+}$  and  $\text{S}^{4+}$  we used the ATOM rates. For other ions we implemented the quasiclassical expressions.

Comparison of the dielectronic recombination rates with other atomic process rates is shown in Figure A.5 for the case of the  $\text{O}^{4+}$  ion with highly-excited electrons on levels  $n = 50$  and  $200$ . It is seen that dielectronic recombination populates lower  $l$ s, but is more efficient at high- $n$  levels. In the case of sufficiently high density the dielectronic recombination to low- $l$  states is followed by rapid redistribution into much higher  $l$ s resulting in enhancement of the recombination line intensities.

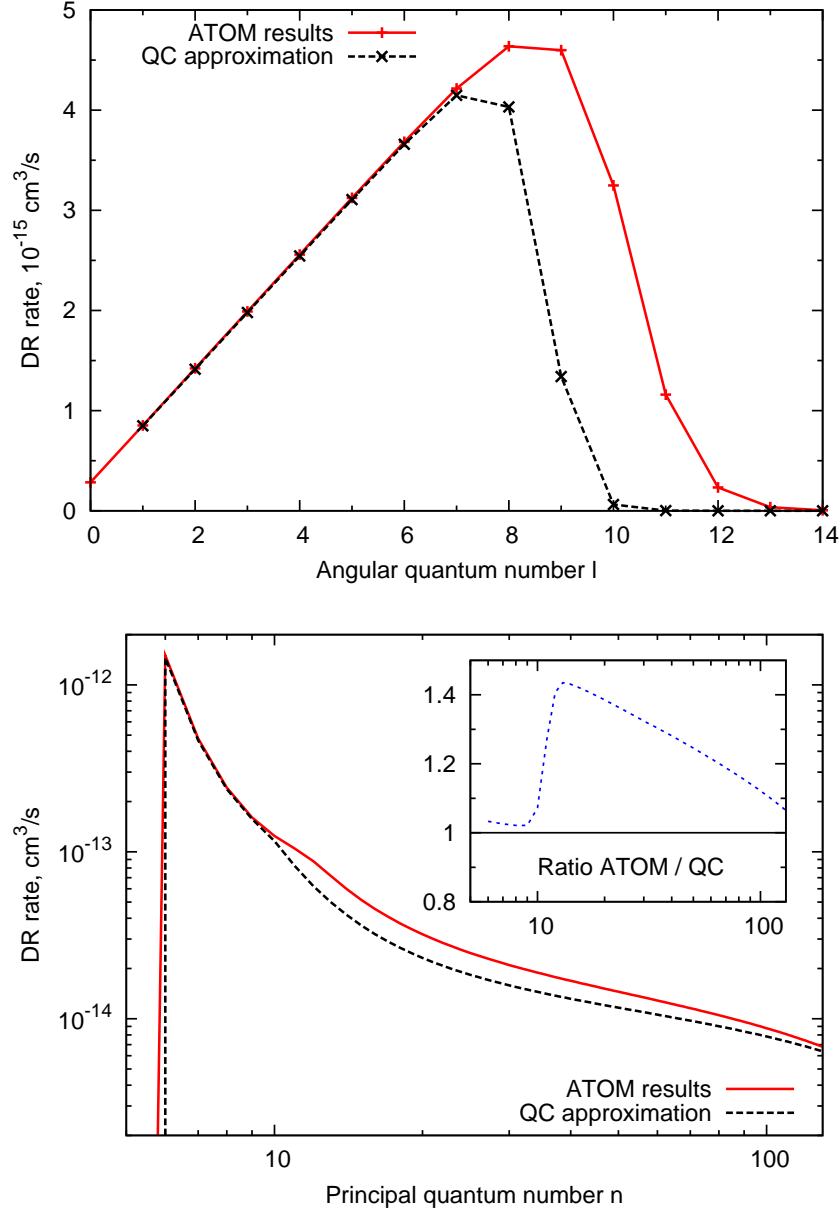


Figure A.3: Comparison of  $l$ -resolved (upper panel) and  $l$ -summed (lower panel)  $\text{O}^{5+}$  ion dielectronic recombination rates computed by the two methods described in the text: the ATOM program and the quasiclassical (QC) approximation. The values are given for  $T_e = 2 \times 10^4$  K, but the curves scale identically with temperature as long as  $T_e \ll 10^6$  K, when  $\Delta n_c > 0$  core excitations start playing a role. The  $l$ -resolved rates are given for  $n = 20$ .



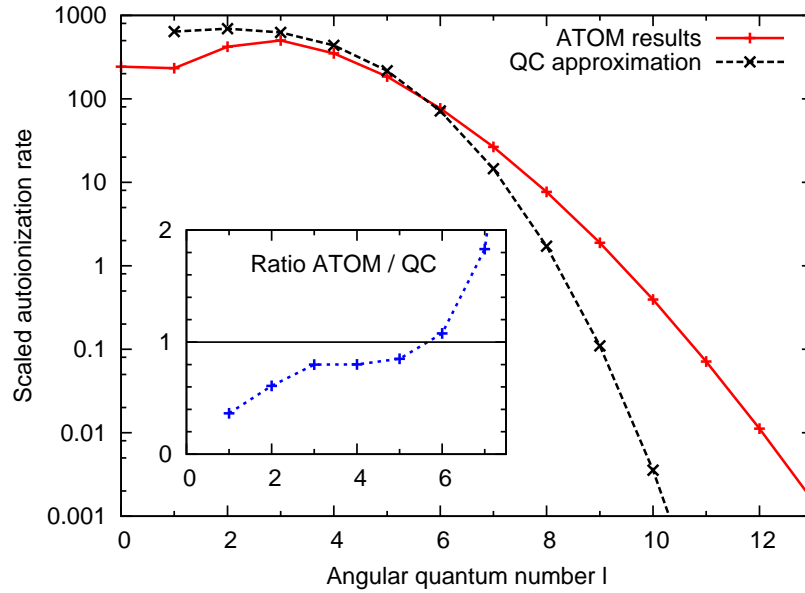


Figure A.4: Comparison of scaled autoionization rates of  $O^{4+}$  ion in  $(2p, nl)$  state autoionizing to  $O^{5+}$  ion in  $2s$  state,  $A_a(2p, nl; 2s) \times n^3$ ,  $10^{13} \text{ s}^{-1}$ , in the quasiclassical approximation and computed by the program ATOM.

## A.4 Highly-excited level energies

In hydrogen atom the energies of  $(nl)$  levels are independent of  $l$  because of the shape of the Coulomb potential. In atoms with several electrons the changes in the potential energy curve introduce variations of the highly-excited level energies  $E(nl)$  with  $l$ . This dependence is usually parametrized by the expression

$$E(nl) = \text{Ry} \frac{z^2}{(n - \mu_{nl})^2},$$

where  $\mu_{nl}$  denotes the quantum defect of the level  $(nl)$  and  $z = Z + 1$  is the ion spectroscopic symbol. The quantum defects  $\mu_{nl}$  rapidly decrease with increasing  $l$  and tend to a constant with increasing  $n$  (Seaton, 1983).

Their values are important in this study for two reasons. Firstly, level energies  $E(nl)$  and  $E(n'l')$  determine transition energies  $E(nl) - E(n'l')$  and, therefore, spectral line wavelengths. Transitions having the same values of  $n$  and  $n'$  have similar wavelengths. Small wavelength differences are in this case determined by the energy differences within  $n$  and  $n'$  groups of states – by the quantum defects of the levels.

Secondly, the collisional transition rates  $C_{nl, n'l'}$  are dependent on the energy level splitting  $|E(nl) - E(n'l')|$ , growing as this splitting decreases. Therefore the quantum defects

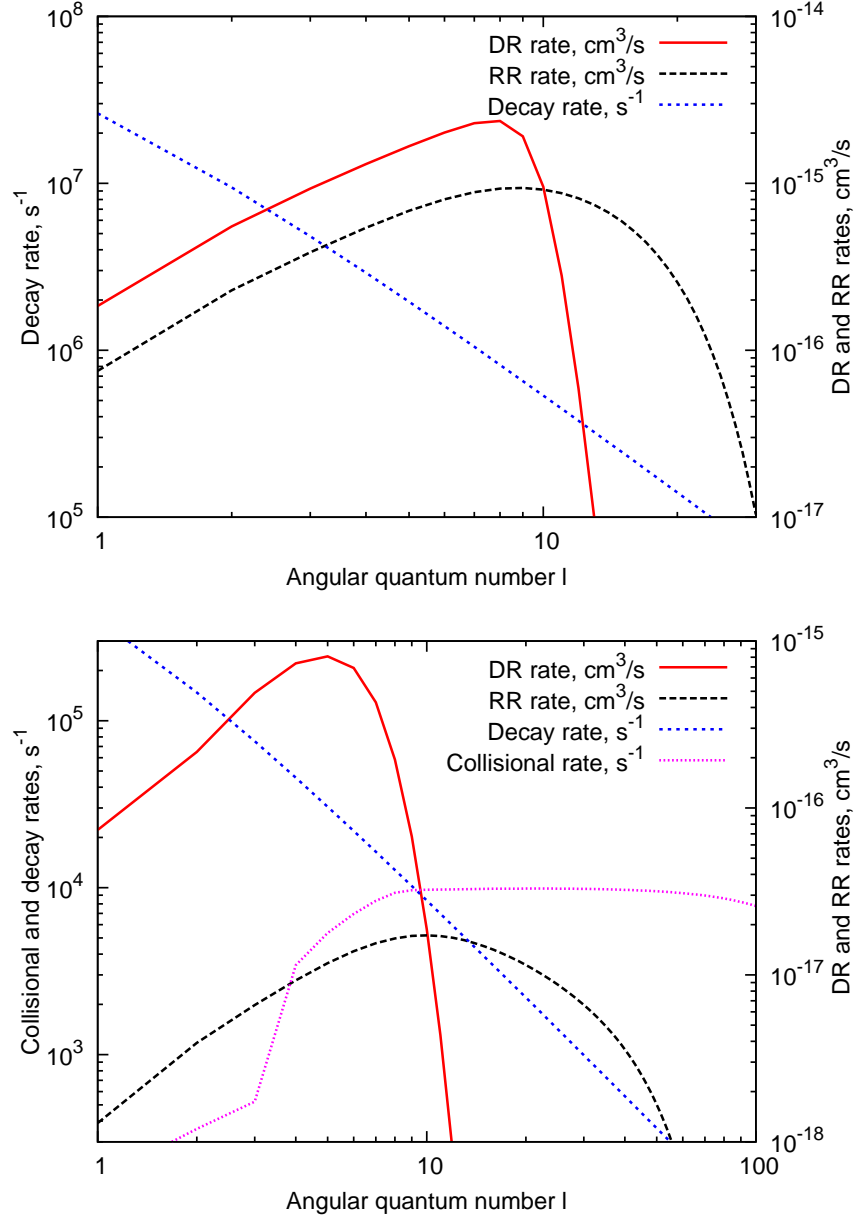


Figure A.5: Elementary process rates for the  $O^{5+}$  ion recombining to form  $O^{4+}$  with highly-excited electrons having  $n = 50$  (upper panel) and  $n = 200$  (lower panel) at electron temperature  $T_e = 2 \times 10^4$  K. Collisional rates (total for transitions to all  $l'$ ) are shown for electron density  $n_e = 5 \times 10^4$   $cm^{-3}$  and are negligibly low for the  $n = 50$  case.

in this case determine rates of  $l$ -redistribution and recombination line flux dependence on electron density in plasma.

In the case of  $l \leq 2$  the quantum defects for most ions are known and have been taken for our study from Ralchenko et al. (2007)<sup>1</sup>. In the next section we describe our method of computation of level energy shift from hydrogenic values  $E_H(nl) = \text{Ry } z^2/n^2$  for  $l > 2$  that can be expressed via quantum defects as

$$\Delta E(nl) \equiv E(nl) - E_H(nl) \approx 2\text{Ry} \frac{z^2}{n^3} \mu_l,$$

where we have assumed that  $\mu_{nl} = \mu_l$ , i.e. that the quantum defect does not depend on  $n$  and that it is small:  $\mu_l \ll 1$ .

The latter assumption is valid in our case of  $l \gg 1$ , when the  $(nl)$  states are “non-penetrating”, i.e., those in which the highly-excited electron wave function significantly differs from zero only outside the atomic core region. This property also allows us to use hydrogenic expressions for the description of such highly-excited states.

## A.5 Computation of the level shifts for high- $l$ states

Following the approach of Watson et al. (1980) and Dickinson (1981), we account for the non-penetrating  $(nl)$  state level shifts arising due to two effects: core polarizability and electrostatic quadrupole interaction with the core.

The energy shift induced by the core polarizability is proportional to the highly-excited electron radial integral  $\langle r_{nl}^{-4} \rangle$  and, expressing it with the hydrogenic formula, gives (Seaton, 1983)

$$\Delta E_p(nl) = \frac{\alpha_c}{a_0^3} \frac{z^4}{n^3} \frac{2(3 - l(l+1)/n^2)}{l(l+1)(2l-1)(2l+1)(2l+3)} \text{Ry}. \quad (\text{A.4})$$

Here  $a_0$  is the Bohr radius and  $\alpha_c$  is the core polarizability, taken for relevant ions from the handbook of Fraga et al. (1976) and the review by Lundeen (2005) and given for reference in Table A.1.

The electrostatic quadrupole interaction is absent for core states having total electronic angular momentum  $J_c < 1$  or total orbital momentum  $L_c < 1$ . If  $J_c \geq 1$ , the highly-excited electron interacts with it, splitting the  $(nl)$  level into  $2J_c + 1$  components numbered by the quantum number  $K$ , where  $\vec{K} = \vec{J}_c + \vec{l}$ . Normally, if the  $K$ -splitting is present, it is larger than the level shift due to core polarizability (Lundeen, 2005).

The quadrupole shift in this case is given by the expression (Chang, 1984):

$$\begin{aligned} \Delta E_q(nl, K) = & (-1)^{l+L_c+S_c+K} (2J_c + 1) \left\{ \begin{matrix} J_c & J_c & 2 \\ L_c & L_c & S_c \end{matrix} \right\} \times \\ & \times \left\{ \begin{matrix} J_c & J_c & 2 \\ l & l & K \end{matrix} \right\} (l || C^{(2)} || l) (L_c || C^{(2)} || L_c) \langle r_c^2 \rangle \langle r_{nl}^{-3} \rangle 2\text{Ry}, \end{aligned} \quad (\text{A.5})$$

---

<sup>1</sup>URL: <http://physics.nist.gov/asd3>

Table A.1: Atomic parameters used for computations of the line substructure.

Ion	$\langle r_c^2 \rangle$	$\alpha_c$	Ion	$\langle r_c^2 \rangle$	$\alpha_c$	Ion	$\langle r_c^2 \rangle$	$\alpha_c$
O II	1.20	1.35	Si II	4.33	11.7	S II	3.72	7.36
O III	0.97	0.94	Si III	3.79	7.42	S III	3.22	4.79
O IV	0.99	0.74	Si IV		0.20	S IV	2.44	3.24
O V	0.89	0.27				S V	2.24	1.28
O V		0.007				S VI		0.07

*Note.* Values are given in atomic units ( $a_0^2$  for  $\langle r_c^2 \rangle$  and  $a_0^3$  for  $\alpha_c$ ). Column “ion” contains the ion spectroscopic symbol.

where  $S_c$  is the total core spin momentum,  $\{::\}$  denotes a  $6j$ -symbol,  $\langle r_c^2 \rangle$  and  $\langle r_{nl}^{-3} \rangle$  are radial integrals in atomic units for core and highly-excited electrons, respectively, and  $(l||C^{(2)}||l)$ s are reduced matrix elements, given explicitly, e.g., by Sobelman (1979):

$$(l||C^{(2)}||l) = -\sqrt{\frac{l(l+1)(2l+1)}{(2l+3)(2l-1)}}.$$

The highly-excited electron radial integral can be determined using hydrogenic expression from, e.g., Bethe & Salpeter (1957). Core radial integrals  $\langle r_c^2 \rangle$  were computed for all relevant ions using radial wave functions produced by the Flexible Atomic Code (FAC, Gu (2003)). Where literature data for the  $\langle r_c^2 \rangle$  were available (Sen, 1979), the differences between them and the FAC values did not exceed about 10-15%. The values of  $\langle r_c^2 \rangle$  used in our calculations are given in Table A.1.

Expression (A.5) may be approximated in the case of P core states ( $L_c = 1$ ) and  $l \gg 1$  by

$$\begin{aligned} \Delta E_{q, \max}(nl) &\approx 0.2 \langle r_c^2 \rangle \langle r_{nl}^{-3} \rangle \text{Ry} \\ &= 0.2 \frac{z^3 \langle r_c^2 \rangle}{n^3 l(l+1)(l+1/2)} \text{Ry}, \end{aligned} \quad (\text{A.6})$$

where in this case  $\Delta E_{q, \max}(nl)$  gives the maximum shift of all the  $K$ -components. Components with both  $\Delta E_{q, \max}(nl)$  and  $-\Delta E_{q, \max}(nl)$  shifts are sometimes present.

Taking into account these effects, the total  $(nl)$  state shift to estimate the collisional  $l$ -redistribution rates was taken to be the maximum possible, i.e.,

$$\Delta E(nl) = \Delta E_{q, \max}(nl) + |\Delta E_p(nl)|.$$

As larger shifts correspond to smaller collisional cross sections, our approach may somewhat underestimate the  $l$ -redistribution rates.

We estimate that the resulting uncertainties of level splittings, in the case of the  $K$ -splitting present, correspond to the uncertainties in the electron density determination from the line ratios (see Section 3.5.2), being within a factor of about two.

## A.6 Computation of the line substructure

As the ions of different elements have different values of  $\alpha_c$  and  $\langle r_c^2 \rangle$ , the recombination line exact wavelengths will depend not only on the ion charge and the principal quantum numbers of the transition, but also on the element and the quantum numbers  $l$ ,  $l'$ ,  $K$  and  $K'$ .

From the above expressions determining energy level shifts it is possible to calculate the positions of all  $nl \rightarrow n'l'$  line components  $nlK \rightarrow n'l'K'$ . Their relative fluxes are determined by the so-called line strengths  $S$  according to the expression (Chang, 1984)

$$S(nlK, n'l'K') \propto (2K' + 1)(2K + 1) \left\{ \begin{matrix} K' & K & 1 \\ l & l' & J_c \end{matrix} \right\}^2, \quad (\text{A.7})$$

if we assume that populations of the  $(nlK)$ -states are proportional to their statistical weights, i.e.  $(2K + 1)$ .

It was shown by Chang (1984) that electrons in the  $l = 3$  levels in Si I still partially penetrate the core. Therefore also in our case the Si and S line substructure is described adequately only for  $l > 3$ . We give results also for  $l = 3$ , but the precision of line position predictions in this case is expected to be rather limited.

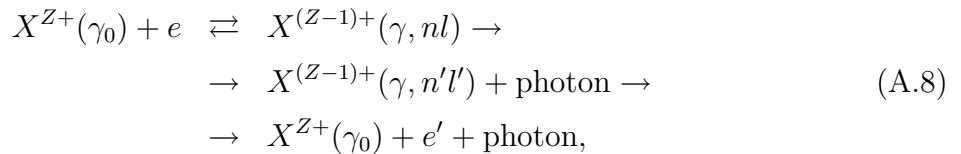
In the post-shock plasma of the fast moving knots, the density is high enough to establish a significant population of lowest excited fine-structure sublevels (Smeding & Pottasch, 1979) that have typical excitation energies corresponding to temperatures of several hundred Kelvin.

In some cases such excited state populations strongly change the line substructure. For example, in the  $\text{O}^{3+}$  ion, the ground state  $^2P_{1/2}$  has  $J_c = 1/2$  and a quadrupole interaction with it is absent. However, the lowest excited state  $^2P_{3/2}$  of this ion has  $J_c = 3/2$ . If the core electron is in the excited state prior to recombination, or arriving there after the DR process, the highly-excited levels will possess  $K$ -splitting and the resulting recombination lines will have a much richer substructure.

In our analysis we assume populations of the  $J_c$  sublevels proportional to their statistical weights.

## A.7 Line emission without recombination

We also account for the following process, mostly not resulting in a recombination, but contributing, sometimes noticeably, to the spectral line emissivities:



i.e., highly-excited electron transitions instead of core transitions, followed by the captured electron autoionization. This process may be quite efficient for increasing  $\Delta n = 1$  transition

emissivities, as the radiative transition rates for the captured electron may be significantly higher than that of the core electron, if the core transition rate is low.

This is the case for  $\Delta n_c = 0$  transitions, mostly contributing to the DR at relatively low temperatures. The rate of the described process (“dielectronic capture with line emission”, DCL) forming a line from the transition  $(nl) \rightarrow (n'l')$  may be easily expressed via the rate of the dielectronic recombination as

$$q_{\text{DCL}}(\gamma, nl, n'l'; T_e) = q_{\text{DR}}(\gamma, nl; T_e) \frac{A_{nl, n'l'}}{A_c}. \quad (\text{A.9})$$

As the autoionization rates are much higher than the radiative transition rates within the ion, the probability of DCL is low and after the first captured electron transition it autoionizes, if it is energetically allowed.

To produce a noticeable effect, highly-excited electron transition rates should be at least comparable to the core transition rates, as DCL does not produce cascades. Therefore, only transitions between lower  $ns$  contribute significantly to the additional emission in lines. In the case of  $\text{O}^{5+}$ , the described process increases the DR contribution to the recombination line emissivity by roughly 5% for the  $8\alpha$  and  $7\alpha$  lines. From Eq. (A.9) it is clear that this fraction does not depend on temperature.

## A.8 Estimates of the resulting uncertainties

Given the number of approximations made to achieve the final results – the metal recombination line emissivities and wavelengths – it might be useful to state explicitly the resulting uncertainties of these quantities.

The least reliable components for the calculation of the recombination line emissivities are dielectronic recombination rates and the upper cutoff position.

For the ions where the ATOM results are available, the low-density emissivity and flux uncertainties are expected to be about 10%. For the ions where the calculations are made using the quasiclassical expressions, the precision is lower and uncertainties may constitute up to 50%.

The choice of the upper cutoff  $n_{\text{max}}$  position results in an additional emissivity uncertainty of less than 10% for the DR-dominated recombinations and an emissivity underestimate of less than 20% for the RR-dominated case.

The density dependences of the line emissivities are not strong and should be reliably modeled with any additional uncertainties being below 5–10%.

The absolute oxygen line fluxes are much less confidently predicted, as their values are based on the theoretical FMK model that shows differences when compared to the observed optical-to-infrared collisional line ratios up to a factor of several (Docenko & Sunyaev, to be submitted).

The line fine structure uncertainties come from the limited precision of the input atomic data (polarizabilities and radial integrals). It is estimated to be not worse than 10–20%, thus the line fine structure should be reliable.

---

The recombination line fine structure component relative intensities are the least reliably predicted as they depend on the recombining ion ground state populations. The results given above assume equilibrium populations; this may not be true at low densities or temperatures. Therefore the observed line structure may be significantly different from expected. However, the observed line structure will allow us to place additional constraints on the electron density and temperature from the fine structure component intensities.





# Appendix B

## *Spitzer* data cube PSF size estimate

As described by Smith et al. (2007), the mathematical transformations performed by the CUBISM software change the point spread function (PSF) of the final data cube as compared to the initial PSF of the *Spitzer* IRS. This effect should be more pronounced on images having only few pixels per PSF width, such as constructed from the *Spitzer* IRS data cubes in the second order of each spectrograph module.

To determine the PSF changes induced by the data cube reconstruction, we have fit a two-dimensional Gaussian function to the shape of a point-like source 2MASS 23233176+5853204 situated in the map of the SL2 module. Such fit showed that (here  $x$  is coordinate along the individual slits and  $y$  – across them):

- The source  $x$  centroid oscillates with wavelength with amplitude of about 0.3 pixels. The  $y$  centroid stays constant to within 0.05 pixels.
- The PSFs both in  $x$  and  $y$  directions are larger than the *Spitzer* IRS true PSF, computed, e.g., by the `stinytim` software. The full width at half maximum (FWHM) in  $x$  and  $y$  directions on the spectral maps are larger than the IRS true PSF by 0.55 pixels and 0.9 pixels.

The presence of these features follows from the CUBISM algorithm description in Smith et al. (2007) paper. Although the values of the increase of PSF dimensions may seem insignificant at first, they are often comparable with the extent of the IRS true PSF (e.g., at 26  $\mu\text{m}$  the initial FWHM of the PSF is equal to 1.2 LL1 module pixel)

Not accounting for the described increase in the PSF size due to processing by the CUBISM software in our case would result in the *Spitzer* maps being seemingly more diffuse than e.g. optical maps smoothed to the IRS angular resolution.

Although we have measured these effects only in SL2 module, we assume that the same PSF broadening *in pixels* is occurring in other modules as well. This conclusion is qualitatively confirmed by visual comparison of optical maps smoothed to corresponding resolution with the data cube spectral line maps.



# Appendix C

## Derivation of the equation (4.4)

In the approximation of two homogeneous emitting regions 1 and 2 the observed line  $a$  and  $b$  flux ratio  $R \equiv I_a/I_b$  may be expressed as

$$R \equiv \frac{I_a}{I_b} = \frac{I_{a,1} + I_{a,2}}{I_{b,1} + I_{b,2}} = \frac{I_{a,1}}{I_{b,1}} \frac{I_{b,1}}{I_{b,1} + I_{b,2}} + \frac{I_{a,2}}{I_{b,2}} \left(1 - \frac{I_{b,1}}{I_{b,1} + I_{b,2}}\right)$$

Denoting the line flux ratios arising in regions 1 and 2 as  $R_1 \equiv I_{a,1}/I_{b,1}$  and  $R_2 \equiv I_{a,2}/I_{b,2}$ , and introducing the fraction of the total line  $b$  emission arising in the region 1 as

$$f_{b,1} \equiv \frac{I_{b,1}}{I_{b,1} + I_{b,2}},$$

we obtain that

$$R = R_1 f_{b,1} + R_2 (1 - f_{b,1}).$$

Expressing  $f_{b,1}$  from this linear relation, we finally derive Equation (4.4):

$$f_{b,1} = \frac{R_2 - R}{R_2 - R_1}.$$



# Bibliography

Aharonian, F., Akhperjanian, A., Barrio, J., Bernlöhr, K., Börst, H., Bojahr, H., Bolz, O., Contreras, J., Cortina, J., Denninghoff, S., Fonseca, V., Gonzalez, J., Götting, N., Heinzelmann, G., Hermann, G., Heusler, A., Hofmann, W., Horns, D., Ibarra, A., Iserlohe, C., Jung, I., Kankanyan, R., Kestel, M., Kettler, J., Kohnle, A., Konopelko, A., Kornmeyer, H., Kranich, D., Krawczynski, H., Lampeitl, H., Lopez, M., Lorenz, E., Lucarelli, F., Magnussen, N., Mang, O., Meyer, H., Mirzoyan, R., Moralejo, A., Ona, E., Padilla, L., Panter, M., Plaga, R., Plyasheshnikov, A., Prahl, J., Pühlhofer, G., Rauterberg, G., Röhring, A., Rhode, W., Rowell, G. P., Sahakian, V., Samorski, M., Schilling, M., Schröder, F., Siems, M., Stamm, W., Tluczykont, M., Völk, H. J., Wiedner, C. A., Wittek, W. (2001), *Evidence for TeV gamma ray emission from Cassiopeia A*, Astron. Astrophys., 370, 112

Albert, J., Aliu, E., Anderhub, H., Antoranz, P., Armada, A., Baixeras, C., Barrio, J. A., Bartko, H., Bastieri, D., Becker, J. K., Bednarek, W., Berger, K., Bigongiari, C., Biland, A., Bock, R. K., Bordas, P., Bosch-Ramon, V., Bretz, T., Britvitch, I., Camara, M., Carmona, E., Chilingarian, A., Coarasa, J. A., Commichau, S., Contreras, J. L., Cortina, J., Costado, M. T., Curtef, V., Danielyan, V., Dazzi, F., de Angelis, A., Delgado, C., de Los Reyes, R., de Lotto, B., Domingo-Santamaría, E., Dorner, D., Doro, M., Errando, M., Fagiolini, M., Ferenc, D., Fernández, E., Firpo, R., Flix, J., Fonseca, M. V., Font, L., Fuchs, M., Galante, N., García-López, R., Garczarczyk, M., Gaug, M., Giller, M., Goebel, F., Hakobyan, D., Hayashida, M., Hengstebeck, T., Herrero, A., Höhne, D., Hose, J., Hsu, C. C., Jacon, P., Jogler, T., Kosyra, R., Kranich, D., Kritzer, R., Laille, A., Lindfors, E., Lombardi, S., Longo, F., López, J., López, M., Lorenz, E., Majumdar, P., Maneva, G., Mannheim, K., Mansutti, O., Mariotti, M., Martínez, M., Mazin, D., Merck, C., Meucci, M., Meyer, M., Miranda, J. M., Mirzoyan, R., Mizobuchi, S., Moralejo, A., Nilsson, K., Ninkovic, J., Oña-Wilhelmi, E., Otte, N., Oya, I., Paneque, D., Panniello, M., Paoletti, R., Paredes, J. M., Pasanen, M., Pascoli, D., Pauss, F., Pegna, R., Persic, M., Peruzzo, L., Piccioli, A., Poller, M., Puchades, N., Prandini, E., Raymers, A., Rhode, W., Ribó, M., Rico, J., Rissi, M., Robert, A., Rügamer, S., Saggion, A., Sánchez, A., Sartori, P., Scalzotto, V., Scapin, V., Schmitt, R., Schweizer, T., Shayduk, M., Shinozaki, K., Shore, S. N., Sidro, N., Sillanpää, A., Sobczynska, D., Stamerra, A., Stark, L. S., Takalo, L., Temnikov, P., Tesaro, D., Teshima, M., Tonello, N., Torres, D. F., Turini, N., Vankov, H., Vitale, V., Wagner, R. M., Wibig, T., Wittek, W., Zandanel, F., Zanin,

- R., Zapatero, J. (2007), *Observation of VHE  $\gamma$ -rays from Cassiopeia A with the MAGIC telescope*, *Astron. Astrophys.*, 474, 937
- Arendt, R. G., Dwek, E., Moseley, S. H. (1999), *Newly Synthesized Elements and Pristine Dust in the Cassiopeia A Supernova Remnant*, *Astrophys. J.*, 521, 234
- Ashworth, Jr., W. B. (1980), *A Probable Flamsteed Observations of the Cassiopeia-A Supernova*, *Journal for the History of Astronomy*, 11, 1
- Baade, W., Minkowski, R. (1954), *Identification of the Radio Sources in Cassiopeia, Cygnus A, and Puppis A*, *Astrophys. J.*, 119, 206
- Baars, J. W. M., Genzel, R., Pauliny-Toth, I. I. K., Witzel, A. (1977), *The absolute spectrum of Cas A - an accurate flux density scale and a set of secondary calibrators*, *Astron. Astrophys.*, 61, 99
- Beigman, I. L., Vainshtein, L. A., Chichkov, B. N. (1981), *Dielectron Recombination*, *Soviet Physics JETP*, 3, 490
- Beigman, I. L., Vainshtein, L. A., Sunyaev, R. A. (1968), *Dielectronic Recombination*, *Soviet Physics Uspekhi*, 11, 411
- Berezhko, E. G., Völk, H. J. (2004), *Direct evidence of efficient cosmic ray acceleration and magnetic field amplification in Cassiopeia A*, *Astron. Astrophys.*, 419, L27
- Berger, P. S., Simon, M. (1972), *Solar Radio Recombination Lines*, *Astrophys. J.*, 171, 191
- Berrington, K. A., Saraph, H. E., Tully, J. A. (1998), *Atomic data from the IRON Project. XXVIII. Electron excitation of the  $^2P_{3/2}^{\circ} \rightarrow ^2P_{1/2}^{\circ}$  fine structure transition in fluorine-like ions at higher temperatures*, *Astron. Astrophys. Suppl. Ser.*, 129, 161
- Bethe, H. A., Salpeter, E. E. (1957), *Quantum Mechanics of One- and Two-Electron Atoms*, New York: Academic Press
- Bieging, J. H., Crutcher, R. M. (1986), *VLA observations of 1667 MHz OH absorption toward Cassiopeia A*, *Astrophys. J.*, 310, 853
- Bieging, J. H., Goss, W. M., Wilcots, E. M. (1991), *VLA observations of 21 centimeter H I absorption toward Cassiopeia A*, *Astrophys. J. Suppl. Ser.*, 75, 999
- Blum, R. D., Pradhan, A. K. (1992), *Rate coefficients for the excitation of infrared and ultraviolet lines in C II, N III, and O IV*, *Astrophys. J. Suppl. Ser.*, 80, 425
- Borkowski, K. J., Shull, J. M. (1990), *Pure-oxygen radiative shocks with electron thermal conduction*, *Astrophys. J.*, 348, 169
- Brault, J., Noyes, R. (1983), *Solar emission lines near 12 microns*, *Astrophys. J.*, 269, L61

- Bregman, J. N. (2007), *The Search for the Missing Baryons at Low Redshift*, Ann. Rev. Astron. Astrophys., 45, 221
- Bregman, J. N., Irwin, J. A. (2007), *The Search for Million Degree Gas through the N VII Hyperfine Line*, Astrophys. J., 666, 139
- Bureyeva, L. A., Lisitsa, V. S. (2000), *A Perturbed Atom*, Astrophysics and Space Physics Reviews, 11(1), 1
- Butler, K., Zeippen, C. J. (1994), *Atomic data from the IRON Project. V. Effective collision strengths for transitions in the ground configuration of oxygen-like ions.*, Astron. Astrophys. Suppl. Ser., 108, 1
- Carlsson, M., Rutten, R. J., Shchukina, N. G. (1992), *The formation of the MG I emission features near 12 microns*, Astron. Astrophys., 253, 567
- Cen, R., Fang, T. (2006), *Where Are the Baryons? III. Nonequilibrium Effects and Observables*, Astrophys. J., 650, 573
- Cen, R., Ostriker, J. P. (1999), *Where Are the Baryons?*, Astrophys. J., 514, 1
- Chang, E. S. (1984), *Non-penetrating Rydberg states of silicon from solar data*, Journal of Physics B: Atomic and Molecular Physics, 17, L11
- Chang, E. S., Noyes, R. W. (1983), *Identification of the solar emission lines near 12 microns*, Astrophys. J., 275, L11
- Chen, X., Weinberg, D. H., Katz, N., Davé, R. (2003), *X-Ray Absorption by the Low-Redshift Intergalactic Medium: A Numerical Study of the  $\Lambda$  Cold Dark Matter Model*, Astrophys. J., 594, 42
- Chen, Y., Wang, Q. D., Gotthelf, E. V., Jiang, B., Chu, Y.-H., Gruendl, R. (2006), *Chandra ACIS Spectroscopy of N157B: A Young Composite Supernova Remnant in a Superbubble*, Astrophys. J., 651, 237
- Chevalier, R. A., Kirshner, R. P. (1978), *Spectra of Cassiopeia A. II - Interpretation*, Astrophys. J., 219, 931
- Chevalier, R. A., Kirshner, R. P. (1979), *Abundance inhomogeneities in the Cassiopeia A supernova remnant*, Astrophys. J., 233, 154
- Churazov, E., Forman, W., Jones, C., Sunyaev, R., Böhringer, H. (2004), *XMM-Newton observations of the Perseus cluster - II. Evidence for gas motions in the core*, MNRAS, 347, 29
- Coursey, J., Schwab, D., Dragoset, R. (2005), *Atomic Weights and Isotopic Compositions (version 2.4.1)*, National Institute of Standards and Technology, Gaithersburg, MD

- Cox, D. P. (1998), *Modeling the Local Bubble*, Lecture Notes in Physics Vol. 506: IAU Colloq. 166: The Local Bubble and Beyond, 506, 121
- Cramphorn, C. K., Sazonov, S. Y., Sunyaev, R. A. (2004), *Scattering in the vicinity of relativistic jets: A method for constraining jet parameters*, Astron. Astrophys., 420, 33
- Cravens, T. E., Robertson, I. P., Snowden, S. L. (2001), *Temporal variations of geocoronal and heliospheric X-ray emission associated with the solar wind interaction with neutrals*, J. Geophys. Res., 106, 24883
- Croft, R. A. C., Di Matteo, T., Davé, R., Hernquist, L., Katz, N., Fardal, M. A., Weinberg, D. H. (2001), *Hydrodynamic Simulation of the Cosmological X-Ray Background*, Astrophys. J., 557, 67
- Danforth, C. W., Shull, J. M. (2005), *The Low- $z$  Intergalactic Medium. I. O VI Baryon Census*, Astrophys. J., 624, 555
- Davé, R., Cen, R., Ostriker, J. P., Bryan, G. L., Hernquist, L., Katz, N., Weinberg, D. H., Norman, M. L., O'Shea, B. (2001), *Baryons in the Warm-Hot Intergalactic Medium*, Astrophys. J., 552, 473
- D'Cruz, N. L., Sarazin, C. L., Dubau, J. (1998), *Excitation of the 3.071 Millimeter Hyperfine Line in Li-like  $^{57}\text{Fe}$  in Astrophysical Plasmas*, Astrophys. J., 501, 414
- de Avillez, M., Breitschwerdt, D. (2004), *From Large to Small Scales: Global Models of the ISM*, Astrophys. Space Sci., 289, 479
- Decourchelle, A., Sauvageot, J. L., Ballet, J., Aschenbach, B. (1997), *ROSAT spectro-imagery of the North Cygnus Loop.*, Astron. Astrophys., 326, 811
- Delaney, T. A. (2004), *A multiwavelength study of Cassiopeia A and Kepler's supernova remnants*, Ph.D. thesis, University of Minnesota
- Dere, K. P., Landi, E., Mason, H. E., Monsignori Fossi, B. C., Young, P. R. (1997), *CHIANTI - an atomic database for emission lines*, Astron. Astrophys. Suppl. Ser., 125, 149
- Dickinson, A. S. (1981), *Collisional L-Mixing of Rydberg States of Carbon due to Thermal Energy Charged Particles*, Astron. Astrophys., 100, 302
- Dinerstein, H. L., Lester, D. F., Rank, D. M., Werner, M. W., Wooden, D. H. (1987), *Observations of infrared emission from a fast-moving knot in Cassiopeia A*, Astrophys. J., 312, 314
- Docenko, D., Sunyaev, R. A. (2007), *Hyperfine Structure Radio Lines from Hot Gas in Elliptical Galaxies and Groups of Galaxies*, in *Heating versus Cooling in Galaxies and Clusters of Galaxies*, edited by H. Böhringer, G. W. Pratt, A. Finoguenov, P. Schuecker, 333–336



- Docenko, D., Sunyaev, R. A. (2008), *Optical and near-infrared recombination lines of oxygen ions from Cassiopeia A knots*, ArXiv e-prints, 0802.1911
- Dopita, M. A., Binette, L., Tuohy, I. R. (1984), *Radiative shock wave theory. III - The nature of the optical emission in young supernova remnants*, *Astrophys. J.*, 282, 142
- Dravskikh, A. F., Dravskikh, Z. V. (1969), *An Attempt to Detect Lines of Highly Charged Ions at 5-cm Wavelength Formed by Dielectronic Recombination in the Solar Corona.*, *Soviet Astronomy*, 13, 360
- Dufton, P. L., Kingston, A. E. (1991), *Effective collision strengths for SI II*, *MNRAS*, 248, 827
- Dunne, L., Morgan, H., Eales, S., Ivison, R., Edmunds, M. (2004), *Dust production in supernovae*, *New Astronomy Review*, 48, 611
- Dupree, A. K. (1968), *The Population of High Atomic Levels in the Solar Corona*, *Astrophys. J.*, 152, L125
- Elmegreen, B. G., Scalo, J. (2004), *Interstellar Turbulence I: Observations and Processes*, *Ann. Rev. Astron. Astrophys.*, 42, 211
- Ennis, J. A., Rudnick, L., Reach, W. T., Smith, J. D., Rho, J., DeLaney, T., Gomez, H., Kozasa, T. (2006), *Spitzer IRAC Images and Sample Spectra of Cassiopeia A's Explosion*, *Astrophys. J.*, 652, 376
- Ferguson, J. W., Korista, K. T., Ferland, G. J. (1997), *Physical Conditions of the Coronal Line Region in Seyfert Galaxies*, *Astrophys. J. Suppl. Ser.*, 110, 287
- Ferland, G. J., Korista, K. T., Verner, D. A., Ferguson, J. W., Kingdon, J. B., Verner, E. M. (1998), *CLOUDY 90: Numerical Simulation of Plasmas and Their Spectra*, *Publ. Astron. Soc. Pacific*, 110, 761
- Fesen, R. A., Hammell, M. C., Morse, J., Chevalier, R. A., Borkowski, K. J., Dopita, M. A., Gerardy, C. L., Lawrence, S. S., Raymond, J. C., van den Bergh, S. (2006), *The Expansion Asymmetry and Age of the Cassiopeia A Supernova Remnant*, *Astrophys. J.*, 645, 283
- Field, G. B. (1958), *Excitation of the Hydrogen 21-CM Line*, *Proceedings of the Institute of Radio Engineers*, 46, 240
- Fisher, V. I., Ralchenko, Y. V., Bernshtam, V. A., Goldgirsh, A., Maron, Y., Vainshtein, L. A., Bray, I. (1997), *Electron-impact-excitation cross sections of lithiumlike ions*, *Phys. Rev. A*, 56, 3726
- Fraga, S., Karkowski, J., Saxena, K. M. S. (1976), *Handbook of Atomic Data*, Elsevier, Amsterdam

- Fröhlich, C., Hauser, P., Liebendörfer, M., Martínez-Pinedo, G., Thielemann, F.-K., Bravo, E., Zinner, N. T., Hix, W. R., Langanke, K., Mezzacappa, A., Nomoto, K. (2006), *Composition of the Innermost Core-Collapse Supernova Ejecta*, *Astrophys. J.*, 637, 415
- Fukugita, M., Peebles, P. J. E. (2004), *The Cosmic Energy Inventory*, *Astrophys. J.*, 616, 643
- Galavis, M. E., Mendoza, C., Zeippen, C. J. (1995), *Atomic data from the IRON Project. X. Effective collision strengths for infrared transitions in silicon- and sulphur-like ions.*, *Astron. Astrophys. Suppl. Ser.*, 111, 347
- Gerardy, C. L., Fesen, R. A. (2001), *Near-Infrared Spectroscopy of the Cassiopeia A and Kepler Supernova Remnants*, *Astron. J.*, 121, 2781
- Gordon, M. A., Sorochenko, R. L. (2002), *Radio Recombination Lines. Their Physics and Astronomical Applications*, *Astrophysics and Space Science Library*, Vol. 282. Kluwer Academic Publishers, Dordrecht
- Gordon, W. (1929), *Zur Berechnung der Matrizen beim Wasserstoffatom*, *Annalen der Physik*, 394(8), 1031
- Greenwood, J. B., Williams, I. D., Smith, S. J., Chutjian, A. (2001), *Experimental investigation of the processes determining x-ray emission intensities from charge-exchange collisions*, *Phys. Rev. A*, 63(6), 062707
- Gregory, P. C., Kronberg, P. P., Seaquist, E. R., Hughes, V. A., Woodsworth, A., Viner, M. R., Retallack, D. (1972), *Discovery of Giant Radio Outburst from Cygnus X-3*, *Nature*, 239, 440
- Grevesse, N., Sauval, A. J. (1998), *Standard Solar Composition*, *Space Science Reviews*, 85, 161
- Griffin, D. C., Badnell, N. R. (2000), *Electron-impact excitation of  $Ne^{4+}$* , *Journal of Physics B Atomic Molecular Physics*, 33, 4389
- Griffin, D. C., Mitnik, D. M., Badnell, N. R. (2001), *Electron-impact excitation of  $Ne^+$* , *Journal of Physics B Atomic Molecular Physics*, 34, 4401
- Gry, C., Swinyard, B., Harwood, A., Trams, N., Leeks, S., Lim, T., Sidher, S., Lloyd, C., Pezzuto, S., Molinari, S., Lorente, R., Caux, E., Polehampton, E., Chan, J., Hutchinson, G., Mueller, T., Burgdorf, M., Grundy, T. (2003), *The ISO Handbook, Volume III - LWS - The Long Wavelength Spectrometer, Version 2.1*, Series edited by T.G. Mueller, J.A.D.L. Blommaert, and P. Garcia-Lario. ESA SP-1262, ISBN No. 92-9092-968-5, ISSN No. 0379-6566. European Space Agency
- Gu, M. F. (2003), *Indirect X-Ray Line-Formation Processes in Iron L-Shell Ions*, *Astrophys. J.*, 582, 1241

- Hartmann, D. H., Predehl, P., Greiner, J., Egger, R., Truemper, J., Aschenbach, B., Iyudin, A. F., Diehl, R. D., Oberlack, U., Schoenfelder, V., Leising, M. D., The, L.-S., Timmes, F. X., Woosley, S. E., Hoffman, R., Langer, N., Garcia-Segura, G. (1997), *On Flamsteed's supernova Cas A*, Nuclear Physics A, 621, 83
- Hellsten, U., Gnedin, N. Y., Miralda-Escudé, J. (1998), *The X-Ray Forest: A New Prediction of Hierarchical Structure Formation Models*, Astrophys. J., 509, 56
- Heng, K., McCray, R. (2007), *Balmer-dominated Shocks Revisited*, Astrophys. J., 654, 923
- Hines, D. C., Rieke, G. H., Gordon, K. D., Rho, J., Misselt, K. A., Woodward, C. E., Werner, M. W., Krause, O., Latter, W. B., Engelbracht, C. W., Egami, E., Kelly, D. M., Muzerolle, J., Stansberry, J. A., Su, K. Y. L., Morrison, J. E., Young, E. T., Noriega-Crespo, A., Padgett, D. L., Gehrz, R. D., Polonski, E., Beeman, J. W., Haller, E. E. (2004), *Imaging of the Supernova Remnant Cassiopeia A with the Multiband Imaging Photometer for Spitzer (MIPS)*, Astrophys. J. Suppl. Ser., 154, 290
- Hughes, J. P., Rakowski, C. E., Burrows, D. N., Slane, P. O. (2000), *Nucleosynthesis and Mixing in Cassiopeia A*, Astrophys. J., 528, L109
- Hurford, A. P., Fesen, R. A. (1996), *Reddening Measurements and Physical Conditions for Cassiopeia A from Optical and Near-Infrared Spectra*, Astrophys. J., 469, 246
- Hwang, U., Flanagan, K. A., Petre, R. (2005), *Chandra X-Ray Observation of a Mature Cloud-Shock Interaction in the Bright Eastern Knot Region of Puppis A*, Astrophys. J., 635, 355
- Hwang, U., Laming, J. M. (2003), *Where Was the Iron Synthesized in Cassiopeia A?*, Astrophys. J., 597, 362
- Hwang, U., Laming, J. M., Badenes, C., Berendse, F., Blondin, J., Cioffi, D., DeLaney, T., Dewey, D., Fesen, R., Flanagan, K. A., Fryer, C. L., Ghavamian, P., Hughes, J. P., Morse, J. A., Plucinsky, P. P., Petre, R., Pohl, M., Rudnick, L., Sankrit, R., Slane, P. O., Smith, R. K., Vink, J., Warren, J. S. (2004), *A Million Second Chandra View of Cassiopeia A*, Astrophys. J., 615, L117
- Inogamov, N. A., Sunyaev, R. A. (2003), *Turbulence in Clusters of Galaxies and X-ray Line Profiles*, Astronomy Letters, 29, 791
- Itoh, H. (1981a), *Shock-Wave Model for the Optical Emission from Oxygen-Rich Supernova Ejecta - Part One - Pure Oxygen Case*, Publ. Astron. Soc. Japan, 33, 1
- Itoh, H. (1981b), *Shockwave Model for the Optical Emission from Oxygen-Rich Supernova Ejecta - Part Two - Precursor Region*, Publ. Astron. Soc. Japan, 33, 521
- Itoh, H. (1986), *Permitted O I line emission from oxygen nebulosities of supernova remnants*, Publ. Astron. Soc. Japan, 38, 717

- Janev, R. K., Presnyakov, L. P., Shevelko, V. P. (1985), *Physics of highly charged ions*, Springer Series in Electrophysics, Berlin: Springer, 1985
- Kaastra, J. S., Werner, N., Herder, J. W. A. d., Paerels, F. B. S., de Plaa, J., Rasmussen, A. P., de Vries, C. P. (2006), *The O VII X-Ray Forest toward Markarian 421: Consistency between XMM-Newton and Chandra*, *Astrophys. J.*, 652, 189
- Kallman, T. R., McCray, R. (1982), *X-ray nebular models*, *Astrophys. J. Suppl. Ser.*, 50, 263
- Kamper, K., van den Bergh, S. (1976), *Optical studies of Cassiopeia A. V - A definitive study of proper motions*, *Astrophys. J. Suppl. Ser.*, 32, 351
- Kamper, K. W. (1980), *Are there historical records of the Cas A supernova?*, *The Observatory*, 100, 3
- Kassim, N. E., Perley, R. A., Dwarakanath, K. S., Erickson, W. C. (1995), *Evidence for Thermal Absorption inside Cassiopeia A*, *Astrophys. J.*, 455, L59
- Keohane, J. W., Rudnick, L., Anderson, M. C. (1996), *A Comparison of X-Ray and Radio Emission from the Supernova Remnant Cassiopeia A*, *Astrophys. J.*, 466, 309
- Kifonidis, K., Plewa, T., Janka, H.-T., Müller, E. (2003), *Non-spherical core collapse supernovae. I. Neutrino-driven convection, Rayleigh-Taylor instabilities, and the formation and propagation of metal clumps*, *Astron. Astrophys.*, 408, 621
- Klein, R. I., Budil, K. S., Perry, T. S., Bach, D. R. (2003), *The Interaction of Supernova Remnants with Interstellar Clouds: Experiments on the Nova Laser*, *Astrophys. J.*, 583, 245
- Laming, J. M., Hwang, U. (2003), *On the Determination of Ejecta Structure and Explosion Asymmetry from the X-Ray Knots of Cassiopeia A*, *Astrophys. J.*, 597, 347
- Landi, E., Del Zanna, G., Young, P. R., Dere, K. P., Mason, H. E., Landini, M. (2006), *CHIANTI-An Atomic Database for Emission Lines. VII. New Data for X-Rays and Other Improvements*, *Astrophys. J. Suppl. Ser.*, 162, 261
- Lazendic, J. S., Dewey, D., Schulz, N. S., Canizares, C. R. (2006), *The Kinematic and Plasma Properties of X-Ray Knots in Cassiopeia A from the Chandra HETGS*, *Astrophys. J.*, 651, 250
- Lennon, D. J., Burke, V. M. (1994), *Atomic data from the IRON project. II. Effective collision strength  $S$  for infrared transitions in carbon-like ions*, *Astron. Astrophys. Suppl. Ser.*, 103, 273
- Liang, H., Dickey, J. M., Moorey, G., Ekers, R. D. (1997), *Observations of the  $^{57}\text{Fe}^{+23}$  hyperfine transition in clusters of galaxies.*, *Astron. Astrophys.*, 326, 108

- Liebe, H. J., Rosenkranz, P. W., Hufford, G. A. (1992), *Atmospheric 60-GHz oxygen spectrum - New laboratory measurements and line parameters*, Journal of Quantitative Spectroscopy and Radiative Transfer, 48, 629
- Liszt, H., Lucas, R. (1999), *86 and 140 GHz radiocontinuum maps of the Cassiopeia A SNR*, Astron. Astrophys., 347, 258
- Liu, X.-W., Luo, S.-G., Barlow, M. J., Danziger, I. J., Storey, P. J. (2001), *Chemical abundances of planetary nebulae from optical recombination lines - III. The Galactic bulge PN M 1-42 and M 2-36*, MNRAS, 327, 141
- Lu, F. J., Aschenbach, B. (2000), *Spatially resolved X-ray spectroscopy of the Vela supernova remnant*, Astron. Astrophys., 362, 1083
- Lundeen, S. R. (2005), *Fine Structure in High-l Rydberg states: A Path to Properties of Positive Ions*, volume 52 of *Advances in Atomic, Molecular, and Optical Physics*, 161–208, Academic Press, edited by Chun C. Lin and Paul Berman
- Malik, G. P., Malik, U., Varma, V. S. (1991), *Recalculation of radial matrix integrals for the electric dipole transitions in hydrogen*, Astrophys. J., 371, 418
- Markert, T. H., Clark, G. W., Winkler, P. F., Canizares, C. R. (1983), *High-velocity, asymmetric Doppler shifts of the X-ray emission lines of Cassiopeia A*, Astrophys. J., 268, 134
- Martin, C. L. (1999), *Properties of Galactic Outflows: Measurements of the Feedback from Star Formation*, Astrophys. J., 513, 156
- Mazzotta, P., Mazzitelli, G., Colafrancesco, S., Vittorio, N. (1998), *Ionization balance for optically thin plasmas: Rate coefficients for all atoms and ions of the elements H to NI*, Astron. Astrophys. Suppl. Ser., 133, 403
- McKee, C. F., Cowie, L. L. (1975), *The interaction between the blast wave of a supernova remnant and interstellar clouds*, Astrophys. J., 195, 715
- McKee, C. F., Ostriker, J. P. (1977), *A theory of the interstellar medium - Three components regulated by supernova explosions in an inhomogeneous substrate*, Astrophys. J., 218, 148
- Megn, A. V., Braude, S. Y., Rashkovskij, S. L., Shepelev, V. A., Sharykin, N. K., Galanin, V. V., Litvinenko, O. A., Inyutin, G. A., Khristenko, A. D., Podgornyy, G. S. (1993), *An investigation of the Cassiopeia A radio-image in the decameter range*, Astrophys. Space Sci., 201, 79
- Minkowski, R. (1957), *Optical investigations of radio sources (Introductory Lecture)*, in *Radio astronomy*, edited by H. C. van de Hulst, volume 4 of *IAU Symposium*, 107

- Minkowski, R., Aller, L. H. (1954), *The Spectrum of the Radio Source in Cassiopeia.*, Astrophys. J., 119, 232
- Murcray, F. J., Goldman, A., Murcray, F. H., Bradford, C. M., Murcray, D. G., Coffey, M. T., Mankin, W. G. (1981), *Observation of new emission lines in the infrared solar spectrum near 12.33, 12.22, and 7.38 microns*, Astrophys. J., 247, L97
- Nicastro, F., Mathur, S., Elvis, M., Drake, J., Fiore, F., Fang, T., Fruscione, A., Krongold, Y., Marshall, H., Williams, R. (2005), *Chandra Detection of the First X-Ray Forest along the Line of Sight To Markarian 421*, Astrophys. J., 629, 700
- Norman, M. L., Bryan, G. L. (1999), *Cluster Turbulence*, in *The Radio Galaxy Messier 87*, edited by H.-J. Röser, K. Meisenheimer, volume 530 of *Lecture Notes in Physics*, Berlin Springer Verlag, 106–115
- Oreshkina, N. S., Glazov, D. A., Volotka, A. V., Shabaev, V. M., Tupitsyn, I. I., Plunien, G. (2008), *Radiative and interelectronic-interaction corrections to the hyperfine splitting in highly charged B-like ions*, Physics Letters A, 372, 675
- Osterbrock, D. E., Ferland, G. J. (2006), *Astrophysics of Gaseous Nebulae and Active Galactic Nuclei, 2nd. ed.*, University Science Books
- Oya, H., Iizima, M. (2003), *Mapping of the Decameter Radio Sources of Cassiopeia A Using a 100 km Range Long-Baseline Interferometer: Verification of a New Method of Phase Calibration of Interferometers*, Publ. Astron. Soc. Japan, 55, 527
- Patnaude, D. J., Fesen, R. A. (2005), *Model Simulations of a Shock-Cloud Interaction in the Cygnus Loop*, Astrophys. J., 633, 240
- Peimbert, M., Peimbert, A., Ruiz, M. T., Esteban, C. (2004), *Physical Conditions of the Planetary Nebula NGC 5315 Derived from VLT Echelle Observations and the  $t^2$  Problem*, Astrophys. J. Suppl. Ser., 150, 431
- Peimbert, M., van den Bergh, S. (1971), *Optical Studies of Cassiopeia A. IV. Physical Conditions in the Gaseous Remnant*, Astrophys. J., 167, 223
- Pelan, J., Berrington, K. A. (1995), *Atomic data from the IRON Project. IX. Electron excitation of the  $^2P_{3/2}^{\circ} - ^2P_{1/2}^{\circ}$  fine-structure transition in chlorine-like ions, from AR II to NI XII.*, Astron. Astrophys. Suppl. Ser., 110, 209
- Pengelly, R. M., Seaton, M. J. (1964), *Recombination spectra, II*, MNRAS, 127, 165
- Pequignot, D., Petitjean, P., Boisson, C. (1991), *Total and effective radiative recombination coefficients*, Astron. Astrophys., 251, 680

- Poglitsch, A., Waelkens, C., Bauer, O. H., Cepa, J., Feuchtgruber, H., Henning, T., van Hoof, C., Kerschbaum, F., Lemke, D., Renotte, E., Rodriguez, L., Saraceno, P., Vandenbussche, B. (2006), *The photodetector array camera and spectrometer (PACS) for the Herschel Space Observatory*, in *Space Telescopes and Instrumentation I: Optical, Infrared, and Millimeter*. Edited by Mather, John C.; MacEwen, Howard A.; de Graauw, Mattheus W. M., volume 6265 of *Proceedings of the SPIE*, 62650B
- Ralchenko, Y., Jou, F.-C., Kelleher, D., Kramida, A., Musgrove, A., Reader, J., Wiese, W., Olsen, K. (2007), *NIST Atomic Spectra Database (version 3.1.3)*, National Institute of Standards and Technology, Gaithersburg, MD
- Ramsbottom, C. A., Hudson, C. E., Norrington, P. H., Scott, M. P. (2007), *Electron-impact excitation of Fe II. Collision strengths and effective collision strengths for low-lying fine-structure forbidden transitions*, *Astron. Astrophys.*, 475, 765
- Rasmussen, A. P., Kahn, S. M., Paerels, F., Herder, J. W. d., Kaastra, J., de Vries, C. (2007), *On the Putative Detection of  $z > 0$  X-Ray Absorption Features in the Spectrum of Mrk 421*, *Astrophys. J.*, 656, 129
- Rebusco, P., Churazov, E., Böhringer, H., Forman, W. (2005), *Impact of stochastic gas motions on galaxy cluster abundance profiles*, *MNRAS*, 359, 1041
- Reed, J. E., Hester, J. J., Fabian, A. C., Winkler, P. F. (1995), *The Three-dimensional Structure of the Cassiopeia A Supernova Remnant. I. The Spherical Shell*, *Astrophys. J.*, 440, 706
- Reynoso, E. M., Goss, W. M. (2002), *Very Large Array Observations of 6 Centimeter  $H_2CO$  in the Direction of Cassiopeia A*, *Astrophys. J.*, 575, 871
- Rho, J., Kozasa, T., Reach, W. T., Smith, J. D., Rudnick, L., DeLaney, T., Ennis, J. A., Gomez, H., Tappe, A. (2008), *Freshly Formed Dust in the Cassiopeia A Supernova Remnant as Revealed by the Spitzer Space Telescope*, *Astrophys. J.*, 673, 271
- Ricker, P. M., Sarazin, C. L. (2001), *Off-Axis Cluster Mergers: Effects of a Strongly Peaked Dark Matter Profile*, *Astrophys. J.*, 561, 621
- Riffel, R., Rodríguez-Ardila, A., Pastoriza, M. G. (2006), *A 0.8-2.4  $\mu m$  spectral atlas of active galactic nuclei*, *Astron. Astrophys.*, 457, 61
- Rubin, R. H., Dufour, R. J., Geballe, T. R., Colgan, S. W. J., Harrington, J. P., Lord, S. D., Liao, A. L., Levine, D. A. (2001), *Infrared Spectroscopy of Atomic Lines in Gaseous Nebulae*, in *Spectroscopic Challenges of Photoionized Plasmas*, edited by G. Ferland, D. W. Savin, volume 247 of *Astronomical Society of the Pacific Conference Series*, 479
- Rybicki, G. B., Lightman, A. P. (1979), *Radiative processes in astrophysics*, New York, Wiley-Interscience, 1979. 393 p.

- Ryde, N., Richter, M. J. (2004), *Nonthermal Mg I Emission at 12 Micron from Procyon*, *Astrophys. J.*, 611, L41
- Ryle, M., Smith, F. G. (1948), *A new intense source of radio frequency radiation in the constellation of Cassiopeia*, *Nature*, 162, 462
- Sanders, W. T., Henry, R. C., Bregman, J. N., Cen, R., Cox, D. P., Croft, R. A. C., Hammond, E. C., Hurwitz, M. V., Kimble, R. A., McCammon, D., McKee, C., Murthy, J., Phillips, L. A., Porter, F. S., Raymond, J. C., Serlemitsos, P. J., Shelton, R. L., Smith, R. K., Stahle, C. K., Szymkowiak, A. E. (2003), *Proposed SMEX to spectrally analyze the diffuse x-ray background: The Baryonic Extragalactic Structure Tracer (BEST)*, in *X-Ray and Gamma-Ray Telescopes and Instruments for Astronomy. Edited by Joachim E. Truemper, Harvey D. Tananbaum.*, edited by J. E. Truemper, H. D. Tananbaum, volume 4851 of *Proceedings of the SPIE*, 388–395
- Sazonov, S. Y., Ostriker, J. P., Sunyaev, R. A. (2004), *Quasars: the characteristic spectrum and the induced radiative heating*, *MNRAS*, 347, 144
- Schekochihin, A. A., Cowley, S. C. (2006), *Turbulence, magnetic fields, and plasma physics in clusters of galaxies*, *Physics of Plasmas*, 13, 6501
- Schild, R. E. (1977), *Interstellar reddening law*, *Astron. J.*, 82, 337
- Schuecker, P., Finoguenov, A., Miniati, F., Böhringer, H., Briel, U. G. (2004), *Probing turbulence in the Coma galaxy cluster*, *Astron. Astrophys.*, 426, 387
- Schwab, F. R., Hogg, D. E. (1989), *Millimeter-Wave Atmospheric Opacity and Transparency Curves*, Technical report, Millimeter Array Memo No. 58
- Seaton, M. J. (1955), *Further Calculations on Electron Excitation of Forbidden Lines: Transitions with Electric Quadrupole Moments*, *Proceedings of the Royal Society of London. Series A, Mathematical and Physical Sciences*, 231(1184), 37
- Seaton, M. J. (1964), *Recombination spectra, III*, *MNRAS*, 127, 177
- Seaton, M. J. (1983), *Quantum defect theory*, *Reports of Progress in Physics*, 46, 167
- Seaton, M. J., Storey, P. J. (1976), *Di-electronic recombination.*, in *Atomic processes and applications. P. G. Burke (ed.)*, North-Holland Publ. Co., Amsterdam, Netherlands, 133–197
- Sen, K. D. (1979), *Atomic quadrupole moments:  $np^2(n+1)s$  excited-state configuration of N, P, As, and Sb*, *Phys. Rev. A*, 20, 2276
- Shabaev, V. M. (1994), *Hyperfine structure of hydrogen-like ions*, *Journal of Physics B Atomic Molecular Physics*, 27, 5825



- Shabaev, V. M., Shabaeva, M. B., Tupitsyn, I. I. (1995), *Hyperfine structure of hydrogenlike and lithiumlike atoms*, Phys. Rev. A, 52, 3686
- Shabaev, V. M., Shabaeva, M. B., Tupitsyn, I. I. (1997), *Hyperfine structure of lithiumlike atoms*, Astronomical and Astrophysical Transactions, 12, 243
- Shevelko, V. P., Vainshtein, L. A. (1993), *Atomic physics for hot plasmas*, Bristol: IOP Publishing
- Shimabukuro, F. I., Wilson, W. J. (1973), *Search for Solar Recombination Lines in the Frequency Range 110-115 GHZ*, Astrophys. J., 183, 1025
- Shklovskii, I. S. (1968), *Supernovae*, London, New York, etc.: Wiley
- Shore, B. W. (1969), *Dielectronic Recombination*, Astrophys. J., 158, 1205
- Simcoe, R. A., Sargent, W. L. W., Rauch, M. (2002), *Characterizing the Warm-Hot Intergalactic Medium at High Redshift: A High-Resolution Survey for O VI at  $z = 2.5$* , Astrophys. J., 578, 737
- Simcoe, R. A., Sargent, W. L. W., Rauch, M. (2004), *The Distribution of Metallicity in the Intergalactic Medium at  $z \sim 2.5$ : O VI and C IV Absorption in the Spectra of Seven QSOs*, Astrophys. J., 606, 92
- Smeding, A. G., Pottasch, S. R. (1979), *Population ratios of fine structure levels*, Astron. Astrophys. Suppl. Ser., 35, 257
- Smith, J. D. T., Armus, L., Dale, D. A., Roussel, H., Sheth, K., Buckalew, B. A., Jarrett, T. H., Helou, G., Kennicutt, Jr., R. C. (2007), *Spectral Mapping Reconstruction of Extended Sources*, Publ. Astron. Soc. Pacific, 119, 1133
- Smith, R. K., Brickhouse, N. S., Liedahl, D. A., Raymond, J. C. (2001), *Collisional Plasma Models with APEC/APED: Emission-Line Diagnostics of Hydrogen-like and Helium-like Ions*, Astrophys. J., 556, L91
- Smith, R. K., Edgar, R. J., Plucinsky, P. P., Wargelin, B. J., Freeman, P. E., Biller, B. A. (2005), *Chandra Observations of MBM 12 and Models of the Local Bubble*, Astrophys. J., 623, 225
- Sobelman, I. I. (1979), *Atomic spectra and radiative transitions*, Springer Series in Chemical Physics, Berlin: Springer
- Sobelman, I. I., Vainshtein, L. A., Yukov, E. A. (1981), *Excitation of atoms and broadening of spectral lines*, Springer Series in Chemical Physics 7, Berlin: Springer
- Sobolev, V. V. (1963), *A treatise on radiative transfer.*, Princeton, N.J., Van Nostrand
- Spitzer, L. (1956), *Physics of Fully Ionized Gases*, New York: Interscience Publishers

- Stephenson, F. R., Green, D. A. (2002), *Historical supernovae and their remnants*, International series in astronomy and astrophysics, vol. 5. Oxford: Clarendon Press, ISBN 0198507666
- Storey, P. J., Hummer, D. G. (1991), *Fast computer evaluation of radiative properties of hydrogenic systems*, Computer Physics Communications, 66, 129
- Summers, H. P. (1977), *The recombination and level populations of ions. II - Resolution of angular momentum states*, MNRAS, 178, 101
- Sun, M., Jones, C., Forman, W., Vikhlinin, A., Donahue, M., Voit, M. (2007), *X-Ray Thermal Coronae of Galaxies in Hot Clusters: Ubiquity of Embedded Mini-Cooling Cores*, Astrophys. J., 657, 197
- Sunyaev, R. A., Churazov, E. M. (1984), *Millimeter Wavelength Lines of Heavy Elements Predicted from the Hot Gas in Supernova Remnants and Galaxy Clusters*, Soviet Astronomy Letters, 10, 201
- Sunyaev, R. A., Docenko, D. O. (2007), *Hydrogen-like nitrogen radio line from hot interstellar and warm-hot intergalactic gas*, Astronomy Letters, 33, 67
- Sunyaev, R. A., Norman, M. L., Bryan, G. L. (2003), *On the Detectability of Turbulence and Bulk Flows in X-ray Clusters*, Astronomy Letters, 29, 783
- Sutherland, R. S., Dopita, M. A. (1993), *Cooling functions for low-density astrophysical plasmas*, Astrophys. J. Suppl. Ser., 88, 253
- Sutherland, R. S., Dopita, M. A. (1995a), *Young oxygen-rich supernova remnants. 1: Observations of three southern remnants*, Astrophys. J., 439, 365
- Sutherland, R. S., Dopita, M. A. (1995b), *Young oxygen-rich supernova remnants. 2: an oxygen-rich emission mechanism*, Astrophys. J., 439, 381
- Takei, Y., Ohashi, T., Henry, J. P., Mitsuda, K., Fujimoto, R., Tamura, T., Yamasaki, N. Y., Hayashida, K., Tawa, N., Matsushita, K., Bautz, M. W., Hughes, J. P., Madejski, G. M., Kelley, R. L., Arnaud, K. A. (2007), *Search for Oxygen Emission from Warm-Hot Intergalactic Medium around A2218 with Suzaku*, Publ. Astron. Soc. Japan, 59, 339
- Tayal, S. S. (2000), *Electron Collision Excitation of Fine-Structure Levels in S IV*, Astrophys. J., 530, 1091
- Tayal, S. S. (2006), *Breit-Pauli R-Matrix Calculation for Electron Collision Rates in O IV*, Astrophys. J. Suppl. Ser., 166, 634
- Tayal, S. S., Gupta, G. P. (1999), *Collision Strengths for Electron Collision Excitation of Fine-Structure Levels in S III*, Astrophys. J., 526, 544

- Thom, C., Chen, H.-W. (2008), *A STIS Survey for OVI Absorption Systems at  $0.12 < z < 0.5$  II.: Physical Conditions of the Ionised Gas*, ArXiv e-prints, 0801.2381
- Thompson, R. I. (1996), *Si X Forbidden Emission in NGC 1068 and NGC 7469*, *Astrophys. J.*, 459, L61
- Townes, C. H., Schawlow, A. L. (1955), *Microwave Spectroscopy*, *Microwave Spectroscopy*, New York: McGraw-Hill, 1955
- Tsuru, T. G., Ozawa, M., Hyodo, Y., Matsumoto, H., Koyama, K., Awaki, H., Fujimoto, R., Griffiths, R., Kilbourne, C., Matsushita, K., Mitsuda, K., Ptak, A., Ranalli, P., Yamasaki, N. Y. (2007), *X-Ray Spectral Study of the Extended Emission, 'the Cap', Located 11.6kpc above the Disk of M82*, *Publ. Astron. Soc. Japan*, 59, 269
- van de Hulst, H. C. (1945), *Radiogolven uit de wereldruimte*, *Nederlands Tijdschrift voor Natuurkunde*, 11, 201
- van den Bergh, S. (1971), *Optical Studies of Cassiopeia A. III. Spectra of the Supernova Remnant*, *Astrophys. J.*, 165, 457
- van den Bergh, S., Dodd, W. W. (1970), *Optical Studies of Cassiopeia A. I. Proper Motions in the Optical Remnant*, *Astrophys. J.*, 162, 485
- Vanden Bout, P. A., Solomon, P. M., Maddalena, R. J. (2004), *High-Redshift HCN Emission: Dense Star-forming Molecular Gas in IRAS F10214+4724*, *Astrophys. J.*, 614, L97
- Vinyaikin, E. N., Nikonov, V. A., Tarasov, A. F., Tokarev, Y. V., Yurishchev, M. A. (1987), *Spectrum of Low-Frequency Radio Emission of Cassiopeia-A*, *Soviet Astronomy*, 31, 517
- Voges, W., Aschenbach, B., Boller, T., Bräuninger, H., Briel, U., Burkert, W., Dennerl, K., Englhauser, J., Gruber, R., Haberl, F., Hartner, G., Hasinger, G., Kürster, M., Pfeffermann, E., Pietsch, W., Predehl, P., Rosso, C., Schmitt, J. H. M. M., Trümper, J., Zimmermann, H. U. (1999), *The ROSAT all-sky survey bright source catalogue*, *Astron. Astrophys.*, 349, 389
- Vogt, C., Enßlin, T. A. (2005), *A Bayesian view on Faraday rotation maps Seeing the magnetic power spectra in galaxy clusters*, *Astron. Astrophys.*, 434, 67
- Vrinceanu, D., Flannery, M. R. (2001), *Classical and quantal collisional Stark mixing at ultralow energies*, *Phys. Rev. A*, 63(3), 032701
- Watson, W. D., Western, L. R., Christensen, R. B. (1980), *A new, dielectronic-like recombination process for low temperatures and the radio recombination lines of carbon*, *Astrophys. J.*, 240, 956

- Wheeler, J. C., Maund, J. R., Couch, S. M. (2008), *The Shape of Cas A*, *Astrophys. J.*, 677, 1091
- Willingale, R., Bleeker, J. A. M., van der Heyden, K. J., Kaastra, J. S. (2003a), *The mass and energy budget of Cassiopeia A*, *Astron. Astrophys.*, 398, 1021
- Willingale, R., Bleeker, J. A. M., van der Heyden, K. J., Kaastra, J. S., Vink, J. (2002), *X-ray spectral imaging and Doppler mapping of Cassiopeia A*, *Astron. Astrophys.*, 381, 1039
- Willingale, R., Hands, A. D. P., Warwick, R. S., Snowden, S. L., Burrows, D. N. (2003b), *The X-ray spectrum of the North Polar Spur*, *MNRAS*, 343, 995
- Wright, M., Dickel, J., Koralesky, B., Rudnick, L. (1999), *The Supernova Remnant Cassiopeia A at Millimeter Wavelengths*, *Astrophys. J.*, 518, 284
- Zel'dovich, Y. B., Raizer, Y. P. (1967), *Physics of shock waves and high-temperature hydrodynamic phenomena*, New York: Academic Press, edited by Hayes, W.D.; Probstein, Ronald F.
- Zhang, H. L., Graziani, M., Pradhan, A. K. (1994), *Atomic data from the IRON project. 3: Rate coefficients for electron impact excitation of boron-like ions: Ne VI, Mg VIII, Al IX, Si X, S XII, Ar XIV, Ca XVI and Fe XXII*, *Astron. Astrophys.*, 283, 319
- Zhang, H. L., Sampson, D. H. (1997), *Effective collision strengths for hyperfine structure transitions of possible astrophysical interest*, *MNRAS*, 292, 133
- Zhang, H. L., Sampson, D. H. (2000), *Effective collision strengths for hyperfine-structure transitions with inclusion of resonance effects*, *Phys. Rev. A*, 61(2), 022707
- Zombeck, M. (2007), *Handbook of Space Astronomy and Astrophysics: Third Edition*, ISBN-10 0-521-78242-2 (HB); ISBN-13 978-0-521-78242-5 (HB). Published by Cambridge University Press, Cambridge, UK

# Acknowledgements

First, I wish to acknowledge the funding provided via the International Max Planck Research School on Astrophysics that made available these exciting studies.

I am deeply thankful to my father, who was my first teacher of physics, and my mother, who motivated me to study science further. My wife was always understanding and helping me and was always cheering me up. I am very thankful to her and to my daughter, who gave me a lot of happy moments without even being aware about it.

Before starting the PhD studies, I was influenced by my teachers of astronomy – Naum Zeitlin at school and Ilgonis Vilks at university. I am deeply grateful to them, as they were those who first showed me the beauty of the starry sky and gave an understanding of how it lives its life.

I am thankful to my thesis supervisor, Rashid Sunyaev, for his belief in my abilities and infrequent but very informative meetings. I was too rarely able to keep up with the pace he was setting for me. He was teaching me as hard as he was taught and it had influenced me and changed me a lot.

To work in science, one has to know both the language of physics and the language of people. Kate O'Shea has trained my English in the course of entire PhD studies (several years ago I might have said “she have taught all the time for me English”). Caroline D'Angelo has resolved some of the most confusing English language questions. Mark Vogelsberger have done the work that I would be totally unable to do myself – he translated the thesis summary into German.

Thank you, my colleagues and friends, both new and old ones. Discussions with Mike Revnivtsev, who was always ready to help, on the observational data analysis contained many useful advices. Discussions with Janis, Roman, Pavel, Sergei, Kate, Natalya, Tanya and Igor were never limited only by deeply scientific topics and were always a pleasure. I wouldn't become what I am now without all of you.



# Curriculum Vitae

**Name** Dmitrijs DOCENKO

## Personal details

Date of birth: 18 April 1979  
Place of birth: Riga, Latvia  
Citizenship: Latvia

## Education

since 2004	PhD student at the International Max-Planck Research School Max-Planck Institute for Astrophysics, Garching bei München, Germany
1996–2002	Master of natural sciences (M.Sc.) in Physics Bachelor of natural sciences (B.Sc.) in Physics with distinction Spectroscopy Technician (speciality) Faculty of Physics and Mathematics, University of Latvia, Riga, Latvia
1996	Purvciema ģimnāzija, Rīga, Latvia
1991–1996	Rīgas ebreju vispārīzglītojoša vidusskola, Rīga, Latvia
1989–1991	Rīgas 60. vidusskola-licejs, Rīga, Latvia
1986–1989	Rīgas 80. vidusskola, Rīga, Latvia

## Additional Scientific Education

2003	2 <sup>nd</sup> Aegean Summer School on the Early Universe, Ermoupoli, Syros, Greece
2003	13 <sup>th</sup> Juväskylä Summer School, successfully participated in courses “ <i>Modern Theory of Critical Phenomena</i> ”, “ <i>Neutrino Physics</i> ”, “ <i>Particle Astrophysics and Cosmology</i> ”, and “ <i>Inflation</i> ”, Juväskylä, Finland

2002	International Workshop “Galaxies and Chaos: Theory and Observations”, Athens, Greece
2002	Summer School on Cosmology and the High-Redshift Universe, oral presentation, Abisko, Sweden
2001	Nordita Summer School “Quantum Field Theory in Particle and Condensed Matter Physics”, Hillerød, Denmark
2001	XVII Course of the International School on Cosmology and Gravitation “Advances in the interplay between quantum and gravity physics”, Erice, Italy
1999	Nordic-Baltic Research Course in Applications of Astrophysical Photometry, oral presentation, Moletai observatory, Lithuania
1999	Nordita Master Class in Physics, Copenhagen, Denmark
1998	Practicum in Measurement Techniques, Sensorics and Lasertechnics, Fachhochschule Merseburg, Merseburg, Germany

## Honors and Awards

2002	Prize of the Latvian Academy of Sciences and stock company “RD ALFA” to students in Physics and its engineering applications
------	------------------------------------------------------------------------------------------------------------------------------

## Work experience

since 2004	Max-Planck Institute for Astrophysics, Garching, Germany Ph.D. student
since 1999	Institute of Astronomy, University of Latvia, Riga, Latvia Programming engineer (on leave)
2000–2004	“Baltic Scientific Instruments”, Ltd., Riga Head of X-ray spectroscopy department
1998	Institute of Atomic Physics and Spectroscopy, University of Latvia Laboratory assistant

## Computer skills

Data analysis	Experience with radiointerferometer (VLA, AIPS package) and X-ray telescope (Chandra, CIAO package) observation data analysis
Astronomical tools	HEAtools, XSPEC, XSTAR, Cloudy, Chianti, AtomDB, etc.
Programming	Fortran 77, IDL, Pascal, Delphi, Perl (basics), plain html
Applications	Experience with OpenOffice, Microsoft Office, Mathematica, L <sup>A</sup> T <sub>E</sub> X, GIMP, Corel Draw etc.



Operating systems   Windows (advanced user), Unix (user)

### **Non-professional interests and activities**

Popularization of astronomy and physics, X-ray fluorescence spectroscopy,  
sport orienteering, aikido

**Languages**   Russian — native, Latvian — fluent, English — fluent, German —  
basics

Garching b. München, July 9, 2008